Yukon University

Design and implementation of early detection and warning systems for transportation infrastructure impacted by permafrost-related geohazards

January 31 2022

Dr. Fabrice Calmels[1], Dr. Michel Allard[2], Dr. Daniel Fortier[3], Frances Amyot[1], Emmanuel L'Hérault[2], Michel Sliger[3], Louis-Philippe Roy[1], Cyrielle Laurent[1], Sarah Gauthier[2]

[1]YukonU Research Centre, 500 University Drive, PO BOX 2799, Whitehorse, YT Y1A 5K4;
[2]Université Laval, Pavillon Abitibi-Price, 2405 rue de la Terrasse, Québec, QC G1V 0A6;
[3]Université de Montréal, Complexe des Sciences, 1375 Avenue Thérèse-Lavoie-Roux, Montréal, QC H2V 0B3

Université de Montréal

UNIVERSITÉ LAVAL

Contributing Authors

Fabrice Calmels	YukonU Research Centre
Michel Allard	Université Laval
Daniel Fortier	Université de Montréal

Editor

Frances Amyot	YukonU Research Centre

Nunavik Chapters

Emmanuel L'Hérault	Université Laval
Sarah Gauthier	Université Laval

Yukon Chapters

Frances Amyot	YukonU Research Centre
Louis-Phillipe Roy	YukonU Research Centre
Cyrielle Laurent	YukonU Research Centre

Un sommaire français se trouve avant la table des matières

This report reflects the views of the authors and not necessarily those of Transport Canada

Executive summary

This report presents the results of a project aiming to develop an automated alarm system to warn transportation infrastructure operators of permafrost-related geohazards. While linear infrastructure like roads or airstrips can themselves cause disturbances to surrounding permafrost, so can climate change. As temperatures warm and precipitation patterns change, permafrost thaw-related geohazards such as ground subsidence and landslides are increasingly likely, which could lead to dangerous conditions and the possibility of isolating communities. To address these hazards, the research team has developed an automated system to collect data in real-time to continuously assess conditions of the ground and infrastructure using site-specific algorithms to define risk levels. Elevated risk levels are automatically communicated to infrastructure operators for action to be taken. This report outlines the three primary components of the project including: 1) conception of the system; 2) site characterizations and analyses; and 3) implementations of the system.

The alarm system uses a LoRaWan network configuration which consists of four main components: data loggers which are equipped with LoRaWan transmitters (the end-nodes), the internet gateways, the network servers, and the application. ULog data loggers were specifically designed by LogR Systems for this project, and can collect, store, and transmit ground data at regular intervals. The data is transmitted to the network servers via a Multitech Conduit internet gateway, which can also store data to prevent data loss in the event or internet or power outages. LogR Systems also developed a complete server infrastructure, which acts as a central database for data transmitted from the end nodes through a secure MQTT (Message Queuing Telemetry Transport) connection. To access and download the data from the servers and to run the risk assessment algorithms and potentially trigger alarms, an API (Application Programming Interface) has also been developed. The overall architecture of the server network and client application has been developed using the docker containers technology to be easily packaged and transferable to the client server.

The implementation phase of the alarm system is divided into two components, the Nunavik component, and the Yukon one. In Nunavik, the airstrips at the Salluit, Tasuijaq and Inukjuak airports were selected. For these sites, in-depth studies of permafrost and associated processes had already been conducted, including the dangers associated with ground subsidence and landslides that could damage the airstrips and surrounding infrastructure. These sites were also already equipped with multiple ground temperature sensors, which were used with the new ULog data loggers. LoRaWan gateways were connected in or on suitable buildings near the loggers to transmit data

from the loggers to the servers. Using the ground temperature data, site-specific algorithms were developed to trigger alarms based on threshold values for warming or active layer depth increase. In the Yukon, two sites were selected, one at kilometer 116 of the Dempster Highway, and the other at kilometer 1456 of the Alaska Highway. These two sites feature retrogressive thaw slumps that are eroding the ground adjacent to the roads and threaten to erode the roads altogether. These sites were therefore selected for in-depth analyses to better understand the geomorphological processes and develop site-appropriate algorithms. Both sites were studied using a combination of geomorphological and ground thermal regime studies, and of UAV (unmanned aerial vehicle) aerial imagery analyses. Using these analyses, strategies have been developed for alarm implementation at both sites. In fall of 2021, a prototype system was set in place to test the data recording and transmission at the Alaska Highway site.

The project has resulted in the conception and implementation of three alarm systems in Nunavik and has paved the way for installation of the alarm systems along the two major roadways of the Yukon. Moving forward, the system will benefit from technological upgrades, including using different types of sensors and using satellite communication systems to implement the systems in remote areas. Additionally, this alarm system has the potential to be adapted to environments and geohazards other than those related to permafrost-thaw in the North.

Sommaire éxécutif

Ce rapport présente les résultats d'un projet visant à développer à système d'alerte automatisé dédié à prévenir les dangers inhérents à la présence du pergélisol au contact ou à proximité des infrastructures de transport. Alors que la présence d'une infrastructure linéaire, telle qu'une route ou une piste d'atterrissage, peut causer de perturbations environnementales induisant le dégel du pergélisol sous-jacent et adjacent, les changements climatiques peuvent également provoquer une dégradation du pergélisol qui résultera dans des processus géomorphologiques, tels que des affaissements et des glissements de pente, qui endommageront sévèrement les infrastructures mais pourront également être cause de grave danger pour les usagers. Dans ce contexte, l'équipe de recherche à développer un système suivant en temps réel les conditions du terrain et de l'infrastructure, tout en envoyant les données de suivi via internet à l'ordinateur de l'opérateur de l'infrastructure. Sur réception des données, des algorithmes évaluent à la fois les risques d'endommagement de l'infrastructure mais également donnent une alerte si un événement de type catastrophique a été détecté. Ce rapport présente les trois étapes principales du projet : 1- conception du système; 2- caractérisation des sites d'implémentations, et 3- implémentation du système.

Le system d'alerte utilise un réseau LoRaWAN qui est constitué de quatre principaux composants, des enregistreurs de données dotés de transmetteurs LoRaWAN (nœuds terminaux), une passerelle internet dédiée, un serveur réseau, et l'application. L'enregistreur de données est un ULog développé par la compagnie LogR systems spécialement pour ce projet. Il mesure et enregistre des données de température à intervalle régulier dans une mémoire interne puis envoi périodiquement ces données au routeur en utilisant le protocole LoRaWAN. La passerelle, un modèle Multitech Conduit, a la capacité d'enregistrer les données transmises par l'enregistreur, les préservant de pertes dues à des coupures d'internet. Pour ce projet, LogR Systems a développé une infrastructure de serveur complète où chaque passerelle envoie les données des nœuds terminaux à un serveur centralisé à l'aide d'un MQTT sécurisé (Message Queuing Telemetry Transport). Pour accéder et télécharger les données depuis le serveur du réseau, une API a également été développée. L'API envoie des requêtes au serveur du réseau afin de récupérer des données ou toute information demandée disponible à l'aide de fonctions spécifiques. Une fois téléchargée, les données sont analysées en utilisant des algorithmes conçus spécifiquement pour le site surveillé. L'architecture globale du réseau serveur et de l'application client a été développée à l'aide de la technologie des conteneurs docker afin d'être facilement packagée et transférable sur le serveur client, le serveur du Centre d'Études Nordiques dans ce cas-ci.

La phase implémentation du système d'alerte se divise en deux volets, un au Nunavik, et un au Yukon. Au Nunavik, les pistes d'atterrissages des aéroports de Salluit, Tasiujaq, et Inukjuak furent sélectionnées pour être instrumentées avec le système d'alerte. Pour ces sites, des études du pergélisol et des processus associées avaient déjà été faites. Les différents dangers liés à des phénomène de subsidence ou de glissement de terrain risquant d'endommager les pistes avaient été caractérisés. Celles-ci avaient également été instrumentées avec de multiples senseurs de température. L'implémentation du système consista donc à connecter les nouveaux enregistreurs ULog sur les câbles de thermistances déjà existants, et de les connecter à une passerelle LoRaWAN situé dans les bâtiments des aéroports. Par la suite, en se basant sur les connaissances déjà acquises, des algorithmes ont été conçu pour chaque site à fin de déclencher une alerte suite à la réception et l'analyse des données si certains seuils critiques de réchauffement et/ou d'épaisseur de couche active étaient atteints. Au Yukon, deux sites, l'un au kilomètre 116 de la Route Dempster et l'autre au kilomètre 1456 de la route de l'Alaska, furent soumis à des investigations poussées. Dans les deux cas, les sections de route étaient menacées par des glissements rétrogressives de dégel risquant de les endommager. Dans ce contexte, une connaissance approfondie des sites et des processus actifs était nécessaire pour concevoir un système d'alerte performant. Chaque site fut étudié avec une combinaison d'études géotechniques, de suivi de température du sol, d'études géophysiques, et d'analyses d'imagerie aérienne obtenue à l'aide de drone. En se basant sur ces évaluations exhaustives, une approche fut suggérée pour l'implémentation de systèmes d'alertes pour les deux sites. Dans le cas du site de l'Alaska Highway, un système complet fut installé durant l'automne 2021 afin de tester les fonctions d'enregistrement et de transmission des données au serveur.

Finalement, le projet a abouti à la conception et l'implémentions de trois systèmes d'alerte au Nunavik, et de paver la voie à l'installation de systèmes d'alerte le long de deux axes routiers majeurs du Yukon. Dans le futur, le système sera appelé à évoluer techniquement, avec le suivi de types variés de capteurs et l'usage de communication cellulaire et/ou satellitaire afin d'améliorer les performances du système en territoire éloigné. Enfin, le système a un fort potentiel de développement au regard de son applications dans des contextes et des environnements autres que ceux des infrastructures de transport en régions nordiques.

Acknowledgments

Contents

1. Introduction

As temperatures warm and precipitation patterns change, transportation infrastructure throughout the North is vulnerable to the changing climate. This project addresses the direct consequences of climate change impacts on infrastructure built on permafrost. The thawing of ice-rich permafrost is responsible for many infrastructure failures that accompany severe hazards such as thaw settlement, slope failures and thermal erosion. Much of the transportation infrastructure in the North is now impacted, and in the most dramatic cases, permafrost related hazards such as landslides and sinkholes can damage infrastructure to such a degree that on-site traffic is completely disrupted, and damaged sections can present an immediate and life-threatening danger to users.

Though these geohazards are often triggered by rapid processes that can be caused by climatic events such as heavy rain, heat waves, and unusually warm summer temperatures, they are often preceded by pre-conditioning processes such as localized heat flow, ground water flow, thaw settlements, and deformation. It is therefore possible to anticipate potential infrastructure failures by installing an array of sensors connected to an alarm system that can alert the infrastructure operators and users about the rising risk of a geohazard. Because each site is unique, it is important to tailor the design of the sensor array and the alarm triggering algorithms to each site based on an in-depth site analysis.

This study focuses on two of the most common permafrost-related geohazards: landslides that can partially or completely erode or bury entire sections of the road, and catastrophic ground subsidence from rapid thaw due to thermo-erosion or fast settlement. These permafrost-related geohazards were studied at five sites: km 115 of the Dempster Highway and km 1456 of the Alaska Highway in the Yukon, and the Tasiujaq airport runway, the Inukjuak airport runway, and the Salluit airport access road in Nunavik. The two sites in the Yukon, and the Salluit airport site are all slide-related geohazards, while the Tasiujaq and Inukjuak sites are subsidence-related geohazards.

For all sites, the alarm-system design process was similarly subdivided into a three-step procedure. First, it is necessary to conduct site evaluations at the vulnerable infrastructure sections, and accurately define the biophysical settings, along with the pre-conditions and processes causing the geohazard risks. This includes measuring the geophysical properties of the ground, ground temperature, ground deformations and stress, and characterizing ground water movements. Second, the alarm system must be designed according to the site evaluation information, the identified potential permafrost related hazards and vulnerable sections of the infrastructure. This includes developing a site-specific algorithm to trigger the alarm based on

a set of conditions, as well as the technology to collect, analyze, and transmit the alarm signal to the infrastructure manager. And finally, with the site characterized and the alarm system tailored for each site, the system can be implemented in the field to test the practical solutions and technologies.

Based on the research history and complexity of each site, the three-step process has been implemented to various stages of completion, as per the timeline of the project. The Nunavik sites (Tasiujaq, Inukjuak and Salluit), had previously undergone extensive site characterizations, thus potential hazard and critical infrastructure zones had already been identified prior to this study. It was therefore possible to design and implement the alarm system. The Yukon sites had yet to be characterized, and therefore this was necessary as a first step before the system could be designed and fully implemented, extending beyond the timeline for the project.

With these five sites at various stages of implementation, it has been possible to assess the potential for such alarm systems, including the site assessment and algorithm creation: the ease of deployment, installation, and operation of the system; the real-time communication capabilities of the system; the end-user experience; the costs and benefits of the systems; and finally, the overall applicability across the northern transportation systems to increase the lifespan of the infrastructure and prevent injuries and casualties attributable to infrastructure failures.

1.1. Early Warning Alarm system: Principle and design.

Among the geohazards that are associated with the gradual or abrupt thawing of permafrost, the ones that can affect transportation infrastructure on roads, runways and railways are those that cause a loss of support from the underlying foundation soil. These geohazards have the potential to render this infrastructure unusable, putting essential transportation corridors at risk. There are six dominant categories of permafrost-related hazards that are cause for concern:

1. Thaw settlement due to the thawing of ice-rich permafrost beneath the infrastructure.
2. Active layer detachment slides, which are a type of landslide that takes place when thaw depth reaches into ice-rich ground on slopes with gradients as low as 2°. These landslides can cut a road and/or eventually move a section of a roadbed.
3. Retrogressive thaw slumps (RTS), which are a type of landslide that occur when ice-rich permafrost thaws causing the ground to slump in a retrogressive manner. As the

permafrost in the scarp thaws, the cliff face crumbles and the headwall retreats. RTS can affect infrastructure either through erosion as the headwall retreats into the infrastructure, or by deposition if material from the headwall is deposited onto the infrastructure below.

4. Erosion of ephemeral caves in the permafrost under infrastructure either through water seeping through permafrost (intra-permafrost) in thawing stratigraphic layers or by fast flowing water through massive ice, often along an ice wedge. An arch may be formed over a void under the infrastructure that can eventually collapse.

5. Ditching by thermo-erosion, which occurs when a ditch is eroded by water flowing over permafrost, for example along an ice wedge network or over disturbed terrain exposing permafrost. This ditching can extend downflow or upflow and erode a road.

6. Overriding of a road by a mudflow originating from erosion upstream from the road, for example from a retrogressive thaw slump or some other type of mass wasting process.

The geomorphological and geotechnical processes that trigger these geohazards are rather well known in general. The required geological conditions and causes of terrain destabilization are also known. Geotechnical factors such as gravity, internal friction angle, water content, slope, internal pressure, and others are well understood.

Data acquired from instrumentation can help us understand the causes and triggers of hazards that have already occurred in a given region or at a particularly sensitive site. Using this data can help establish threshold values for different variables that are surpassed for hazards to occur. This data is collected using data dataloggers at various time intervals (hourly, daily, weekly), and is downloaded on a regular basis. Most surficial and internal hazard-related processes in permafrost terrain operate on timescales of days and hours (ex. thaw rate) and are the end-results of evolution over the previous weeks and months (ex. seasonal warming of the temperature profile, deepening of the thaw front in a summer), or even years (warming of the permafrost temperature). Table 1 provides a summary of the potential hazards for infrastructure, the key parameters to measure, the type of sensors to use, the key variables to be calculated with the data, the types of necessary algorithms to program and the optimal rates of data acquisition.

Table 1 Main hazards, parameters, sensors, variables, algorithms and data acquisition frequencies for designing pre-warning systems for geohazards in permafrost along transportation infrastructures.

Hazard	Key parameters	Measurement Device	Variables calculated from the parameters	Algorithm	Optimum frequency for data acquisition
Thaw settlement	-Temperature (T)	- Thermistors	-Depth of 0 °C isotherm -Temperature profile -Thaw rate -Air degree-days	-Interpolation -Depth vs time -Degree-days curve slope	Daily
Active layer detachment failures	- Temperature -Intertistial pressure (P)	-Thermistors -Pressure sensors	-Temperature profile -Thaw rate -Depth of 0 °C isotherm -Air degree-days - Pressure	-Interpolation -Depth vs time -Degree-days curve slope -Treshold trespassing	Daily
RTS headscarp retreat	-Visual observation -Strain (rate of slope movement, extension rate) (σ) -Interstitial pressure -Temperature	-Camera -Strain gauge -Inclinometers -Extensometers -Pressure sensors -Thermistors	-Observation -Distance (mm, cm) -Pressure -Temperature	-Photo/video -Detection of rate increase -Idem -Idem	Hourly, daily
Cavities (arches) Seepage (supra, intra, sub permafrost)	-Water temperature -Water pressure	-Thermistors -Pressure sensors	-Temperature - Pressure	-If rise ≥ ≈ 0 °C - Rapid rate of rise	Hourly, Daily
Upstream or downstream thermo-erosion	-Visual observation (Context Known /mapped)	-Camera -Rain gauge	-Observation -precipitation /snowmelt	-Photo/video -Cumulative precipitation	Hourly, daily
Mud/debris flow from upstream	-Visual observation	-Camera	-Observation	-Photo/video	Hourly, daily

Once the processes that form a hazard and its triggering mechanisms are known, the challenges for designing a pre-warning system that will alert the transportation infrastructure operator of its imminent occurrence are multiple:

Because instruments measure individual parameters such as temperature, pressure, distance, and water content, pertinent data must be analyzed to inform on the progression of terrain conditions towards the trigger of the hazard.

Thus, calculations must be made with the acquired data to detect or to anticipate the potential surpassing of threshold values for the hazard. Depending on the hazard type, the thresholds could be based on a rate of thaw penetration, a temperature or a pressure increase over time, an acceleration of the rate of change in a slope angle, a rate of deformation in an inclinometer, a rate of head scarp retreat, the nearing or surpassing of a threshold value thaw depth, among others. Each time data is acquired, the calculations must be redone to assess the situation on

an ongoing basis. Therefore, in an automated system this implies the automatic launching and functioning of a mathematical algorithm written as a computer program.

The frequency of data acquisition must be high enough to make these automated calculations timely to assess the level of risk. This implies that data from the monitoring site be retrieved in real-time (daily, hourly, or even more frequently). Therefore, data transmission to a base station is necessary via a means of telecommunication (radio, satellite, phone or internet). If the alert system fails or transmits an advance pre-warning, it may be necessary to have access to the data acquisition system in the field to change data acquisition frequency or obtain instantaneous validation; therefore, the base station must also be able to communicate with the datalogger in the field. Communication capabilities must be bi-directional as shown in Figure 1.
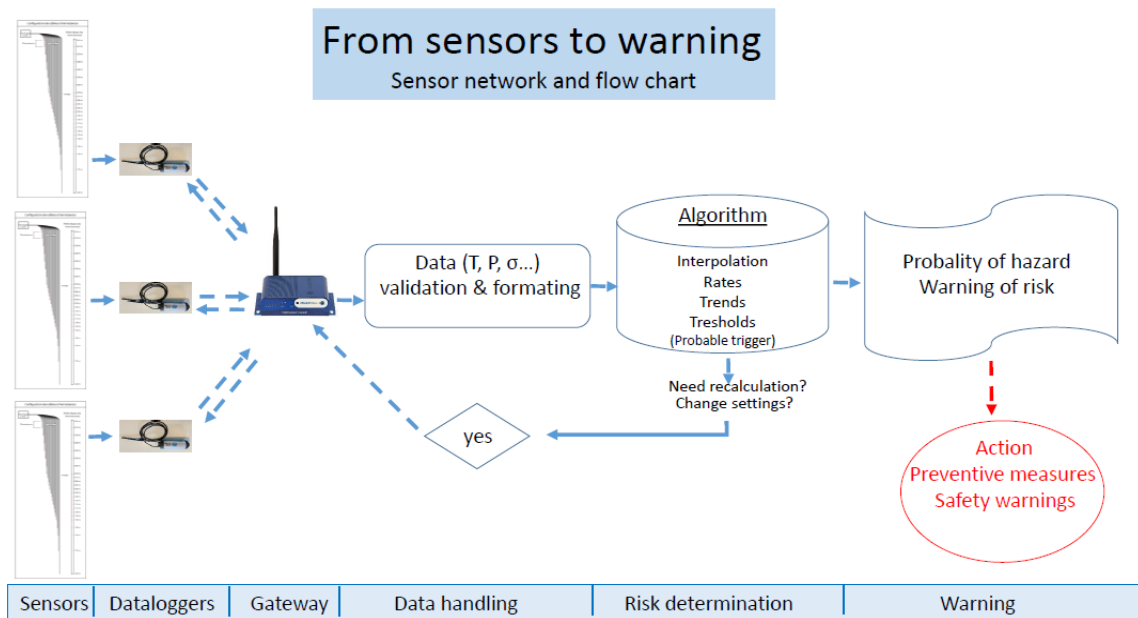
Figure 1 Flow diagram from sensors to warning launch. The sensors in the field are linked to transmitting/receiving dataloggers. The transmitted data are received in a base station called a gateway, which re-transmits the data to a computer (server). The data are validated, and quality checked by software before being introduced into the algorithm. From the output of the algorithm, a warning signal is sent if deemed necessary. The program settings of the dataloggers can be modified as required.

It is important to remember that, by definition, the triggering of a geomorphological or geotechnical hazard cannot be predicted in space and time with 100% certainty. However, since

the conditions under which they occur are well understood, the level of risk of hazard incidence can be assessed and forecasted both in time and by approximate location with the knowledge of site context. As such, the 'warning' information transmitted to the infrastructure operator is the level of risk of hazard occurrence, which can be set at a pre-selected level of risk.

In this study, the instrumentations and warning systems were only tested on three types of hazards documented at five field sites: active layer detachment slides along a road (Salluit, Nunavik), headscarp retreat of a retrogressive thaw slump along a road (near Whitehorse in Yukon), and thaw settlement/collapse of infrastructure (Inukjuak and Tasiujaq airports in Nunavik and Dempster Highway in Yukon). The technology developed for data acquisition and transmission was designed for the purposes of this project as its core objective. A first version of a software for automated data processing and risk assessment was also written.

1.2. LoRa Physical Layer and LoRaWAN Networking Protocol Overview

IoT (Internet of things) related wireless technologies developed in recent years are extremely heterogeneous in terms of protocols, performance, reliability, latency, cost effectiveness, and coverage (Cilfone et al., 2019). After consideration of feasibility, practicability, accessibility and costs of the various transmission technologies, the most appropriate technology for the alarm system consists in creating local networks of dataloggers connected to a base station (gateway) using the LoRa (long-range) radiofrequency of 902-928 MHz.

In contrast to existing short-range wireless communication technologies currently used for indoor IoT sensors (e.g., Bluetooth and Wi-Fi), LoRa/LoRaWAN provide long-range and outdoor wireless communication. The wireless communication takes advantage of the long-range characteristics of the LoRa physical layer (LoRa PHY), allowing for a single-hop link between the end-node and one or many gateways. LoRa PHY is a proprietary chirp spread spectrum (CSS) scheme that uses the sub-1 GHz wireless frequency band. All devices (nodes) are capable of bi-directional communication supporting tasks such as Firmware Over-The-Air (FOTA) upgrades or modification of acquisition parameters (i.e., data acquisition time step, data transmission rate, etc.). The advantages of LoRa technology include long range and secure data transmission over license-free sub-gigahertz radiofrequency with low power consumption, reducing infrastructure investment, battery replacement expense, and ultimately operating expenses. According to the LoRa PHY chipset manufacturer, transmission range can reach up to 20 km in

open areas making this technology sufficient for most current long-range IoT applications. The trade-off to achieve such extended data transmission ranges under very low power consumption is lowering the data transmission rate (Figure 2A). The communication frequencies, data rate, and power for all devices are determined through the LoRaWAN protocol, a cloud-based medium access control (MAC) layer protocol that manages the communication between gateways and end-node devices as a routing protocol (Figure 2B).
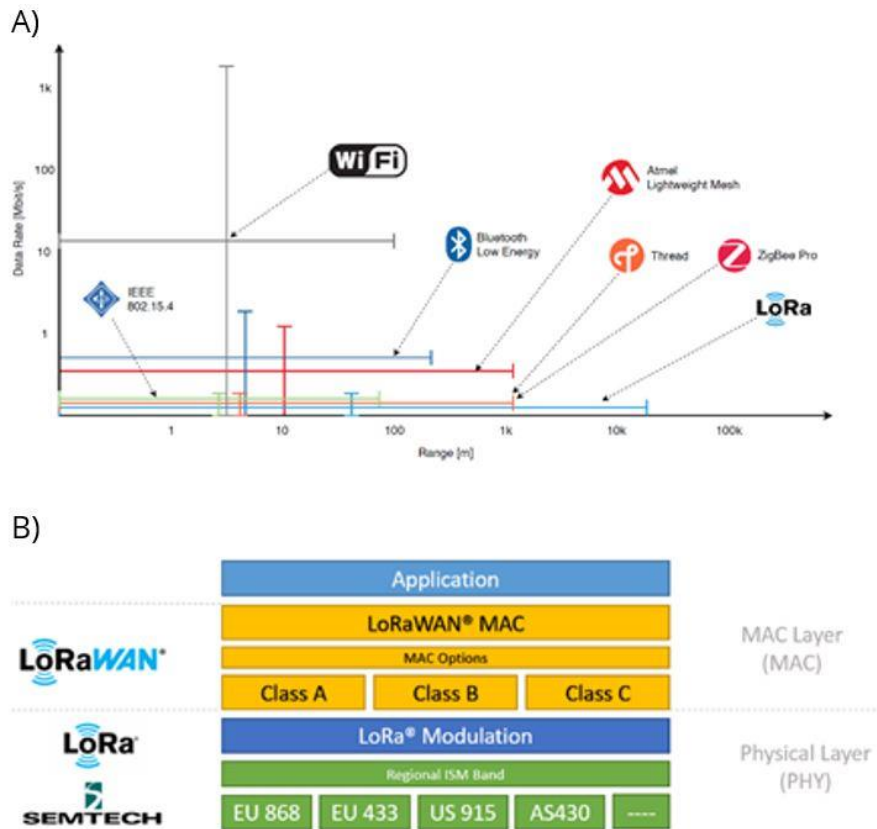
Figure 2 A) Comparison of different wireless technologies and communication protocols based on data rate and transmission range (modified from Cilfone et al., 2019). B) The device-to-infrastructure of LoRa physical layer parameters and the LoRaWAN protocol (Semtech, 2019).

LoRaWAN defines the networking protocol for LoRa based devices. It specifies different device types, different keys, and encryption capabilities to build a secure wireless network. According to the LoRaWAN specifications, there are three different classes for the network end-nodes (Class A, B and C). Class A devices support bi-directional communication, in which each end-node has two short down-link receiving windows after an up-link transmission. Class B end-

nodes also support bi-directional communication, but have additional receiving windows, which are determined by time-synchronized beacons from the gateway to allow the server to know when the end-node is listening. Finally, Class C devices allow continuous reception of data due to its maximal receiving slots. In LoRaWAN networks, the cryptographic security is handled using A 128-bit AES keys providing multiple layers of encryption to secure packets at the network and application level.

A typical LoRa network consists of four different components: the end-nodes, the gateways, the network server and the application (Figure 3). The end-nodes (class A) are devices with embedded LoRa PHY transceivers. Each end-node measures and saves their readings into their internal memory and periodically transmits the data to the gateway using the LoRa PHY transmission Chirp Spread Spectrum and the LoRaWAN protocol. The gateway (class C) forms the bridge between end-nodes and the network server. Gateways have simple tasks that consist of scanning the spectrum and receiving LoRa packets from end-nodes and forward their data to a network server. Compared to end-nodes, gateways use higher bandwidth such as Wi-Fi, Ethernet or Cellular to link up to thousands of end-nodes to the network server. The network server makes further validation of the packets, colligates packets received from the end-nodes and classifies and stores the data into a database. The application is the component that access and analyze the data stored in the database hosted by the server. The application can make further interpretation to solve specific problems.

Since LoRa allows for long-range communications, reaching up to 20 km in optimal conditions, the classical topology of a LoRaWAN network is a star topology. A star network consists of end-nodes and gateways and in which gateways gather and relay messages between end-nodes to the network server (Figure 3A). The default class for the end-nodes is class A, which means communication is always initiated by the end-node and is fully asynchronous. Each uplink transmission can be sent at any time and is followed by two short downlink windows, allowing for bi-directional communication, or network control commands if needed. Consequently, the end-node is able to enter low-power sleep mode for as long as defined by the application, thus making the power-consumption of end-nodes very low while still allowing for uplink communication. To reduce the latency, gateways are defined as class C meaning that their receivers are open at all times to promote downlink transmission at any time initiated by the network server. The compromise is the power drain of the gateway which, compared to class A end-nodes, is considerable and forces the use of continuous AC power alimentation or at least a 12 V rechargeable battery with solar-panels. Gateways are connected to the internet through

a variety of methods including Wi-Fi, cellular, or Ethernet connections. End-nodes in such networks are asynchronous and transmit when they have data available to send. Data transmitted by an end-node is received by a gateway, which forwards the data to a centralized network server that filters duplicate packets, performs security checks, and forwards the data to application servers. This approach allows for the creation of local networks near remote northern communities with coverage ranging from 5-20 km depending on the regional topography. With slight improvements, it shall be possible in the future to connect the gateway either to cellular networks in inhabited regions or to remote satellite transmitting stations for remote applications.

For highly mountainous or dense urban areas, there may be the necessity for multi-gateway (multi-hop) support to preclude the deployment of a larger number of gateways. In that case, the LoRaWAN network topology can be changed for a mesh network. However, even if a mesh network is technically possible under the current LoRaWAN protocol (existence of class B relay device), no official development and implementation of such routing protocols to bring multi-hop capabilities to LoRaWAN are available (Cilffone et al., 2019). Some methods are being tested, but still need development (Lee and Ke, 2018). Mesh versus star network topology also reduces the overall power efficiency of the network while increasing the program complexity. In fact, bi-directional end-nodes (class B instead of class A) need to be synchronized to the network using periodic beacons at the expense of some additional power consumption in the end-nodes.
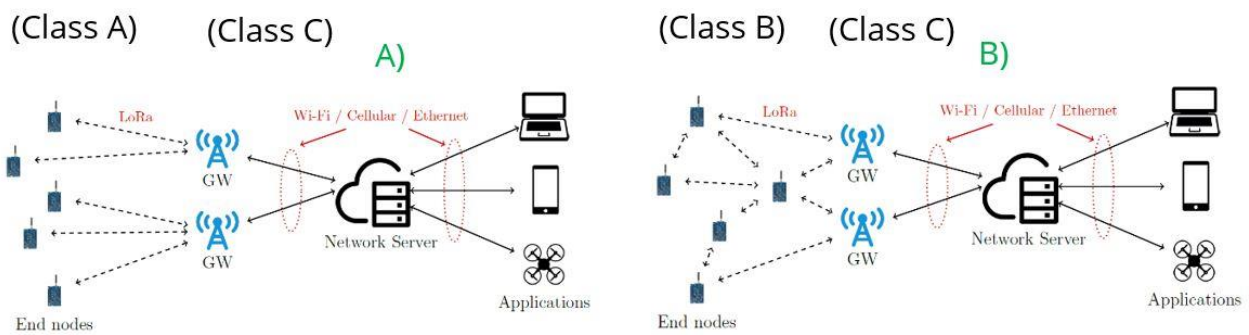
Figure 3 A) Star versus B) mesh network topology in LoRaWAN network (modified from Cilfone et al., 2019).

1.3. LoRaWAN network and components characteristics of the current project

1.3.1. End-nodes (ULog Datalogger)

Since power management is critical and represents the cornerstone for a reliable wireless transmission network of sensing devices in northern environments; and since coverage provided by a star configuration meets the project requirements, the possibility of creating a mesh-network has been discarded to reduce the overall complexity and development cost (i.e. risk) for the current project. In cases where extended transmission range beyond the LoRa capability is needed, a star of star networks could be implemented where a second gateway will act as a relay device and transfer the data to another gateway connected to a server. In the current project, the LogR systems dataloggers will act as the end-nodes of the network. Each end-node will measure and save their readings into their internal memory and will periodically transmit the data to the gateway using the LoRaWAN protocol.

To maximize RF transmission performance, an external antenna connected to the datalogger is recommended, as seen in Figure 4. However, it is possible to install an internal antenna inside the dataloggers in cases where enhanced protection is needed. The external antenna can be extended up to several meters away from the datalogger in order to enhance signal reception and transmission when deployed in environments with physical constraints or obstacles.
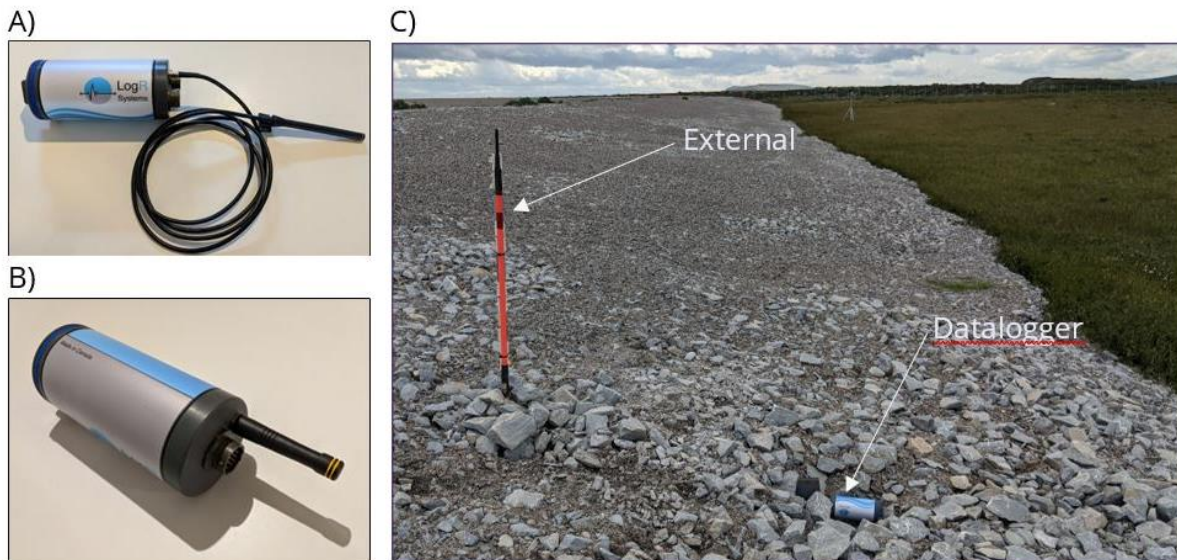
Figure 4 The ULog datalogger (end-node) with A) external antenna with 2 m lead cable or B) directly attached to the enclosure. C) End-node installation at the Tasiujaq runway test site using an external antenna configuration.

1.3.2. Gateway

According to the objectives of the project, an extensive review of existing third-party commercial gateways has been conducted. From the two gateways selected as potential candidates, the Laird Sentrius RG191 LoRaWan gateways and the Multitech Conduit gateway, the latter was ultimately chosen. The choice was justified by the software and firmware compatibility as well as the programming environment and flexibility of the Multitech Conduit gateway. Another important specification of this gateway is its internal memory capacity. This is a very relevant aspect because it will prevent data loss in the event of internet service interruptions. In the case of an internet interruption, the gateway will stock the data transmitted from the end-nodes and will transfer all data stocked to the database server as soon as the internet connection is re-established. Using the Multitech Conduit gateway in combination with an Uninterrupted Power Supply (UPS) unit (to prevent power outage) will also decrease the risk of data loss and network malfunctions. The technical specifications of the Multitech Conduit gateway are shown in Table 2.

To comply with FCC and RF exposure compliance and certifications, Multitech proposes a selection of three antennas to use with their gateway. The three antenna options are presented in Table 3 along with their technical specifications. The three options offer a range of gains which is a key metric that combines the antenna's directivity and electrical efficiency. Generally speaking, the gain describes how well the antenna converts radio waves arriving from a specified direction into electrical power, the higher the gain, the better the reception and the higher the transmission range.

Table 2 The Multitech Conduit gateway technical specifications.

Specifications	
Input Voltage	9 VDC 1.7A input provided to 100 - 240 VAC 50/60 Hz external adaptor or fused DC Power Cable
Processor and Memory	ARM9 processor with 32-Bit ARM & 16-Bit Thumb instruction sets 400 MHz • 16K Data Cache • 16K Instruction Cache • 128X16 MB DDR RAM • 256 MB Flash Memory
Wi-Fi/Bluetooth (-247 models)	GNSS for LoRa Packet Time Stamping Concurrent GNSS connections: 3 GNSS Systems Supported: (default: concurrent GPS/QZSS/SBAS and GLONASS)
LoRa Frequency Band	915 MHz
LoRa Channel Plan	US915
Channel Capacity	8-channels (half-duplex)
LoRa Power Output	27 dBm maximum output power before antenna
SD Card (under nameplate)	Micro SD Card, 32GB (HSMCI) max (industrial temperature range recommended)
Antennas	Cellular, GPS, LoRa: female SMA / LoRa: reverse polarity female SMA
Operating Temperature	-30° to +70° C*
Storage Temperature	-40° to +85° C
Humidity	Relative humidity 20% to 90%, non-condensing
EMC Compliance	US: FCC Part 15 Class B Canada: ICES-003 Class B Australia: CISPR 32 EU: EN 55023 Class B, EN 301 489-3 V2.1.1, EN 301 489-1 V2.2.0, EN 301-489-52 V1.1.0
Radio Compliance	US: FCC Part 22, 24, 27 Canada: ISED-003 AU: AS/NZS 4268:2012 + A1:2013 MPE Standard 2014

Table 3 The Multitech Conduit gateway's antenna options proposed with their technical specifications

Model number	W1063	ANT-916-ID-2000-RPS	FG9026
Image			
Manufacturer	PulseLarsen Antennas	Linx Technologies Inc.	Laird Connectivity Inc.
Frequency Group	UHF (300MHz ~ 1GHz)	UHF (300MHz ~ 1GHz)	UHF (300MHz ~ 1GHz)
Frequency (Center/Band)	898MHz	915MHz	915MHz
Frequency Range	868MHz ~ 915MHz	895MHz ~ 945MHz	902MHz ~ 928MHz
Antenna Type	Whip, Tilt	Whip, Straight	Whip, Straight
Radiation	Omni	Omni	Omni
Number of Bands	1	1	1
Gain	3dBi	1.6dBi	8.15dBi
Termination	RP-SMA Female	RP-SMA Male	N Type Female
Height (Max)	8.000" (203.20mm)	4.906"" (124.60mm)	65.000" (165.10cm)
Ingress Protection		IP67	IP67

1.3.3. Network Server and client application

In the current project, LogR Systems developed a complete server infrastructure where each gateway sends the end-nodes data in .json format to a centralized server using a secure MQTT (Message Queuing Telemetry Transport) connection. MQTT is an open, lightweight, publish-subscribe network protocol that transports messages between devices. The protocol usually runs over TCP/IP that provides ordered, lossless, bi-directional connections and was specifically designed for networks with a limited bandwidth such as LoRaWAN networks. The overall architecture of the server network and client application has been developed using the docker containers technology in order to be easily packaged and transferable to the client server (CEN server in this case) (Figure 5).
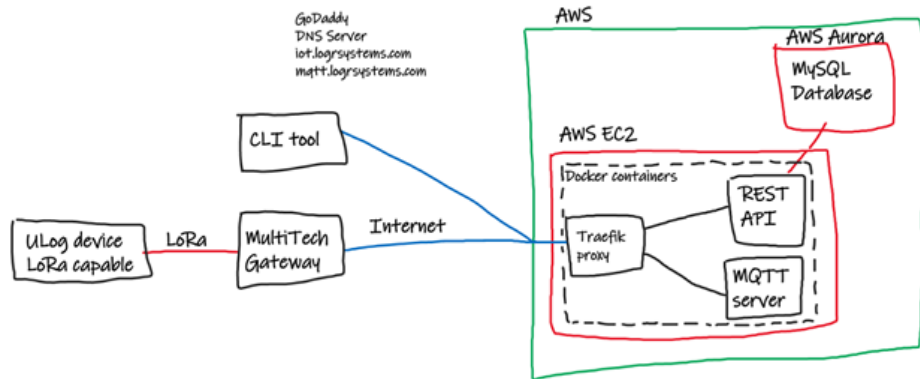
Figure 5 The complete server infrastructure developed using a secure MQTT protocol.

All end-nodes (dataloggers) have an Extended Unique Identifier (EUI). Based on the EUI assigned to an end-node, the network server colligates the segmented data packets received through the gateway and stores the data into a single temporary table. This temporary table allows for the classification of the segmented data packets for each end-node of the network and to proceed to validation to confirm that all data packets for a specific data transmission have been received. Once this validation is made, the assembled data are converted from the base 64 compressed format into readable raw data values under each specific field and saved to a permanent table (ulog_data) in the MySQL database hosted on the network server.

To access and download the data from the network server, an API (Application Programming Interface) has also been developed. The API sends requests to the network server in order to retrieve data or any requested information available using specific functions. For instance, the POST /authentication function is be used to identify the user and generate a token from which the user can list all its devices and to download the data. The authentication information (username/password) is placed in the request body under the form x-www-form-urlencoded and acts as a security check to access the data. The function 'GET /device' returns the complete list of available devices a user has access to (by serial number), and the function 'GET /device/<serial number>/data' will return all the data for a specific device using the serial number unique identifier. In that function, the use of additional parameters like « from » and « to » in the request can be used to filter the data to download. The 'from' and 'to' parameters use the timestamp in the file data to constrain the search. If the 'from' and 'to' are not defined during the request, all the data available will be downloaded.

The capabilities of the application are limitless. For instance, data interpretation and visualization modules can be developed inside the API. Moreover, various types of alarm systems could be developed using the same data with new threshold values, or even in other geohazard environments.

1.3.4. Safety measures implemented to avoid data loss

LoRaWAN networks are composed of several components (end-nodes, gateway, and server) that exchange information across the network either by using uplink (end-nodes to the gateway to the server) or downlink (server to the gateway to end-nodes) communications (Figure 6). Common mechanisms to ensure proper reception and data integrity during the communication process is called acknowledgment. Consequently, every time data are transferred from one component to the other, a transmitter must receive acknowledgement from the receiver before moving with the transmission process. While in theory, this is quite simple, it is relatively common for the links between these network components to be altered or broken. Since acknowledgement is needed in order to keep track either a message has been successfully transmitted across the network, or not, a lack of response from the components will lead to a temporary or permanent network failure.

Each network component can be exposed to specific threats that might cause communication failures. The most common threat affecting the links between the end-nodes and the gateway are signal losses (caused by an electromagnetic interference or simply a specific meteorological condition) or a power outage of the gateway. Both threats could cause non-acknowledgement of data integrity during uplink or downlink transmissions, thus postponing data transmission until the links are fully recovered. The most common threat that is likely to affect the link between the gateway and the server is an internet outage either caused by a power outage (internet router down) or a network outage (internet service disruption). In order to avoid any data loss or gaps when such hazards occur, several safety transmission mechanisms were implemented to increase the resilience of the network and will be specifically described in the following section.
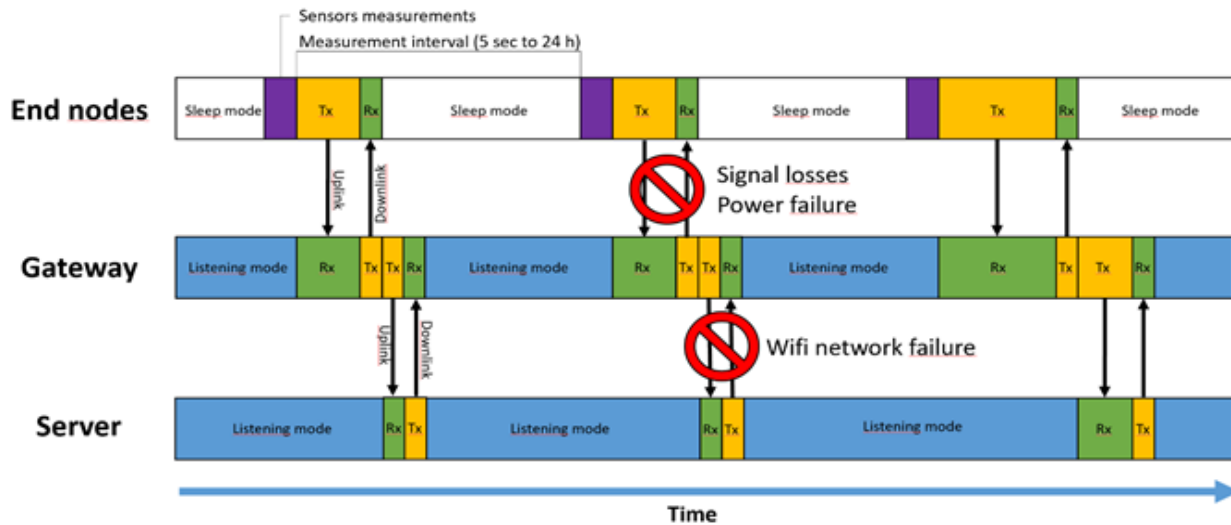
Figure 6 Most common hazard likely to affect the links between the network components during uplink or downlink transmission.

1.3.4.1. Communication failure between end-nodes and the gateway

Several causes may lead to a communication failure between the end-node and the gateway. The most common cause of communication failure would be a signal loss between the end-nodes and the gateway. Since RF signal quality is highly affected by the physical environment (topography, vegetation, and buildings) and the propagation medium properties (dry or moist air), signal strength/quality may vary over time. For most of the sites, the environmental conditions are expected remain the same over time. However, this is not the case for the propagation medium properties that might fluctuate according to meteorological conditions. For instance, snowstorms, and foggy or rainy periods might decrease the signal strength, thus increasing the risk of a communication failure between the end-nodes and the gateway. During such communication failure events, safety mechanisms between the end-nodes and the gateway have been implemented in order to save the end-node battery and also to minimize transmission back-log and data access latency.

The first mechanism implemented is called the retry. For every message sent by the end node to the gateway, acknowledgment must be received from the gateway to ensure data integrity before sending any other split or full message (sampling event). If, for any reason, the end node does not receive the acknowledge message after transmission, another transmission attempt of the same message will be made. In case of repeated non-acknowledgement, the end-node will retry the transmission up to 8 times. After 8 transmission attempts without acknowledge

16

from the gateway, the end-node will go into sleep mode for a minimal sleep time interval before trying another transmission attempt (up to another eight retries if needed) (Figure 10). If the second transmission attempt is still unsuccessful, the transmission sequence will be considered a failure and the end-node will go back into sleep mode until the next planned sampling log interval. Just before the planned sampling log interval, the end-node will try another complete LoRa transmissions sequence.

After two transmission sequence failures, the LoRa transmission task will consider the gateway as lost (Figure 10, LoRa lost gateway sequence). A lost gateway will force the end-node to go back into sleep mode until the next planned sampling log interval. Then, the end-node will reinitialize the LoRa radio module and attempt a join procedure until the gateway acknowledges the join request. If the join request is unsuccessful, another join request will be made 15 minutes later by the end-node. In case of several unsuccessful join requests in a row, the delay between the join requests will increase exponentially. This second mechanism prevents the drainage of the end-node battery while trying to re-establish communication with a lost gateway. For instance, if the gateway is down for a week, after two days, the end-node will only try to re-establish communication by sending a join request every 24 hours.

At any time, data measurements are saved inside the end-node internal memory and are not deleted until the user intentionally decides otherwise using the LogR application. As soon as the communication is re-established between the end-node and the gateway, all the non-acknowledgement messages (backlog events) will be progressively sent to the gateway. This third mechanism is called the backlog recovery mode and promotes the transmission of all the non-acknowledgement messages (sampling events) starting from the oldest record. During the backlog recovery mode, the end-node will send as many backlogged events as possible before the next sampling event while respecting the minimal sleep time interval required to respect the LoRaWAN protocol (time on air and duty cycle limitations). Note that due to these limitations, backlog transmission may take several days to complete depending on the number of backlogged events, the data rate mode and the sampling interval. Higher data rate mode (DR3 and DR4) will take less time to empty the backlog events. If the end-node internal memory becomes full, the LoRa transmission will stop, and the end-node will enter a permanent sleep mode (no more sampling).

1.3.4.2. Power outage

Most of the Arctic sites are subject to frequent power outages caused by power line damage due to high wind. A power outrage will lead to a gateway shut down, thus interrupting the communication between the end-nodes and the gateway. First, to avoid any data loss, it is important to state that every measurement made by the end-node is saved into the device's internal memory and, unless otherwise specified, will not be deleted at any time. Thus, in the event of a major failure that will require either a gateway or an internet router replacement, data will always be recoverable by downloading the end-node in the field. To increase the resilience of the network to power outages, we suggest the use of a UPS (uninterruptible power supply) with an internal battery. The use of such a device will protect the internet router and the gateway from peak surcharges while ensuring a constant power load to keep the units running until the power is reestablished. Depending on the UPS model, the run-time may vary from a few minutes to a few hours. Tests have been conducted with a Tripp Lite SMART1500 UPS. With this model, the power load provided was sufficient to keep the gateway running for up to six hours. Depending on the site specificities (i.e: mean duration of power outage), additional batteries can be added to increase the run-time in the event of a of service interruption.

1.3.4.3. Internet outage

Internet outage is a common concern in remote locations. In Northern Quebec for instance, the principal internet provider is Tamaani, a Kativik Regional Government division responsible for providing internet service to the 14 Nunavik communities. The Tamaani internet service is gradually switching from satellite broadband to LTE modems and fiber optic broadband. Internet service interruption is quite common in northern remote locations due to either power outage or simply bad signal quality from the local internet tower. To avoid any data loss due to the internet service disruption that is not due to a power outage, a saving mechanism has been implemented in the gateway. Since the links between the end-nodes and the gateway will still be preserved, the gateway will accumulate data from the end-nodes into its internal memory until it becomes full. Depending on the number of end-nodes and the sampling rate, the gateway will be able to accumulate data for a period ranging from days to months. Once the communication link between the gateway and the server is reestablished, data saved in the gateway will be transferred to the server in the following few hours. If the communication is not restored before the gateway's internal memory becomes full, unsent data will accumulate in the end-node and will be flagged as backlog events and sent as soon as possible following the backlog recovery mode protocol.

This safety measure was put to the test in the freshly installed network at the Inukjuak airport in September 2021. A contractor doing repair work in the airport garage where the gateway was installed accidentally disconnected the internet for many weeks. However, as soon as the service was re-established all the data stored in the end nodes (the dataloggers along the runway) and in the gateway were transmitted to the server in Québec city in less than a few hours.

2. Case studies, associate geohazards, and system implementation

2.1. Nunavik sites

2.1.1. Salluit

2.1.1.1. Site history

Sallluit is a village of about 1700 inhabitants located on the shore of a fjord at the extreme north of Nunavik (62 ° 14 'N, 75 ° 38' W) (Figure 7). Located in the continuous permafrost zone (L'Hérault et al., 2016) and characterized by a low Arctic climate (INTERACT, 2014), the community occupies a site which ensures accessibility to the sea and protection against strong winds. For historical reasons, the community has grown over the years in an unfavorable geomorphological environment. In fact, most of the urban concentration is currently located in a narrow valley delineated by steep rocky slopes (Figure 7). The dominant Quaternary sediments are post-glacial marine silty clay in the valley bottom and glacial till of variable thickness overlaying the bedrock on slopes and plateaus. Both sediment types are frozen into very ice-rich epigenetic permafrost (Figure), which is sometimes locally covered by a thin layer of ice-rich syngenetic permafrost (colluvium). Geotechnical investigations done over the years has confirmed the presence of ice-rich permafrost at a depth of about one meter below the surface (Allard et al, 2004; 2010; L'Hérault, 2009; L'Hérault et al., 2012) and making the area very sensitive to permafrost thaw related hazard occurrences (Figure 9).

For instance, the whole valley bottom of Salluit is affected by recurrent active layer detachment failures, i.e. active layer detachment slides (ALDS) (Figure 10). ALDS have occurred in 1993, 1998, 2005, 2006 and 2010, almost systematically at the end (late August-early September) of summers that were warmer than the average when the depth of thaw reached at the base of the active layer into ice-rich soil horizons. Active layer slides are a major concern for the safety and land use management of the community. For example, the 1998 landslide prompted the

decision to pause the expansion of highly needed housing in the community for 12 years until a proper permafrost assessment was done. Construction of new buildings is prohibited by a zoning by-law on slopes with angles ≥ 4 % on clay soils, in a valley where space for growth is already restricted because of the topography. The 2005, 2006 and 2010 landslides came close to the airport access road and the Ministère des Transport du Quebec (MTQ) stabilized the scar with gravel fill as a preventive measure.

The local airport and the access road were originally built in 1987 and 1988. The road runs on marine silty clays in the valley before climbing uphill on the plateau where the airport sits at an elevation of about 225 m a.s.l. The road section in the valley is on an embankment built over ice-rich clays on sloping terrain. The road was paved in 2003. After which, the combined effect of climate warming, bad drainage conditions on the transverse slope, snow accumulation on the sides and, likely, the low albedo of the pavement resulted in major deteriorations due to differential thaw settlements in the underlying permafrost. That section of the road was rebuilt by the MTQ in 2012 and 2013. Major modifications and engineering adaptation measures were then made, including the design and construction of a gentle slope on the uphill side of the road with a shallow ditch draining through multiple culverts, the removal of the pavement and the installation of heat drains on the downhill side of the embankment. Performance assessment of these mitigation techniques has recently been completed (L'Hérault et al. 2021). Many thermistor strings monitor the temperature regime and active layer depth underneath the embankment. Since its adaptation in 2012, the road has remained relatively stable until recently, where longitudinal cracks have formed on the embankment shoulders, suggesting ongoing slow creep (Figure 11). Though it runs on sloping and ice rich ground, the access road to the airport is essential to public safety and socio-economic activity. Therefore, being able to send pre-warnings of risk of occurrence of landslides in the valley will allow decision makers to prepare and plan for preventive or corrective actions if needed.

The process of active layer detachment sliding is associated with thaw penetration in a high ice-content soil. The ice content near the active layer/permafrost boundary increases (this layer is also called the transitional layer) in colder years when the active layer is shallower (formation of aggradation ice). When an especially warm summer occurs resulting in deeper thaw penetration, the melting of ground ice creates an increase of pore pressure at the thawed/frozen interface that may overcome the shear strength of the soil. The active layer on slopes may "detach" and slide over the icy ground, with the interface acting as a shear plane. In Salluit, below the transition layer beginning at a depth of 90-100 cm is the very ice rich

permafrost. Under the road, the first one meter at permafrost top has volumetric ice contents above 90%. With the expected warming of the climate, the thermal regime of the permafrost will necessarily shift toward warmer temperatures leading to warmer permafrost temperature but also the thickening of the active layer. As the thaw front will slowly penetrate the ice rich permafrost table, localized thaw settlements will develop and landslides on slopes are likely to occur.

Previous studies using climate data and data from thermistor cables have shown that two simple parameters can be used to assess the level of risk for a landslide to happen for a given summer in near real time: 1- air temperatures calculated as the sum of thawing degree-days since the start of the season, and 2- ground temperatures (particularly the depth of the 0 °C isotherm), the two being related by a power function (L'Hérault, 2009). A computer program was written to measure these two parameters on an hourly basis and to automatically make the necessary calculations to assess the risk of occurrence of a landslide.

Figure 7 Location map of the Inuit community of Salluit, Nunavik; the community is sheltered in a U-shaped glacial valley running north-south and opening onto the Sugluk Fjord.

Figure 8 Ice-rich permafrost cores extracted from A) the post-glacial marine silty clay at the valley bottom and B) the silty till deposits covering the slopes and plateaus.
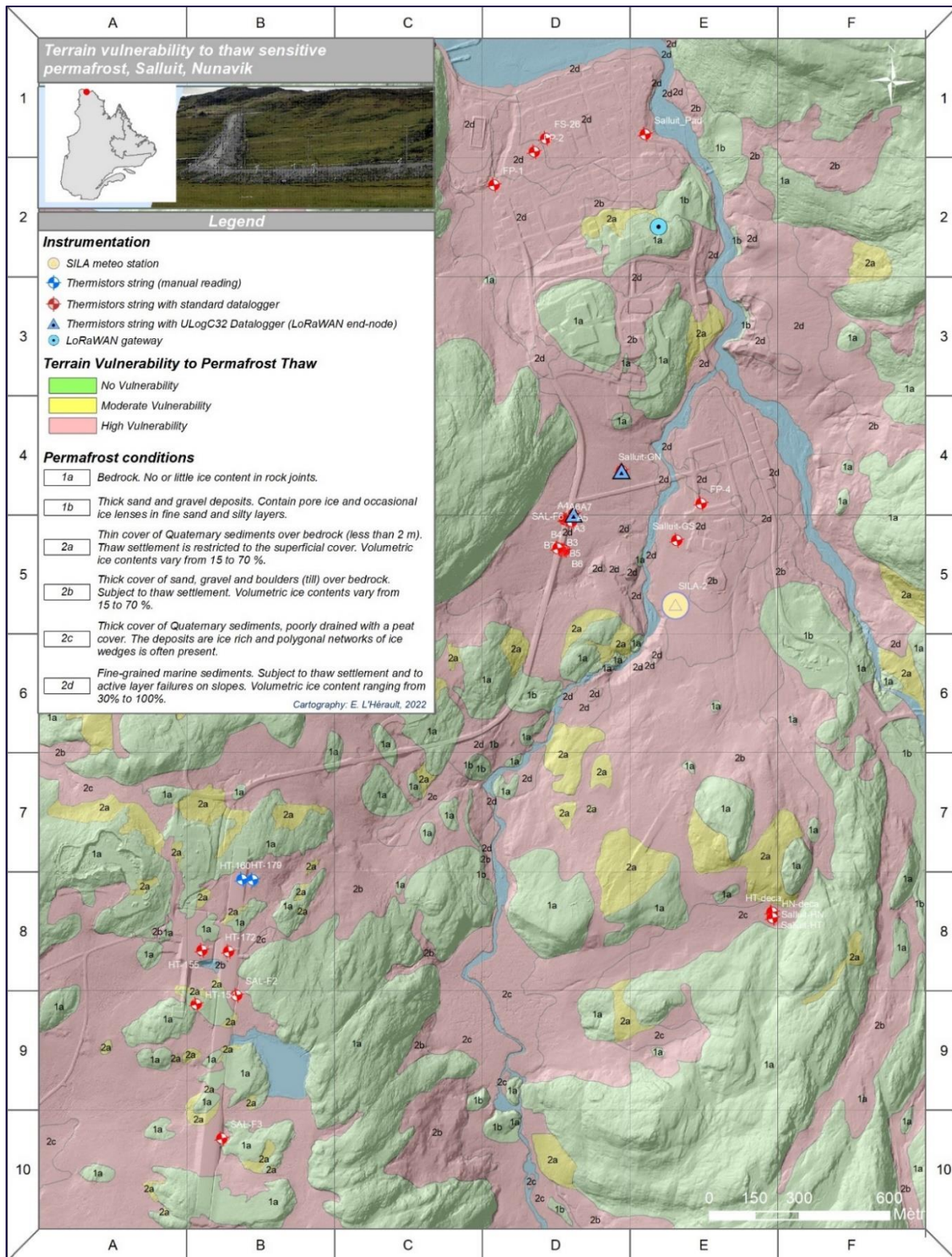
Figure 9 Map of the terrain vulnerability to permafrost thaw and the available instrumentation, Salluit, Nunavik.

Figure 10 Active layer detachment slides in Salluit. Top: 5 September 1998 event; the planned housing development was halted, existing houses were moved. Reconstruction restarted after 2010 in the area on adapted foundations. Middle: summer 1998 event located on a riverside slope near the Kuuguluk river. Bottom left: Summer 2005 event (initial event), note the road embankment near the head scarp. Bottom left: subsequent event further north in the same area, August 2010.
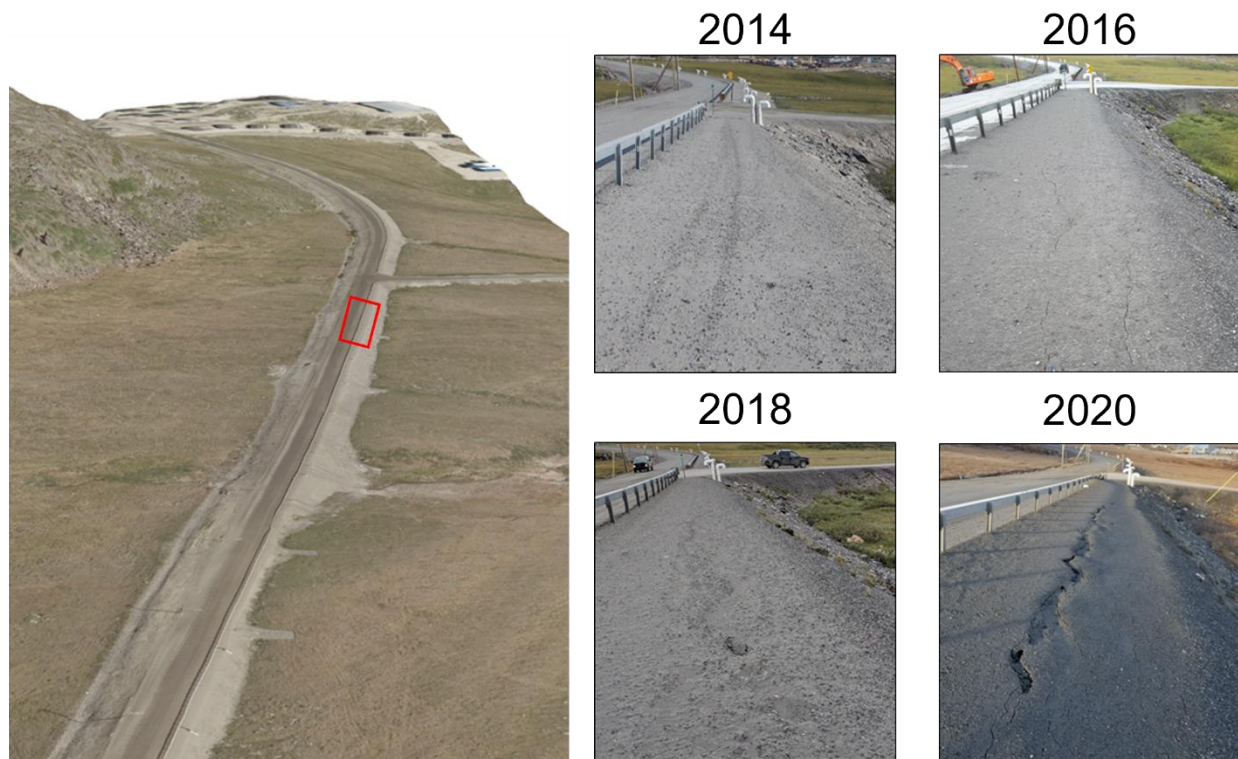
Figure 11 Active embankment shoulder creep processes affecting a section of the Salluit airport access road from 2014 to 2020.

2.1.1.2.   Instrumentation

For this study site, two existing thermistor strings were selected and equipped with the new ULogC32 LoRa datalogger in 2021 to feed the near real time data required to make the whole warning system operational. The first thermistor string (GN-2) is in an open field area close to the road (Figure 9). The instrumentation was installed in 2010 as part of a PhD project and has been in operation since. The thermistor string has 15 thermistors (model YSI 44033) directly buried into the ground to ensure optimal thermal conductivity between the thermistors and the surrounding ground. For this site, the monitoring equipment setup along with the thermistor string configuration are presented in Table 4 and the final field installation overview is illustrated in Figure 13C. The initial purpose of the GN-2 thermistor string was to provide high resolution temperature profiles across the active layer and the permafrost table, thus making it the most suitable instrumentation site to track thaw depth change with great accuracy on a natural slope subject to active layer detachment slide (ALDS) occurrence.

The other thermistor string (SAL-F6) equipped with the new ULogC32 LoRa datalogger is located at the toe of the access road embankment (downslope side) in a section affected by slow downslope movement induced by creep processes (L'Hérault et al., 2021) (Figure 9). This thermistor string was installed into a 14-meter-deep geotechnical borehole in 2009 (L'Hérault et al., 2012). For this site, the monitoring equipment setup along with the thermistor string configuration are presented in Table 5 and the final field installation overview is illustrated in Figure 13D.

Air temperatures are provided by an automatic meteorological station (SILA) located in the valley bottom near the access road (Figure 9) and transmits data through the GOES satellite system. The ground temperatures and the air temperature are merged in the program (see section 2.1.1.4). In the future, the instrumentation for the warning system can be improved by adding pressure gauges in the ground and slope movement indicators, thus increasing the quality of the risk evaluation by coupling thermal and mechanical parameters.

Table 4 GN-2 thermistors string monitoring equipment setup and configuration.

Monitoring equipment setup	Sensor ID	Depth (m)	Thermistor model
	T1	-0.02	YSI 44033
	T2	-0.1	YSI 44033
	T3	-0.2	YSI 44033
	T4	-0.3	YSI 44033
	T5	-0.4	YSI 44033
	T6	-0.5	YSI 44033
	T7	-0.6	YSI 44033
	T8	-0.7	YSI 44033
	T9	-0.8	YSI 44033
	T10	-0.9	YSI 44033
	T11	-1	YSI 44033
	T12	-1.25	YSI 44033
	T13	-1.5	YSI 44033
	T14	-1.75	YSI 44033
	T15	-2	YSI 44033

Table 5 Sal-F6 thermistors string monitoring equipment setup and configuration.

Monitoring equipment setup	Sensor ID	Depth (m)	Thermistor model
	T1	-0.5	YSI 44033
	T2	-0.75	YSI 44033
	T3	-1	YSI 44033
	T4	-1.25	YSI 44033
	T5	-1.5	YSI 44033
	T6	-2	YSI 44033
	T7	-2.5	YSI 44033
	T8	-3	YSI 44033
	T9	-4	YSI 44033
	T10	-5	YSI 44033
	T11	-6	YSI 44033
	T12	-8	YSI 44033
	T13	-10	YSI 44033
	T14	na	na
	T15	-0.05	PR222J2
	T16	-0.25	PR222J2

2.1.1.3. LoRaWAN network implementation

For the Salluit test site, two potential locations for the gateway were selected prior to the field work. Those locations where chosen based on internet connection and power supply availability. The two potential sites are: inside the CEN research station with the use of an external antenna attached to the roof of the building at a height of about 10 m (site A) or inside an existing instrumentation enclosure (DTS station) located at the north end of the access road near the two thermistors strings (site B). In both cases, the sites are equipped with internet router and have on-grid 110-volt power supply.

Based on the site configuration (topography and land cover), the end-node and gateway antenna specifications (height and gain) and the LoRa spectrum characteristics (transmission power, receiver sensibility, etc), coverage signal maps were produced for each gateway location using an Irregular Terrain (ITS) radio propagation model. The coverage maps were produced using the Radio Mobile Online application (copyright of Roger Coudé, VE2DBE). Parameters used to generate the coverage maps are summarized in Table 6. The objective of the RF propagation map was to evaluate the best location for the gateway based on the antenna specifications of the end-nodes and the gateway, the local topography and the surrounding buildings that may reduce RF signal propagation, thus the signal that would ensure reliable wireless transmission.

Table 6 Parameter values entered as inputs in the ITS radio propagation model used to compute the radio coverage map

Parameters	Location A	Location B
Gateway Antenna Height (m above ground):	10	5
Gateway Antenna Type:	Omni	Omni
Gateway Antenna Gain (dBi):	8.15	8.15
End-node Antenna Height (m):	2	2
End-node Antenna Gain (dBi):	1.6	1.6
Frequency (MHz):	915	915
Tx power (Watts):	0.1	0.1
Tx line loss (dB):	1	1
Rx line loss (dB):	3.2	3.2
Rx threshold (dBm):	-127	-127
Required reliability (%):	95	95
Strong Signal Margin (dB):	10	10

For the two potential gateway locations, the computed RF propagation maps are shown in Figure 12. According to these results, the gateway installed at location A (CEN research station) promotes a strong and reliable signal coverage for most of the valley except a small area close to the access road and where the two ground temperature stations are located. Note that between the CEN research station and the ground temperature stations, the presence of a little hill covered with tall building creates a significant shadow effect that reduces the signal strength. This shadow effect produces a zone of potentially poor signal reception that covers both thermistor string locations. Despite an increase of both antenna height (gateway and end-node), this zone of poor signal strength cannot be minimized. The RF propagation map generated using the site B parameters (DTS station enclosure) offers better signal coverage over the area of interest. However, even though location B produces the best signal coverage, location A remained the preferred option due to significant logistic advantages.

After the installation of the gateway in the CEN research station in late summer 2021 Figure 13A), in situ signal strength measurements and transmission reliability assessments were conducted at the ground temperature monitoring stations GN-2 and SAL-F6 (Figure 13C and D), but also across the community and beyond. The final gateway external antenna height was slightly lower than planned (6 m) (Figure 13B), but despite the lower elevation, the signal strength (RSSI) at GN-2 was about –111 dBm with transmission retries ranging from 0 to 5 signal strength at the SAL-F6 monitoring station was much better (–98 dBm), thus lowering transmission retries to less than two on average. The monitoring station has been transmitting ground temperatures every hour and there is no missing data since it was implemented on August 12th, 2021. Note that the internet connection at the Salluit research station was interrupted for a period of seven weeks, between October 4th and November 17th. Once the internet service was restored, saved data in the gateway were transferred to the server in less than an hour confirming that the internet outage safety mechanism is effective in avoiding any data loss.
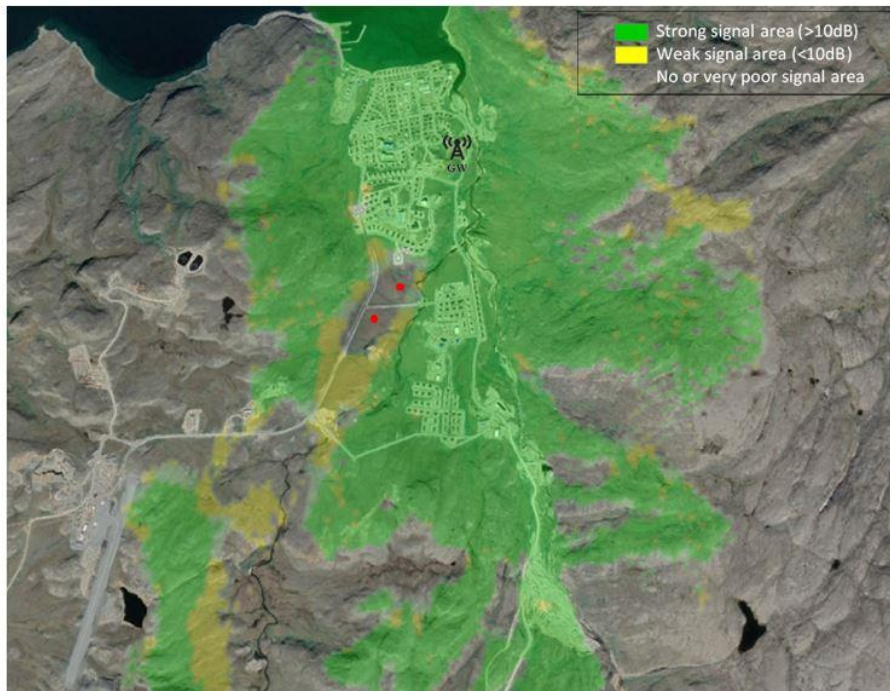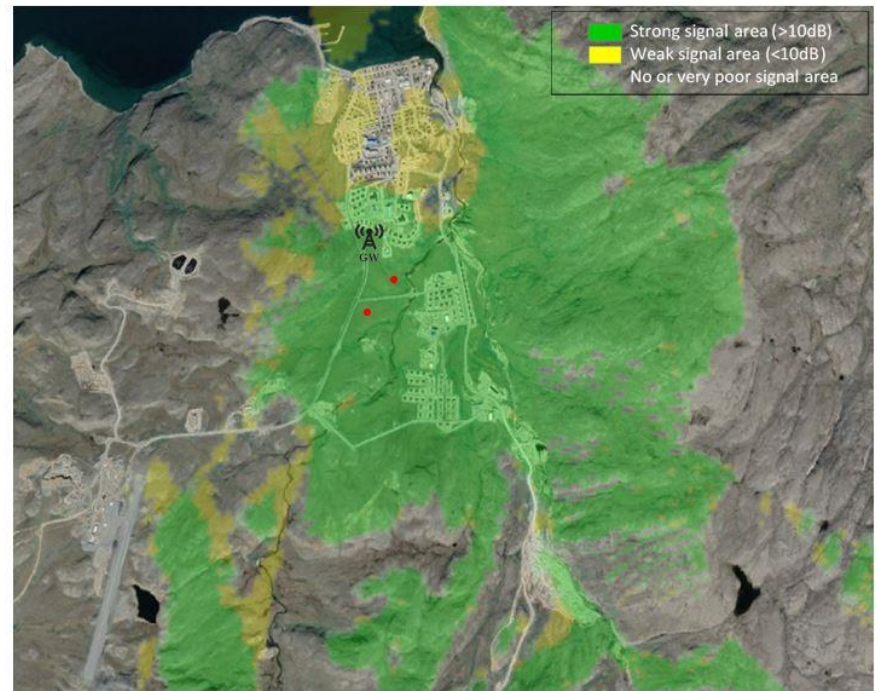
Figure 12 Gateway signal coverage for two gateway locations at the Salluit test site. Location A is inside the CEN research station building with the use of an external antenna and location B is inside the DTS data acquisition enclosure with also the use of an external antenna and location B is inside the DTS data acquisition enclosure with also the use of an external antenna. Locations of the ground monitoring stations GN-2 and SAL-F6 are illustrated on the map by the red dots.
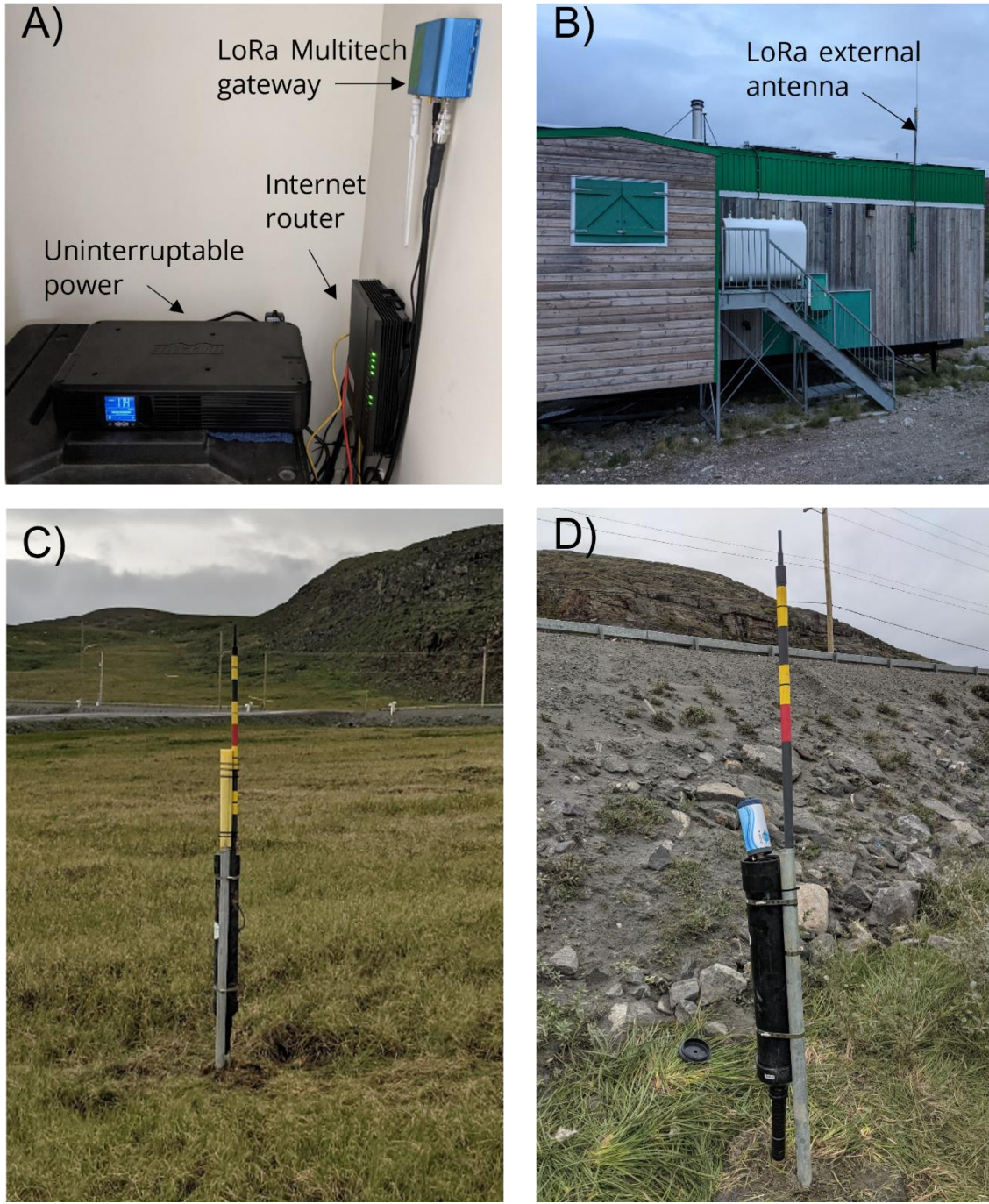
Figure 13 A) LoRaWAN gateway components installed inside the CEN's research station in Salluit with the use of B) an external antenna. Ground temperature monitoring stations C) GN-2 and D) SAL-F6 equipped with the new ULogC32 LoRa dataloggers.

2.1.1.4.   Algorithm parameters, thresholds and expected outcomes

Based on the site characteristics as presented above, an algorithm was developed to assess the level of risk of ALDS, particularly in the vicinity or alongside the access road to the Salluit airport. The road is in a valley, on an embankment built across a slope (i.e. roughly parallel to contours) over very ice rich marine silty clay (≈ 90% volumetric ice content). Landslides have occurred during warm summers in the valley in 1993, 1998, 2005, 2006 and 2010, with the latest slide's headscarp only a few meters from the road (see section 2.1.1.1). A previous analysis of ground temperature data collected since 2002 revealed that the landslides took place at the end of summers with above average air temperature as measured by thaw degree-days (cumulative sum of temperatures above 0°C) (L'Hérault, 2009). In these warmer summers, the thaw front reached into the ice-enrichment zone at the interface between the active layer and the permafrost. This layer may have formed, i.e., accumulated, aggradation ice in the previous cooler years or may also simply be the top of the ice-rich permafrost. In this case, the design of the algorithm is based on the surpassing of thresholds that are related to two key parameters: a climate threshold and a critical depth reached by the thaw front as it gets increasingly deeper in the active layer during a summer. As such, the algorithm is based on the relationship between cumulative degree-days and thaw front depth, a direct application of Stefan's equation.

This threshold is reached when the cumulative degree-days reach a value 30% above the previous year's total, which roughly corresponds to a critical depth of thaw 9% greater than the previous year.

 In summary, in order to generate a landslide risk warning, the algorithm operates according to the following sequence:

- Hourly data are daily transmitted from the loggers in the field to the getaway located in town. Then the getaway relays them by internet to the server at the university.

- As soon as they are received, the data are validated and checked for their quality by a programmed protocol (e.g. wrong signals, values out of possible range, etc.)

- The data are then entered in the algorithm which calculates the daily mean and sums with the previous day's accumulated thawing degree-days for air temperature and

thaw depth. Air temperatures are collected from an automated met station called SILA. Thaw depths (0 °C isotherm in the ground) come from thermistor cables equipped with closely spaced thermistors and LoRa capable dataloggers.

- When the sum gets close to the defined threshold of the previous year, a pre-warning e-mail is automatically generated and sent to the administrator, municipal officers, the regional government services (land use managers and public safety department) and the owner of the road (Ministère des Transport du Quebec), stating that the risk is intermediate and will continue to rise.

- The day the sum overpasses the threshold, a warning of high-level risk is sent.

- The data files and the calculations are updated every day at 15:00.

- The same algorithm can easily be applied to roads and airport runways that are at risk of thaw settlement by the deepening of the active layer into ice rich permafrost under the infrastructure. The threshold value then is either the deepest thaw depth previously observed from thermistor cables under the infrastructure or a known depth of the top of ice rich permafrost obtained by drilling or from reports dating back to pre-construction geotechnical surveys.

The automation process from data acquisition to the sending a warning of risk was made possible by writing a script using Python 3.8.5 (Gauthier, in prep.). The program was developed in the Spyder 4.2.5 environment. Python is a widely used programming language especially for scientific data analysis, and Spyder is an open-sourced interface the facilitates data analysis, in which python libraries and packages can be accessed. This programming language was selected because it is so widely used, and because it is compatible with ESRI software including ArcGIS Pro and ArcGIS Online making it possible to publish the data in web maps to be used by planners. In fact, making the data available in near real time on a parallel platform to the potential users and administrators of infrastructure is valuable as it helps explain the risk within its spatial context.

Our main program (principal.py) calls the various modules containing the classes or sub-programs that execute the various tasks (Table 7). The code of the main program and the sub-programs are available online on GitHub (Centre d'Etudes Nordiques, 2021a). The classes and modules necessary for the execution of the program were developed from the libraries available from Python and are listed in table 8.

Table 7 The program modules, with short descriptions.

Modules	Description
Principal.py	Main executed program that calls the modules in order to upload, clean, transform and analyse the data and publish them online. It also estimates the level of risk of occurrence of an active layer slide and sends pre-warning signals if needed.
Donnees_sila.py Classe DonneesSila	Collects the climate data from the SILA climate station on MELCC's website and formats the table with the new data.
Connexion_serveur_ftpcen.py	Establishes a secure connexion with CEN's or LogRsystem's server and upload thermistor data from cables.
Donnees_pergelisol.py Classe DonneesPergelisol	Formats the table with the new data and calculates daily averages from hourly values.
Validation_donnees.py Classe ValidationDonnees	Cleans and validates data quality according to the set criteria and transforms resistance data into temperature values.
Indices_cilmatiques_quotidiens.py Classe IndicesClimatiques	Determines the dates of beginning and end of the freezing and the thawing seasons and calculates climate indices (sum of degree-days).
Couches_web.py Classe CoucheWeb	Connexion to CEN's ArcGIS Online account and update of the web data with the newly uploaded data.
Signal_risque_glissement.py Classe AlerteRisqueCourriel	Produces two daily reports in PDF: assessment of level of risk of occurrence of an active layer landslide and sending of the warning signal.

Table 8 Main Python librairies used for program development (PyPi, 2021; Python, 2021).

Python libraries	Description
Pandas 1.1.3	Manipulation and analyses of large datasets using data frames.
Numpy 1.20.2	Manipulation of data tables and et mathematical functions.
ArcGIS 1.8.5	Manipulation, analysis, and visualisation of geospatial data. Compatible with ArcGIS Online.
Scipy 1.6.2	Numerical integration, interpolation, optimisation, linear algebra, and statistics.
Matplotlib 3.3.4	Creates figures for data visualisation.
Paramiko 2.7.2	SSHv2 Protocol in Python with client and server functionalities.
Dataframe_image 0.1.1	Conversion in graphics of data tables produced with Pandas.
Yagmail 0.14.26	Sending of personalized e-mails.
FPDF 1.7.2	Creation of personalized PDF files.

The program automatically starts at 15:00 daily and is executed through the launch of the main program *principal.py* with a command file (*batch file;* extension .bat) by the task planner. The task is planned on a standing operating computer at the Centre d'Etudes Nordiques at Université Laval (UL). Once launched, the main program calls the different modules to read the data from the LoRA server and accomplishes the tasks of averaging hourly data, calculating degree-days, summation of degree-days, interpolate thaw depth (0 °C isotherm) between thermistors, and assess the level of risk by comparison with the set threshold. The call sequence of the modules is shown in the logical diagram (Figure 14).
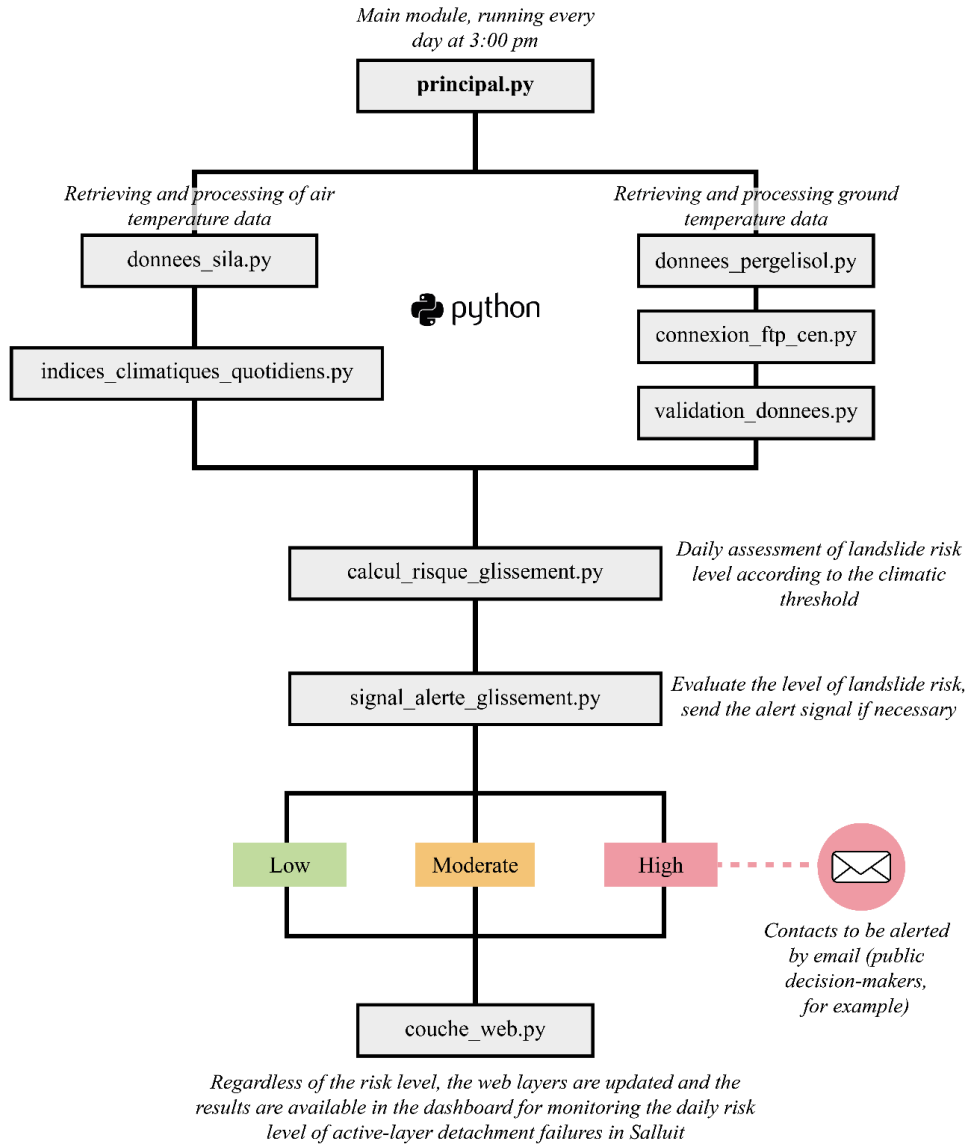
Figure 14 Logical diagram of the sequence of modules, showing the structure and functioning of the main program and its modules (sub-routines).

The program is launched at the set time even if the standing computer is offline. If for some reason the computer is turned off or a network failure prevents the launch, the program will automatically be executed the next day at 15:00. A standard READ_ME.txt file is available with the source code, which describes the code in detail.

2.1.1.5. Dashboard application overview for the Salluit active layer detachment slide risk level

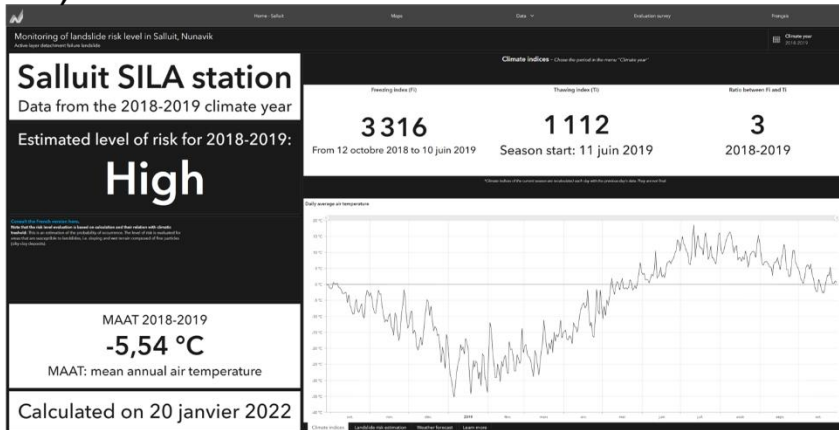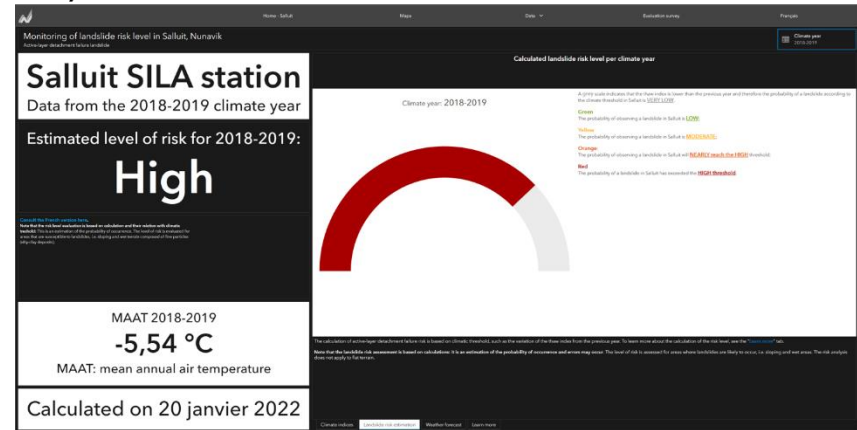The daily active layer detachment slide risk level for the Salluit airport access road is available online through a dashboard application specifically developed to inform the public. The dashboard application has been developed by Gauthier (in prep.) using the ArcGIS Dashboard web application (Esri, 2021b) and is accessible <u>online</u> (Centre d'Etudes Nordique, 2021b).

The dashboard application window is divided into two main sections, a lateral panel on the left-hand side and a main window on the right-hand side. The lateral panel presents the current risk level or the historical risk levels calculated for previous years. A specific climatic year can be selected on the top right corner of the dashboard application (Figure 15). Along with the risk level, the lateral panel contains information related to the monitoring station used and the date of the last update. The main window provides a range of complementary information related to the active layer detachment slide process and its risk evaluation. This complementary information is subdivided into four tabs located at the bottom of the main window. The first tab gives the climate parameters used in the risk calculation including the daily temperature, the cumulative thawing index, and the freezing/thawing index ratio (Figure 15A). The second tab gives the risk level with a legend (Figure 15B), the third tab contains the 7-day weather forecast from Environment Canada for Salluit (Figure 15C) and the last tab gives background information about the active layer detachment slide processes and how its risk evaluation is computed (Figure 15D).
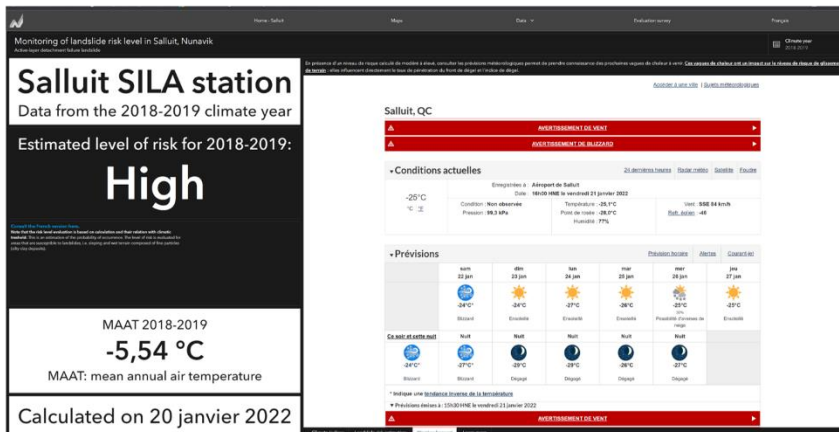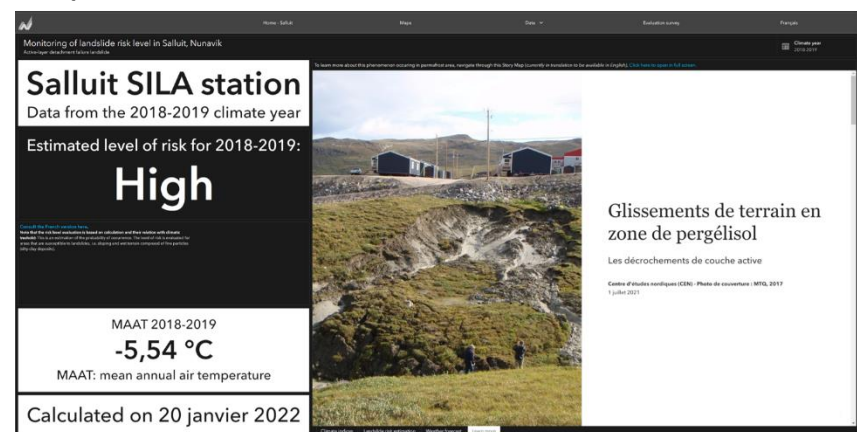
Figure 15 Screenshots of the dashboard application along with the different tabs content

2.1.2. Tasiujaq

2.1.2.1. Site history

Located in the continuous permafrost zone in Southern Nunavik, the Tasiujaq airport was first built in 1989-1990 on a fluvial terrasse along the Bérard River at an elevation of approximately 30 meters above sea level. The entire runway was built over warm, brackish, and ice-rich permafrost with mean annual ground temperatures between - 2° C and -3° C (Allard et al., 2020).

The runway is 1190 m long and 44 m wide, and was originally built with an embankment height of about 2.5 m. During the initial construction, a layer of insulation was added between the contact of the first and second sedimentary layer along a 50 m section of the runway. Thermistor strings were installed beneath these sections, as well as in natural soil nearby as a reference to assess the effectiveness of the insulation.

The local geology for this site is very well known thanks to extensive studies of the area using a variety of methods including stratigraphic cross sections analyses along the riverbanks, drilling, electrical resistivity tomography (ERT) and ground penetrating radar (GPR) surveys (Savard, 2006; Allard et al., 2007; L'Hérault et al., 2012). The runway was built entirely over a marine regression sequence of unconsolidated sediments, that is relatively consistent across the runway (L'Hérault et al., 2012). The layered sedimentary sequence consists of four units, as seen in Figure 16. The first unit is the surface layer that extends 1 m deep and consists of sand and gravel laid by tidal channels during the emergence of the post-glacial d'Iberville Sea. The second unit extends to about 5-6 m deep and consists of low-tide mudflat sediments including poorly sorted silt and some sand and stones. Within this unit are thin layers of segregated ice lenses. This unit is also slightly saline, which has the effect of lowering the freezing point by an average of 0.5° C, and a maximum of 1.1° C in some samples. The third unit is about 4 m thick and is composed of loosely stratified sand and gravel with some boulders with abundant shell fragments and cemented by pore ice. This layer was likely laid in a pro-glacial submarine environment. Finally, at about 10-11 m deep the fourth unit consists of marine clay with thick ice lenses and sub-vertical ice veins. The depth to bedrock is unknown, though it exceeds 25 m.
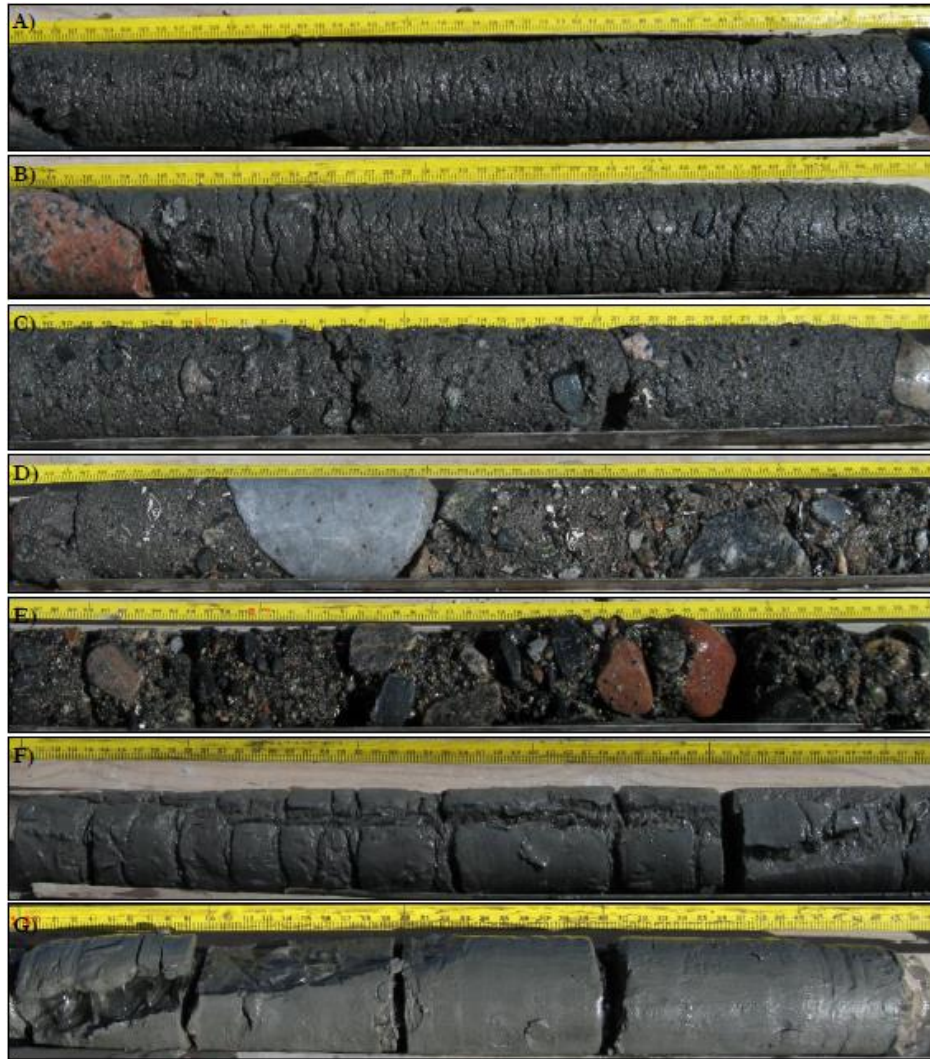
Figure 16 Cores of the stratigraphic units beneath the Tasiujaq runway: A and B) Poorly sorted and brackish intertidal silts of from unit 2, between 2.5 and 3.6 m deep; C) Increase in coarseness with depth and transitional, base of unit 2 at ~ 5 m depth; D and E) Sand and gravel with shell fragments of unit 3, depth of 7.8 to 8.4 m; F and G) Marine clay with interspersed ice lenses and vertical ice veins, depth from 10.1 to 14.5 m

The second unit, which is icy and silty appears to be the layer within which permafrost thaw is inducing important settlement along the runway. There are several areas where differential settlement has occurred, particularly along the eastern shoulder (Beaulac and Doré, 2006). In 2004, significant settlements of up to 50 cm, along with tension cracks were observed near the taxiway, between the 5+100 and 5+140 m chains (Allard et al., 2007) (Figure 17A and B).

Signs of localized degradation on the edges of the runway suggests that the permafrost under the shoulders is severely affected (L'Hérault et al., 2012). Given the orientation of the runway relative to the prevailing winds, large amounts of snow can accumulate at the foot of the embankment. Additionally, shrubs have grown along the foot of the embankment which furthers snow accumulation. The insulation resulting from snow accumulations cause ground temperatures to increase and permafrost to thaw. This process is exacerbated by the pooling of water at the foot of the embankment due to poor drainage in these newly depressed areas (L'Hérault et al., 2012) (Figure 17C). The combination of snow accumulation and poor drainage leads to warmer soil temperatures, which causes changes in the thermal regime of the permafrost towards thawing conditions. Drilling in 2009 showed that permafrost under the depressions at the foot of the embankment had thawed to depths in excess of 6 m, or almost completely through the intertidal sediments (L'Hérault et al., 2012). In 2010, a transverse depression was observed, and it is probably associated with a transverse groundwater seepage flowing across the embankment from east to west. This depression was still visible during the fieldwork carried out by Université Laval in the fall of 2018 (Figure 17D). A topographic survey of the runway surface carried out by a contractor before the remediation work has highlighted the extent and amplitude of the surface deformations due to thaw settlements (Figure 17E).

Over the years, the runway has been resurfaced many times, including in 2007 to remediate degradation identified in Allard et al. (2007). The airport was also a site for engineering adaptation measures including air convection embankment, heat drain, and gentle slope embankment. Major remediation work was undertaken in 2018 which included lowering the embankment slope from 1:4 to 1:6 for about 2/3 of the runway perimeter and the creation of wide and shallow drainage ditches that were built a short distance away from the embankment to prevent water from pooling at the foot of the embankment. While it appears that the lower slope is somewhat effective in cooling ground temperatures, the infrastructure remains at risk to degradation. Temperature data from thermistor strings located in the runway at the end of the summer of 2020 show that the active layer thickness reached up to 3.64 m in the non-insulated section of the runway, which is nearly into the thaw-sensitive ice-rich silt layer that underlies the entire runway. Therefore, the risk of general degradation along the runway remains high in the face of a changing climate. The existing array of instrumentation that has been set

up at this site along with the ongoing monitoring will support the risk evaluation algorithm developed to emit timely warning when important settlement is expected.
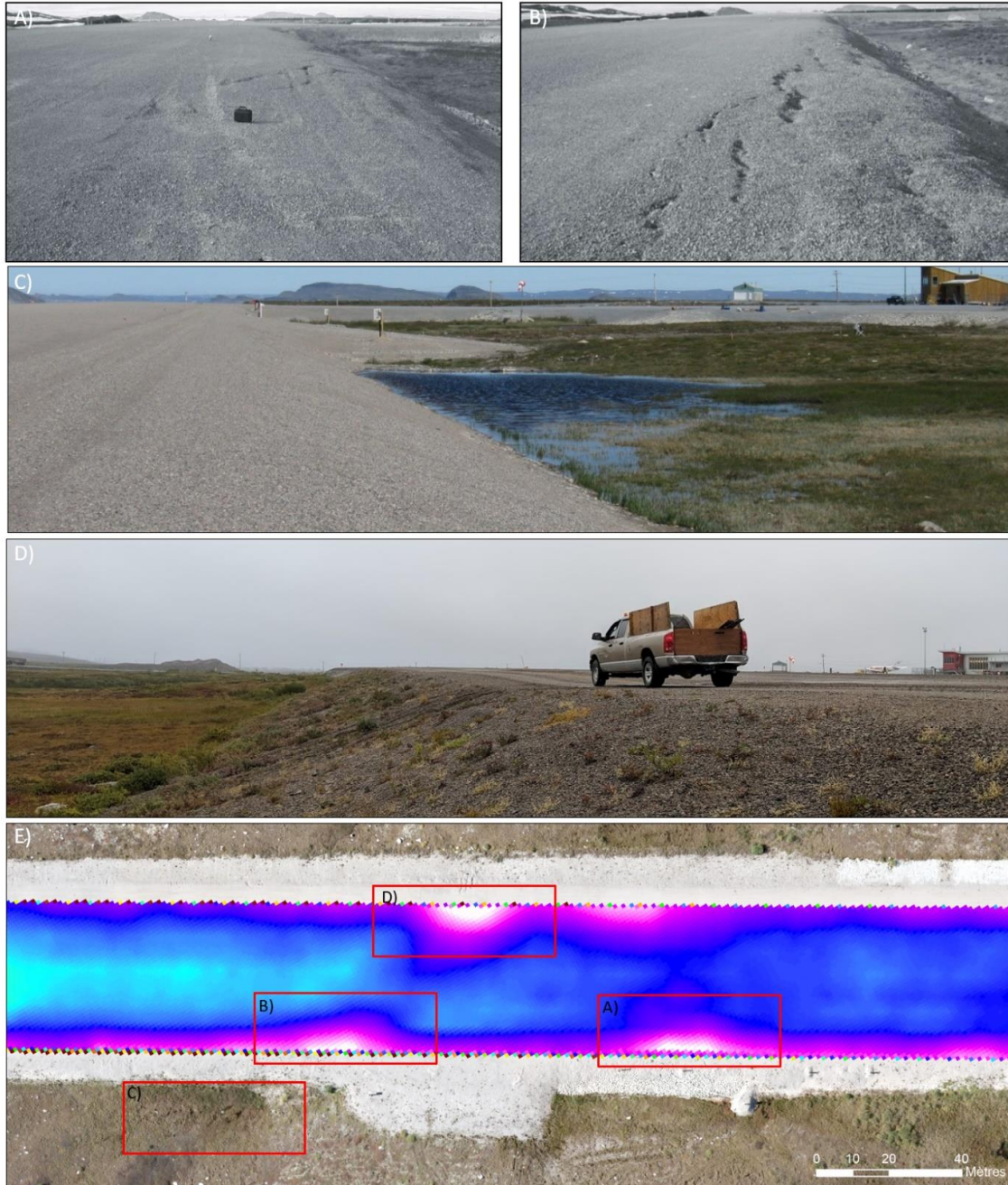
Figure 17 A) and B) Significant depressions with longitudinal cracks as observed in 2004 on the east side of the Tasiujaq runway. C) Accumulation of water at the foot of the embankment on the east side in July 2009. D) Major depression on the west side observed in the fall of 2018 during the adaptation work. E) Topographic survey carried out during the summer of 2018 highlighting major depressions still affecting the runway. (From L'Hérault et al, 2021)

2.1.2.2. Instrumentation

The Tasiujaq runway is equipped with numerous ground temperature stations, some of which have been in operation since the early 90s. An overview of the instrumentation available at the Tasiujaq runway site is shown in Figure 18. From the existing instrumentation available at this site, two ground temperature stations were selected to be equipped with the new ULogC32 LoRa datalogger. One station is located at the south-west end of the runway (TAS-F1A) and monitors the ground temperature under the gentle slope embankment and the other station is located mid-runway (HT-181) also on the west side of the embankment. HT-181 monitors ground temperature at the center of the embankment, but also the ground temperature in a borehole located about 10 m away from the runway (TAS-F2A), which is often used as a reference. Configurations of the thermistor string for each ground temperature monitoring stations are summarized in the table in Figure 18.
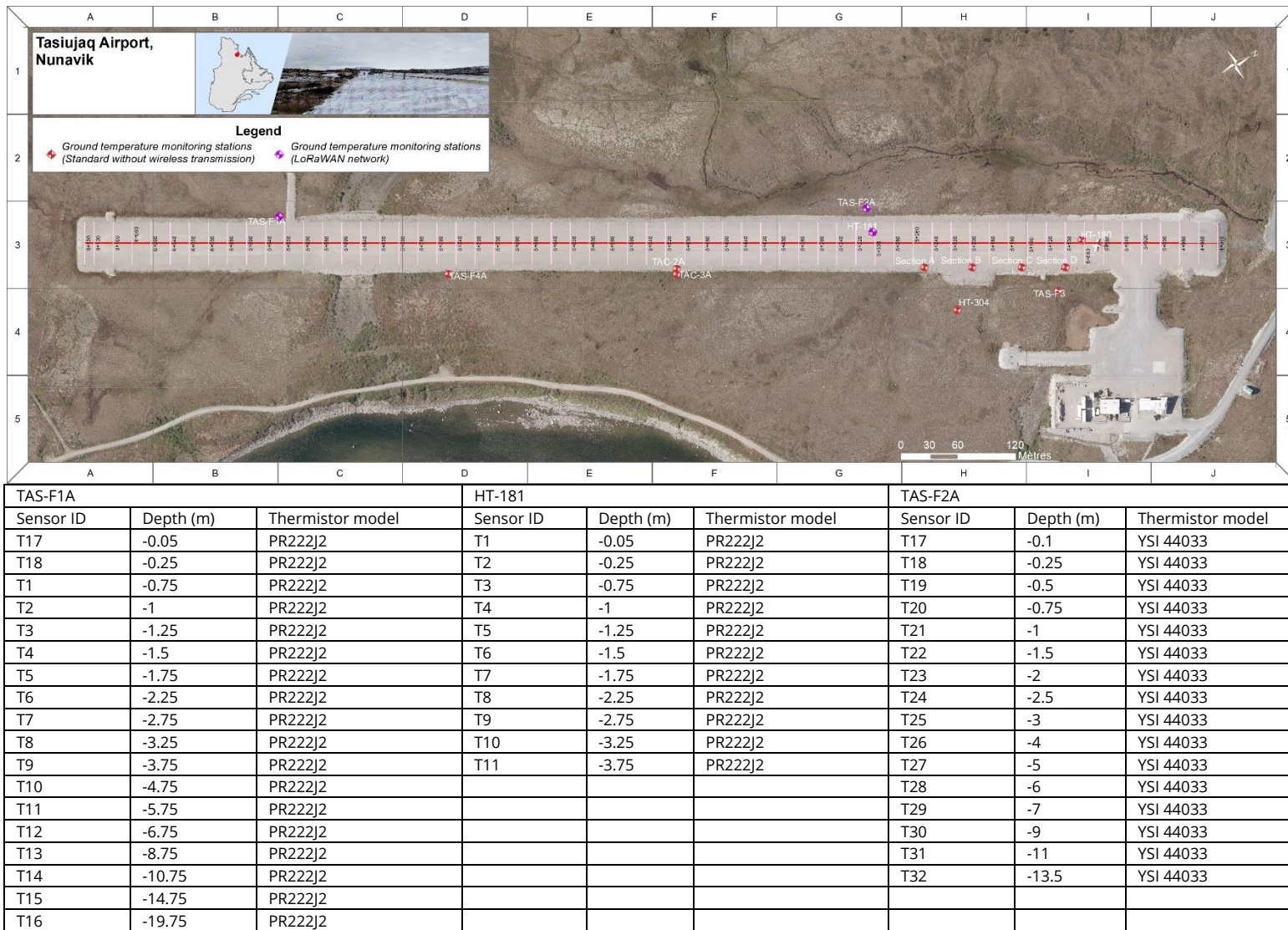
TAS-F1A			HT-181			TAS-F2A		
Sensor ID	Depth (m)	Thermistor model	Sensor ID	Depth (m)	Thermistor model	Sensor ID	Depth (m)	Thermistor model
T17	-0.05	PR222J2	T1	-0.05	PR222J2	T17	-0.1	YSI 44033
T18	-0.25	PR222J2	T2	-0.25	PR222J2	T18	-0.25	YSI 44033
T1	-0.75	PR222J2	T3	-0.75	PR222J2	T19	-0.5	YSI 44033
T2	-1	PR222J2	T4	-1	PR222J2	T20	-0.75	YSI 44033
T3	-1.25	PR222J2	T5	-1.25	PR222J2	T21	-1	YSI 44033
T4	-1.5	PR222J2	T6	-1.5	PR222J2	T22	-1.5	YSI 44033
T5	-1.75	PR222J2	T7	-1.75	PR222J2	T23	-2	YSI 44033
T6	-2.25	PR222J2	T8	-2.25	PR222J2	T24	-2.5	YSI 44033
T7	-2.75	PR222J2	T9	-2.75	PR222J2	T25	-3	YSI 44033
T8	-3.25	PR222J2	T10	-3.25	PR222J2	T26	-4	YSI 44033
T9	-3.75	PR222J2	T11	-3.75	PR222J2	T27	-5	YSI 44033
T10	-4.75	PR222J2				T28	-6	YSI 44033
T11	-5.75	PR222J2				T29	-7	YSI 44033
T12	-6.75	PR222J2				T30	-9	YSI 44033
T13	-8.75	PR222J2				T31	-11	YSI 44033
T14	-10.75	PR222J2				T32	-13.5	YSI 44033
T15	-14.75	PR222J2						
T16	-19.75	PR222J2						

Figure 18 Ground temperature instrumentation available at the Tasiujaq runway site. The selected monitoring stations to be part of the LoRaWAN network along with their thermistors strings configurations are summarized in the table.

2.1.2.3.　LoRaWAN network implementation

Prior to the field deployment of the LoRaWAN network at the Tasiujaq Airport, an RF coverage map was produced using the parameters shown in Table 9. The resulting RF coverage map suggests a very good signal coverage for the whole runway and beyond (Figure 19). In fact, due to the very flat topography of the area, good signal coverage can easily reach up to 12 km from the gateway.

Table 9 Parameters values entered as inputs in the ITS radio propagation model used to compute the radio coverage map, Tasiujaq runway site.

Parameters	Value
Gateway Antenna Height (m above ground):	8
Gateway Antenna Type:	Omni
Gateway Antenna Gain (dBi):	8.15
End-node Antenna Height (m):	1
End-node Antenna Gain (dBi):	1.6
Frequency (MHz):	915
Tx power (Watts):	0.1
Tx line loss (dB):	1
Rx line loss (dB):	3.2
Rx threshold (dBm):	-127
Required reliability (%):	95
Strong Signal Margin (dB):	10

Green: Strong signal margin (> 10 dB, 95% of the time)
Yellow: Weak signal margin (< 10 dB, 95% of the time)
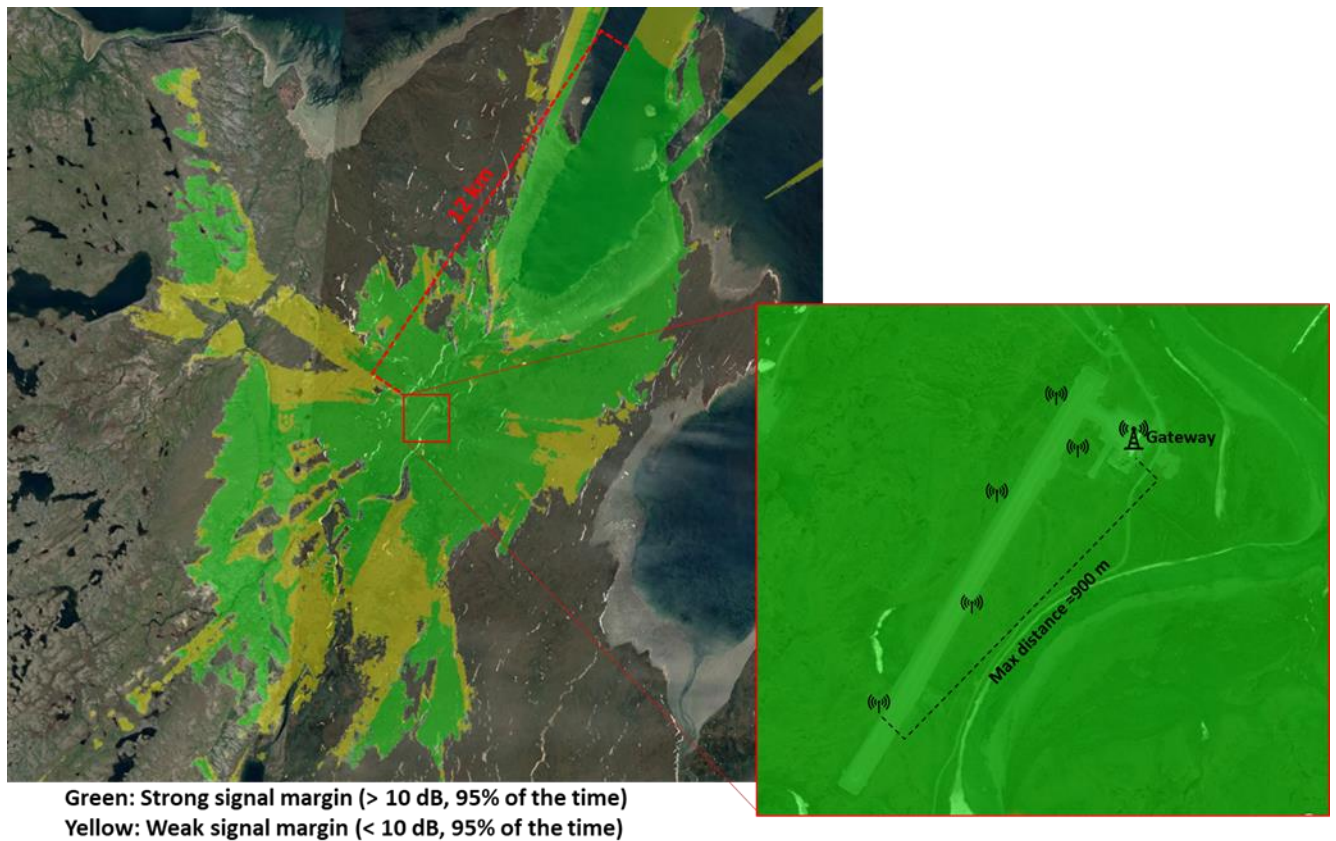
Figure 19 Gateway RF coverage for the Tasiujaq runway site.

During the implementation of the LoRaWAN network in the summer of 2021, extensive in situ signal strength and transmission reliability measurements were conducted across the area using two different external antenna models (e.g.: ANT-916-ID-2000-RPS and FG9026). Due to the small area of interest and the distance from the farthest ground monitoring station to the gateway, the antenna with the lowest gain value (antenna model ANT-916-ID-2000-RPS, 1.6 dBi) was installed instead of the higher gain antenna (antenna model FG9026, 8.5 dBi). RF signal coverage tests using different antenna heights and locations around the airport's garage building were also conducted on-site. These tests suggest that a 3 m height antenna fixed directly on the north-west wall of the airport garage was sufficient to ensure proper RF signal coverage across the area of interest, while allowing for easy installation (Figure 20A). For this reason, even though the reduced height and the less-than-optimal location of the external antenna likely reduces the signal coverage performance, the latter antenna configuration was chosen (Figure 20B). With the current gateway antenna configuration, a surprisingly reliable
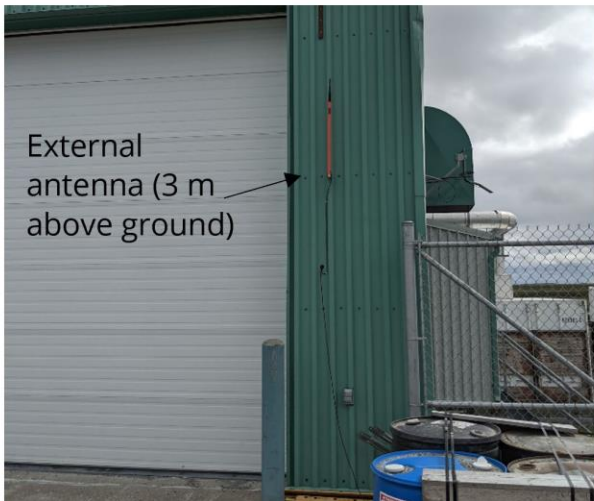
50

signal was measured over a 9 km radius around the gateway. The gateway was installed inside the airport garage and connected to the secured KRG transport WIFI network (Figure 20C).

Due to Transport Canada regulations, the ground temperature monitoring station external antennas (end-nodes) must stay lower than the runway center-line elevation. A typical ground temperature monitoring station installation with external antenna located along the runway embankment slope is shown in Figure 21A. For the TAS-F1 ground monitoring station located on the embankment slope, the antenna sits at a height of only 90 cm above the ground and is likely to be snow covered during winter (Figure 21B). For this reason, transmission reliability is expected to be reduced during wintertime for this station. However, as of January 12, 2022, data transmission is still active and there is no missing data since its implementation in August 2021. For the HT-181 ground temperature monitoring station located a few meters away from the embankment toe, antenna height restriction was not an issue. For this station, the antenna was installed at a height of about 2 m above the ground level (Figure 21C).

Figure 20 A) Tasiujaq runway LoRaWAN network configuration with the proposed gateway location and end-nodes locations (ground temperature monitoring stations). B) Gateway external antenna fixed to the north-west wall at a height of about 3 m. C) Gateway located inside the airport garage.
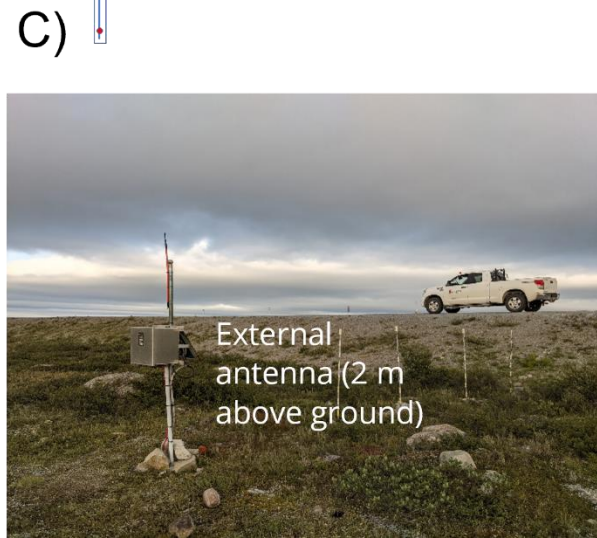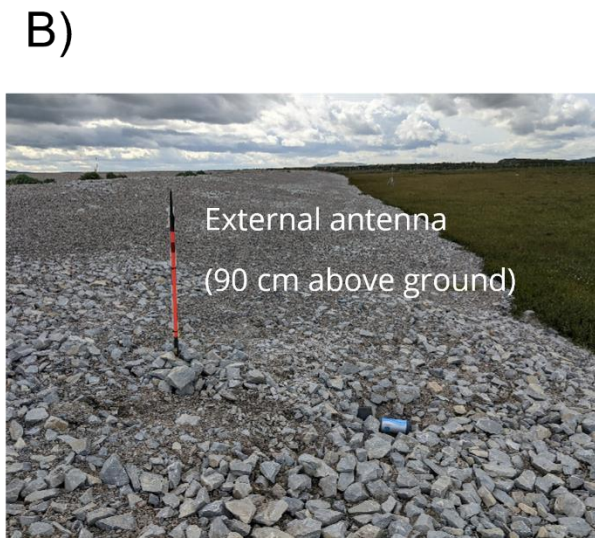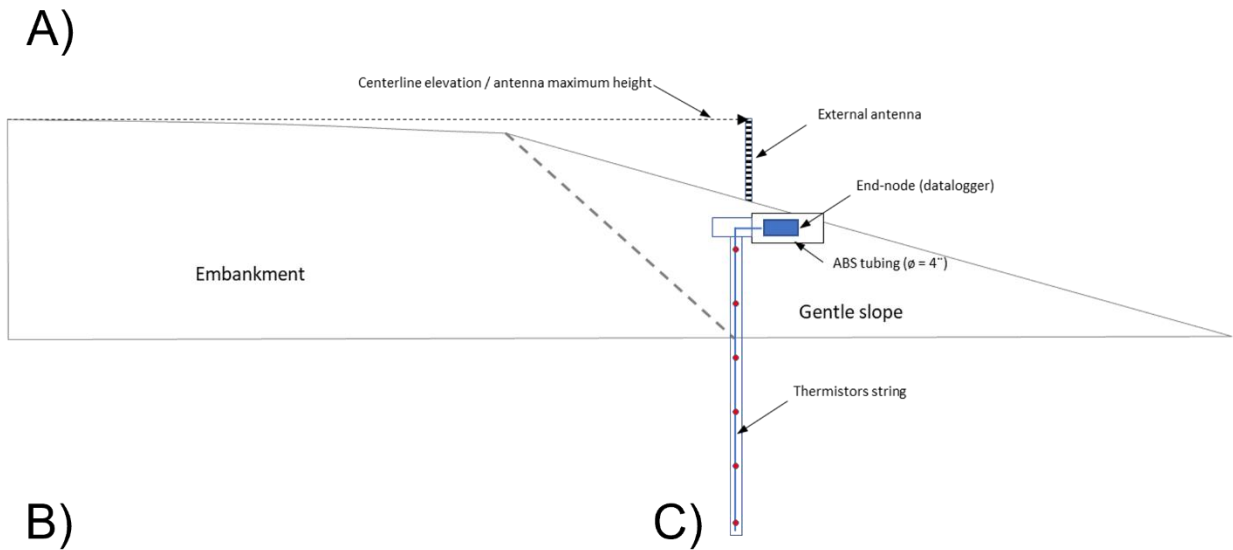
Figure 21 Typical installation with external antenna for end-node located along the runway embankment slope. Ground temperature monitoring station (end-nodes) B) TAS-F1 and C) HT-181.

2.1.2.4. Algorithm parameters, thresholds and expected outcomes

Thaw settlement is the soil volume change that occurs when the ice contained in the permafrost melts upon thawing and the soil consolidates under the existing overburden pressures (Figure 22A). Thaw settlement is usually a slow phenomenon that develops as the thaw front penetrates an ice-rich frozen layer that contains ice exceeding the porosity of the material. However, in some cases, it can evolve rapidly in presence of anthropogenic disturbances or environmental factors that accelerates the permafrost thawing. The thaw settlement ratio is expected to slightly increase under thawed overburden pressure and the load of the embankment (Figure 22A). In permafrost regions, fine-grained soils are prone to contain significant amounts of excess ice, thus leading to a generally high thaw settlement ratio (Figure 22B). A well-defined stratigraphy along with a historical record regarding the active layer thickness variations are crucial to adequately assess the thaw settlement potential for a specific site.
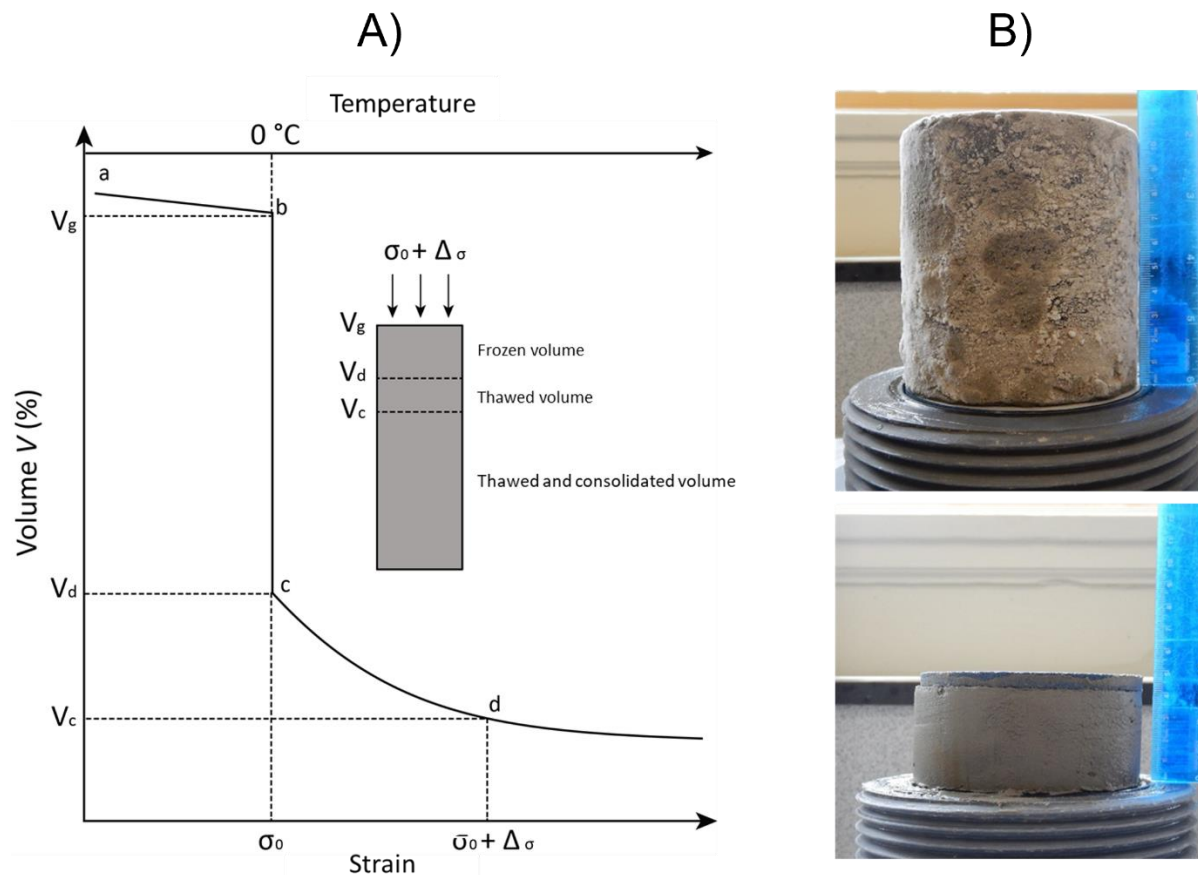

Figure 22 A) Typical volume change versus strain for ice-rich frozen soil subjected to thawing (modified from Andersland and Ladanyi, 2003). B) Ice-rich permafrost sample before and after thaw settlement laboratory test.

In order to evaluate the risk of occurrence of thaw settlement according to the thickening of the active layer due to either an increase in the air temperature or anthropogenic disturbances, a simple algorithm was developed and implemented for the Tasiujaq runway. This algorithm uses the daily thaw depth estimated from available ground temperature measured by the LoRaWAN network end-nodes (TAS-F1 and HT-181) and the soil stratigraphy at the monitoring sites. Note that the daily thaw depth corresponds to the 0degC isotherm but could be lowered in the presence of saline permafrost. Based on the site stratigraphy, specific cryostratigraphic positions are defined and act as risk level thresholds (Figure 23).

Based on these cryostratigraphic positions, four levels of risk for the thaw settlement hazard have been defined: none, low, moderate and high. The embankment and subgrade interface corresponds to the threshold between no and low risk level while the prior-to-construction (PTC) thaw depth and the ice-rich permafrost contact sets the threshold between the low and the high-risk level. In the case where the permafrost below the PTC thaw depth is ice-poor (case A), a moderate risk level is added between the low and the high-risk levels. For this moderate risk level, the upper threshold corresponds to the position of the PTC maximum thaw depth and the lower boundary as defined by the contact between the base of the ice-poor layer and the top of the ice-rich permafrost layer.

If the thaw depth is constrained inside the embankment, the thaw settlement risk is considered nonexistent. However, as the thaw front slowly penetrates the subgrade, the risk level becomes low until the thaw depth reaches the maximum PTC thaw depth. When the thaw front exceeds the PTC thaw depth, but does not reach the ice-rich permafrost, the risk is considered moderate (case A) (Figure 23). If the thaw front exceeds PTC levels and penetrates the ice-rich permafrost, the thaw settlement risk becomes high (case B) (Figure 23).
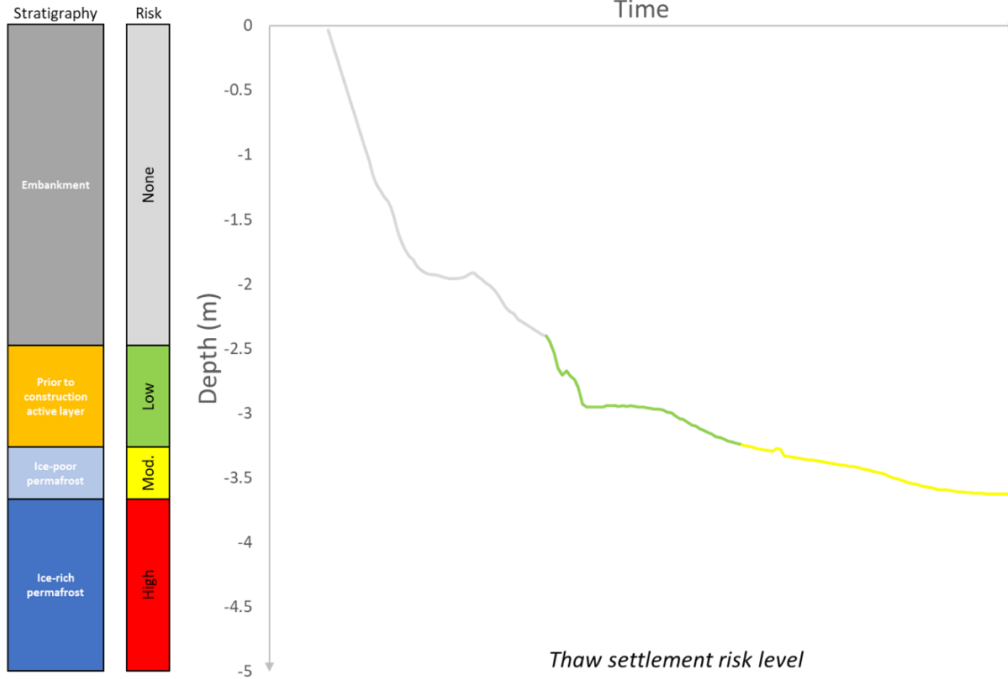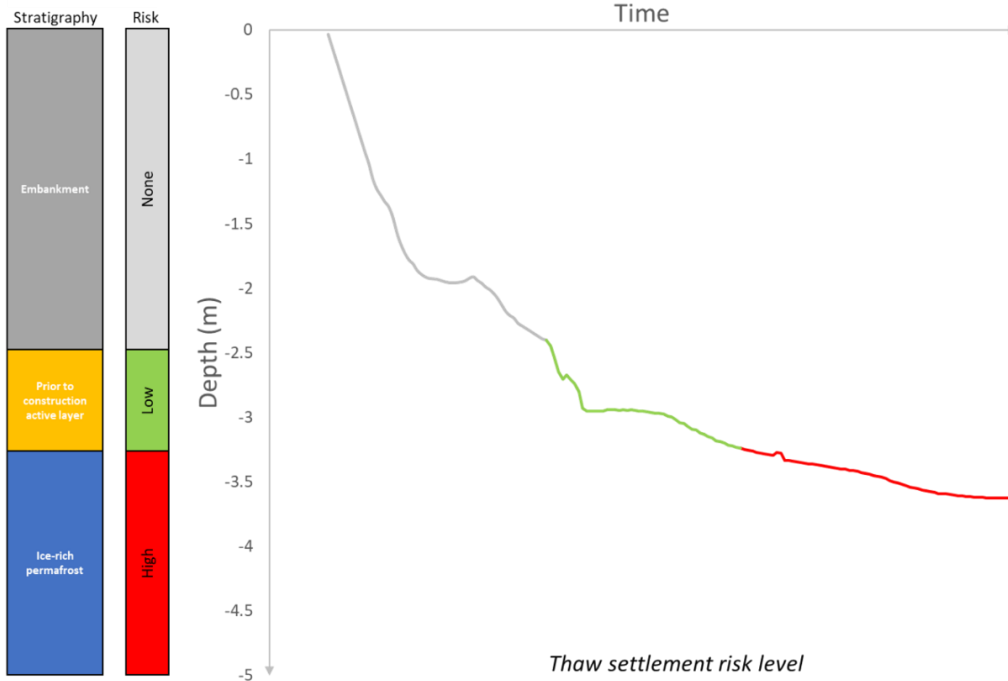
Figure 23 Daily evolution of the thaw settlement risk warning during the thawing season based on the site stratigraphy, the cryostratigraphy and the daily thaw depths estimated from the ground temperatures reading. Without (Case A) or with (Case B) an intermediate layer of ice-poor permafrost located below the prior to construction maximum thaw depth.

In the algorithm, the threshold between the moderate and high-risk level, initially defined by the maximum thaw depth before construction or the depth of the ice-rich permafrost (Th_0), may increase over time (Figure 24). This shift in the threshold position accounts for the geotechnical changes induced by the thawing of the upper part of the ice-rich permafrost layer. In fact, when the upper section of the ice-rich permafrost layer thaws and the excess water is drained, the thawed material consolidates resulting in settlement. The following summer, if the thaw front penetrates this previously thawed and consolidated layer once again, no more significant settlement will be expected since it has already occurred during the initial thawing phase. As such, this new maximum thaw depth will become the new threshold value delineating the moderate and the high-risk level (Th_1). By constantly adjusting the threshold between the moderate and high-risk level to the maximum thaw depth occurred in previous summers, the algorithm accounts for the historical record in the thaw settlement risk evaluation for a site. For this reason, if the thaw depth for a current summer is greater than the previous summer but don't exceed the maximum historical thaw depth, the thaw settlement risk level will remain moderate. An example of the influence of the past thaw depth variations on the moderate/high risk threshold is illustrated figure 24. In this figure, the moderate/high risk threshold is initially set by the depth of the ice-rich permafrost layer (Th_0) but will shift to Th_1, th_2 and Th_n positions as the thaw depth increases over time.
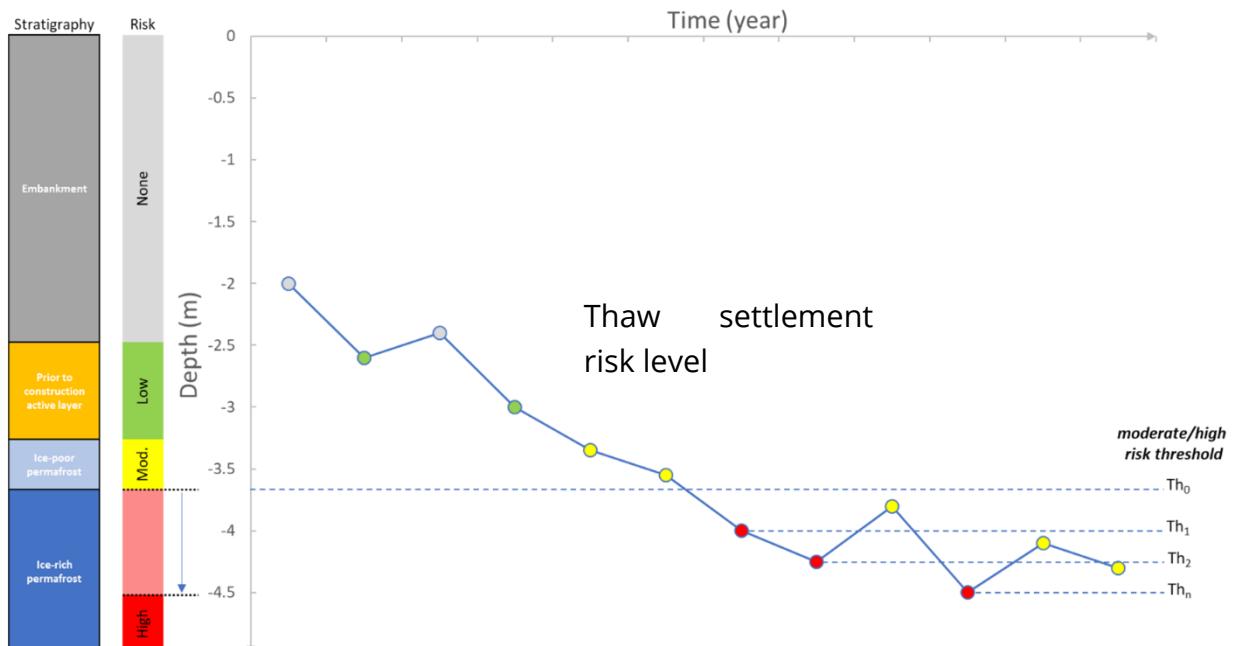
Case A

Figure 24 Thaw depth variations and the associated thaw settlement risk based on the site stratigraphy. Maximum thaw depth position from previous years defines the new moderate/high risk threshold.

To automate the thaw settlement risk assessment for the Tasiujaq runway, a python program was written using the general structure and some of the sub-routines and functions used in the active layer detachment slide program (see section 2.1.1.4). The automation process from data acquisition to warning is outlined in the main program logical diagram shown in figure 25. The program automatically starts at 15:00 daily and is executed through the launch of the main program *ts_main.py* with a command file (*batch file;* extension .bat) by the task planner. The task is planned on a standing operating computer at Centre d'Etudes Nordiques at l'Université Laval (UL). Once launched, the main program calls the different modules to read the data from the LoRA server and accomplishes the tasks of averaging hourly data, calculating degree-days, summation of degree-days, interpolating thaw depth (0 °C isotherm) between thermistors in order to assess the risk level based on the defined threshold according to the site stratigraphy and past maximum thaw depths (if available). The associated risk level is then updated daily on the Tasiujaq runway dashboard. If the thaw settlement risk level becomes high, an email is automatically sent to specific contact persons. In the case of the Tasiujaq runway, the contacts are the MTQ (owner of the infrastructure) and the

Kativik Transport (local manager charged of the operation and maintenance of the airport).
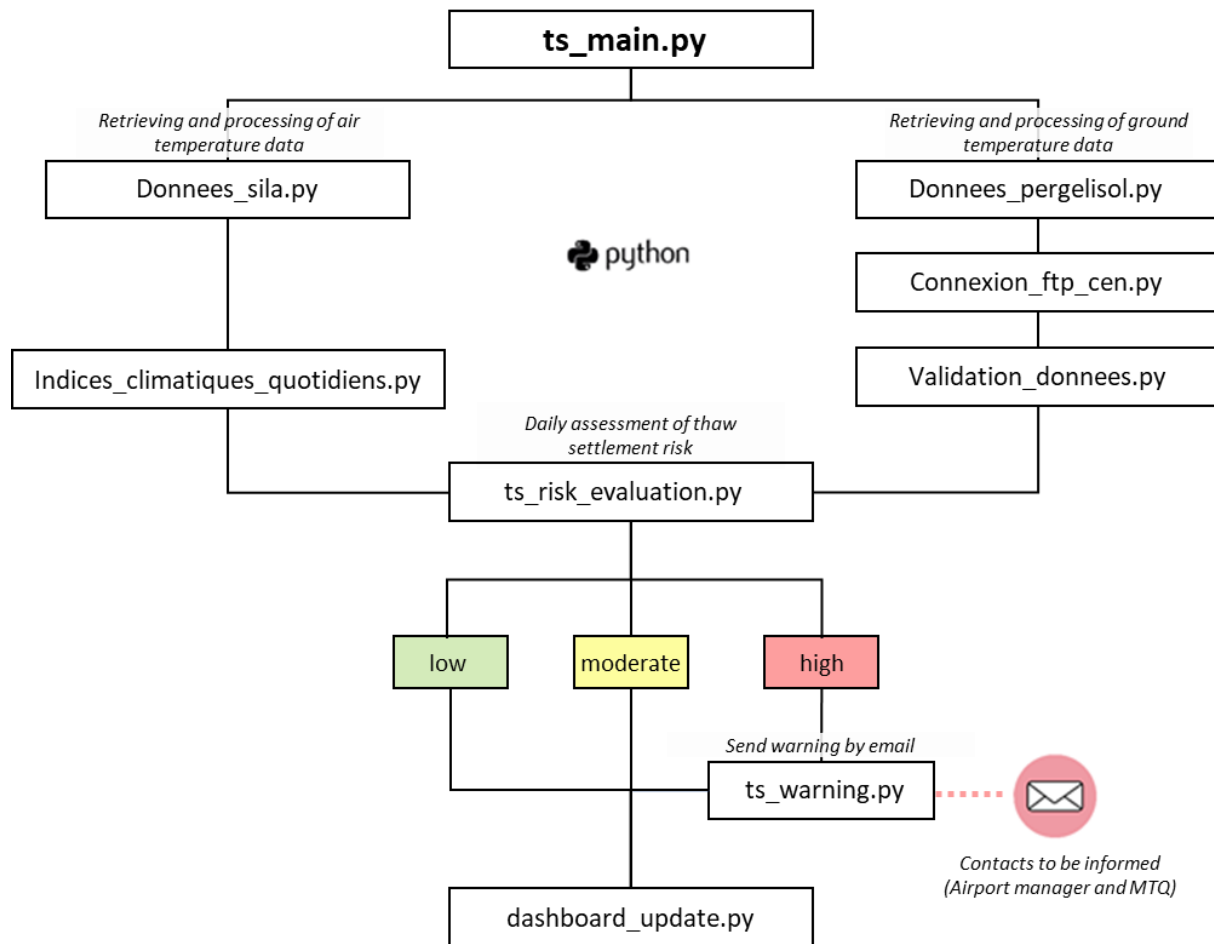

Figure 25 Logical diagram of the thaw settlement hazard warning program (ts_main.py) and its sub-modules and functions.

For the Tasiujaq runway, the ice rich layer corresponds to the interface between the alluvial and the intertidal deposit located at a depth ranging from 1.5 to 2 m under the embankment. Temperature readings at the HT-181 thermistors strings indicate that thaw depths from the past 10 years have fluctuated between 3.3 to 3.7 m from the surface. The thaw depth reached the closest position to the intertidal deposit containing excess ice during the warm summers of 2010 and 2012. According to the embankment thickness and site stratigraphy, the thaw front is now penetrating beyond the thawing depth before construction but is still limited to the ice-poor permafrost layer.

Consequently, according to the thaw settlement warning algorithm, the risk of thaw settlement for the center part of the runway has remained moderate (Figure 26).
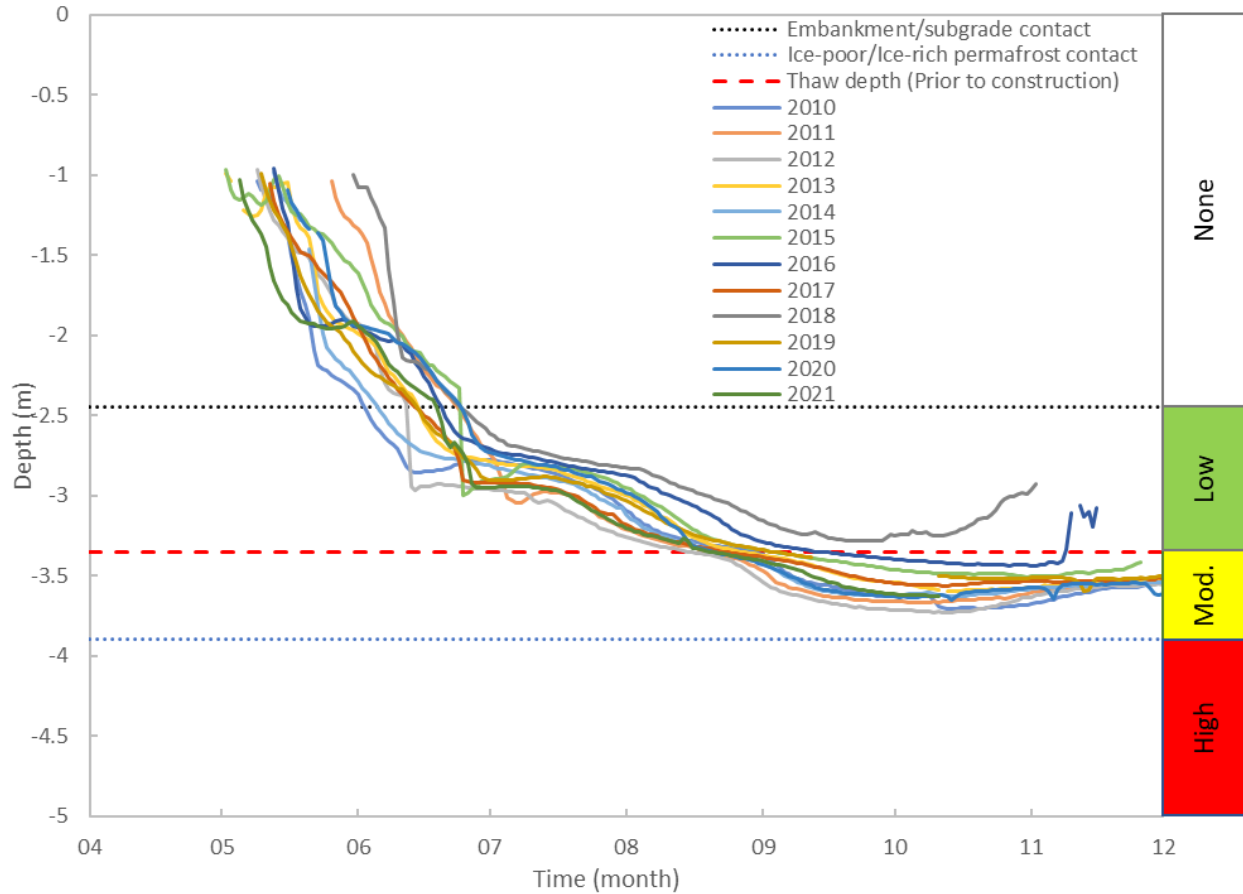

Figure 26 Thaw depth progression for the 2010-2021 period estimated from ground temperature data provided by the monitoring site HT-181, Tasiujaq runway centerline.

Future improvements to the algorithm could include a total thaw settlement estimation based on the thaw consolidation ratio for each soil unit using a multilayer system (Figure 27).
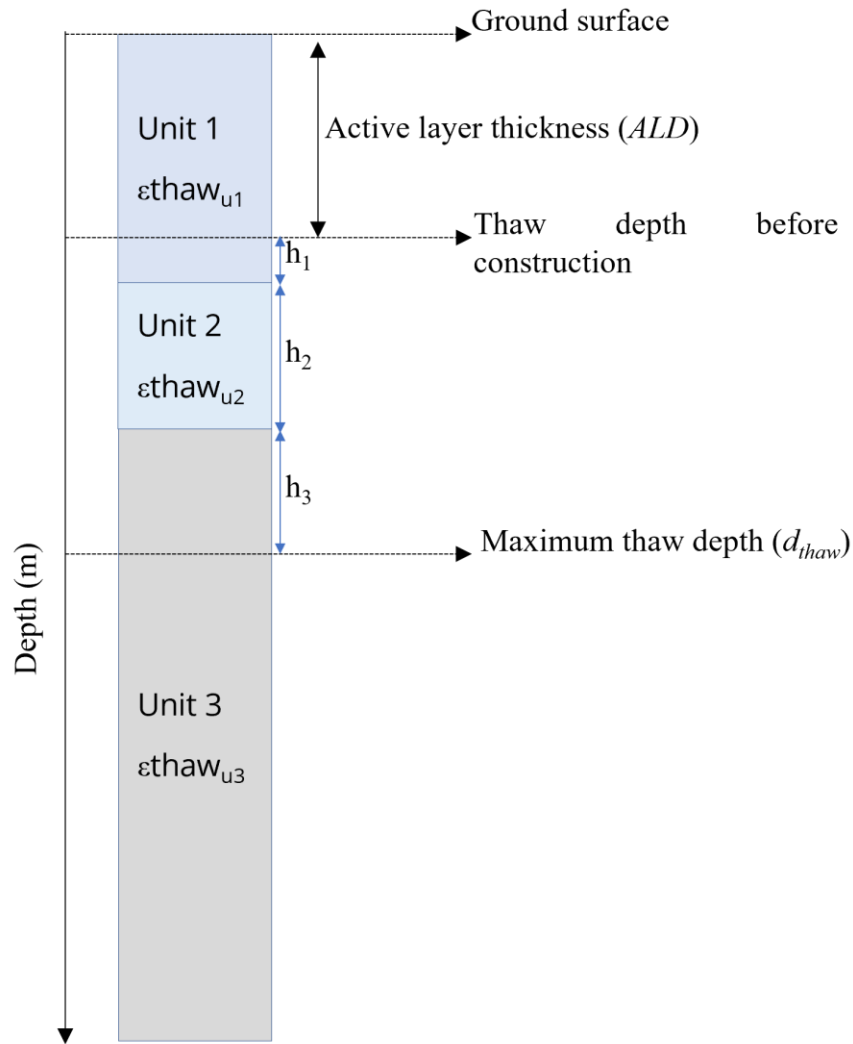
Figure 27 Evaluation of total thaw settlement under an embankment in a multilayer system. The algorithm would consider the initial active layer (ALD), the daily thaw depth position (dthaw). Total thaw settlement is computed by summing the products between the thicknesses of the different soil layers that will be thawed (hi) and their respective settlement values (εthawi).

The anticipated total settlement would then be calculated by evaluating the penetration of the thaw front (d_{thaw}) beyond the maximum thaw depth before construction or the previous summers and by summing the products between the thicknesses of the different soil layers that will be thawed (h_i) and their respective settlement values ($\varepsilon thaw_{ui}$). This process of estimating total settlement is written by the following equation:

$$\varepsilon thaw_{\text{total}} = \sum_{i}^{n} h_i \cdot \varepsilon thaw_i = (h_1 * \varepsilon thaw_{u1}) + (h_2 * \varepsilon thaw_{u2}) + (h_3 * \varepsilon thaw_{u3})$$

By estimating the total thaw settlement, the algorithm could consider the infrastructure tolerance to surface deformation in the risk calculation rather than simply emit warning when the thaw front approaching or penetrates into an ice-rich layer. The tolerance to thaw settlement is the amount of ground subsidence resulting from thawing that would not affect either the function of the infrastructure or user safety. The tolerance might vary depending on the type of infrastructure (road, railway or runway) but also where the affected zones are located. For instance, tolerance to thaw settlement is expected to be lower for runways and railways compared to roads due to the narrow range of safe operable conditions for aircrafts and trains. It is also expected that tolerance would be lower in the landing or takeoff zone of a runway or before a road curve. Ultimately, considering the infrastructure tolerance to surface deformation would greatly improve the risk evaluation for the thaw settlement hazard, but such integration requires further research and development.

Future improvements to the algorithm could also include a thaw depth forecasting component where thaw depth could be estimated two weeks ahead using the Environment Canada 14-day air temperature forecasts as an input. The thaw depth could either be estimated using an index of the empirical correlation between an air temperature and thaw depth specific to the site (L'Hérault, 2009) or the commonly used Modified Berggren equations. Such predictive capabilities would allow the warning system to issue a pre-warning days or weeks in advance instead of at the time the thaw front reaches the critical ice-rich layer.

2.1.3. Inukjuak

2.1.3.1. Site history

The Inukjuak airport (Figure 28A) was constructed in 1987. It is built on an embankment laid on poorly drained terrain. The soil stratigraphy under the runway consists of a surficial sand layer that was deposited in a wave-dominated coastal environment as the land emerged from the post-glacial Tyrrell Sea. At about 1-2 m deep, the sediments grade into a finer texture material consisting of silt and silty sand (Figure 28B, C and D). This shell-bearing material is ice-rich and is believed to have been laid in an intertidal environment. This stratigraphic unit grades downward into massive sand with alternating gravel beds and silt beds; it belongs to a geological formation of late-glacial submarine glacio-fluvial fans. The bedrock was reached at depths varying from 4.6 to 10.9 m in three holes drilled in 2008 (L'Hérault et al., 2012) (Figure 29). The mapping of this general stratigraphic sequence was refined recently with ground-penetrating radar profiles (Bilodeau et al. 2020) (Figure 29).

In the 2000s, thaw settlements, depressions and linear cracks along the sides of the runway were surveyed by the MTQ. Drilling at the foot of the embankment revealed that the permafrost had thawed to depths of 5-6 m under snowbanks that had accumulated on the sides of the embankment, and under pools of standing water in the ditches alongside the runway (L'Hérault et al., 2012). Since no drilling was done in the runway itself, it is impossible to determine the permafrost composition, the maximum thaw depth, and whether permafrost is still within the embankment or if it has reached the underlying subgrade. The GPR surveys, though, do suggest that the thaw depth penetrates the thin superficial sandy sediments overlying the ice-rich permafrost except for the western end of the runway where the embankment is much thicker. A recent geotechnical investigation conducted during the summer of 2021 which included drilling shallow boreholes, confirms the presence of ice-rich permafrost under most of the runway, which highlights the high vulnerability of this infrastructure to permafrost thaw (Figure 30).

To prevent the further thawing of permafrost along the edges of the runway and to hopefully help the freeze back of the ground, the MTQ undertook remediation steps in the summer of 2021. These steps included building gentler slopes on the sides of the runway to reduce snow accumulation and to move the ditches several meters away.

These renovations allowed for the installation of new thermistor cables in the runway, under the gentle slopes where permafrost had thawed and in the natural terrain for an undisturbed reference. Therefore, it is now possible to measure the critical depth of thaw beneath the infrastructure beyond which thaw settlement will affect the runway. The temperature regime of the permafrost under the runway is now monitored and the thermal performance of the gentle slopes will be assessed.

Figure 28 A) The Inukjuak airport around 2018. Note the drainage ditches with standing water on both sides. Ice-rich permafrost cores recovered during the geotechnical investigation done in summer 2021 (L'Hérault et al., in prep.); B) Cores from INU-2021-FS1 (1.61 to 1.91 m depth); C) Cores from INU-2021-FS3 (0.75 to 1.08 m depth); and D) Cores from INU-2021-FS1 (1.25 to 1.6 m depth).
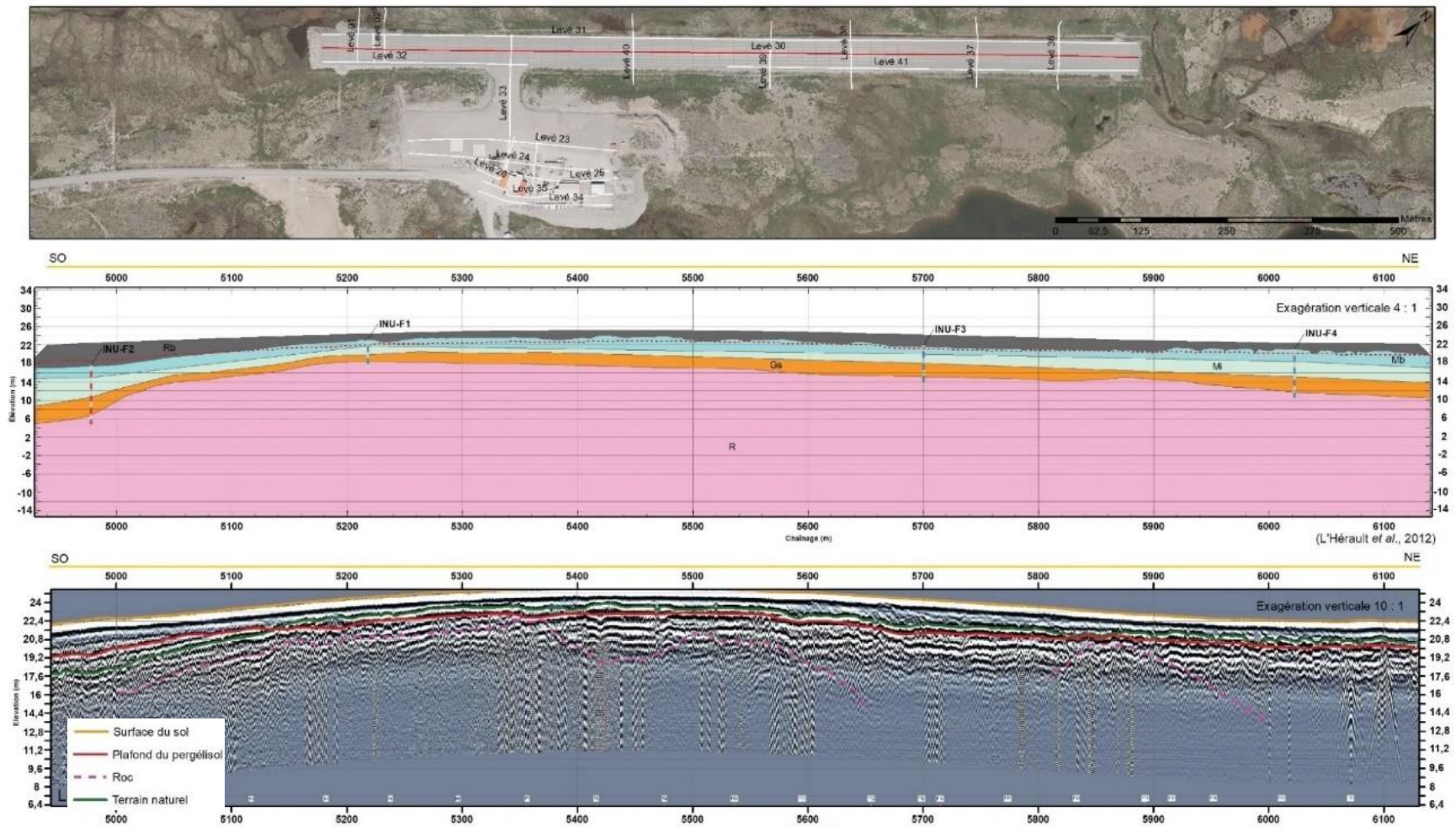
Figure 29 Top) Aerial view with plan of GPR survey lines; Middle) The general stratigraphy under the runway; Rb, embankment; Mb, sandy coastal sediments; Mi, silty ice rich intertidal sediments; Gs submarine fluvio-glacial outwash sediments made of sands with interstratified silt layers; R, bedrock; Bottom) GPR profile along the center-line of the runway showing the permafrost table, the natural ground surface beneath the embankment and a reinterpretation of the bedrock topography (dashed pink line).
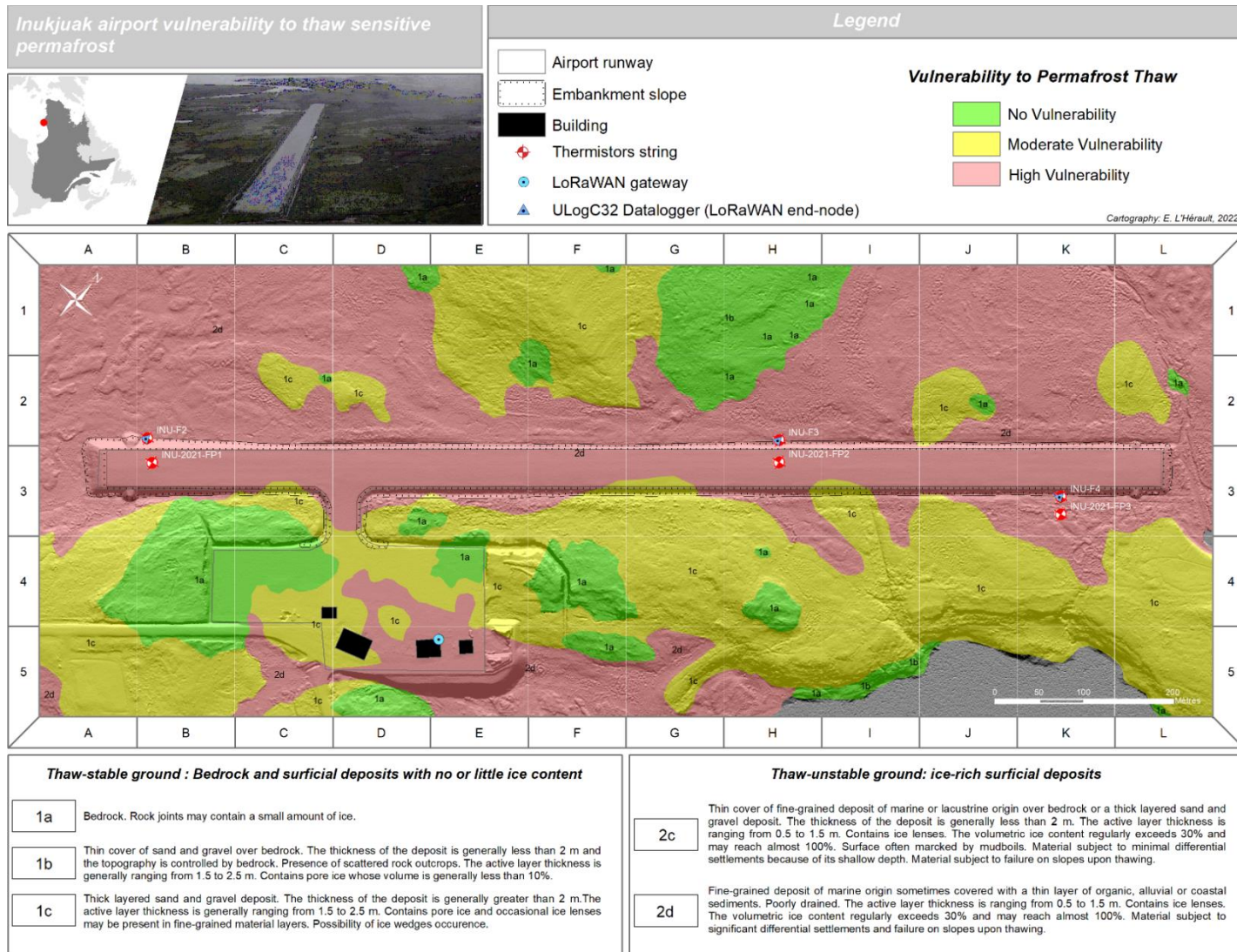
65

Figure 30 Map of the terrain vulnerability to permafrost thaw and the available instrumentation, Inukjuak runway, Nunavik.

2.1.3.2. Instrumentation

Unlike most of the Nunavik runways operated by the Quebec Ministry of Transport, the Inukjuak airport runway did not have any temperature monitoring stations. In 2008, during a geotechnical investigation conducted by L'Hérault et al. (2012), three boreholes located at the toe of the embankment were equipped with thermistor strings and named INU-F2, INU-F3 and INU-F4 respectively (Figure 30). As previously mentioned, remediation work was conducted in the summer of 2021 to implement gentler embankment slopes and to improve drainage patterns. In the course of this work, two of the three existing thermistor strings were buried under the new embankment slope, and all three were kept operational.

Three thermistor strings were added to the existing thermal monitoring network in the summer of 2021 to remedy the lack of ground temperature data for the centerline of the embankment and for undisturbed terrain. Two of these thermistor strings were installed through the embankment and subgrade near the centerline (INU-2021-FP1 and INU-2021-FP2) (Figure 30). One thermistor string is located in the thick embankment section at the southwest end of the runway (INU-2021-FP1) while the other is located near the middle of the runway in a thin embankment section (INU-2021-FP2). The third thermistor string is used as a reference and is located at the northeast end of the runway in the natural environment (INU-2021-FP3) (Figure 30). Even if all the thermistor strings have been equipped with a ULog LoRa datalogger (two strings per datalogger, three dataloggers in total) and all the recorded data are sent to the gateway on an hourly basis, only the recorded data from the centerline thermistors strings are currently used as part of the warning system. The technical specifications for all the thermistors strings that monitor the ground temperature at the Inukjuak runway site are summarized in table 10.

Table 10 The thermistors strings configurations for the Inukjuak runway.

INU-F2			INU-F3			INU-F4		
Sensor ID	Depth (m)	Thermistor model	Sensor ID	Depth (m)	Thermistor model	Sensor ID	Depth (m)	Thermistor model
T1		YSI 44033	T1		YSI 44033	T1		YSI 44033
T2		YSI 44033	T2		YSI 44033	T2		YSI 44033
T3		YSI 44033	T3		YSI 44033	T3		YSI 44033
T4		YSI 44033	T4		YSI 44033	T4		YSI 44033
T5		YSI 44033	T5		YSI 44033	T5		YSI 44033
T6		YSI 44033	T6		YSI 44033	T6		YSI 44033
T7		YSI 44033	T7		YSI 44033	T7		YSI 44033
T8		YSI 44033	T8		YSI 44033	T8		YSI 44033
T9		YSI 44033	T9		YSI 44033	T9		YSI 44033
T10		YSI 44033	T10		YSI 44033	T10		YSI 44033
T11		YSI 44033	T11		YSI 44033	T11		YSI 44033
T12		YSI 44033	T12		YSI 44033	T12		YSI 44033
T13		YSI 44033	T13		YSI 44033	T13		YSI 44033
T14		YSI 44033	T14		YSI 44033	T14		YSI 44033
T15		YSI 44033	T15		YSI 44033	T15		YSI 44033
T16		YSI 44033	T16		YSI 44033	T16		YSI 44033
INU-2021-FP1			INU-2021-FP2			INU-2021-FP3		
Sensor ID	Depth (m)	Thermistor model	Sensor ID	Depth (m)	Thermistor model	Sensor ID	Depth (m)	Thermistor model
T1	-0.25	PR222J2	T1	-0.25	PR222J2	T1	1.5 (air)	PR222J2
T2	-1	PR222J2	T2	-0.5	PR222J2	T2	-0.05	PR222J2
T3	-2	PR222J2	T3	-0.75	PR222J2	T3	-0.25	PR222J2
T4	-3	PR222J2	T4	-1	PR222J2	T4	-0.5	PR222J2
T5	-4	PR222J2	T5	-1.5	PR222J2	T5	-1	PR222J2
T6	-5	PR222J2	T6	-2	PR222J2	T6	-1.5	PR222J2
T7	-5.5	PR222J2	T7	-2.5	PR222J2	T7	-2	PR222J2
T8	-6	PR222J2	T8	-3	PR222J2	T8	-2.5	PR222J2
T9	-6.5	PR222J2	T9	-3.5	PR222J2	T9	-3	PR222J2
T10	-7	PR222J2	T10	-4	PR222J2	T10	-4	PR222J2
T11	-7.5	PR222J2	T11	-4.5	PR222J2	T11	-5	PR222J2
T12	-8	PR222J2	T12	-5	PR222J2	T12	-6	PR222J2
T13	-9	PR222J2	T13	-6	PR222J2	T13	-8	PR222J2
T14	-10	PR222J2	T14	-7	PR222J2	T14	-10	PR222J2
T15	-12	PR222J2	T15	-8	PR222J2	T15	-14	PR222J2
T16	-16	PR222J2	T16	-10	PR222J2	T16	-18	PR222J2

2.1.3.3.　Implementation

During the summer of 2021, all the existing dataloggers that were automatically measuring and saving the ground temperature data for the INU-F2, INU-F3 and INU-F4 thermistors strings were replaced by LogR Systems ULogC32 LoRa dataloggers, which allow for the connection of up to 32 temperature sensors per datalogger. Two thermistor strings were connected to each datalogger, with one thermistor string located in the centerline and the other at the embankment slope, following the typical installation methodology.

For each datalogger on the embankment slope, the external antenna for the LoRa wireless communication was installed on frangible post at a height of about 1 m. Special care was taken during the antenna installations to respect the maximum height allowed by Transport Canada airport regulations. The setups for the three monitoring stations are shown in figure 31 and pictures of the final installation shown in figure 32A, B and C.

The LoRaWAN gateway was installed inside the Inukjuak airport garage using an external antenna attached to the west-facing wall of the building at a height of 4 m (Figure 32D). Due to the small area of interest and distance from the furthest ground monitoring station to the gateway, the antenna with the lowest gain value (antenna model ANT-916-ID-2000-RPS, 1.6 dBi) was installed instead of the higher-gain antenna (antenna model FG9026, 8.5 dBi). The Multitech gateway was connected to the internet through the Kativik Transport wi-fi network. Using this configuration, it was possible for the LogR Systems logger to transmit the recorded ground temperatures to the Multitech gateway each hour and then to the database host on an internet server. The Inukjuak runway LoRaWAN network was implemented on September 24th, 2021. The hourly ground temperatures are remotely accessible from a desktop computer and analyzed using the same python program used for the Tasiujaq runway warning system (Figure 25).
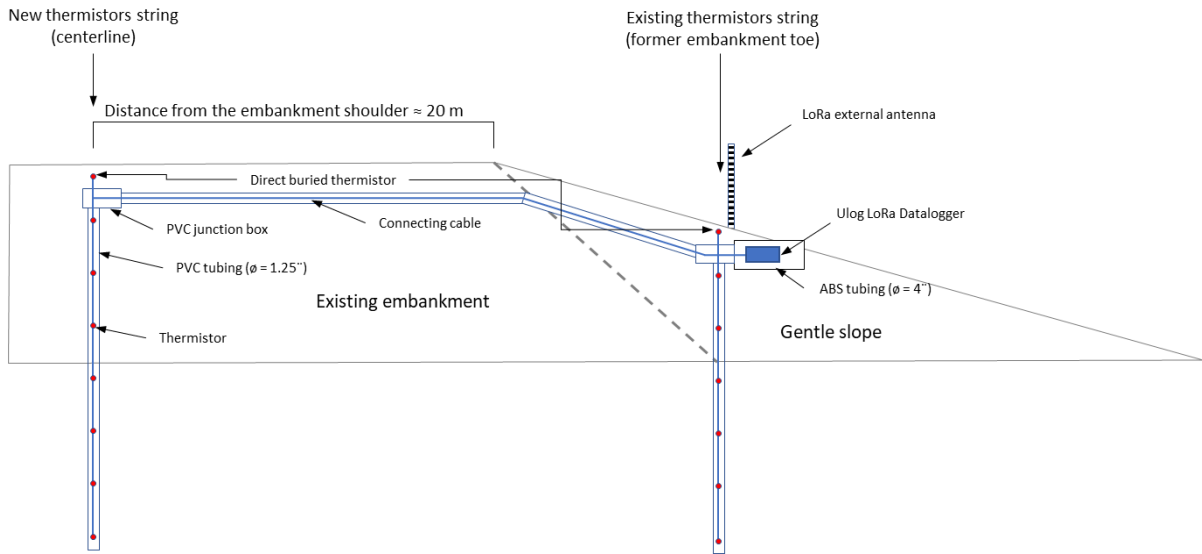
Figure 31 Typical installation with external antenna for end-nodes (dataloggers) located along the Inukjuak runway embankment slope.

Figure 32 ULogC32 LoRa datalogger protected inside ABS casing and located on the embankment gentle slope at A) INU-F2, B) INU-F3 and C) INU-F4. Gateway external antenna fixed on the west-facing wall of the airport garage at a height of 4 m.

2.1.3.4. Algorithm parameters/threshold and expected outcome

The proposed algorithm for the Inukjuak runway is the same as the algorithm developed for the Tasiujaq runway. The only difference between the two sites is the soil stratigraphy. For the Inukjuak runway, two sections near the center of the runway were equipped with thermistors strings: a thick embankment section (INU-2021-FP1) and a thin embankment section (INU-2021-P3) (see location map). Since the thermistors strings were installed late summer 2021, there are no historical records for the thaw depth dating back to the runway construction in the early 90s. For this reason, the threshold between the moderate and the high-risk level for the thaw settlement hazard corresponds to the maximum thaw depth retrieved from old geotechnical reports before

the runway construction, which was about 80 cm. A recent geotechnical drilling campaign completed during the summer of 2021 (L'Hérault et al., 2022, in prep.) suggests the presence of an ice-rich permafrost layer directly below active layer from before the runway construction under most of the runway length.

To date, due to the embankment thickness and the stratigraphy at the two monitoring sites located in the centerline of the runway (INU-2021-FP1 et INU-2021-FP3), the thaw settlement risk level remains non-existent since the maximum thaw depth during the summer of 2021 remained within the embankment.
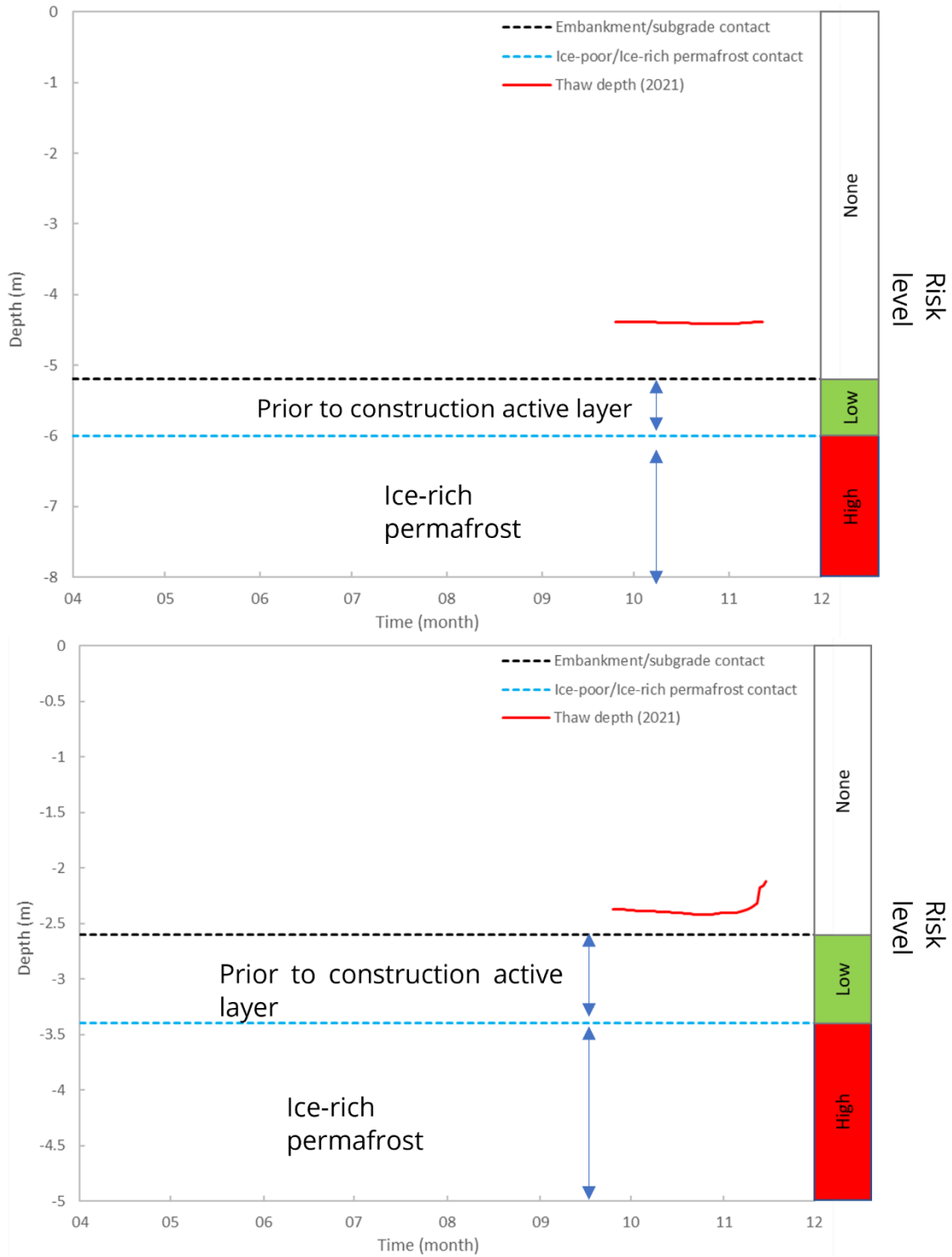
Figure 33 Thaw depth progression for the end of summer 2021 estimated from ground temperature data provided by the centerline thermistors strings A) INU-2021-FP1 (thick embankment section) and B) INU-2021-FP2 (thin embankment section).

2.2. Yukon sites

2.2.1. Dempster Highway study site: Chapman Lake area (km 116)

2.2.1.1. Introduction

The Dempster Highway is the only road connection to the western Arctic. Since it has been connected to the Inuvik-Tuktoyaktuk Highway, it is part of the infrastructure linking southern Canada with the Arctic Ocean. Extensive reconstruction of the Dempster Highway has been completed on the NWT side of the territorial border in response to degradation of the road surface and embankments. Recognizing the need to ensure year-round availability of the Dempster Highway in the context of increasing traffic in a changing climate, the Yukon Government Department of Highways and Public Works (YHPW) has initiated a project to create a functional plan that specifically considers contributions of climate change to geohazards along the highway. The Yukon U Research Centre was involved in this project as in the collection and analysis of data to assess climate and geohazard vulnerability for the functional plan.

During the geohazard vulnerability assessment, one specific site stood out, located at km 116 of the Dempster Highway. Several thaw slumps that affected the road have occurred at this location since 2006, forcing YHPW to move the embankment in 2006 and then again in 2018.

At the time of the assessment, this specific site evaluation was brief, because of time constraints and the many sites that required assessment along the 465 km transportation corridor. A preliminary assessment and a review of existing surveys and studies were performed for km 116 and the surrounding area. Additional information such as articles, air photos, satellite imagery, geological and surficial geological maps have also been reviewed to gain insight about the geomorphic conditions and surficial geology of the area. Field work included a combination of drilling, electrical resistivity tomography (ERT), and the installation of ground temperature monitoring instruments.

As a result of this preliminary assessment, it was determined that there was a significant threat to the infrastructure. Further evaluation was therefore required, and, as a remediation strategy was to be conceived, the site was a good candidate for the development and implementation of an early warning alarm system.

The present work is intended to determine the nature of the issues at Chapman Lake, develop an understanding of the processes causing damage to the road, identify the

proxies that could be used to design a geohazard alarm system, and create a prototype for such a system.

2.2.1.2. Background information

This section presents information acquired from literature and previous surveys.

2.2.1.2.1. Location and history

This site, referred as Chapman Lake, is located at km 116 of the Dempster Highway (64° 50.428'N, 138° 20.671'W). The Chapman Lake area was first investigated in 2017 during the development of a climate-resilient functional plan for dempster Highway in partnership with Yukon Highways and Public Works (Calmels et al. 2018).

The original assessment detected several issues in this area. In addition to major subsidence occurring along some sections of the highway, several landslides occurred close to the road embankment, where the road passes between Chapman Lake (north/left-hand side) and the Blackstone River (south/right-hand side). HPW was forced to realign the highway to the north as a result of landslides that occurred along the cliff above the river bank in 2006 and 2018 (Figure 34).

Figure 34 Satellite and aerial picture showing 2006 and 2007 landslides in the Chapman Lake area.

2.2.1.2.1.1.   2006 thaw slump

The first landslide and realignment occurred in 2006. Ground ice was visible on the bluff indicating that the thawing of ice-rich permafrost was responsible for the slumping process. When the embankment was moved, the surface water run-off induced thermal erosion which caused tunneling below the road, along the ice-wedge complex (Figure 35)

Figure 35 Degradation observed in summer 2006 along the newly built embankment at km 116. A- thermal erosion along the left-hand side shoulder; B- water tunneling under the embankment along an ice-wedge.

2.2.1.2.1.2.   2017 thaw slump

The second landslide and realignment occurred in 2017, 600 m south of the first 2006 thaw slump. The former road embankment displayed structural damage, including longitudinal cracking and subsidence (Figure 36 A) and the thaw slump was reactivated, where an ice-wedge was visible on the headwall (Figure 36 B) suggesting that slumping was driven by permafrost thaw and the melt of the wedge ice (Figure 37). Because this thaw slump was occurring only meters away from the road embankment, YHPW moved the embankment during the summer of 2018 (Figure 38) and the slump was covered with a layer of peat to promote stabilization (Figure 39). This site has been visited at least once a year since 2017. No additional movement has been observed since 2017.
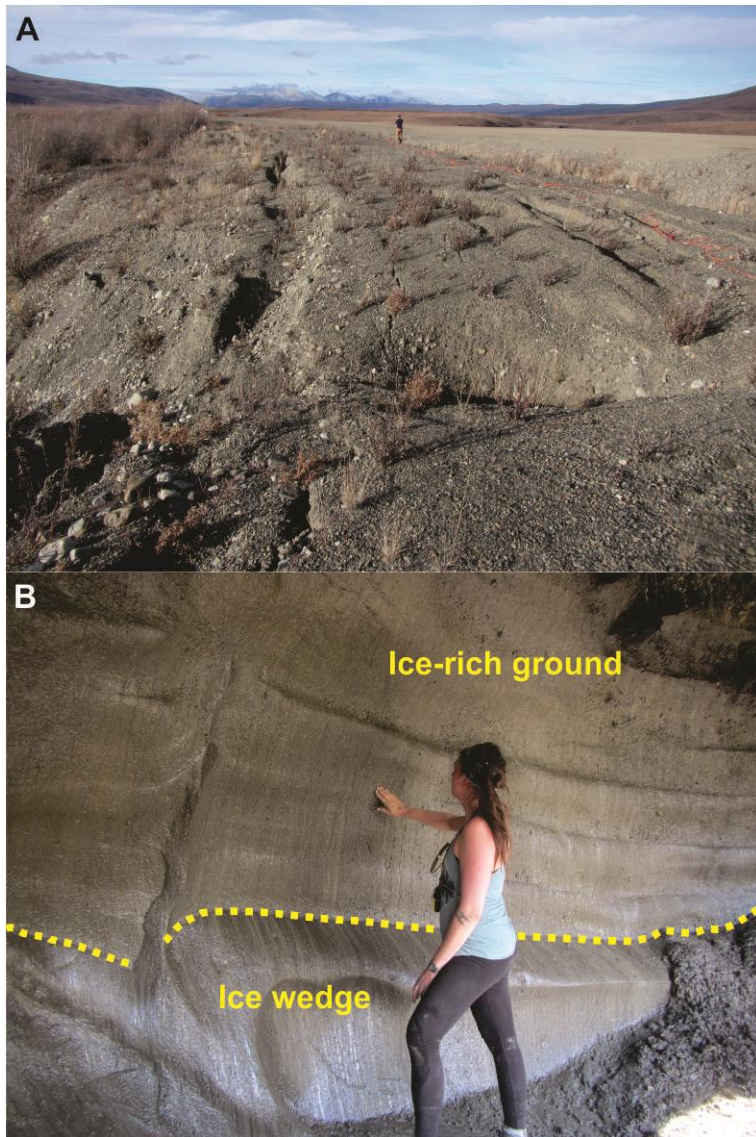
Figure 36 Degradations observed at DH116. A- Former embankment at the right-hand side affected by permafrost degradation; B- ice-rich ground and ice-wedge observed at landslides along the cliff.

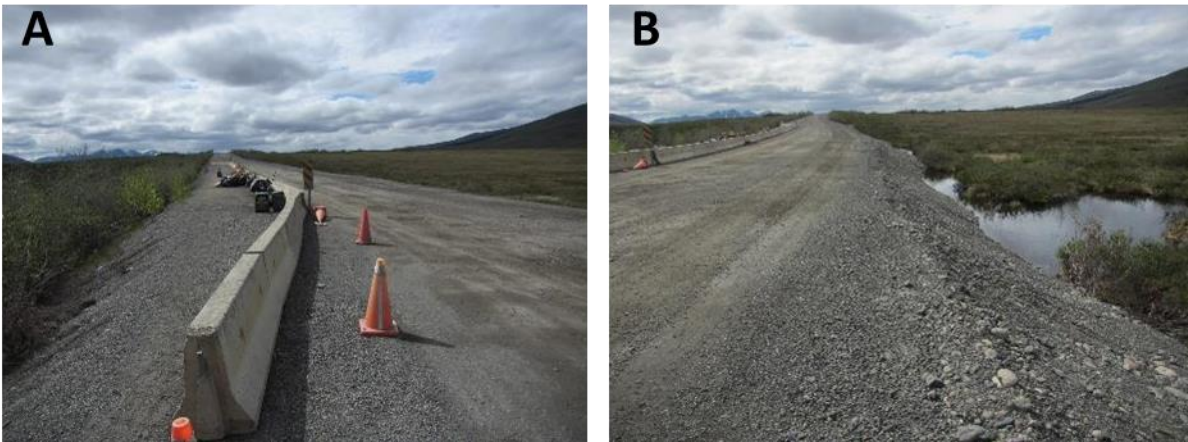**Figure 37** Headwall of the 2017 thaw slump with visible ice-wedge in June 2017.

Figure 38 Road section moved in at 2017 thaw slump site (September 2018). A- concrete fence at slump side (right-hand side); B- new shoulder build over thermokarst pond (left-hand side).

Figure 39 Peat cover installed in September 2018 to the 2017 thaw slump.

2.2.1.2.2.   Biophysical context

This section, while not an exhaustive review, presents key knowledge about the biophysical setting of the study site that is required to better understand the thaw slump and associated subsidence processes.

2.2.1.2.2.1.   Geology   and   Glacial History

The study site is located in a "U" shaped valley carved during glaciations by glaciers in the Ogilvie Mountains, on the Blackstone uplands (km 74 –160). Surficial materials in the area mostly consist of glacial till, colluvium, and outwash deposits. The site is located north of the last glacial maximum limit (Beierle, 2002). The Yukon Geological Survey surficial materials map (Figure 40) indicates that this section of the road crosses over a lacustrine silt deposit. The lacustrine unit borders on aeolian deposits to the north and fluvial deposits to the south. A patch of morainal material is present to the west. The sediment deposition sequence likely began with glacial deposits (moraine), followed by lacustrine, then fluvial, and finally aeolian at the current surface. Lacustrine and aeolian material are fine-grained and frost susceptible and are likely to be associated with ground ice such as wedge ice. The morainal and fluvial deposits are coarser and less frost

79

susceptible; nevertheless, such deposits can contain massive ice bodies, relict from a previous glacial period.
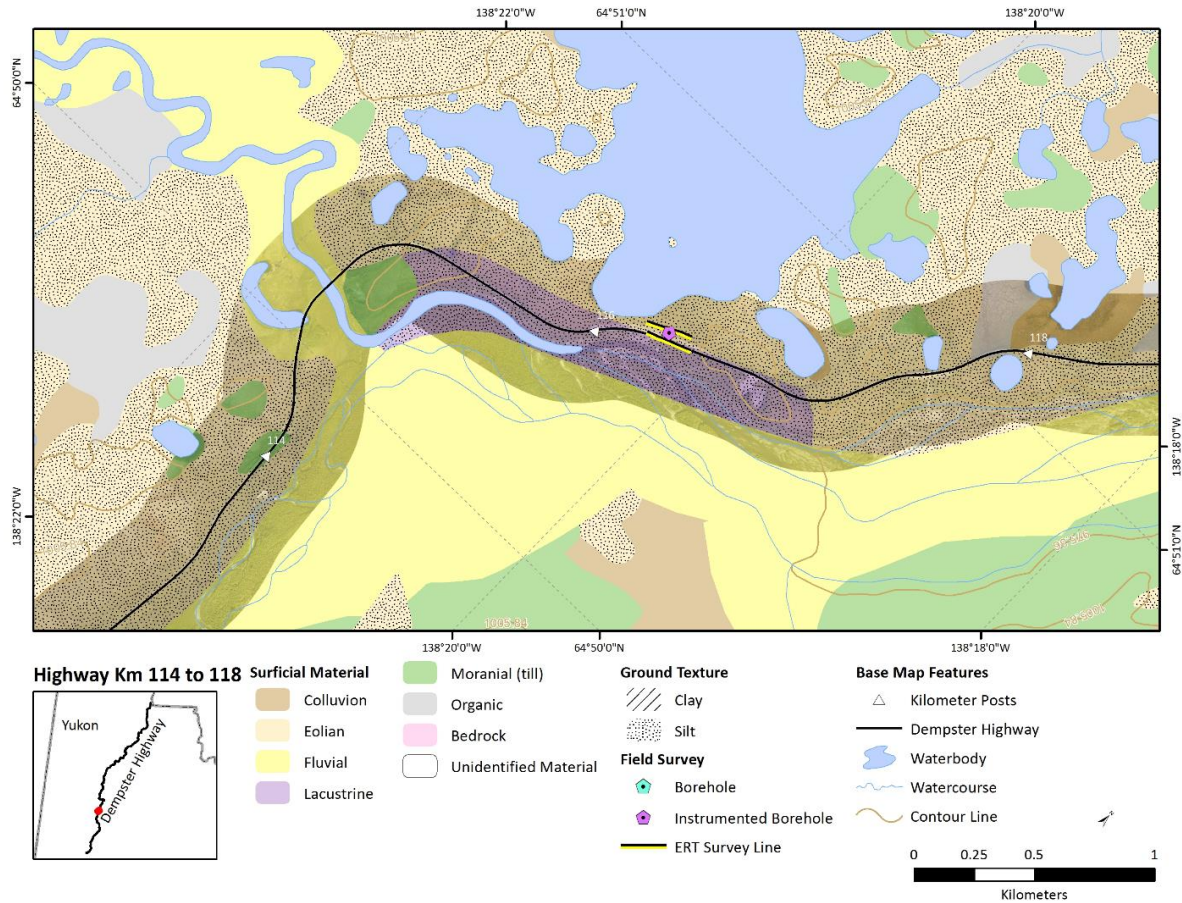

Figure 40 Surficial geology map of the KM 116 Chapman Lake area

The study sites are in an area that has been glaciated numerous times by the Cordilleran Ice Sheet and by local mountain glaciers. Bostock (1966) identified a series of four advances and retreats of Cordilleran continental glaciers beginning with the Nansen glaciation followed by the Klaza and Reid glaciations and ending with the McConnell glaciation most recently. Each glaciation was less extensive than the previous one. The extent and age of the Nansen and Klaza glaciations are poorly defined across the central Yukon Territory; while the extent of the younger Reid and McConnell glaciations are clearly defined by terminal moraine systems (Froese and Zazula, 2003). Glaciations have left a variable imprint on the landscape. For example, a central section of the highway, from km 116 to km 495, passes through terrain that was not glaciated by either the

Cordilleran or Laurentide ice sheets. As a result, these sections of the road are dominated by colluvial sediments, or weathered bedrock. In contrast, southern sections of the road, between km 75 and km 116 km (Figure 1), experienced valley glaciation during the Wisconsinan Glacial period (110,000 –11,700ka), while north and east of km 495 the Peel Plateau and the plains of NWT were covered by the Laurentide ice sheet (Burn et al., 2015).

2.2.1.2.2.2.   Climate

The climate of the region is continental sub-Arctic with long cold winters, short mild summers, and relatively low precipitation. Lacelle et al (2007) reports that mean annual air temperatures recorded at the Mayo (504 m a.s.l.) and Keno (1472 m a.s.l.) meteorological station, located approximately 170 km southeast of the study site, are $-3.6\,°C$ and $-5.1\,°C$, respectively (Smith et al, 2004). There are orographic effects inducing topographically controlled temperature inversions in winter, while in summer, temperatures may be ~5 °C cooler in the highlands (Burn, 1994). These effects also enhance precipitation at higher elevations, as illustrated by the data from Mayo (318 mm·yr^{-1}) and Keno (590 mm·yr^{-1}).

2.2.1.2.2.3.   Permafrost

The Blackstone uplands are located in the continuous permafrost zone (Heginbottom et al., 1995). Preliminary surveys performed at km 124, near the Chapman Lake airstrip, 8 km north of the study site provided a first overview of permafrost conditions in the research area (Burn and al. 2015, Idrees and al. 2015). These surveys included drilling boreholes at the road centerline, at the toe of the embankment, and in the field adjacent to the road, to assess the subsurface conditions, and to instrument boreholes with temperature sensors.

The temperature data showed low near-surface annual mean ground temperatures (< -4.0 °C). Unfrozen ground and water were encountered at depth in all boreholes. Foliated massive ice, which is likely wedge ice, was recovered in the silts overlying the gravel, and a 0.35 m layer of pool ice was found within the permafrost. The silts were ice rich; the two tested samples had excess ice contents of 49 and 69%. The underlying outwash gravels included a range of clast sizes including boulders, which prevented further drilling. Permafrost has degraded completely beneath the toe of the embankment, and the base of permafrost is at approximately 7 m of depth at the centerline site and in the field adjacent to the road. The thin layer of permafrost is likely due to heat transfer from groundwater flowing through the glacial outwash at the site. Permafrost is not found at

the toe due to insulation from snow accumulation at the edge of the road from plowed and wind-blown snow, and its associated spring runoff. At the centerline of the embankment, permafrost is present; its temperature just below the active layer is comparable with the field site at -2.4 °C.

Preliminary surveys performed in 2017 at km 116 suggested that similar conditions and processes may be present (Calmels et al. 2018). A shallow borehole was drilled and instrumented in the field adjacent to the road, and an ERT survey was done at the same location. An ice-wedge was cored, and ground temperatures were warmer than at km 124 (≈ -2°C). Massive ice identified as wedge ice was observed at the retrogressive thaw slumps; and ERT survey suggested that massive ice bodies of unknown nature might be present deeper in the profile. This survey is presented in section 2.2.1.2.4.3 along with others collected for the current study.

2.2.1.2.2.4. Ground ice

In this section, multiple types of ground ice that have been observed in the region and are likely to be involved in subsidence and thaw slump processes are described.

Buried Ice

Exposed buried glacier ice has been found in moraine sediments at km 110 near Chapman Lake (Lacelle et al., 2007). The massive ground-ice body was exposed following a retrogressive thaw slump on a hillside cut near the highway. The age of the glacier ice in this location is not known, but as mentioned above, the Blackstone uplands were likely glaciated on numerous occasions during the Pleistocene but prior to the Cordilleran glaciation. The exposed section was located on a northeast facing hillslope. The thaw slump had a low gradient slump floor and a near vertical 4-m-high headwall. Two units of ice were visible in the exposed face. The first unit consisted of relatively clean massive ground ice that was ≥2 m thick, with a few striated clast layers suspended within it. On the north side of the exposure, alternating near-vertical layers of debris-rich and clear ice were found. The second unit overlaid the first and consisted of an icy diamicton at least 2 m thick with a reticulate ice structure near its lower contact that graded upward to a parallel-layered lenticular pattern at the active layer boundary. The contact between the massive ice and the overlying icy diamicton was sharp, suggesting an erosional surface or a thaw unconformity. The contact between the massive ground ice and underlying sediments was covered by slumped debris and could not be observed.

Ice wedges

Ice-wedge polygon complexes are present throughout the study area, especially in the valley floor, and are present at the km 116 study site. These polygons display hummocky terrain, with characteristic depressions (troughs) above the wedges, and hummocks between them. There are no raised rims around the hummocks suggesting that the ice wedges are not actively growing. At some locations, the ice wedges are degrading, and their troughs are filled with water.

Segregated ice

Throughout the study area, segregated ice is likely to be found in the uppermost layers of permafrost where there are unconsolidated, fine-grained sediments. Segregated ice has been observed in the valley floor in the silt veneer overlying the coarse morainal or outwash deposits. This type of ground ice can be syngenetic, developing near the top of permafrost and remain there if the permafrost table rises because of sedimentation and aggradation of the surface, or a rise of the permafrost table in response to periods of colder climate (e.g., French and Shur, 2010). The ice-rich zone where segregated ice occurs has been called the transient layer of permafrost and is common in frost-susceptible soils. Because it is constrained mostly to the uppermost meters of permafrost and may be much more diffuse downward, it is unlikely to be the major cause of the thaw slumps.

2.2.1.2.3.   Geohazard evaluation survey based on aerial imagery

This section presents a geohazard evaluation based on the interpretation of a variety of geospatial data including surficial geology maps, orthophotos, aerial photography, satellite imagery and LiDAR data. These data were then used to create a vulnerability map based on three criteria: the active layer thickness (ALT), the permafrost-related ground movement potential (PGMP) and the periglacial processes or features (PPF). The details of these criteria are summarized in Table 11.

Table 11 Criteria for vulnerability mapping

Criteria	Possible values	Comments
Active layer thickness (**ALT**)	**Thin** (<1 m) **Thick** (>1 m)	-Based largely on **vegetative/drainage indicators** and experience investigating similar environments with soil pits or auger holes -Important indicator of likelihood of encountering permafrost during excavation of the trench for cable installation
Permafrost-related ground movement potential (**PGMP**)	**High** – ground movement *likely* following disturbance **Moderate** – ground movement *possible* following disturbance **Low** – ground movement *unlikely* following disturbance	Considers predicted **material texture** (e.g., silty/clayey, sandy/gravelly, matrix- vs. clast supported) and **ground ice potential** (e.g., massive, segregated, pore) based on interpretation of surficial geology, hydrogeomorphic setting, etc.
Periglacial processes or features (**PPF**)	Cryoturbation (**C**) Solifluction (**S**) Thermal erosion (**Xe**) Active layer detachment (**Xf**) Retrogressive thaw slump (**Xh**) Palsa (**Xp**) Slopewash (**Xs**) Thermokarst subsidence (**Xt**) Ice-wedge polygons (**Xw**)	Identification of these processes/features strengthen the "high" classification of ground movement potential within the delineated area, and is intended to draw attention to areas where the greatest challenges and costs may be encountered

The resulting map of surficial deposits and mass movement geohazards is presented in Figure 42 and the map of Permafrost-related ground movement potential and periglacial process/features is shown in Figure 42 for the Chapman lake area. Figure 41 shows that the road is almost completely located on silt of lacustrine origin. This type of soil tends to be thaw-sensitive due to the possibility of high excess ice content based on the fine texture of the soil. Figure 42 show that the active layer has been classified as thin, or less than 1 m thick. Four types of periglacial features are observed (Figure 42): 1) retrogressive thaw slumps and active layer detachments (Xhf) are located along the

Tombstone River banks, on the south side of the road at three locations; 2) thermokarst subsidence (Xt), visible in the former road embankment (pre-2006) and along the north-side toe of the embankment in the same area; 3) ice wedge polygons (Xw) visible on either side of the road throughout the site, and 4) ice wedge polygons with thermokarst subsidence (Xwt) that are especially noticeable in the lower, north side of the road, facing 2017 thaw slump. Overall, these periglacial features emphasize the presence of an important amount of ground ice at the site, mostly in the form of wedge ice. The thawing of this ice likely resulted in the formation of retrogressive thaw slumps and active layer detachments as well as thermokarst subsidence, as observed along the road where thermokarst ponds are resulting from ice wedge degradation. Field observations have shown that the widths of the ice wedges are variable, up to 3.2 m wide and 6m in height.

The major mass movement geohazards are retrogressive thaw slumps and thermokarst subsidence (Figure 41). Besides the RTS already mentioned, a large area located on the south side in the upper section is undergoing major thermokarst subsidence. The location is an ancient gravel pit where material extraction has resulted in intense permafrost degradation and collapsing. This process likely results from the thaw of massive ice of unknown origin. Due to the gravelly nature of the sediment, ice wedges are unlikely to be present.

Because of the nature of the sediment, the ground-ice content, and the observed periglacial features and processes, the permafrost-related ground movement potential (PGMP) is considered as high for the whole section (Figure 42).
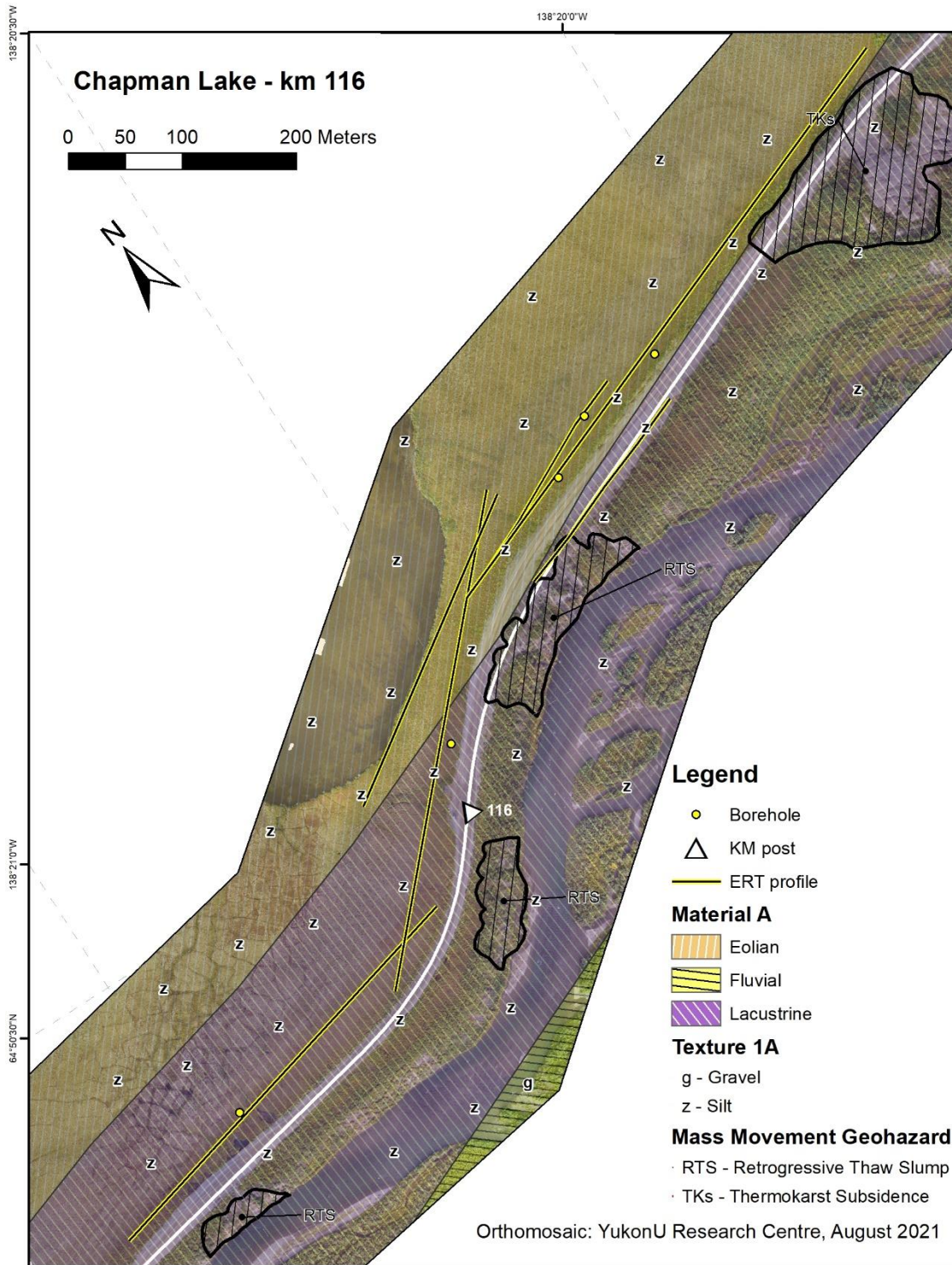
Figure 41 Map of the surficial deposits and mass movement geohazards along Chapman Lake study site (km 116)
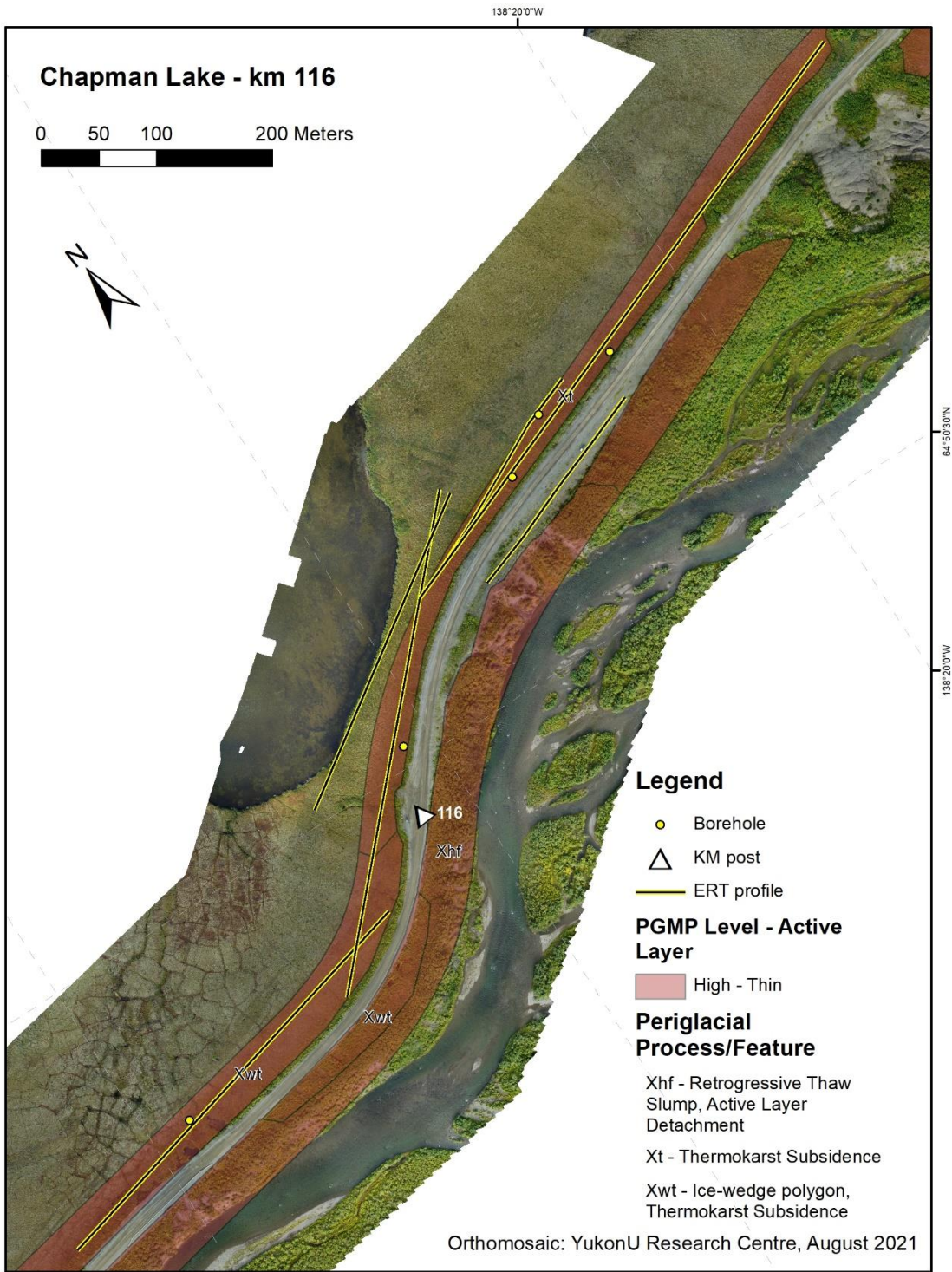
Figure 42 Map of Permafrost-related ground movement potential and periglacial process/features along Chapman Lake study site (km 116)

2.2.1.2.4. Field-based assessments

This section presents the results from the field assessments performed during the project. Preliminary results obtained during a previous project (Calmels et al. 2018) have been integrated to the current study.

Various methods were used for the field study. Boreholes were either drilled by the research team with a portable drill or by a driller contracted by Yukon Highway and Public Work. Those boreholes provided two types of data: geotechnical assessments from the collected cores and ground thermal assessment from temperature records using permafrost monitoring stations. Additionally, geophysical surveys were performed using Electrical Resistivity Tomography (ERT) and Ground Penetrating Radar (GPR).

At this specific site, surface-to-groundwater constitutes a significant hazard to the permafrost and road stability. To inform the source and patterns of the potentially problematic water, a specific approach was developed. The first step was to use the available topographical surveys and field observations to create a map of surface and subsurface water preferential flow paths. To gather information on water, soil and the permafrost table, samples were collected and the cryostratigraphy was described. This information is useful for assessing the structure of the ground's upper section where the subsurface water circulates. The deep boreholes, electrical resistivity tomography and permafrost temperature monitoring were also used to provide information on the lower ground structure, the ground-ice conditions, and vulnerability to thermal erosion (thermal and mechanical erosion). Finally, the principal measurements made on the water and soil samples include stable isotopes and hydro geochemistry.

The sampling strategy and characteristics of each survey is provided in the result sections below, and the detailed methodology for each survey type is presented in Appendix 2.2.1-A. Figure 43 presents the location of the boreholes and ERT surveys, and Figure 44 show the location of the GPR surveys and Figure 45 locates where the surface water and soil samples were gathered.

Figure 43 Locations of the boreholes and ERT surveys at Chapman Lake section (km 116).
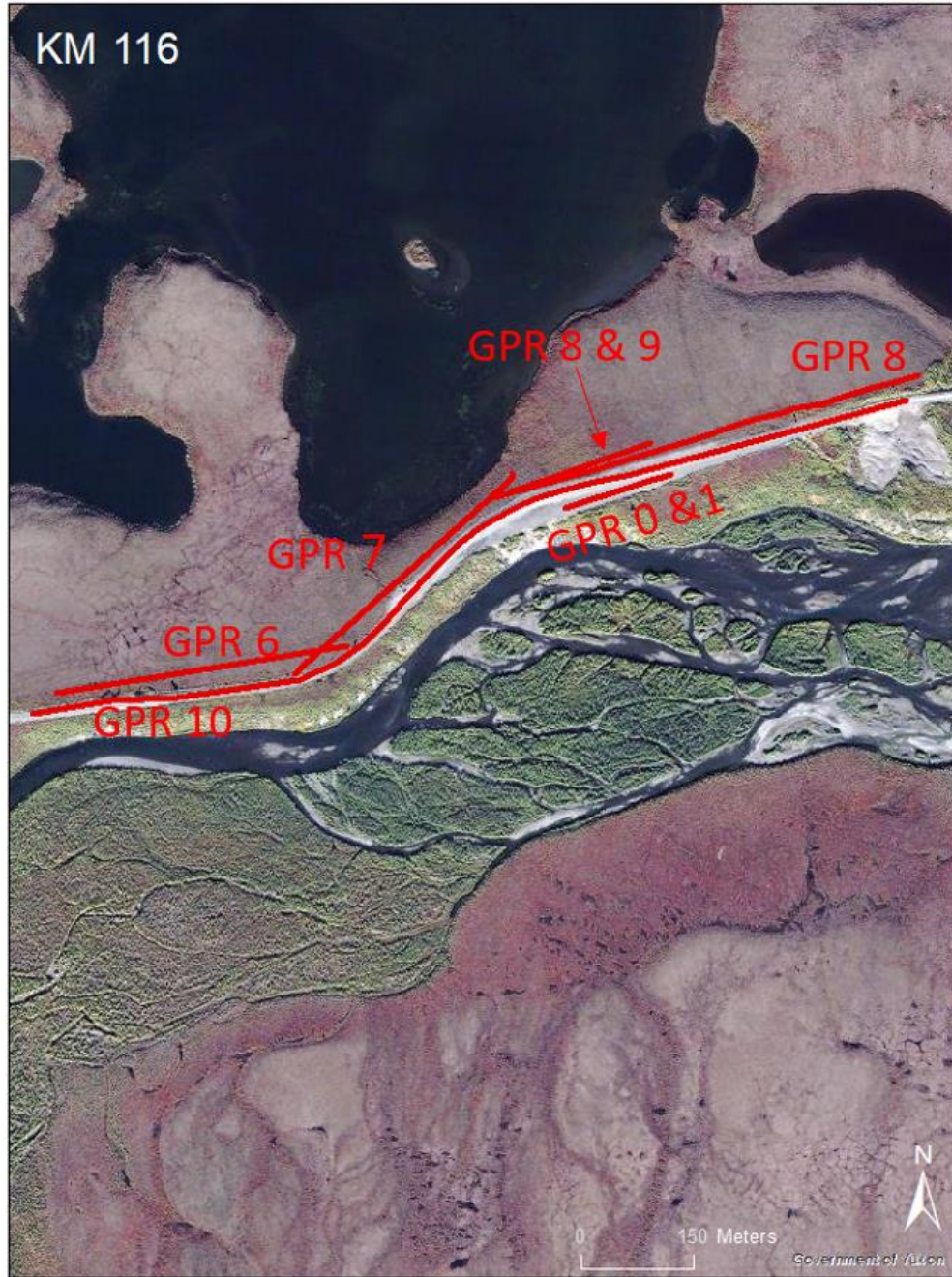
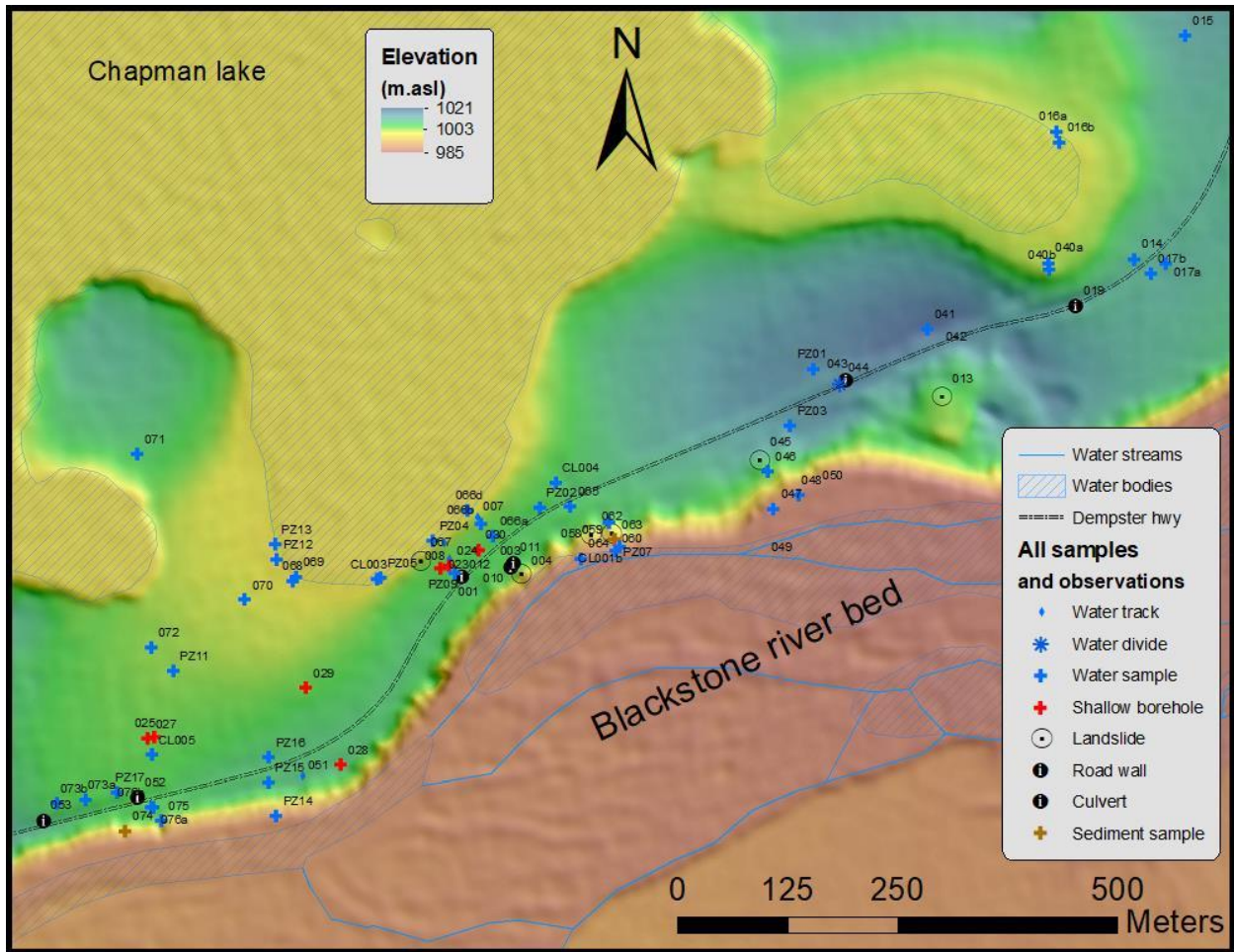**Figure 44** Locations of the GPR surveys at Chapman Lake section (km 116).

Figure 45 General localization map of the survey and sample points at Chapman Lake. The background of the image shows a terrain model.

A total of 5 Boreholes were drilled on site. Locations, depths, and noticeable features are provided in Table 12. The first borehole, Bh-IW-1, was drilled in summer 2017, along ERT survey LHS 2017, between the road and Chapman Lake (Figure 43). The placement of the borehole was chosen based on its location along the ERT survey and the fact that it was representative of the area. The thaw front was at 12 cm depth on June 6th, 2017. The soil stratigraphy consists of moss and peat from 0 to 0.30 m, followed by sand mixed with organics down to 0.90 m. Deeper down, the soil was sandy silt to a depth of 1.35 m, at which depth there was contact with wedge ice. Wedge ice was continuous down to 4.50 m depth. Below, silty and sandy gravel was present down to 4.68 m which was the maximum depth of the borehole. Excess ice content ranged from 27% in the sediment, to 100% in the ice wedge (Figure 46). The mean volumetric excess ice content was 47%, without considering the ice-wedge cores.

Table 12 Borehole information table.

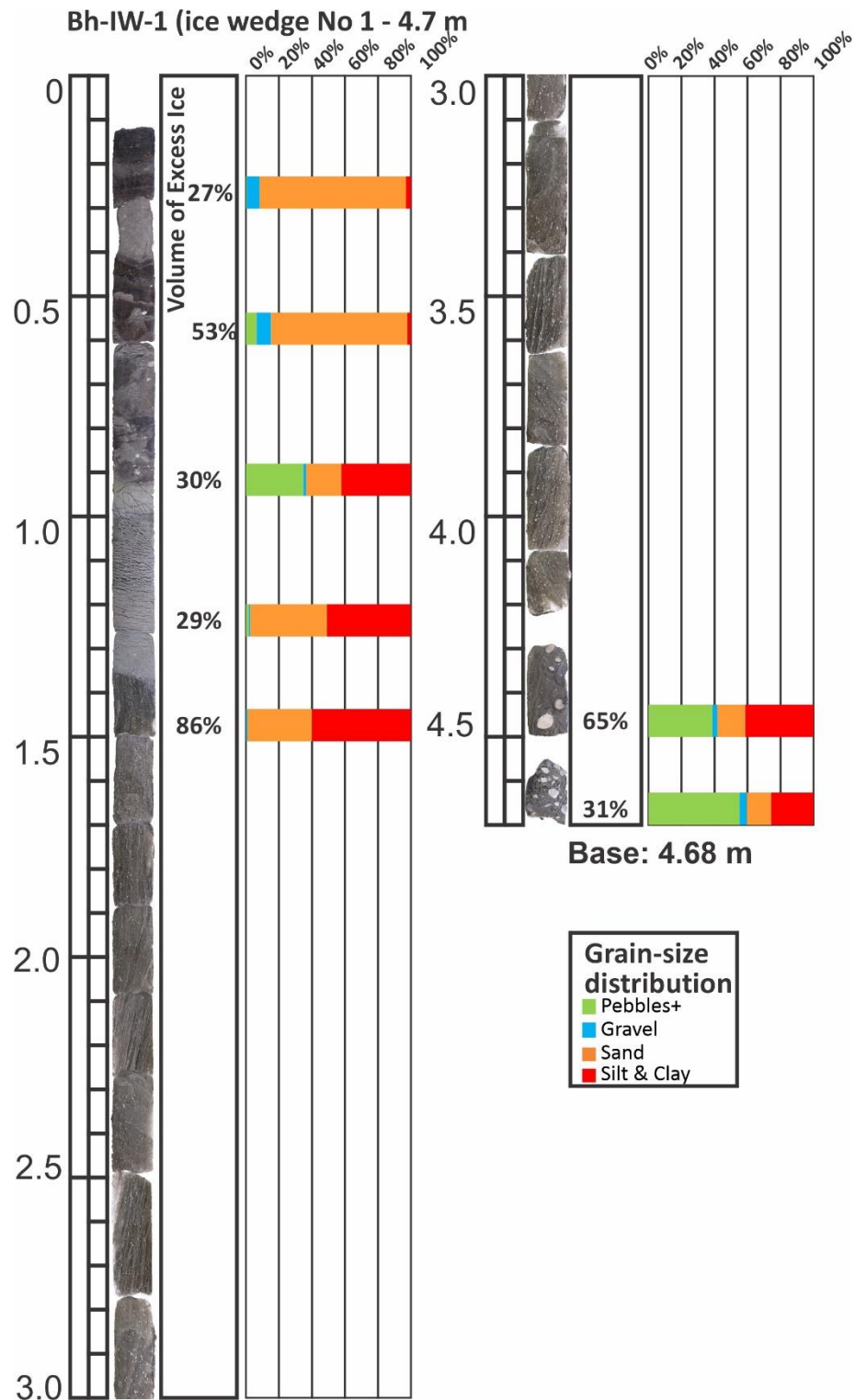| Borehole name	Location	Depth	Noticeable feature
Bh-IW-1	N64.84313 W138.33785	4.68 m	Ice Wedge
Bh-IW-2	N64.84030 W138.34911	19.80 m	Ice wedge
Bh-BI-1	N64.84345 W138.33686	19.80 m	Buried ice
Bh-BI-2	N64.84359 W138.33508	26.0 m	Buried ice
Bh-W	N64.84179 W138.34219	26.0 m	N/A

Figure 46 Log of borehole Bh-IW-1 with soil texture and excess ice content.

Later the same year, two boreholes were contracted by HPW and drilled on October 28th, 2017. The first, Bh-BI-1 was located based indications of massive ice bodies from the HS

2017 ERT survey LHS 2017 (see section 2.2.1.2.4.3). The active layer thickness was 38 cm at the time. The profile consisted of organic cover from 0 to 0.30 m, organic sandy-silt from 0.30 to 1.9 m, sandy silt with gravel from 1.9 to 7.50 m, then a layer of ice (possibly wedge ice) from 7.50 to 8.80 m, followed by gravelly sandy-silt, possibly unfrozen from 8.80 to12.20 m, followed by silty-sand and sandy silt with gravel down to 13.70 m. Finally, massive ice was found from 13.7 m to 19.80 m the maximum borehole depth (Figure 47). The nature of this massive ice was undetermined, although the absence of foliation and presence of granular material within the ice rules out wedge ice. The second of these contracted boreholes, Bh-IW-2 (Figure 48), was drilled in the field adjacent to the road on the left-hand side, facing the major slide that occurred that summer (2017 thaw slump), about 600 m south of the previously mentioned boreholes. These cores showed the presence of wedge ice from approximately 4 m to 7.5 m in depth. No ice was found below between this depth and 19.8 m, which was the maximum depth of the borehole.

Finally, a last set of two boreholes were contracted by YHPW and drilled on February 2nd-5th, 2019. The borehole locations were chosen based on additional ERT surveys performed in summer 2018. The first of these boreholes, Bh-BI-2 aimed to intercept and sample the deeper ice bodies (Figure 49). The active layer was completely frozen at the time. The profile consisted of organic cover from 0 to 0.30 m, organic silt from 0.30 to 1.9 m, sand with gravel from 1.9 to 8.80 m, then a layer of gravelly sandy-silt from 8.80 m to 12.2 m, then thin layer of gravel (12.2-12.50 m), followed by sand with gravel down to 18 m. Finally, massive ice was encountered from 18.0 m to 24.3 m, with sediment present in the ice from 18 m to 21.2 m. Below was gravely sandy-silt from 24.3 m to 26.0 m the maximum depth of the borehole (Figure 49). The second borehole, Bh-Wr (Figure 50), was drilled in the narrow stretch between the lake and the river with the objective of intercepting potential groundwater flow along the ground profile. The active layer was completely frozen and drilling started in frozen organics down to 0.4m. This was followed by ice-rich dark brown organic silt displaying occasional ice lenses down to 1.5 m. Sand with gravel was observed from 1.5 m down to 3.5m. Darker sand with gravel that became coarser with depth was observed from 3.5 m to 5.5m, followed by sand down to 6.6 m, and poorly graded gravel down to 9.0 m with some silt at 8m. Between 10 m and 13.8 m there was poorly graded sand with some silt, followed by stiff, dark grey, clay with gravel down to 16.2m, then poorly graded sand down to 18.3, and silty gravel down to 20m. Finally, there was fine sand with gravelly and silty layers down to 25.8 m which was the maximum depth of the borehole.
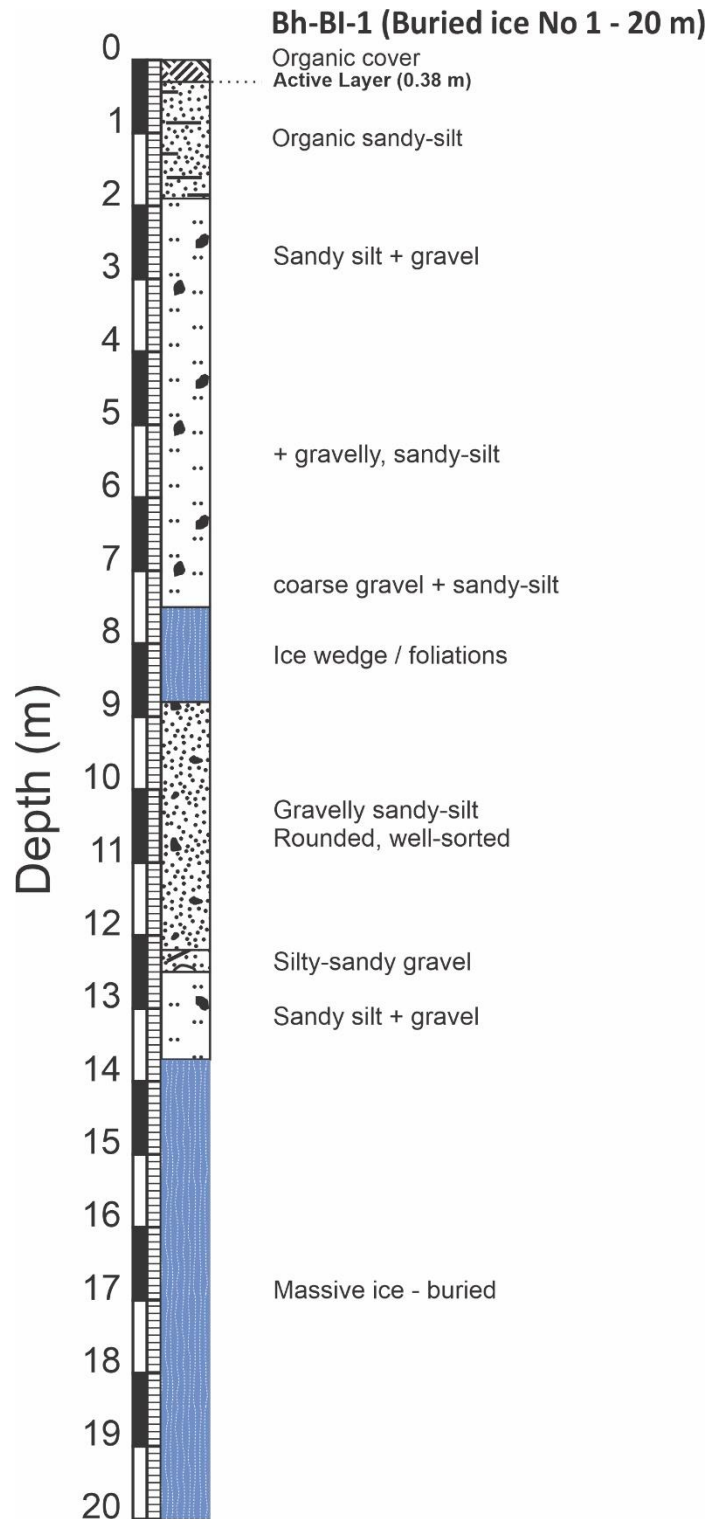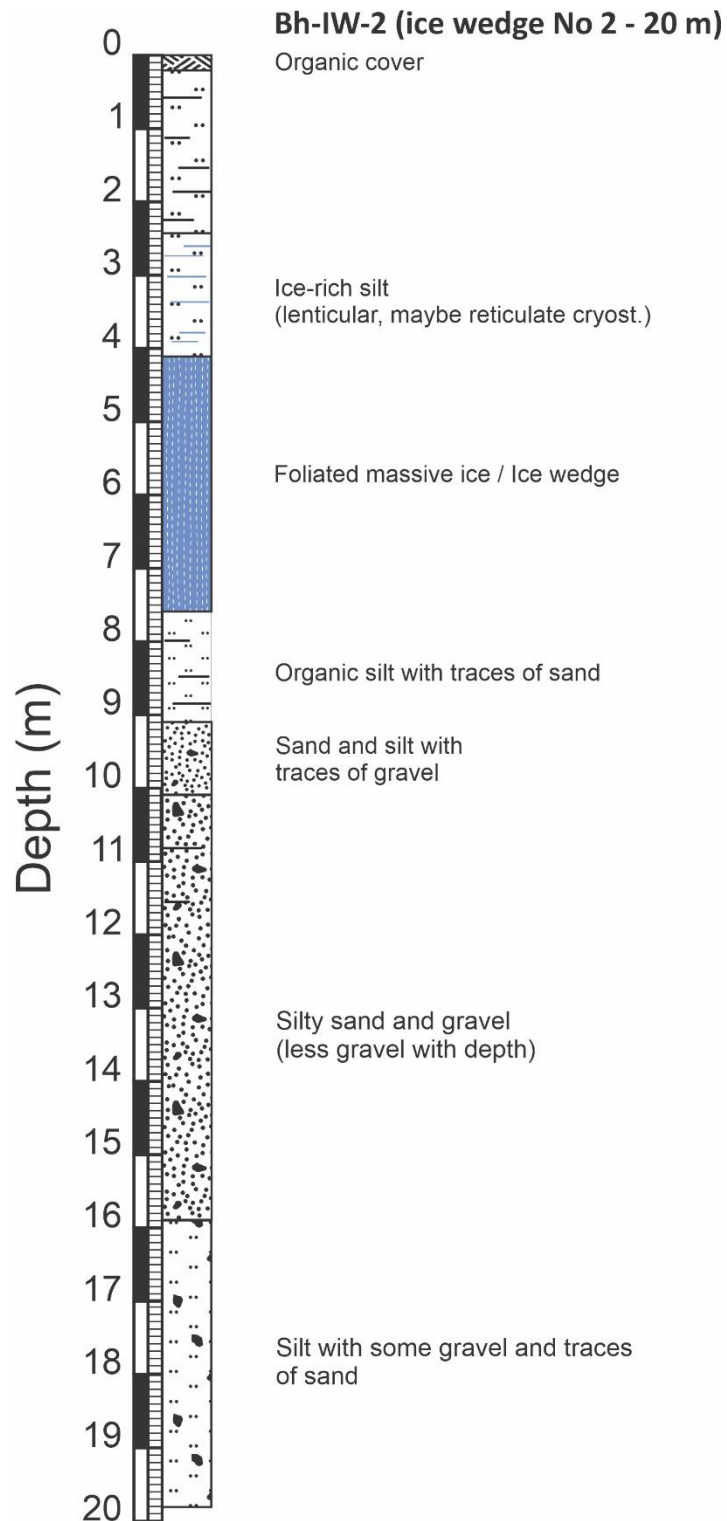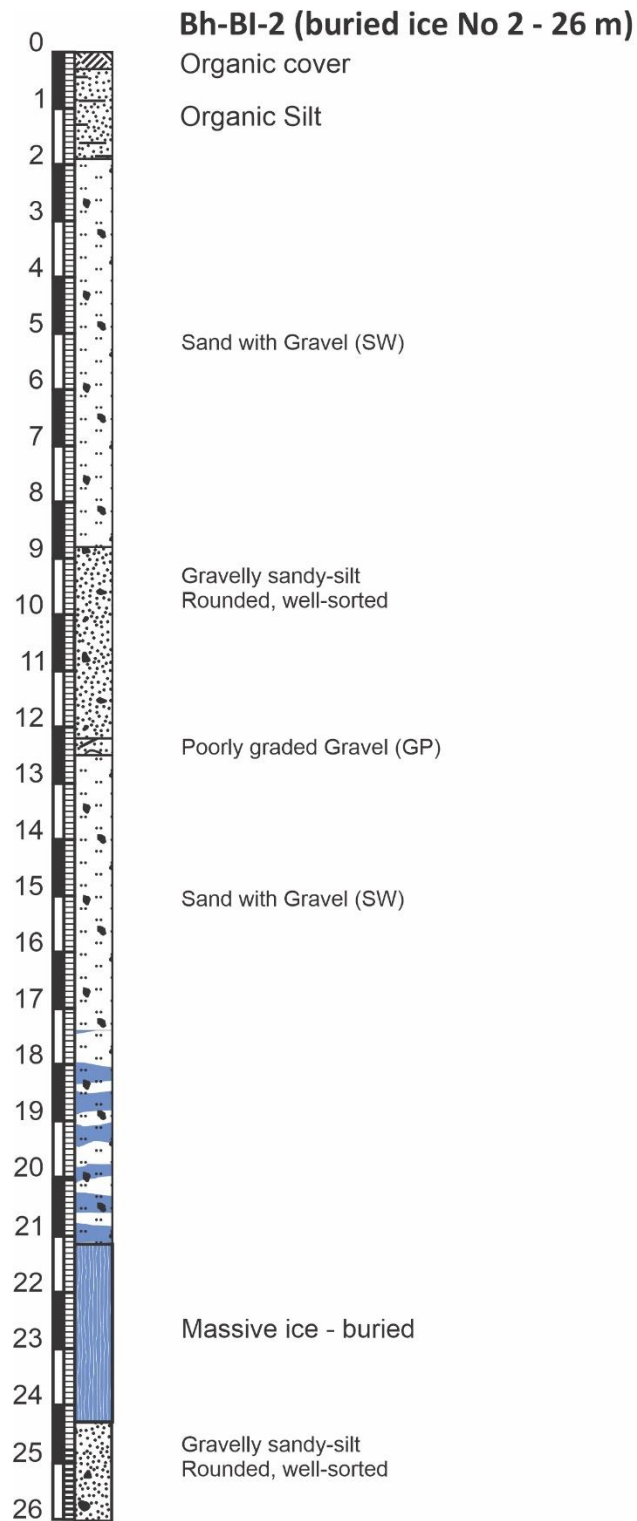
Figure 47 Log of borehole Bh-BI-1.

Bh-IW-2 (ice wedge No 2 - 20 m)

Organic cover

Ice-rich silt
(lenticular, maybe reticulate cryost.)

Foliated massive ice / Ice wedge

Organic silt with traces of sand

Sand and silt with
traces of gravel

Silty sand and gravel
(less gravel with depth)

Silt with some gravel and traces
of sand

Figure 48 Log of borehole Bh-IW-2.

Bh-BI-2 (buried ice No 2 - 26 m)

Organic cover

Organic Silt

Sand with Gravel (SW)

Gravelly sandy-silt
Rounded, well-sorted

Poorly graded Gravel (GP)

Sand with Gravel (SW)

Massive ice - buried

Gravelly sandy-silt
Rounded, well-sorted

Figure 49 Log of borehole Bh-BI-2.
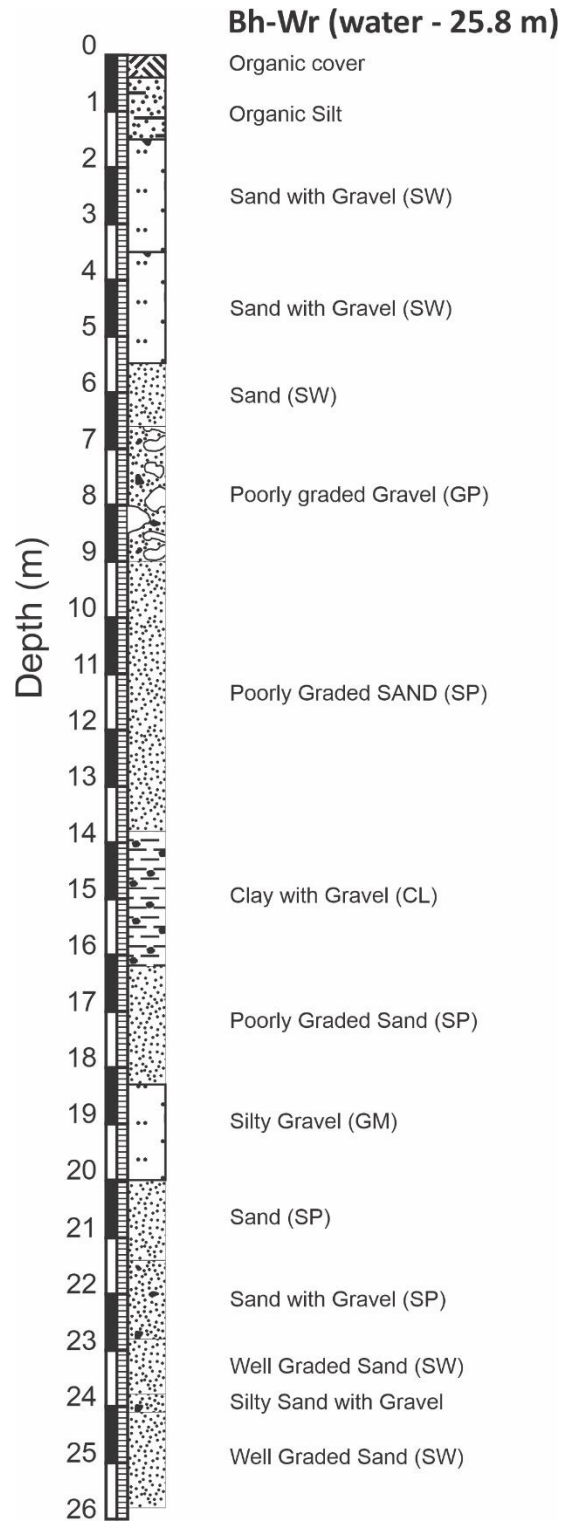
Figure 50 Log of borehole Bh-Wr.

98

Key points:

- Two types of massive ice complexes have been identified: an ice wedge complex spreading from 1.5 to 10 m depth, and buried massive ice from 14 m down to 24+ m.
- No groundwater springs were observed during the drilling operations.
- No bedrock was reached.
- The sediment is either sandy silt or silty sand with gravel and tends to become coarser with depth.
- Coarse sediments may result from deposition from glaciofluvial melt water, which can quickly bury relict glacial ice during glacier retreat.

2.2.1.2.4.2. Ground temperature

Between 2017 and 2019, all of the boreholes drilled at the study site have been instrumented with thermistor strings connected to data loggers of various types. Each borehole was lined with PVC piping, fitted with the temperature sensors, then filled with silicone oil to prevent convection within the piping and provide more accurate temperature readings. Chronologically, Borehole Bh-IW-1was the first to be instrumented, to a depth of 4.65 m with two Onset UX-120 4-channel loggers in June 2017. Boreholes Bh-BI-1 and Bh-IW-2 were instrumented to 20.0 m and 15.0 m in depth, respectively, in June 2018 with the same type of logger. Because of delays in maintenance resulting from COVID-19 travel restrictions, Bh-IW-1 was impacted by several battery failures and malfunctions on one of its loggers, and Bh-BI-1 and Bh-IW-2 were affected by battery failures resulting in some data gaps. Boreholes Bh-BI-2 and Bh-Wr were first instrumented in July 2019 with Onset loggers down to 16.0 m and 9.0 m depth, respectively but were later upgraded to LogR logger systems in June and August 2020 respectively, down to 25.0 m depth for both.

The ground thermal regime of each borehole was studied using two approaches. First, a trumpet curve, comparable to the one presented in Figure 51, was produced for each borehole for a 12-month period. The variation in ground temperature during a single year is obtained by plotting the minimum, maximum, and average temperature for each monitored depth. When the borehole is deep enough, the trumpet curve can be used to determine the permafrost limits (active layer thickness and base of permafrost) and the depth of zero annual amplitude (ZAA), which is the depth below the surface at which the ground is not impacted by fluctuations in air temperature during the year, or where the

annual variation in temperature is less than 0.1°C (Figure 51). Underneath the ZAA, the temperature of the soil gradually increases as depth increases, due to the geothermic heat originating from the Earth's core. The soil temperature can reach 0°C again and become positive. This point therefore separates the frozen soil from the unfrozen soil and indicates the lower limit of permafrost. Second, ground temperatures were plotted with time and depth using the gridding software Surfer. This representation depicts the evolution of ground temperature iso-curves over time and highlights phenomena such as the evolution of the active layer or the warming effect of groundwater.
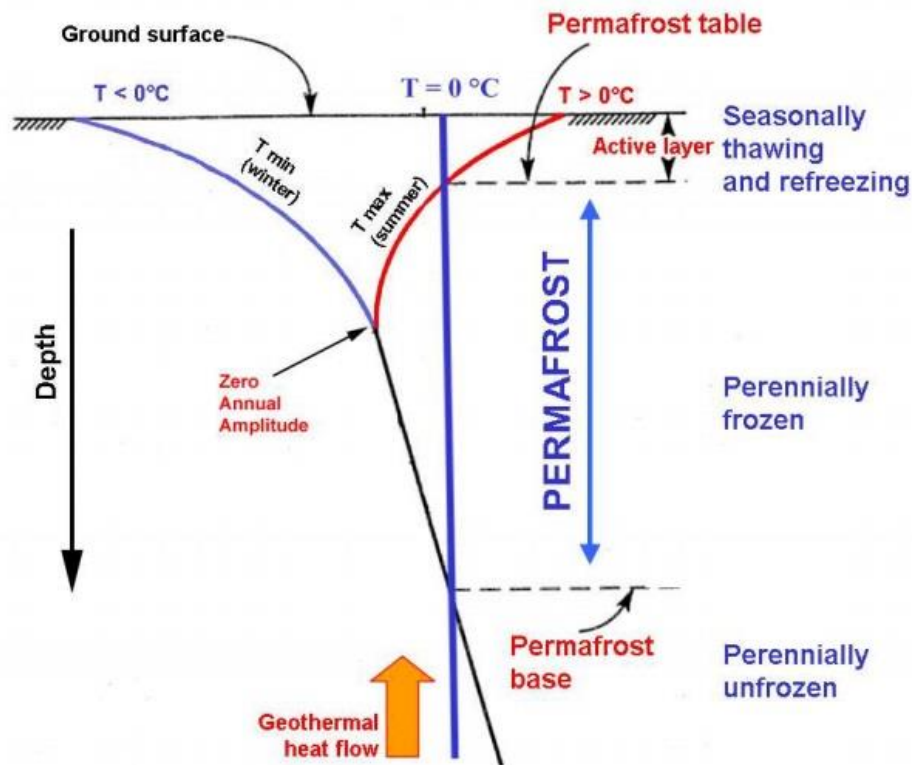
Figure 51 Typical temperature trumpet curve with the depth of zero annual amplitude (PermaNet Alpine Space).

The ground temperature information from borehole Bh-WI-1is presented in Figure 52 and Figure 53. Though the ZAA was not reached, it is possible to infer that permafrost temperature is around -2.2°C, with an active layer thickness of 1 m (Figure 52). The temporal analysis of ground thermal regime does not show any anomalies (Figure 53).
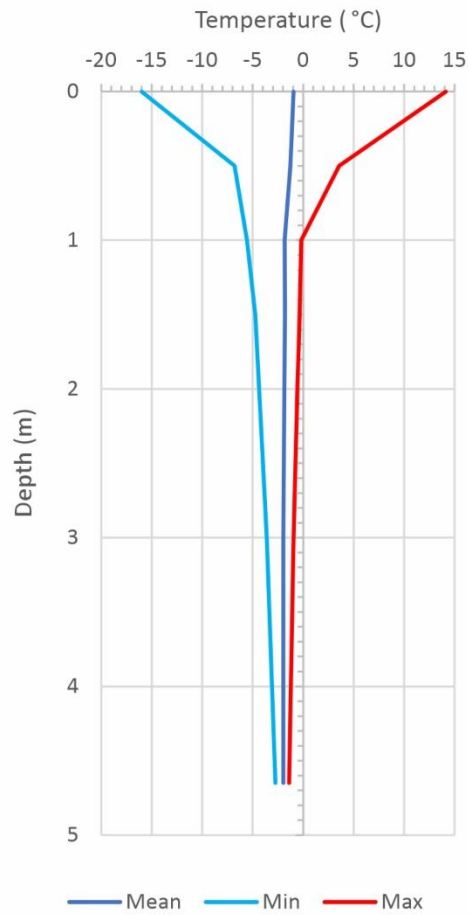
100

Bh-IW-1

2019								
Depth	0.00 m	1.50 m	5.00 m	9.00 m	10.50 m	12.00 m	15.00 m	20.00 m
Mean	-0.2 °C	-2.3 °C	-2.5 °C	-2.5 °C	-2.5 °C	-2.4 °C	-2.3 °C	-2.2 °C
Min	-10.9 °C	-5.9 °C	-3.6 °C	-2.7 °C	-2.7 °C	-2.5 °C	-2.4 °C	-2.3 °C
Max	13.8 °C	-0.4 °C	-1.6 °C	-2.2 °C	-2.4 °C	-2.3 °C	-2.3 °C	-2.2 °C

Figure 52 Ground temperature trumpet curves at borehole Bh-IW-1 in 2019.
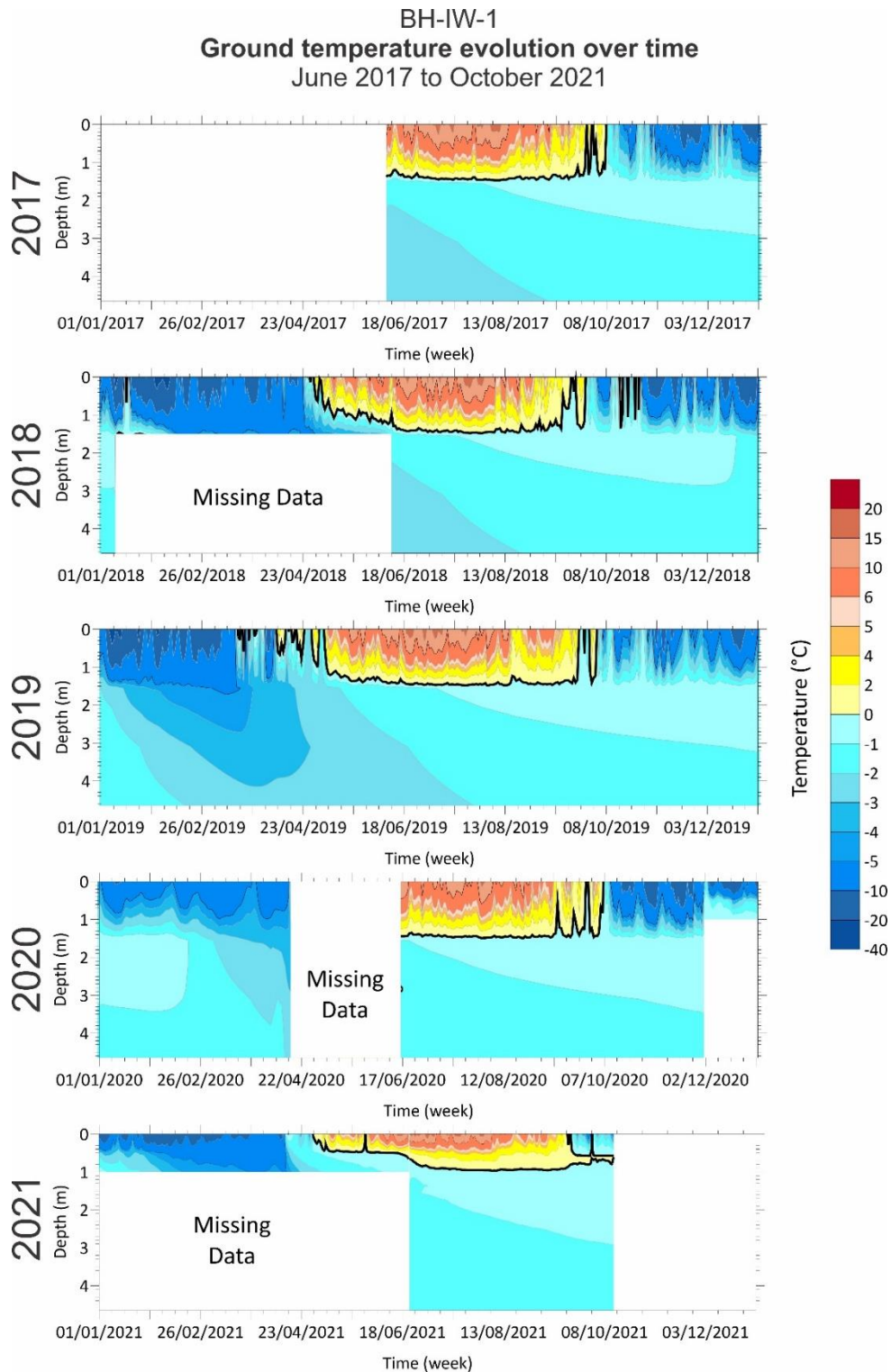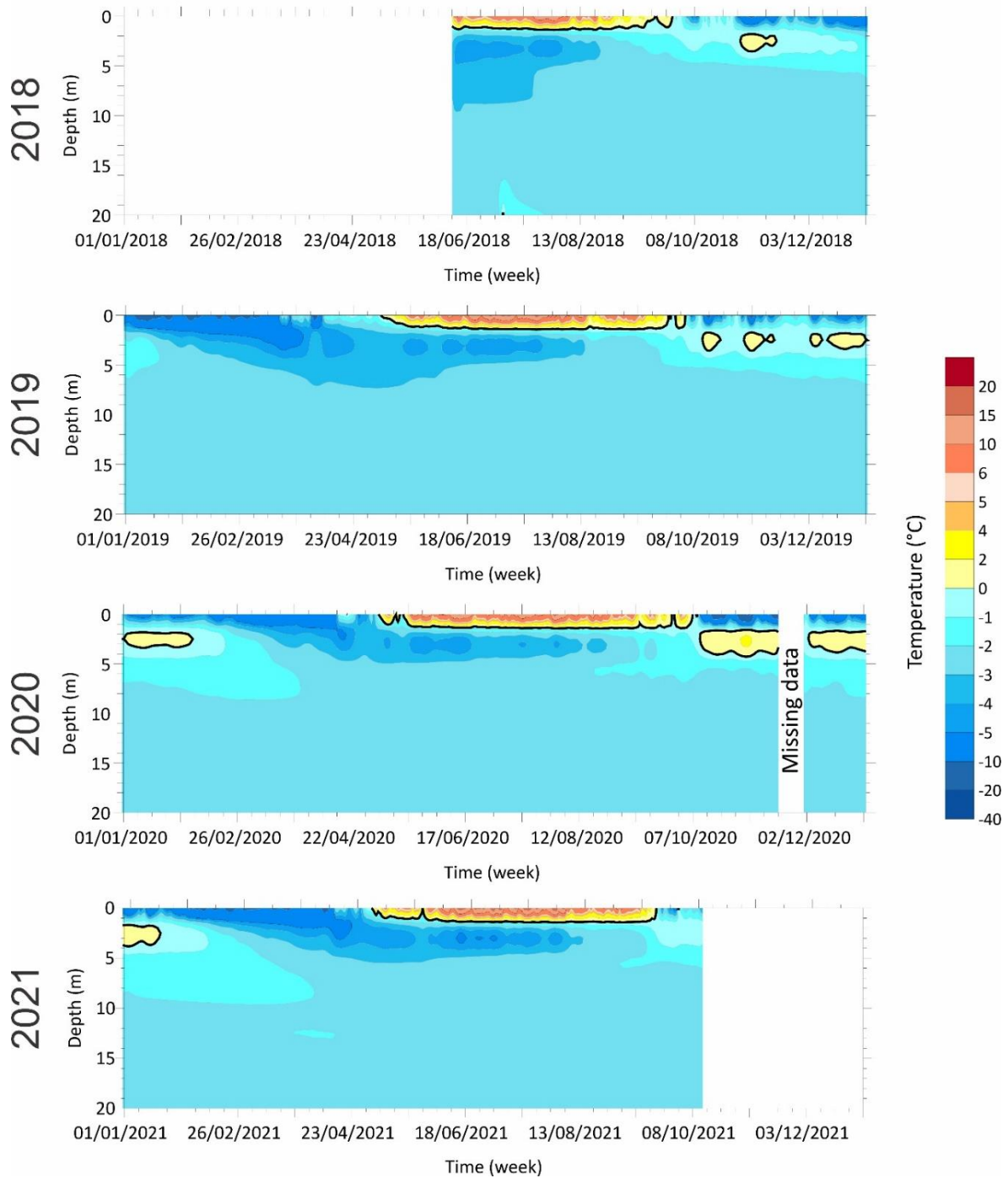
Figure 53 Ground thermal regime in borehole Bh-IW-1 from 2018 to 2021.

The ground temperature information from borehole Bh-BI-1is presented in Figure 54 and Figure 55. The ZAA was reached at a depth of 15 m, with a permafrost temperature

of -2.4°C, and an active layer thickness of 1.5 m (Figure 54). The temporal analysis of the ground thermal regime shows a temperature spike at the base of the borehole in early July 2018 when the sensor quickly thawed and then refroze in several days (Figure 55). Because the presence of silicone oil in the piping would lead to heat rising if convection were to occur, this phenomenon is attributed to a short burst of water flowing at this depth despite the presence of massive ice. Another noticeable feature is the warm temperatures from December to January between approximately 2 and 4.5 m in depth, as this is below the active layer and well after freeze-back had begun. The phenomenon occurred sporadically during the winters of 2018-2019 and 2019-2020 and became continuous during the winter of 2020-2021. This warming suggests that groundwater is flowing at these depths.

Bh-BI-1
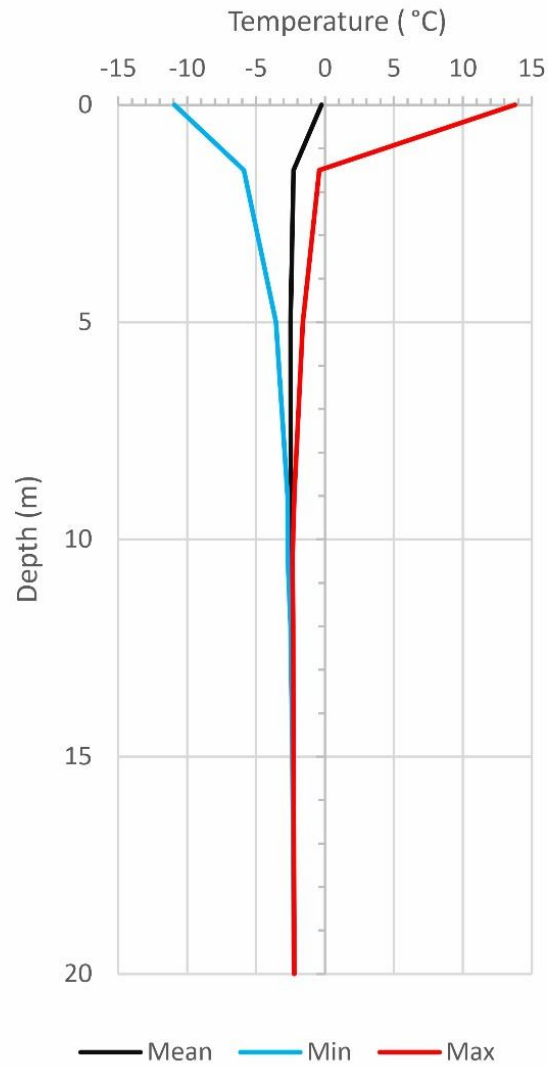
2019								
Depth	0.00 m	1.50 m	5.00 m	9.00 m	10.50 m	12.00 m	15.00 m	20.00 m
Mean	-0.2 °C	-2.3 °C	-2.5 °C	-2.5 °C	-2.5 °C	-2.4 °C	-2.3 °C	-2.2 °C
Min	-10.9 °C	-5.9 °C	-3.6 °C	-2.7 °C	-2.7 °C	-2.5 °C	-2.4 °C	-2.3 °C
Max	13.8 °C	-0.4 °C	-1.6 °C	-2.2 °C	-2.4 °C	-2.3 °C	-2.3 °C	-2.2 °C

Figure 54 Ground temperature trumpet curves at borehole Bh-BI-1 in2019.

Figure 55 Ground thermal regime in borehole Bh-BI-1 from 2018 to 2021.

The ground temperature information from borehole Bh-BW-2 is presented in Figure 56 and Figure 57. The ZAA was reached at a depth of 15 m, with a permafrost temperature of -2.4°C, and an active layer thickness of 1.3 m (Figure 56). The temporal analysis of the ground thermal regime does not show any temperature spikes deep in the borehole like in Bh-BI-1. Nevertheless, some short hot bursts are observed at a depth of 2-3 m, like in Bh-BI-1, but in a more discontinuous fashion (Figure 57). Here also, the spike occurs below the active layer and after freeze-back had begun.

Bh-IW-2
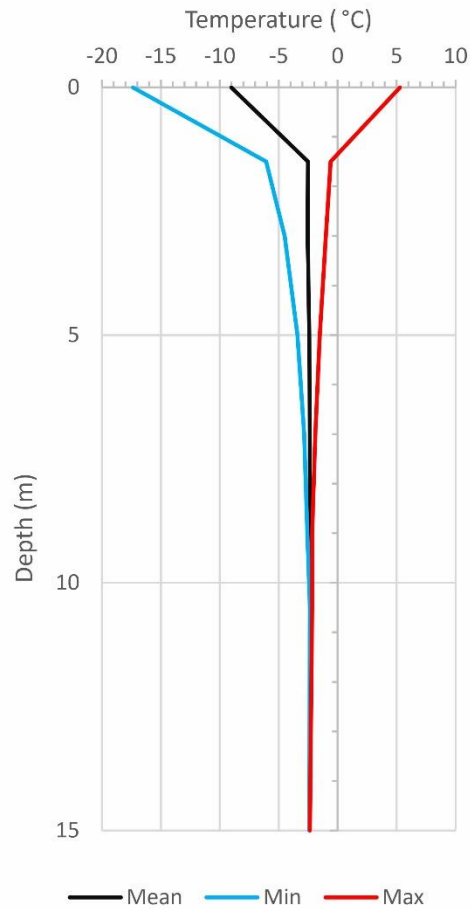
		2019						
Depth	0.00 m	1.50 m	3.00 m	5.00 m	7.00 m	9.00 m	10.50 m	15.00 m
Mean	-9.0 °C	-2.5 °C	-2.5 °C	-2.4 °C	-2.4 °C	-2.4 °C	-2.3 °C	-2.4 °C
Min	-17.4 °C	-6.1 °C	-4.5 °C	-3.4 °C	-2.8 °C	-2.6 °C	-2.4 °C	-2.4 °C
Max	5.3 °C	-0.6 °C	-1.0 °C	-1.5 °C	-1.9 °C	-2.2 °C	-2.2 °C	-2.4 °C

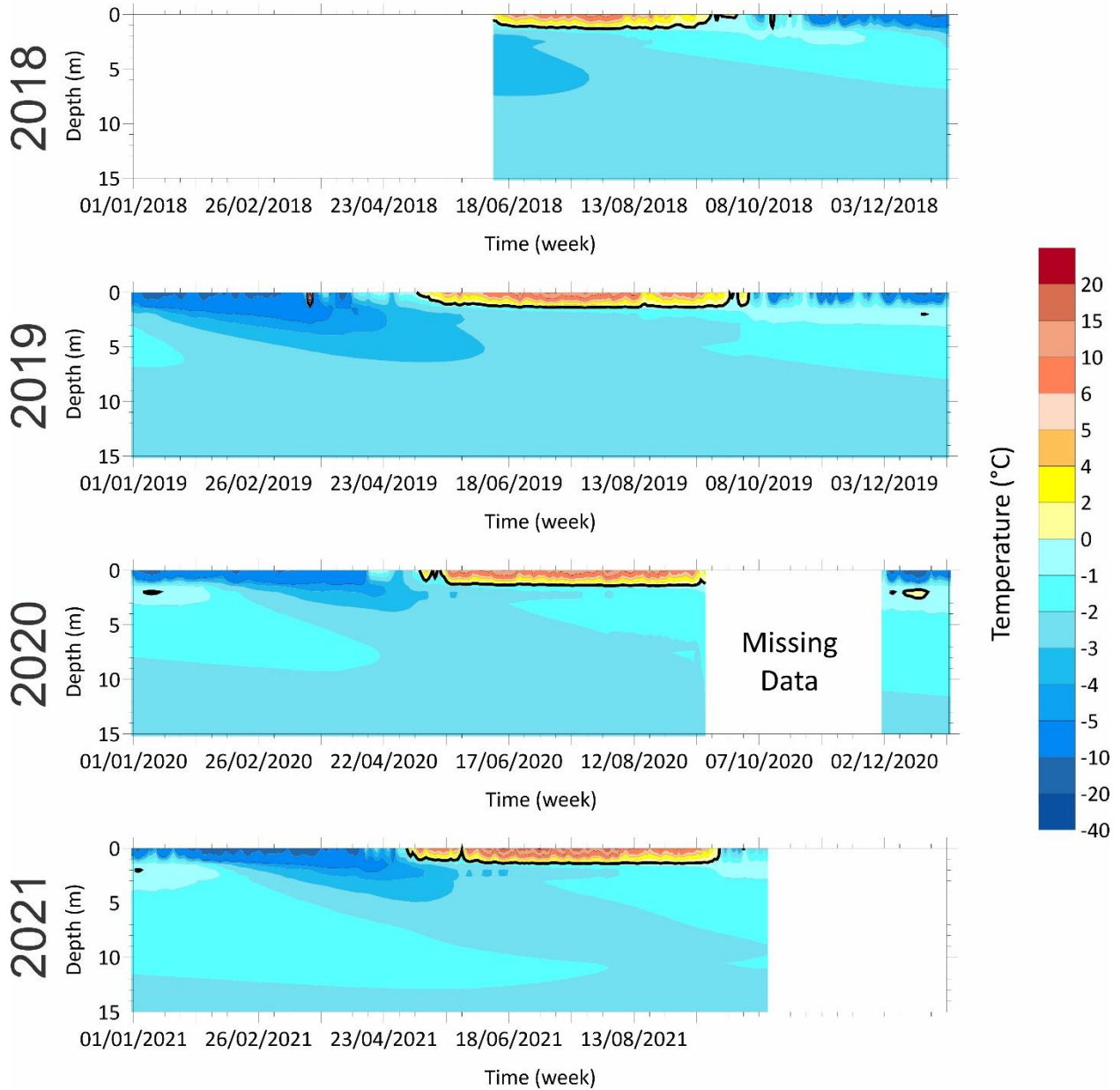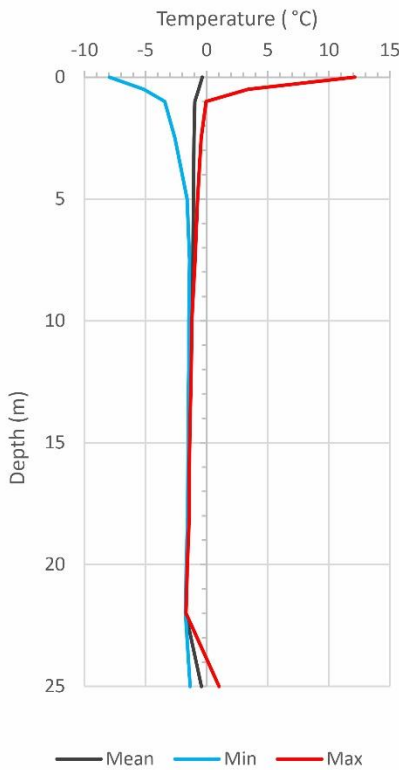**Figure 56** Ground temperature trumpet curves at borehole Bh-IW-2 in 2019.

106

Figure 57 Ground thermal regime in borehole Bh-IW-2 from 2018 to 2021.

The ground temperature information from borehole Bh-BI-2 is presented in Figure 58 and Figure 59. The ZAA was reached at a depth of 16 m, with a permafrost temperature of -1.5°C, and an active layer thickness of 1.0 m. The lower limit of permafrost was reached at 24 m, which was the same depth as the lower limit of massive ice (Figure 58). Indeed, the temporal analysis of the ground thermal regime shows that the lowest part of the profile (24-25 m) is unfrozen from June 2020 to January 2021 and is frozen afterward (Figure 59). Much like in Bh-BI-1 and Bh-IW-2, sporadic and continuous heat events occur around 2-3 m depth during the winters of 2019-2020 and 2020-2021.

Depth	0.00 m	0.50 m	1.00 m	2.50 m	5.00 m	7.50 m	10.00 m	12.00 m	14.00 m	16.00 m	18.00 m	20.00 m	22.00 m	25.00 m
Mean	-0.4 °C	-0.7 °C	-1.0 °C	-1.0 °C	-1.1 °C	-1.1 °C	-1.3 °C	-1.4 °C	-1.4 °C	-1.5 °C	-1.5 °C	-1.6 °C	-1.7 °C	-0.4 °C
Min	-8.0 °C	-5.2 °C	-3.4 °C	-2.6 °C	-1.6 °C	-1.4 °C	-1.5 °C	-1.5 °C	-1.5 °C	-1.5 °C	-1.6 °C	-1.7 °C	-1.7 °C	-1.4 °C
Max	12.1 °C	3.4 °C	0.0 °C	-0.5 °C	-0.7 °C	-1.0 °C	-1.2 °C	-1.3 °C	-1.4 °C	-1.4 °C	-1.4 °C	-1.6 °C	-1.7 °C	1.0 °C

Figure 58 Ground temperature trumpet curves at borehole Bh-BI-2 in 2020/2021.
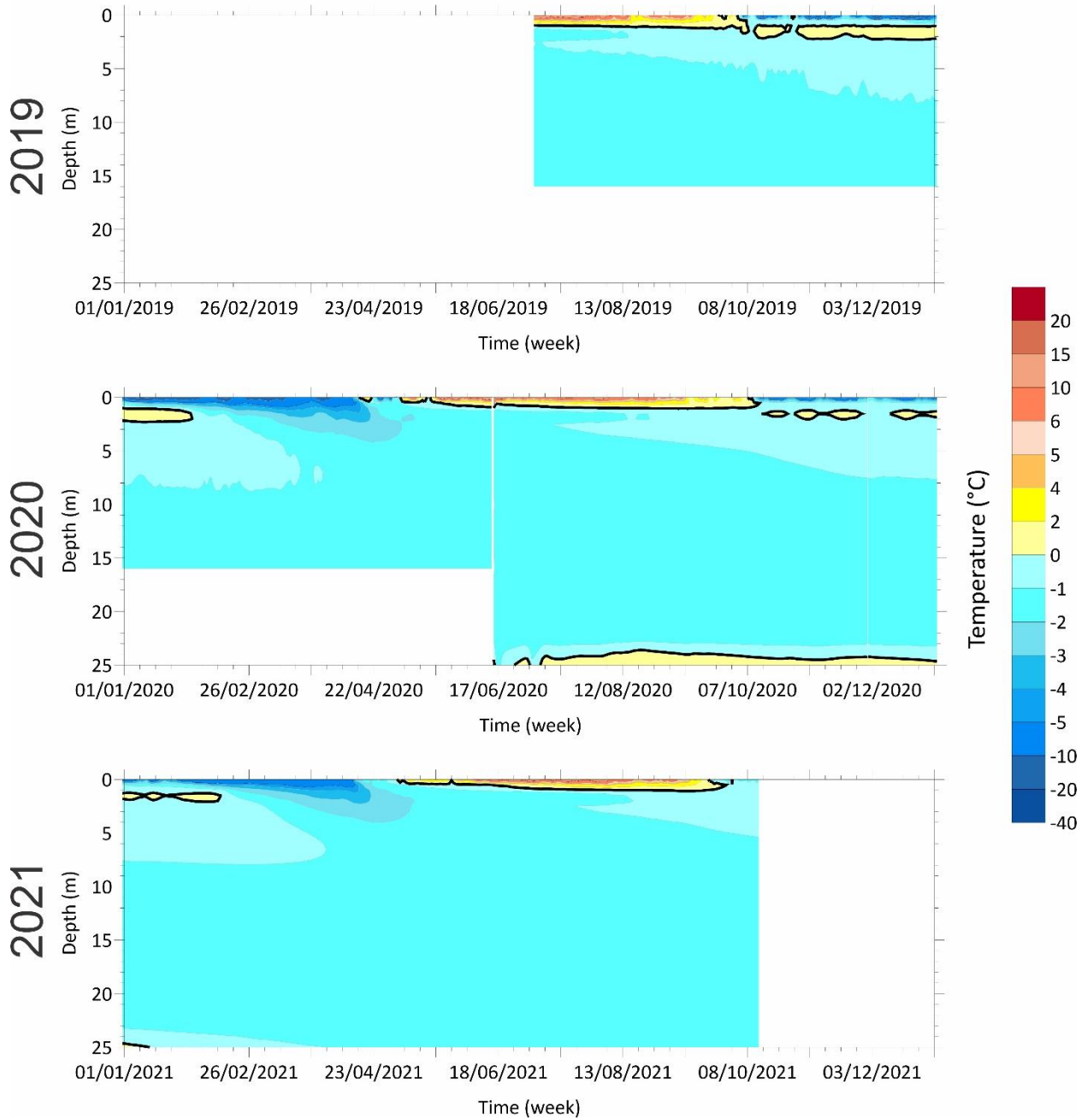
Figure 59 Ground thermal regime in borehole Bh-BI-2 from 2019 to 2021.

The ground temperature information from borehole Bh-Wr is presented in Figure 60 and Figure 61. The ZAA was reached at a depth of 16 m, a permafrost temperature of -1.7°C,

and an active layer thickness of 2.4 m. The lower limit of permafrost was not reached with ground temperatures of -1.7°C at a depth of 25 m (Figure 60). The temporal analysis of the ground thermal regime shows discontinuous heat events around 2-3 m in depth during the winter of 2020-2021 but not the previous winter (2019-2020) (Figure 61).
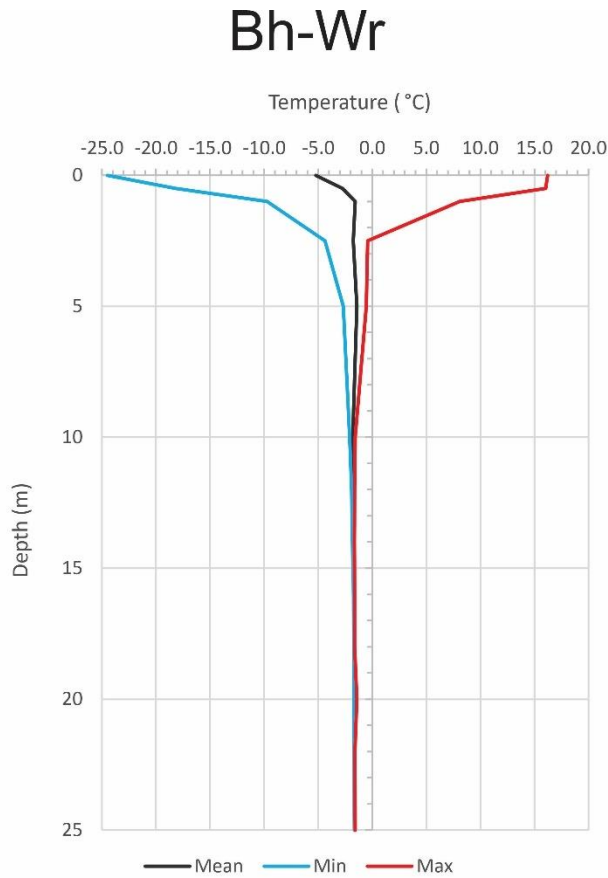
September 2020 - August 2021 (12 months)

Depth	0.00 m	0.50 m	1.00 m	2.50 m	5.00 m	10.00 m	12.00 m	14.00 m	16.00 m	18.00 m	20.00 m	22.00 m	25.00 m
Mean	-5.2 °C	-2.8 °C	-1.6 °C	-1.8 °C	-1.4 °C	-1.8 °C	-1.8 °C	-1.7 °C	-1.7 °C	-1.7 °C	-1.6 °C	-1.6 °C	-1.6 °C
Min	-24.5 °C	-18.2 °C	-9.7 °C	-4.4 °C	-2.7 °C	-2.1 °C	-1.9 °C	-1.8 °C	-1.7 °C	-1.7 °C	-1.7 °C	-1.7 °C	-1.7 °C
Max	16.2 °C	16.0 °C	8.1 °C	-0.4 °C	-0.5 °C	-1.6 °C	-1.6 °C	-1.7 °C	-1.6 °C	-1.6 °C	-1.4 °C	-1.6 °C	-1.6 °C

Figure 60 Ground temperature trumpet curves at borehole Bh-Wr in 2020/2021.
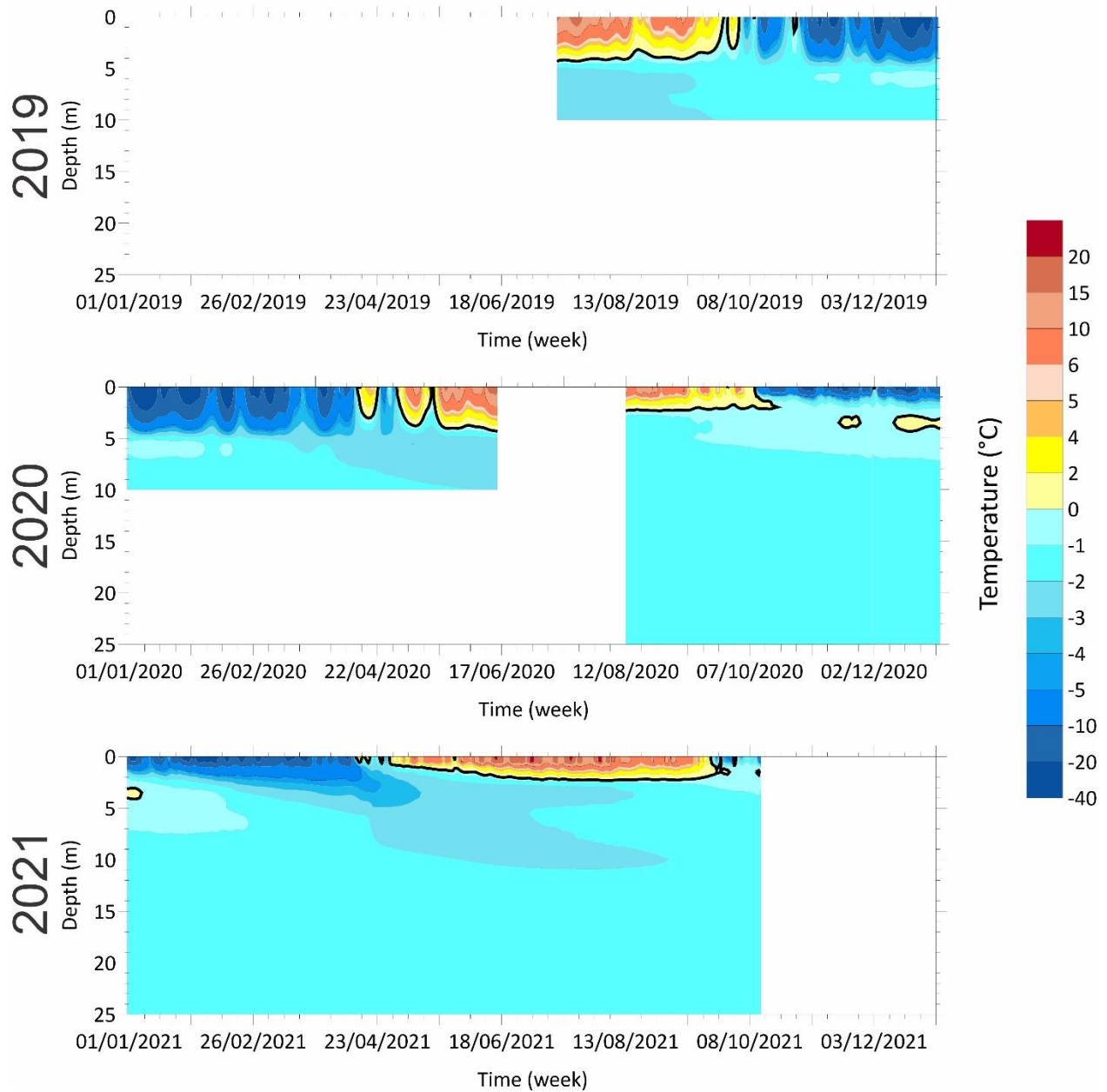
Figure 61 Ground thermal regime in borehole Bh-Wr from 2019 to 2021.

Key points:

- The permafrost temperatures in the study area range from -1.5 to -2.4°C.

- One sporadic heat event was observed at the base of one borehole (Bh-BI-1) and a longer event in another one (Bh-BI-2). The two boreholes are located in the same "buried ice" zone.
- Heat events are observed at 2-3 m depth in several boreholes from December to January. It is possible that these events are related to the active layer freeze-back, where groundwater is circulating on the top of the ice wedge complex, which could in turn be degrading the ice-wedges.
- All heat-spike events seem be related to heat transfer from groundwater flow.

2.2.1.2.4.3. ERT surveys

Electrical resistivity tomography (ERT) surveys were performed at the site from 2016 to 2019. Previous ERT surveys and/or borehole findings informed the location of ERT surveys, just as the ERT surveys informed the drilling locations. The first surveys were performed in 2016 and 2017 in area of the 2006 thaw slump: RHS 2016 in the field adjacent to the road on the left-hand side, and LHS 2017 in the former road's embankment on the right-hand side of the current road (Figure 43). In 2018, an ERT survey of the entire road section was performed in three survey-sections in the field adjacent to the left-hand side of the road: ERT 2018 Survey 1 is 400 m long and located along the southern section facing the 2017 thaw slump; ERT 2018 Survey 3 in 450 m long and located in the central section between the lake and the rest area facing the 2006 thaw slump; and ERT 2018 Survey 2 is 600 m long and located along the northern section up the excavated area (Figure 43). All the surveys were surveyed using the dipole-dipole ERT array configuration which has been found to be best-suited for permafrost environments in the Yukon (Calmels et al. 2018).

2016 and 2017 surveys

The ERT profiles for 2016 and 2017 are show in Figure 62 and Figure 63, respectively, both of which display two survey profiles. The first profile is produced using a robust inversion, and the second one is created with a smoothness constraint in the inversion process. The robust inversion is typically used when sharp boundaries are expected, like between ice and unfrozen ground, while a smoothness constraint tends to ensure that the resulting model shows a smooth variation in the resistivity values, usually producing a model with a larger apparent resistivity RMS error. It is helpful to produce and analyze both types of inversions to better interpret the results.

In the 2016 survey of the right-hand side of the road (RHS 2016) shown in Figure 62, the RMS error obtained after several iterations (from 4 to 13) is between 15 and 18%, which is relatively high. Because of this high error, the results of the survey must be considered with caution. In general, the profiles show a red/orange, low-resistivity layer that is 4-5 m thick located in the upper part of the profile, overlying a blue, highly resistive material (Figure 62). These results could be interpreted as the ice-poor, warm old road embankment overlying relatively ice-rich, colder frozen ground. The most resistive values are obtained deep in the profile, staring at about 20 m deep. This is deeper than the ice-wedges observed in the field and on the head wall of the slumps, which suggests the possible presence of deep bodies of massive ice.

DH116 RHS DipoleDipole 2016 Robust 5th iteration RMS error 18.3%
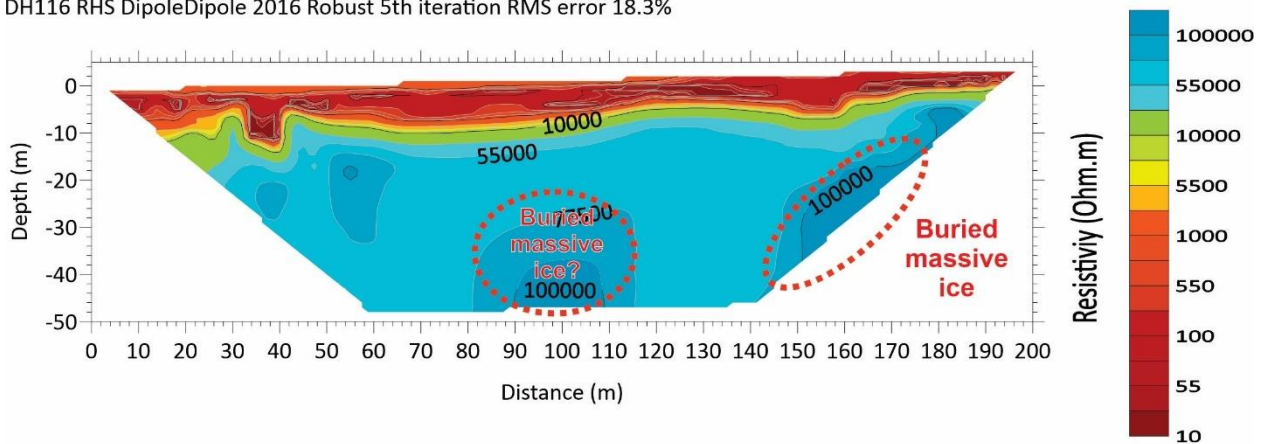
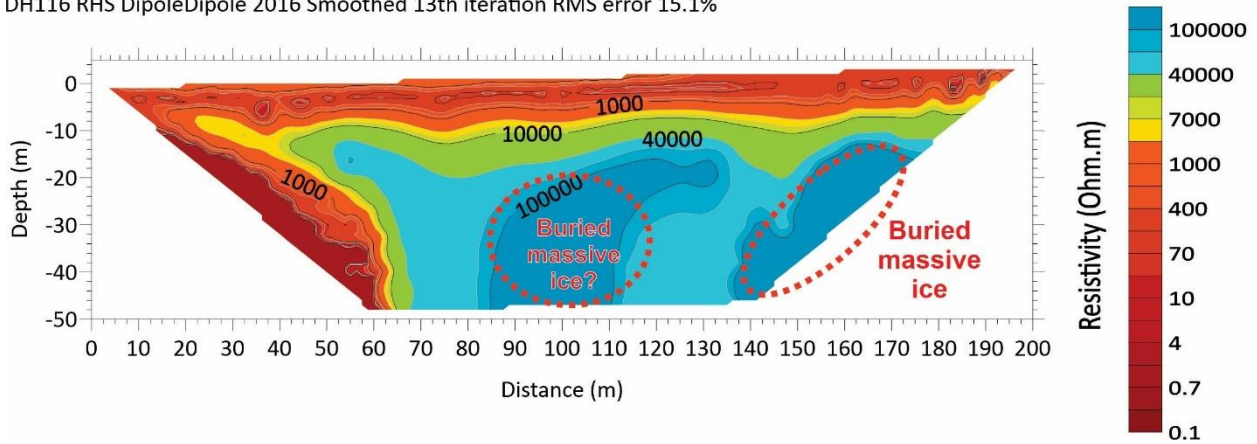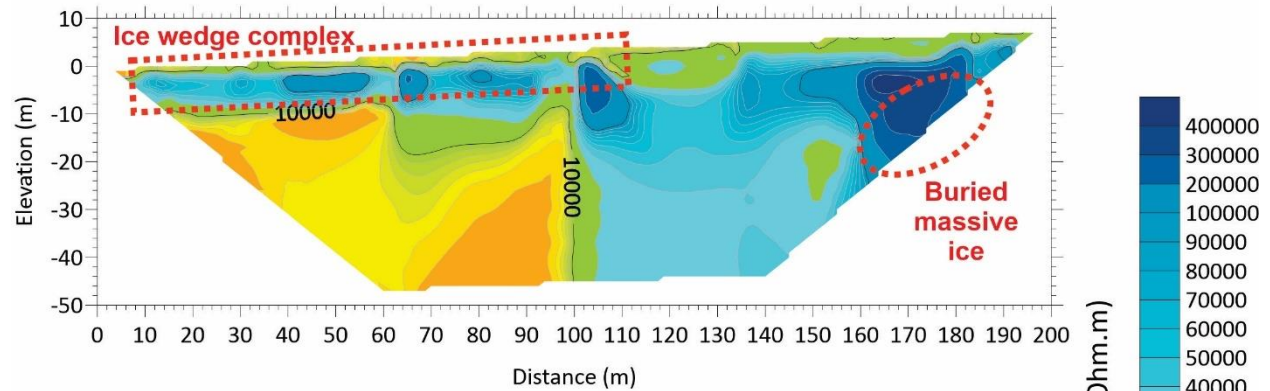DH116 RHS DipoleDipole 2016 Smoothed 13th iteration RMS error 15.1%

Figure 62 Dipole-dipole ERT surveys at site DH116, right-hand side (RHS) from 2016, using robust and smoothed inversion processes.

In the 2017 survey of the left-hand side of the road (LHS 2017), there are several highly resistive areas (depicted in blue) that are present between the ground surface and a depth of 10 m, all along the profile (Figure 63). Below 10 m of depth, there is a clear difference between the western and eastern halves of the survey, with the west side showing lower resistivity values and the east side showing higher resistivity values. The red/orange lower resistivity value areas could be due to a decrease in ice content, warmer permafrost, or the presence of liquid water; while the higher resistivity values (dark blue) could represent coarser, more ice-rich, and/or colder permafrost. These observations informed the location of borehole Bh-BI-1. Using the combined observations from the slump headwalls, borehole Bh-IW-1 and Bh-BI-1, the ERT can be interpreted with a high-level of confidence: the highly resistive areas (blue) present between the surface and a depth of 10 m correspond to an ice wedge complex, and the

114

deeper higher resistivity values on the eastern side indicate the presence of massive ice bodies.

DH116 LHS DipoleDipole 2017 Robust 4th iteration RMS error 3.8%

DH116 LHS DipoleDipole 2017 HC Smooth 4th iteration RMS error 6.9%
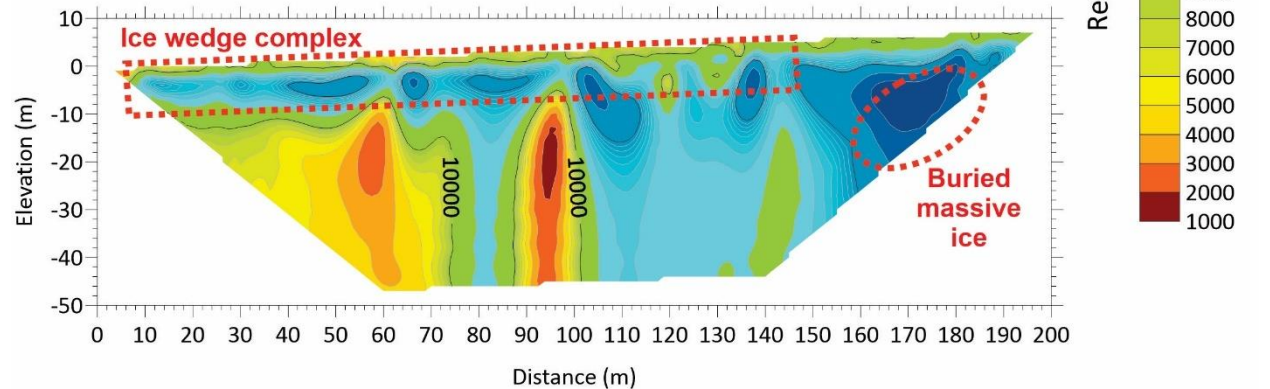

Figure 63 Dipole-dipole ERT surveys at site DH116, left-hand side (LHS) from 2017, using robust and smoothed inversion processes.

2018 ERT surveys

The three surveys performed in 2018 are shown together in Figure 64, from south to north (ERT 2018 Survey 1, ERT 2018 Survey 3, 2018 Survey 2), including a spatially accurate representation of the survey distribution at the bottom of the figure. Based on the information provided by the 2016 and 2017 ERT surveys, the principal objectives of the 2018 ERT surveys were to map the presence of both ice wedge complexes and deeper massive ice bodies using the LHS 2017 survey and the boreholes as guides.

115

In the LHS 2017 survey, several highly resistive areas are present between the ground surface and 10 m of depth in all three profiles, all along the profile (Figure 64). This upper resistivity layer corresponds to the ice wedge complexes that are widespread across the entire area. Below 10 m of depth, there is only one limited indicator of deep massive ice body in the southern survey (at approximately 150 m along the survey transect), and two occurrences in the central survey (at approximately 180 m and 270 m along the survey transect). The presence of deep massive ice bodies is more conspicuous in the northern survey, where large, highly resistive areas are visible at depth all along the profile. These observations suggest that the distribution of deep massive ice bodies is patchy in the southern sections and becomes denser and more widespread towards the north. Another noticeable feature is the presence of very low resistivity value areas at various locations in the profile; 130 m along the southern survey, 230 m, 300 m and 400 m along the central survey, and 430 m along the northern survey. These low-resistivity areas could be indicative of wet areas within the permafrost, possibility resulting from groundwater movement between the ice-wedge layer and the deep massive ice layer.

2019 ERT surveys

The objective of the two ERT surveys performed in 2019 (2019 ERT 6 and 2019 ERT 7) was to complete the geophysical assessment for two points of interest. The 2019 ERT 6 survey was performed along the shore of Chapman Lake with the intent to locate potential groundwater flows (Figure 65), and the 2019 ERT 7 survey aimed to assess deep massive ice distribution further north of km 116 (Figure 66).

The 2019 ERT 6 survey, along the lake shore, displays similar features than the other surveys including the ice wedge complexes present in the first 10 m in depth of the ground profile. However, no deep massive ice bodies are seen in this survey. Another noticeable feature is the presence of multiple low resistivity areas below the ice wedges. Some low resistivity values also are present deeper in the profile, such as 250 m along the profile. These areas could be representative of groundwater flowing from the lake towards the Tombstone River.

The 2019 ERT 7 survey, on a plateau north of the study site (Figure 43) shows the same three main features observed in the other surveys: 1- the ice wedge complexes present in the first 10 m of depth of the ground profile; 2- deep massive ice bodies staring at about 20 m depth (which is consistent with observation made in borehole Bh-BI-2 - Figure 49); and the possible presence of groundwater flow at 45 m, 110 m, and 140 m along the profile. The most noticeable fact is that the deep massive ice appears to be

widespread across the entire profile. This increase in massive ice occurrence is consistent with the observation from the 2018 ERT profiles.
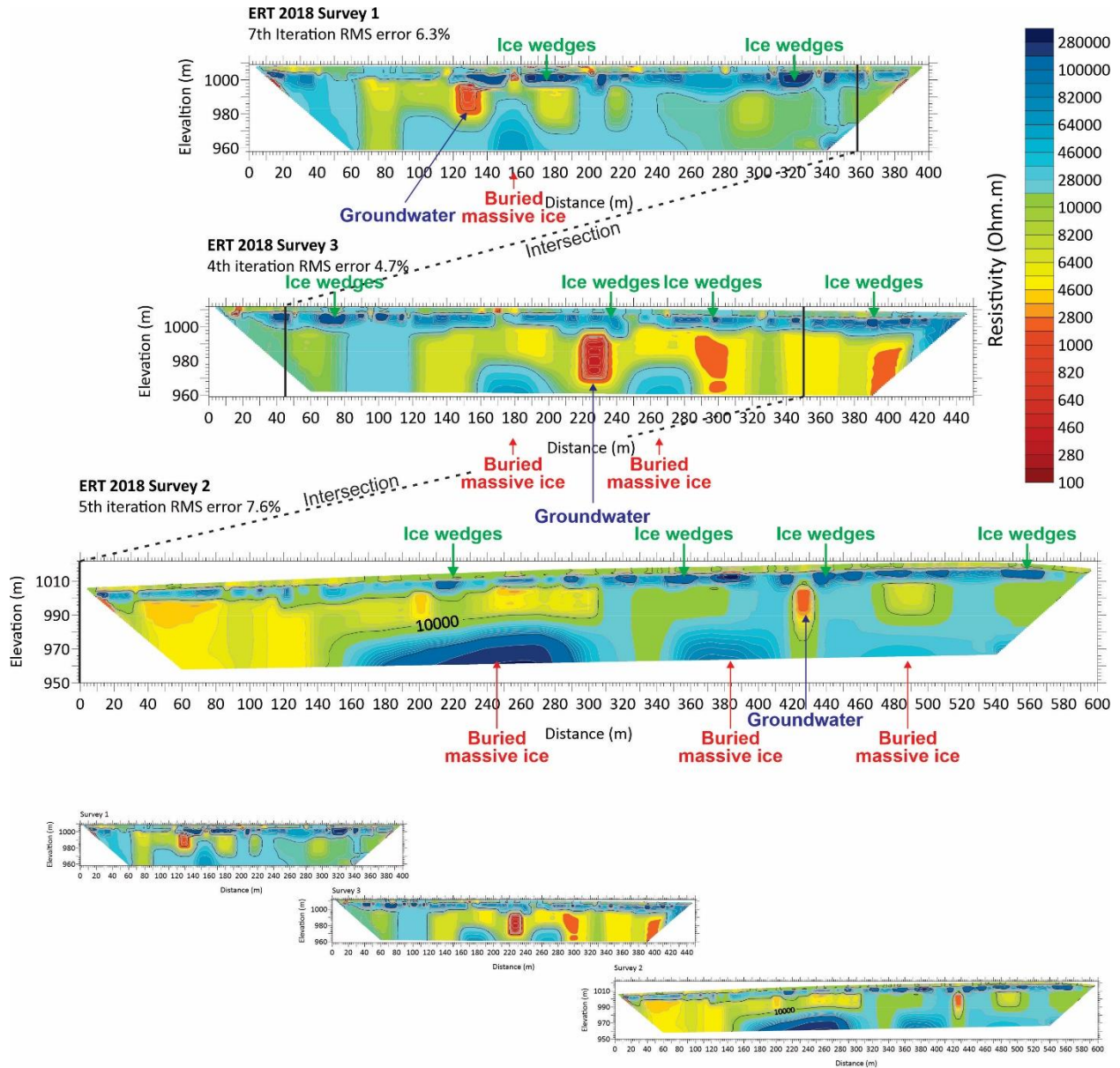

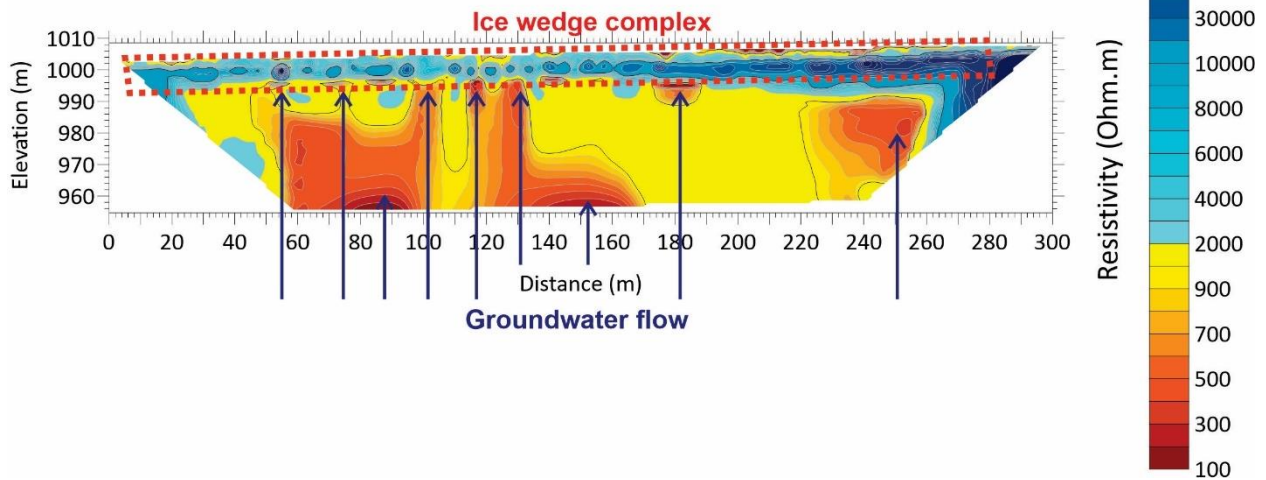**Figure 64** Dipole-dipole 2018 ERT surveys at site DH116, LHS from 2018.

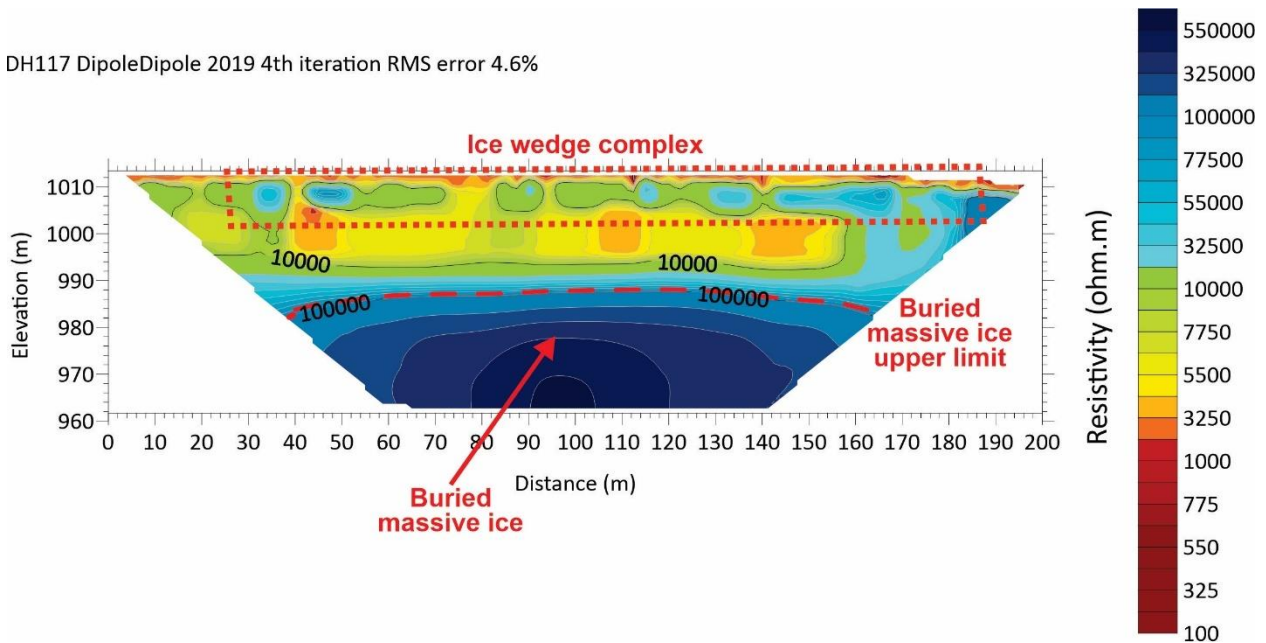**Figure 65** Dipole-dipole 2019 ERT 6 survey at site DH116, near the shore of Chapman lake, from 2019.

Figure 66 Dipole-dipole 2019 ERT 7survey at km117, left-hand side (LHS) from 2019.

The ground penetrating radar (GPR) surveys were performed in partnership with Laval University researchers using a Sensors & Software PulseEKKO with both 50 and 100 MHz antennas. The surveys were performed at the same locations as the 2016, 2017 and 2018 ERT surveys. In addition, a single long survey was performed directly on the top of the road embankment along the whole study site. Because of the relatively low depth of penetration of GPR waves for the frequencies used, the main purpose of these surveys was to locate ice wedges and old buried culverts.

The locations of the GPR surveys are shown in Figure 44 and the overlap between ERT and GPR surveys is presented in Table 13. A total of eight GPR surveys were conducted at km 116 in 2017 and 2018, on the LHS and RHS of the road. In 2017, lines 0,1 were surveyed on the RHS, and lines 8 and 9 were surveyed on the LHS. In 2018, lines 6, 7, and 8 were surveyed on the LHS, and lines 9 and 10 followed the road. Line 9 was incomplete and is thus not presented in this report.

Table 13 Corresponding ERT and GPR surveys.

ERT Lines	Corresponding GPR surveys
2016 RHS	GPR 0 and 1
2017 LHS	GPR 8 and 9
2018 survey 1 (south)	GPR 6
2018 survey 1 (central)	GPR 7
2018 survey 2 (north)	GPR 8
2018 surveys from the road	GPR 10

2017 surveys

RHS - Lines 0 (100 MHz) (Figure 67) and line 1 (50 MHz) (Figure 68) are 120 and 150m long, respectively, and are located on the old embankment, mainly following the 2016 RHS ERT survey. They both show hyperbolae along the profile, likely representing ice wedges. There are also horizontal signals that likely represent infill, and for line 1 the deeper penetration more clearly shows a horizontal signal that likely represents the permafrost table. Additionally, in line 0, the shallower penetration shows hyperbolae near the surface, which could represent old culverts or buried metal within the embankment.
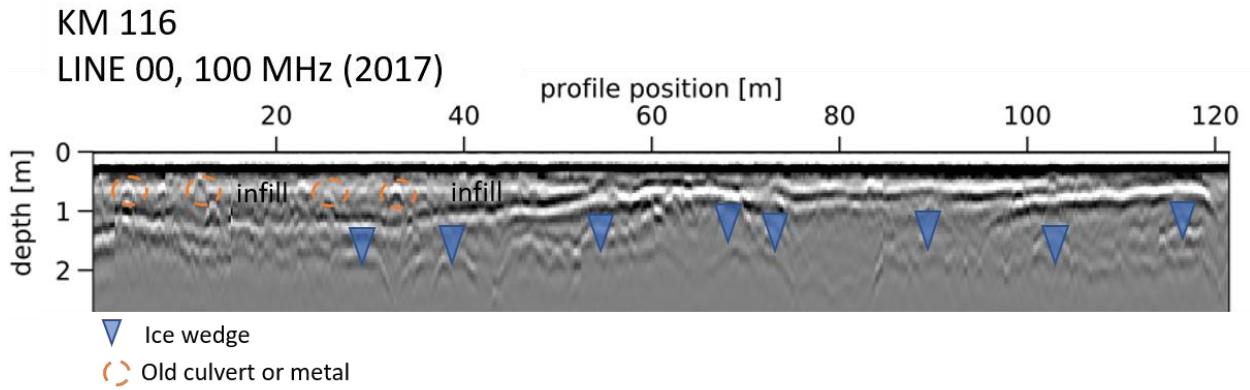
Figure 67 GPR line 00 (2017) at RHS of Km 116 (100 MHz), migrated to 0.1 m/ns.
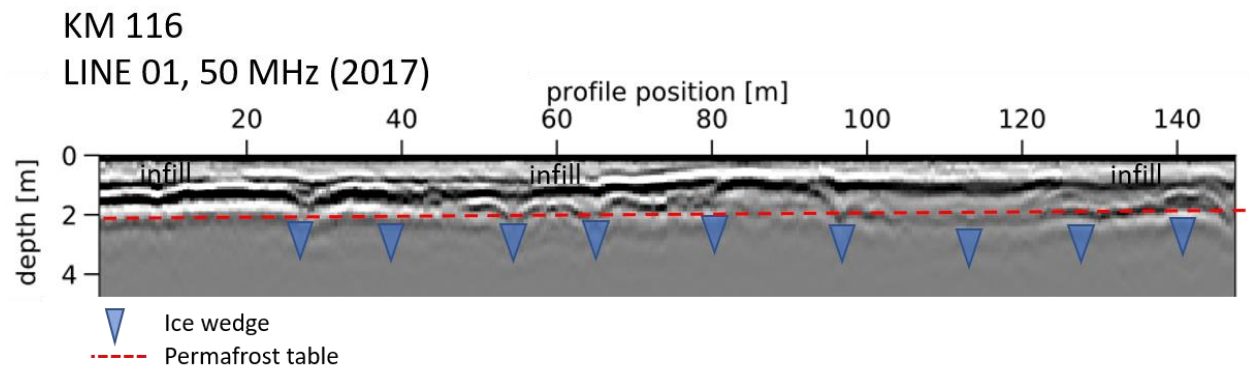
Figure 68 GPR line 01 (2017) at RHS of Km 116 (50 MHz), migrated to 0.1 m/ns.

LHS - Line 8 (100 MHz) (Figure 69) and line 9 (50 MHz) (Figure 70) are on the LHS of the road, in the field adjacent to the road, and are both 200 m long, following the 2017 LHS ERT survey transect. These GPR surveys show many hyperbolae that likely represent ice wedges. There is also a clear horizontal signal between 0.5 and 1 m depth that likely represents the permafrost table.
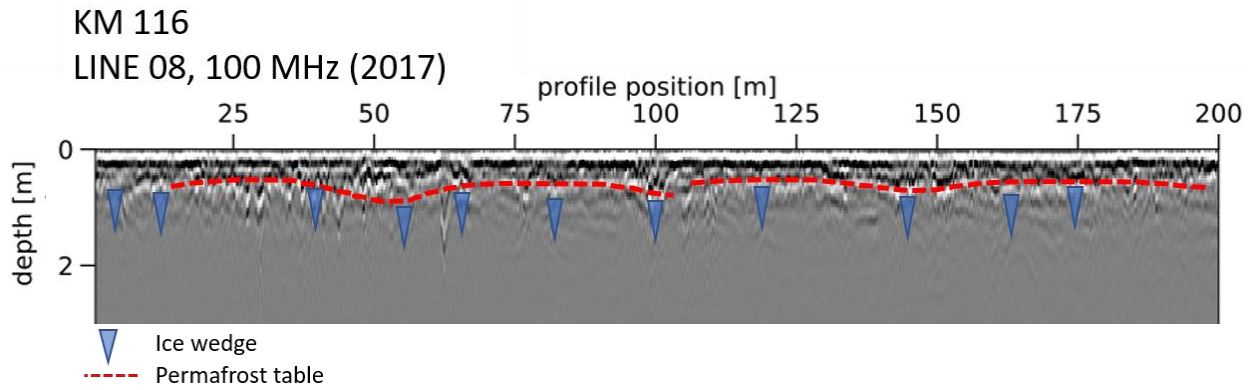
KM 116
LINE 08, 100 MHz (2017)

Figure 69 GPR line 08 (2017) at LHS of Km 116 (100 MHz), migrated to 0.1 m/ns.
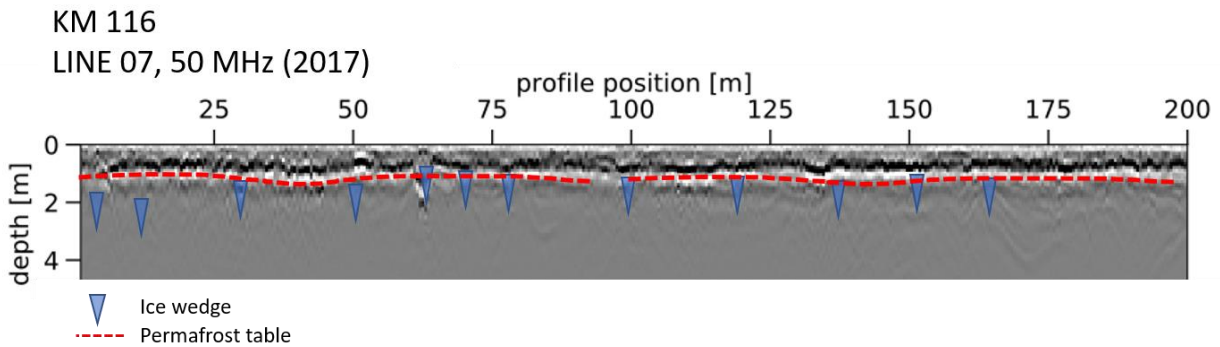

KM 116
LINE 07, 50 MHz (2017)

Figure 70 GPR line 09 (2017) at LHS of Km 116 (50 MHz), migrated to 0.1 m/ns.

2018 surveys

LHS - Lines 6, 7, and 8 are on the LHS of the road (Figure 71, Figure 72, and Figure 73) and were all three collected using a 100 MHz antenna. Line 6, surveyed following the 2018 ERT survey 1 (south) transect is 400 m long and shows numerous hyperbolae along the profile, which likely represent ice wedges. There is a section from 50-150m that shows stronger reflections, representing an area where ponding occurs. Line 7 which covers the same transect as the 2018 ERT survey 3 (central) and line 8 which follows the same transect as the 2018 ERT survey 3 (north) are 400 and 600 m long, respectively, and show many hyperbolae that likely represent ice wedges.

KM 116
LINE 06, 100 MHz

Ice wedge
Ponding
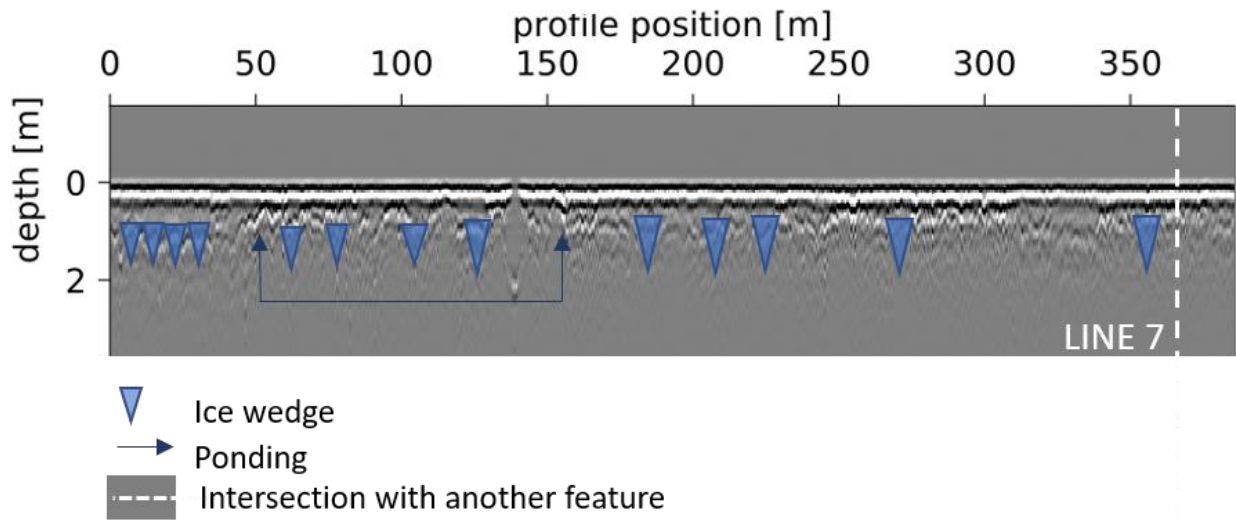Intersection with another feature

Figure 71 GPR line 06 at Km 116 (100 MHz), migrated to 0.1 m/ns.

KM 116
LINE 07, 100 MHz
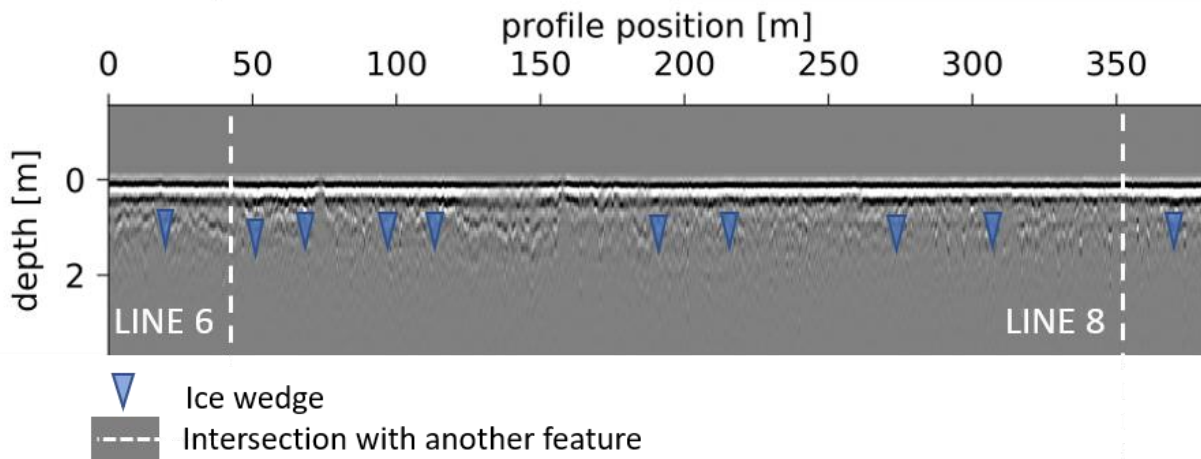
Ice wedge
Intersection with another feature

Figure 72 GPR line 07 at Km 116 (100 MHz), migrated to 0.1 m/ns.
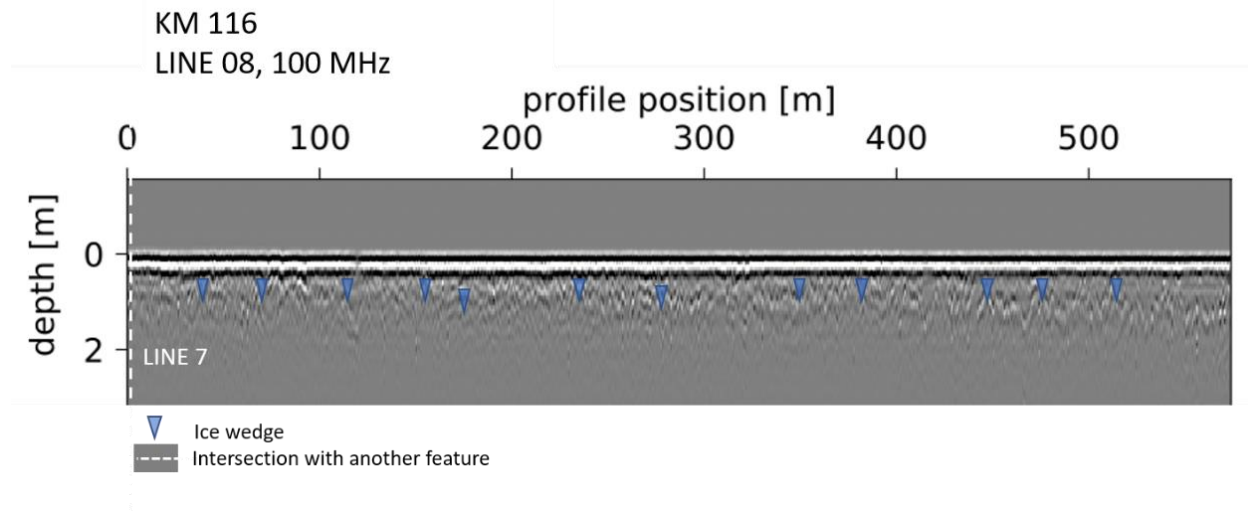
Figure 73 GPR line 08 at Km 116 (100 MHz), migrated to 0.1 m/ns.

Road survey

Line 10 is >1200 m and is presented in two 600 m sections in figures Figure 74 and Figure 75. Part one (Figure 74) shows many hyperbolae which likely represent ice wedges. From 90-200 m the signal suggest that there is degradation, and this coincides with ponding in the field adjacent to this section. Above the hyperbolae along the profile there are horizontal signals which likely represent layers of infill added to these degraded areas. Part two (Figure 75) shows a similar pattern of hyperbolae with horizontal signals above. From 650-850 m of part two, the signals suggest that there is degradation, and this coincides with the area of active slumping along the RHS of the road. Overall, this appears to be an area with many ice wedges and degradation.

Figure 74 GPR line 10 part 1 at Km 116 (100 MHz), migrated to 0.1 m/ns.

Figure 75 GPR line 10 part 2 at Km 116 (100 MHz), migrated to 0.1 m/ns.

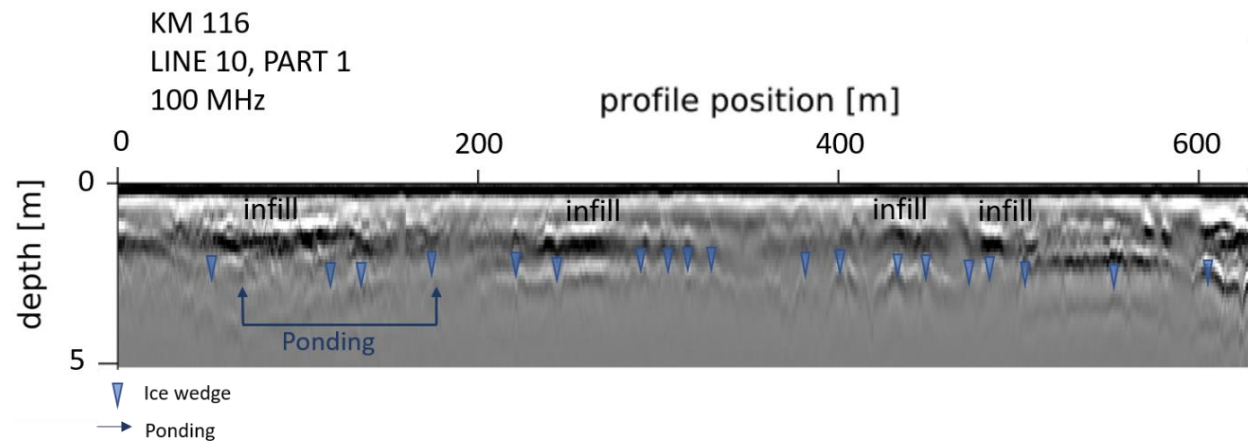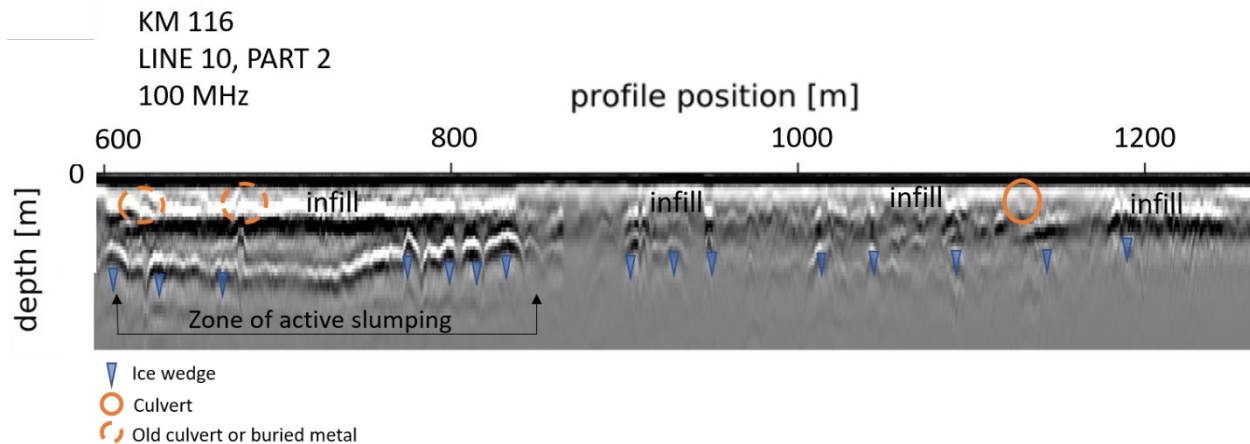### 2.2.1.2.4.5. Bathymetry of Chapman Lake

The progression of the 2006 retrogressive thaw slump in the direction of Chapman Lake is the main cause of concern for YHPW. Based on drone imagery acquired in August 2021, the shore of the lake currently is 52 m away from the road embankment and 86 m from the edge of the thaw slump. Should the RTS continue to progress, it may eventually reach the lake shore, which could lead to catastrophic drainage. It is also possible for the lake to begin draining more slowly if water begins to channelize and flow through permafrost. Because the lake can have such an important impact on the area potentially causing road failure, the characteristics of the lake were studied including a bathymetric survey of the lake.

Yukon Highway and Public Works contracted Lamerton Land Surveys to perform a bathymetric survey of Chapman Lake in August and September 2018. The survey was performed using Topcon dual frequency, dual constellation GNSS receivers in both post processed and real time kinematic modes (RTK and PPK). High-precision points were measured to create a ground control network in order to increase the quality of the survey. This was done using Natural Resource Canada's Canadian Spatial Reference System Precise Point Positioning (CSR-PPP) and Topcon post-processing software. In Addition to the bathymetry, the shoreline of the lake was measured at 20 to 30 meters intervals. The YukonU team collected the data from YHPW and postprocessed it to produce graphic representations using ArcMap and Surfer. The figure processed in ArcMap shows the shoreline and depth for each bathymetric data point (Figure 76), and the interpolated bathymetric model gridded in Surfer can be seen in Figure 77.

The survey reveals that most of Chapman Lake is less than 2 meters deep with some deeper sections on the western side of the lake that are as deep as 15.1 m. The volume of the main lake is 3,048,506 m^3 and the volume of the small lake to the west of the main body is 777 m^3.

While the deeper sections are small and do not impact the overall volume of the lake in an important way, they have an important geomorphologic significance. These deep areas suggest that Chapman Lake is at least partially a kettle lake. Kettles, or kettle holes or lakes, form when a block of stagnant glacier ice detaches from a glacier in an outwash plain formed by retreating glaciers or draining floodwaters. The relic glacier ice becomes wholly or partially buried in sediment and slowly melts, leaving behind a pit. Later, water fills the depression and forms a pond or lake called a kettle. Kettles can be meters or kilometers long, but they are usually relatively shallow. The deep bathymetric holes suggest that the buried relic glacial ice bodies may have been 10-15 m thick.

Consequently, the bathymetric survey supports the hypothesis that the deep massive ice bodies observed in the boreholes and ERT surveys are buried glacier ice.
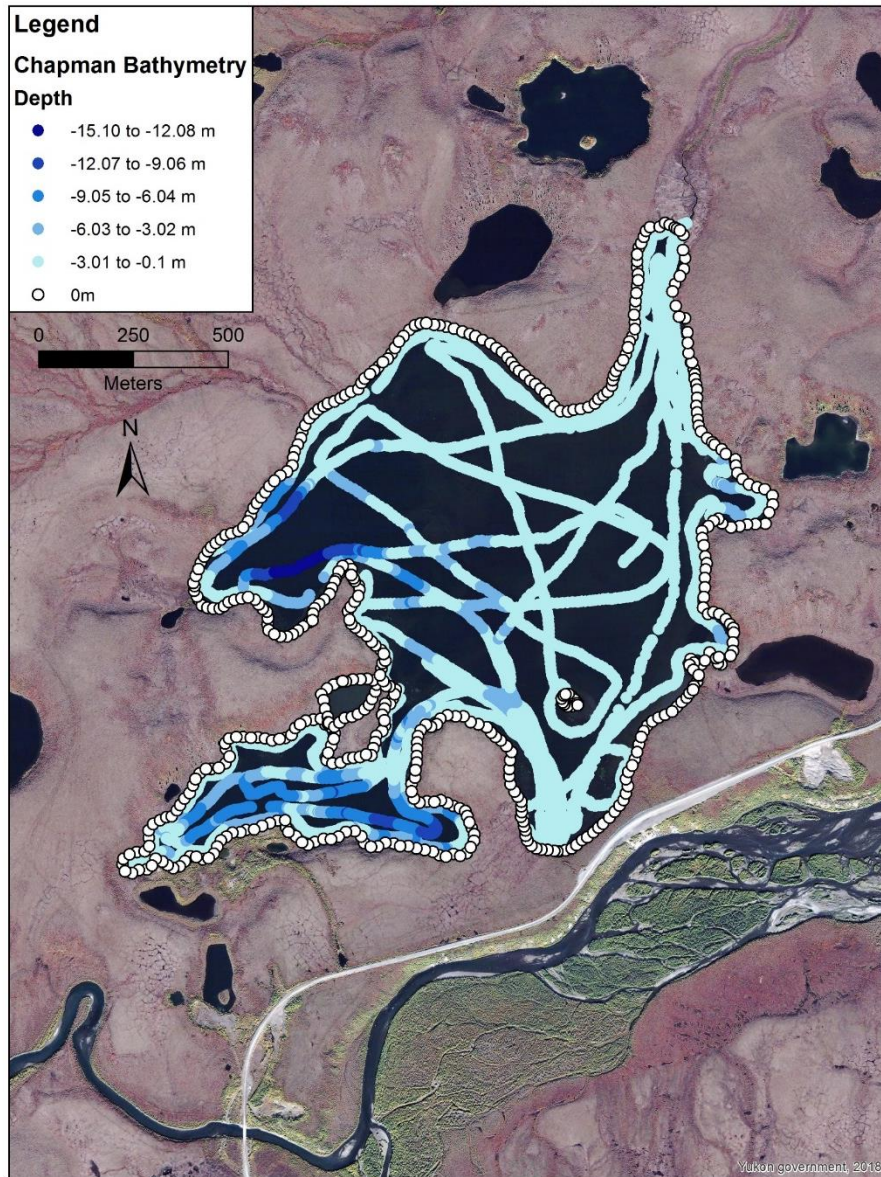
Figure 76 Chapman Lake bathymetric and shore survey, with depth measurement range for each data point.
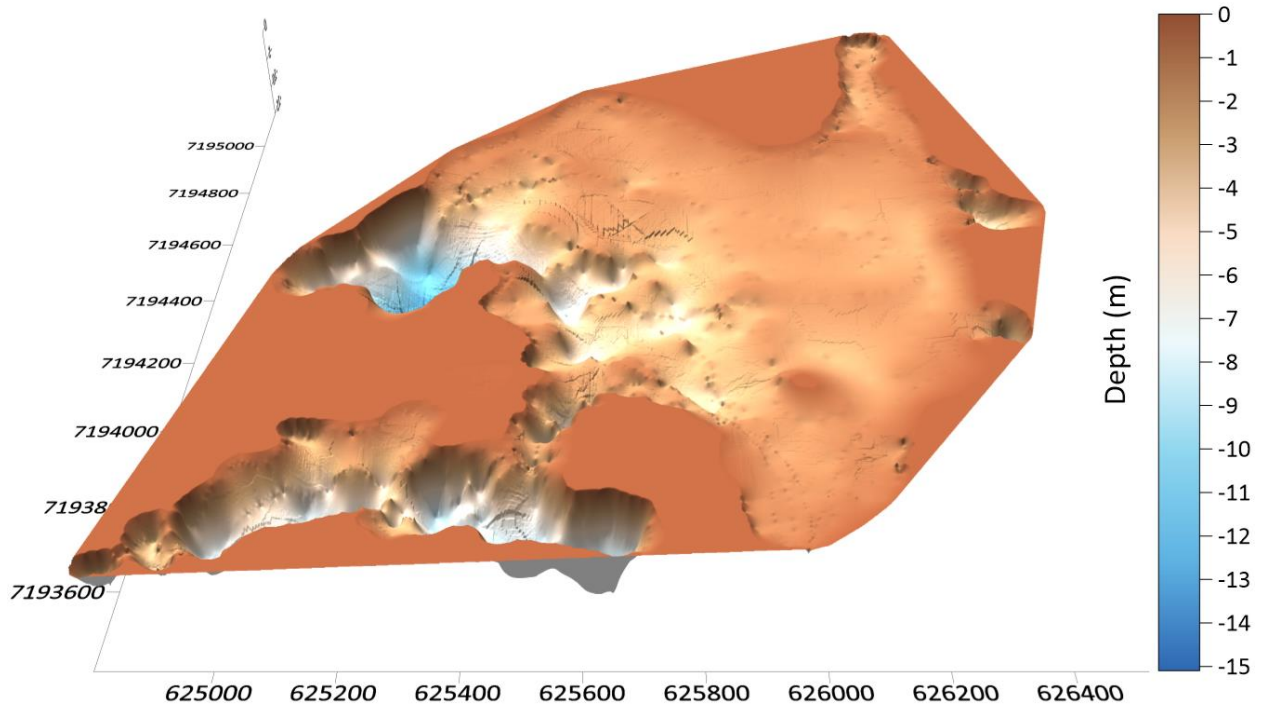
Figure 77 Chapman Lake digital bathymetric model with a vertical exaggeration of 15.

2.2.1.2.4.6. Topographical analysis

The topographical analyses were performed on five different areas of the field site, as referenced on Figure 78. Figure 79 and Figure 80 are shown as an example of the analysis' output between G and H (on Figure 78). The detailed results and methodology are shown in the Appendix 3.2.1-B. Briefly, the relevant observations out of this analysis and some interpretations follow.

The terrain is hilly with mostly convex slopes, with relatively steeper north faces, especially around water bodies and/or flats wetlands. The lake bottom is generally shallow (2 m) but has a deep depression (10 m) in the section just north of the polygon field, the lake bottom's slopes are relatively smooth but quite steep where the bottom is deep. Around the polygon field (G on Figure 78) the lake bottom's elevation is similar to the riverbed, while its elevation near the isthmus (E on Figure 78) is more similar to the buried ice level found in the boreholes (BH2).

On its own, the topographical analysis rules out the probability that the lake breaches off by the bottom of the active layer of the permafrost separating it from the river and drains down to the latter.

The road profile is convex throughout the site so the surface water drains into the ditches, but the embankment can be an infiltration site of this water on both sides, especially where the hill has been cut for the road alignment, at the easternmost end of the site. Culverts have been observed but it is unclear if they were designed to transfer ditch water from one side fo the road to the other, or to expel the groundwater under the road. In either case, they were well above the bottom of the ditches, and they remained dry during our visit despite rain.

Water can flow underground either along or across the centerline, and will likely drain out through the bluff. Channelling, piping and/or post-thaw under consolidation of icy material can lead the way to preferential groundwater flow under the road, especially where surface water can accumulate.

Surface water accumulates in some specific areas, most noticeably near the most recent landslide (2017) where three ponds persist on the left-hand side of the road (Figure 38B).

A significant part of the surface and subsurface water filling these ponds is sourced from the bigger pond uphill at the westernmost end of the site (beside the old trail to old camp, lower left corner on Figure 45)

Between the three ponds and the current alignment, an older road alignment results in a higher ground level that creates a divergence in the surface and subsurface flow, The

old alignment seems to prevent ormal drainage of this area toward the Chapman Lake via the polygon field. Questions remain: 1) is the higher elevation of the old alignment related to quasi-syngenetic permafrost aggradation and 2) are the ponds adjacent to the road still affected by thermal erosion?

The concordance between the three ponds with the most recent landslide strongly suggests that they drain off under the road and favor the thermal erosion of the underlying ground-ice.
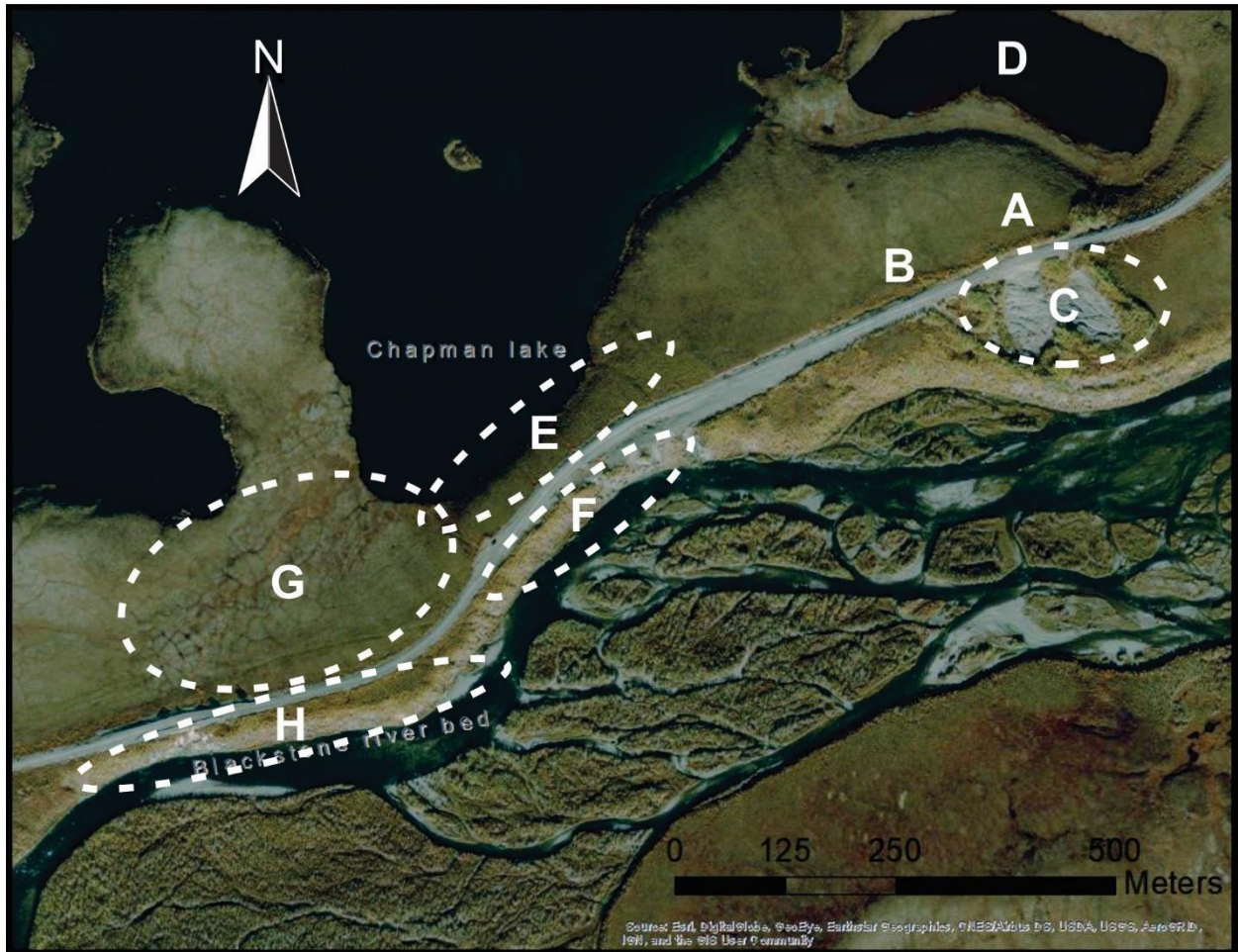
Figure 78 Localization of the eight discriminated zones of the topographical analysis.
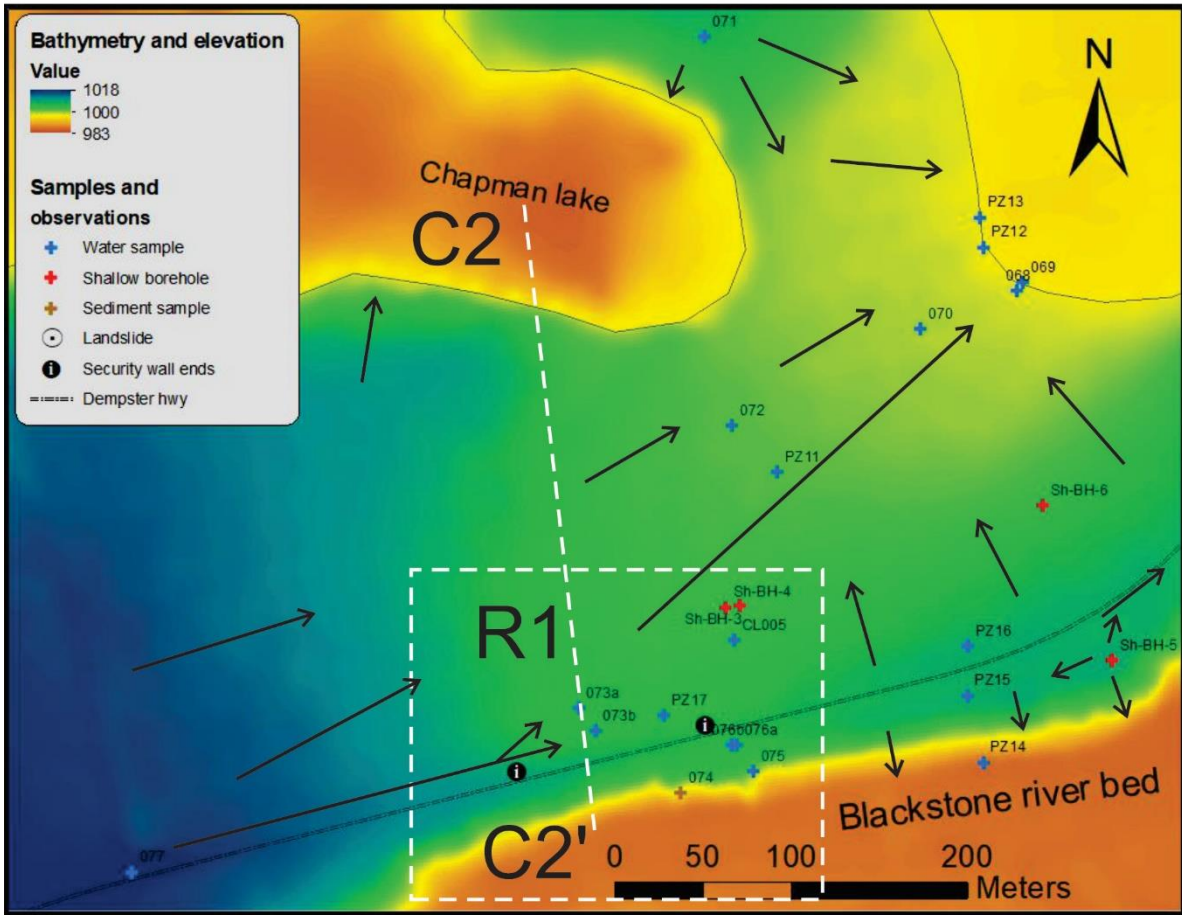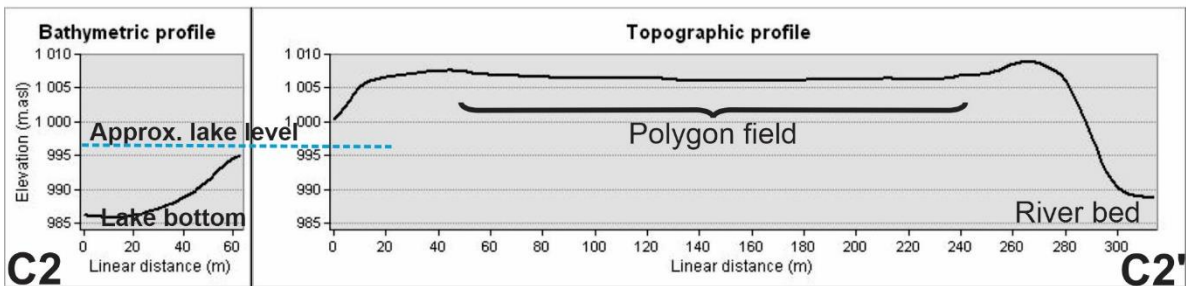
Figure 79 A) Surface water direction map of zones G and H (Polygon field and riverbank) printed on the elevation model from the Arctic DEM dataset and the bathymetric survey, B) Bathymetric and topographic profile C2-C2'. Note that R1 zoom windows refers to Figure 53 below.
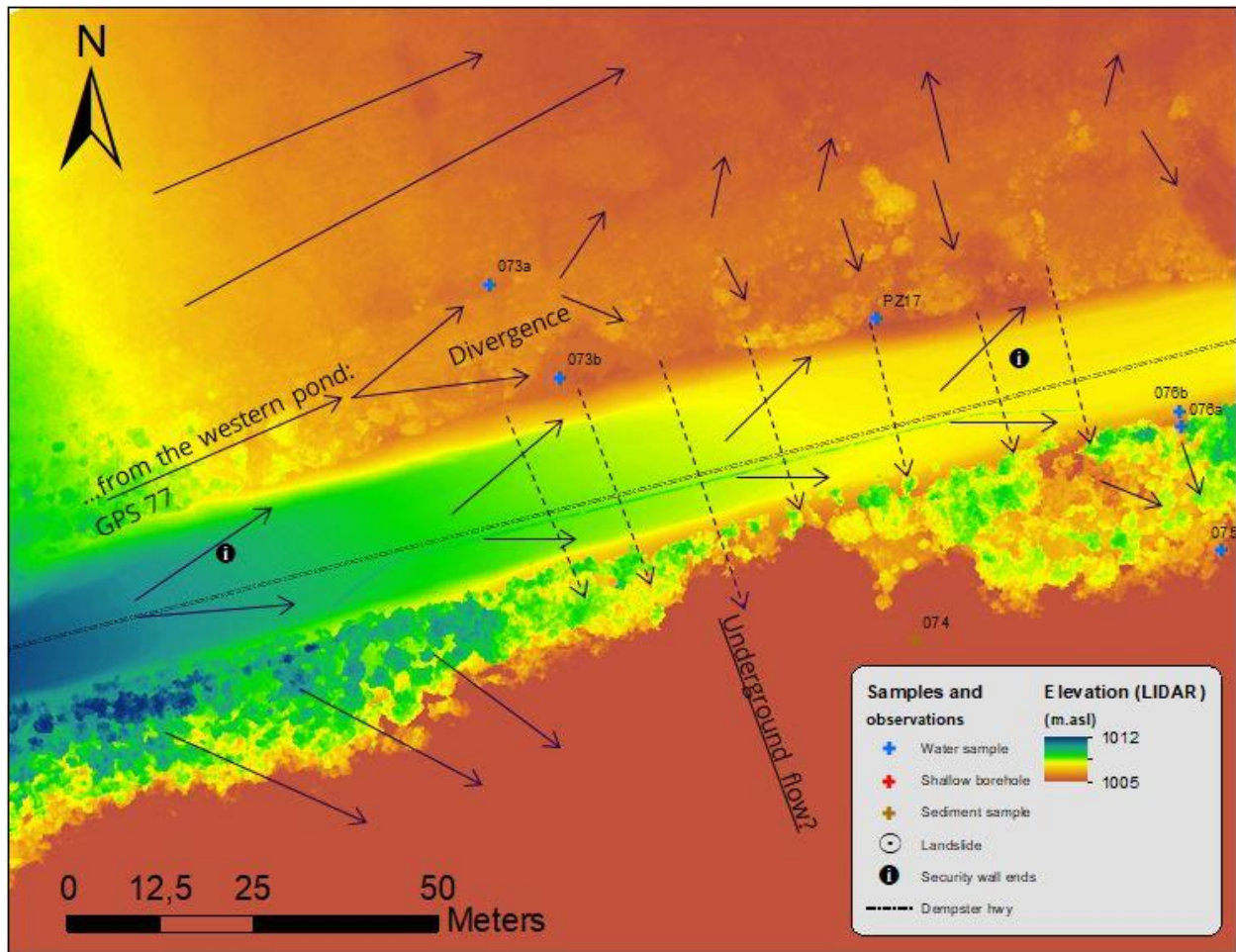
Figure 80 Surface water direction map of the zoom window R1 (see Figure 79) printed on the elevation model from the same source. Note the zone on the left-hand side of the road where the water pond, a good picture of this area is found in Figure 38.

Key points:

- The local landforms are typical of an ice-cored moraine and include slopes representative of kettle lakes
- The lowest point of the lake has a similar elevation to that of the riverbed
- The slopes separating the road from the lake are long enough to minimize the risk of a breach from forming in the landform by the permafrost table near the ground surface
- There are many areas where surface and subsurface water can infiltrate near the road, exit by the bluff, and contribute to permafrost degradation by heat advection along its path

131

- Surface water especially accumulates at some specific areas, most noticeably near the most recent landslide (2017) where three ponds persist on the left-hand side of the road (Figure 79B)
- Even without permafrost degradation, material oversaturation increases the potential for slope destabilization

The soil and permafrost table's cryostratigraphies are detailed in the Appendix 3.2.1- C. The details of the topographic analyses visible in the same appendix locate the sampling points. Measurements of grain-size distribution, organic matter content and XRD elemental identification were executed on a selection of representative samples. Briefly, the relevant observations out of this analysis and some interpretations follow.

The measurements of organic matter content and the visual assessment of the extracted soil and permafrost table support the widespread presence of cryoturbation features.

Massive ice was found at the bottom of most of the shallow boreholes (4/7) around 1.5 to 2.5 m-depth. The massive ice displayed the characteristics of wedge-ice including sub-vertical foliations, small air-bubbles, lots of sandy sediments and organic fragments.

The active layer thickness in wet areas was between 35 and 45 cm-deep while the only borehole in the upslope mesic location (Sh-BH-5) had a thicker active layer (60 cm). There was no massive ice at the bottom of this shallow borehole (209 cm).

Across the site the soil and permafrost table were composed mainly of organic matter (more or less decayed peat and organic fibers), silt and fine sand. The organic mat was generally thick (around 30 cm) but thinner in the upslope location (Sh-BH-5). Sparse rounded gravels and pebbles were found related to water tracks between the road and Chapman lake in the isthmus area (Sh-BH-1 and 7). Gravels, pebbles, and coarser sand are fond at the bottom of the upslope location (Sh-BH-5).

Aside from the massive ice, most of the ground ice found in the shallow boreholes included micro lenticular to reticulate cryostructures in the mineral sediments and invisible to visible pore ice in organic sediments. Ice veins (around 1 mm) and thicker lenses (less than 1 cm) were found in both. The contacts between layers were generally diffuse but some were very sharp at higher elevations and on the steepest slope (Sh-BH-5 and 6 respectively).

Key points:

- Throughout the site the soil and permafrost table were composed mainly of organic matter (more or less decayed peat and organic fibers), silt and fine sand

- Massive ice was found at the bottom of most of the shallow boreholes (4/7) around 1.5 to 2.5 m-depth. It displayed the characteristics of wedge-ice

- Aside from the massive ice, most of the ground ice found in the shallow boreholes was micro lenticular to reticulate cryostructures in the mineral sediments and invisible to visible pore ice in organic sediments. The permafrost is therefore ice-rich.

- The active layer thickness in wet areas was between 35 and 45 cm-deep while the only borehole in the upslope location (Sh-BH-5) had a thicker active layer (60 cm).

2.2.1.2.4.8. Properties of deep boreholes

The deep borehole, Bh-BI-2's properties are detailed in Appendix 3.2.1-D. Measurements of grain-size distribution, organic matter content, XRD elemental identification and crystallography were executed on a selection of representative samples. The deep borehole's property measurements resulted in some interesting observations.

The real-color pictures of the ice thin-sections show that in Chap1 and Chap2 (concordance with Bh-BI-1 and 2 respectively), the ice is mostly clear white with some pale brown sections due to the diffusion of fine sediments in cloud-like shapes. The ice is bubble-rich as small spherical bubbles are mostly evenly distributed while the bigger elongated bubbles are disposed in clusters. The cores extracted by the CREEL corer clearly display the inter-crystal bands of small bubbles that separate the relatively big polygonal crystals as seen in Figure 81A.

The polarized-light-filtered pictures show that all the cores have a network of small crystals at their periphery, which is an artifact of drilling (crushed ice). They all have been affected by ice metamorphosis related to drilling, frozen preservation and/or partial thawing. Big crystals with inter crystal bubble seams typical of glacier ice are still visible in some samples, mostly in the ones extracted by the CREEL corer, as seen in Figure 81B.

The drilling technique has strongly affected the massive ice's crystal structure. The cores extracted by the CREEL corer show the typical crystallography of glacier ice. Doubts remain about the hydrochemical contamination of the cores extracted by the sonic drill as surface water, rock abrasion and/or drilling fluids could have altered the chemical signature of the water extracted from the cores.

The organic matter content measured in the sediments above and below the buried ice is uniform. Doubts remain about the measurements of organic matter by lost-on-ignition due to the relatively high values, as 2 % in a moraine is unusual.

Key points:

- The cores show the typical glacier ice crystallography (buried glacier ice).

- Doubts remain about the hydrochemical analysis as there is possible contamination of the cores that were extracted by the sonic drill.
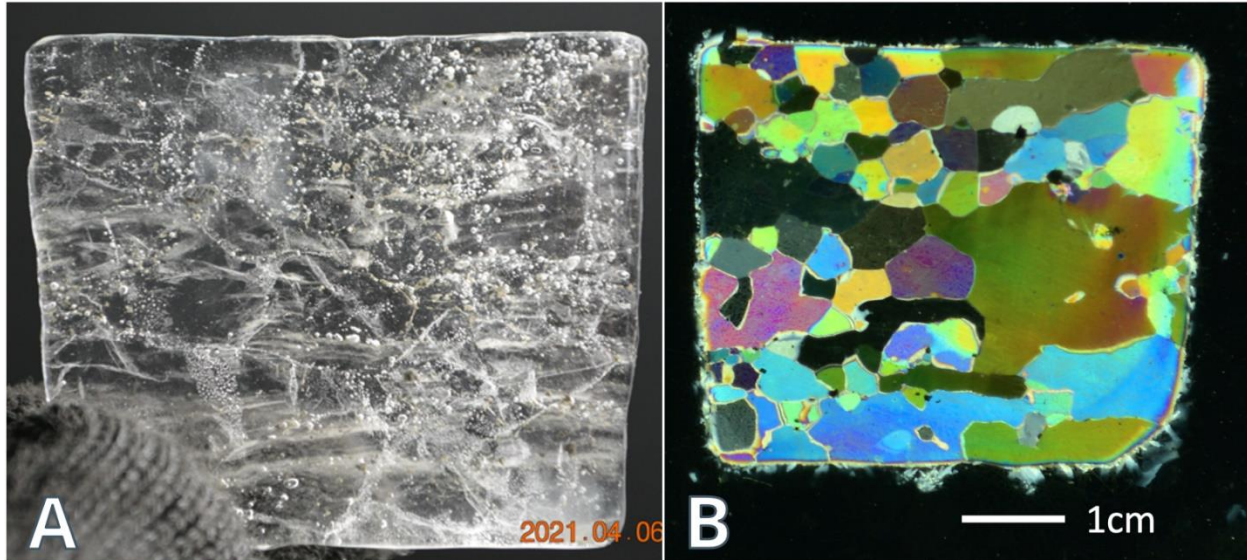
Figure 81 A) Vertical thin section of Chap2-75' CREEL seen under the natural light and B) polarized light.

2.2.1.2.4.9. Isotopic analysis

The results of the isotopic analysis are useful in a general manner for elaborating on the water connectivity among the various reservoirs at the site and informing on which water paths able to negatively affect the local landforms and road stability. The complete data are visible in Figure 82A, and the detailed method is given in the Appendix 3.2.1-E. Some isotopic analysis results are presented.

Snow, river and rain water roughly sit on the trendline as they were used to generate it. Lake water has a coherent isotopic signature that varies noticeably, and among all the samples shows the highest values of deuterium and O18, as well as the strongest negative deviation from the trendline. River water isotopic values vary very little and suggest that it is composed of about 1/3 snow and 2/3 rain water. Snow water has a coherent isotopic signature that varies noticeably, among all the samples it shows relatively low values of deuterium and among the lowest values of O18. Only one value was found for rainwater but it appears to have a useable isotopic signature.

The massive ice found in the deep boreholes have a coherent isotopic signature that varies noticeably, it has relatively low values of deuterium and O18, and it has a very strong negative deviation from the trendline much like the lake water does. The wedge/massive ice found in the shallow boreholes have the most extended range of isotopic values, all more negative than river water and expressing a larger negative deviation from the trendline when farther from the river isotopic signature. The lowest deuterium value of all relates to the ice-wedge at the bottom of the shallow borehole in the steep-side slope of the polygon field (Sh-BH-6), less than 2 m-deep. The ice wedge signatures have a steeper linear regression than the trendline that intercepts other values of massive ice and could be used to extrapolate the value of the rain.

All the soil water, from the active layer, water tracks or at the head of a basin, have an isotopic signature range that is relatively wide, but never close to snow or massive ice values and never higher than rain. Most of the soil water has higher values than the river water. Their deviation from the trendline is only slightly negative and not very variable. The water from ice-lenses in the permafrost table show an isotopic signature very similar to that of soil water but most of the lense water scores lower than the river. Their deviation from the trendline is negligable.

The water from the roadside is similar to the soil water, systematically higher values than the river, and showing an increasing negative deviation from the trendline when farther from the river values, similar to the values of the lake water. The water from the seepages down the bluff has an isotopic signature that is not very variable, it is has a deuterium content that is slightly more negative than the river, soil, lens and road water, and has a noticeably stronger negative deviation with the trendline. It could be a mix of roadside water and various type of ground ice. The Figure 82B shows fewer signals to better highlight the roadside and seepage water isotopic signatures.

The mixing of lake water is not likely due to the negative values that tend more toward the massive-ice isotopic signature. As shown from the topographic analysis, the source of the water must be from the roadside and/or the proximal soil. The lake water could still migrate below the permafrost since its thickness is estimated at 20 m, but no hazard should result from this ground water flow.

Key points:

- Natural soil water is slightly but significantly different from the roadside water.
- The water seeping out from the bluff appears to be a mix of roadside water and various type of massive ground ice (wedge and/or buried).

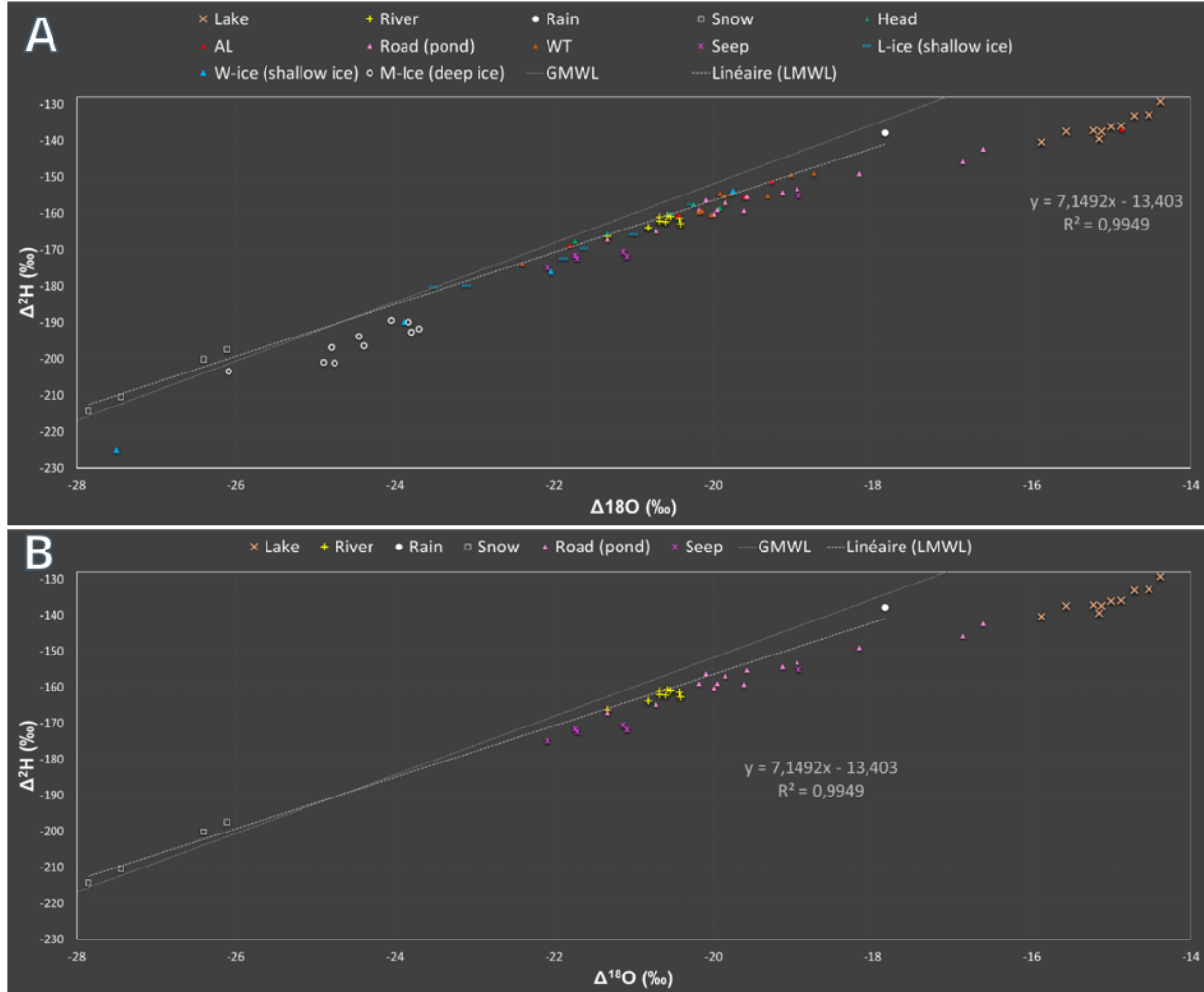- No isotopic signature from the lake water was detected in the water seeping from bluff.

Figure 82 A) Isotopic signature of every ice and water sample from the 2019 field campaign at the research site plot over the GMWL and the LMWL. B) Alleviated version to highlight the relative position of the values of the roadside and seepage water.

2.2.1.2.4.10. Hydro geochemical analysis

The results of the hydro geochemical analysis were limited to the major cations (Li, Na, k, Mg, Ca, NH4). They are also useful in a general manner for elaborating on the water connectivity among the various terrain units. The electrical conductivity and the pH are also measured and reported. The result should coarsely reflect the overall ionic content of the solution and its free hydrogen content. The detailed data and methods are given in the Appendix 3.2.1-F. The hydrochemistry results reinforce the interpretation from the isotopic analysis, as seen in the following observations.

The dilution water of sediments in the borehole drilled using the sonic drill was very concentrated (an order of magnitude higher) in every major cation but ammonium. These values were not included in the analysis; the high solute concentrations strongly suggest that something occurred during drilling. Two hypotheses follow: 1) drilling fluids or surface water was injected and diffused in the sediments' porosity; or 2) the vibrating-pushing action smashed the rock and allowed the release of fresh and easily dissolvable materials. Local surface water injection is not a preferred hypothesis due to the low ammonia content (NH4+) of the deep borehole sediments [d-bh]. No difference appears between the ice geochemistry drilled by both techniques (sonic and CREEL).

The lithium content remains very low everywhere, near the detection limit, but is noticeable in roadside, seepage and soil dilution water. The lithium in the water from the roadside and seepage is relatively concentrated. Higher sodium concentrations are found in the ice lenses, soil from the permafrost table and to a lesser degree in seepage water. Water from the bottom of the active layer shows a low but still significant amount of sodium. Potassium is mainly concentrated in the dilution water of the active layer and, in a minor proportion, the dilution water of the permafrost table, the ice lenses, seepage and roadside water.

Magnesium is especially concentrated in seepage and roadside water, and shallow permafrost table soil water dilution. It is also noticeable in the active layer water, in the ice lenses, in the river, lakes and water tracks. Calcium follows the same accumulation pattern as magnesium but with twice the concentration.

Most of the ammonia is in the permafrost table in the form of ice-lenses and in soil dilution water. Some wedge/massive ice in the bottom of shallow boreholes also show some ammonium accumulation.

Though few measurements were taken, the overall electrical conductivity is very high in the seepage water and relatively so in ice lenses and permafrost table dilution water.

Key points:

- The very high overall electrical conductivity of the seepage water is mostly due to meltwater from ice lenses within the permafrost table and dilution water from the surrounding soil.
- Ammonia is found in the permafrost table, soil and ice lenses but rarely in wedge ice, none is found in the deep borehole, meaning that the chemical inheritance of recent soil processes in the bottom of shallow boreholes is uncertain and some surficial ice wedge could be relatively old.
- All the metallic major cations (Li, Na, k, Mg and Ca) support that seepage water is partially sourced from the roadside as well as from the natural soil.

2.2.1.3. Synthesis

All the ERT surveys at km 116 show an ice wedge complex extending down to approximately 10 m in depth. These high-resistivity bodies have a nodule-shape signature pattern that is recognizable across all the ERT surveys. Some of these ice wedges were drilled and cored in Bh-IW-1 and Bh-IW-2.

Based on the observations of very high resistivity sections deep in the eastern profiles, HPW contracted geotechnical drilling to investigate and sample cores below 10 m in depth. The drilling of Bh-BI-1 and Bh-BI-2 showed that massive ice was present much deeper than 10 m. Massive ice starts at about 15-20 m in depth and may extend below 25 m in depth. Observations from both boreholes suggest that the thickness of this massive ice is at least 6 m in some places.

Digital elevation models (DEM) derived from unmanned aerial vehicle (UAV) imagery acquired in August 2021 were used to relate the borehole logs to the surrounding water bodies (Figure 83). The Blackstone River is at an average elevation of 987 m and the surface of Chapman Lake is at 997 m. The elevations of the borehole surfaces range from 1005 m to 1014 m from west to east. Therefore, the elevation of the deeper massive ice contact is almost below the water level in Chapman Lake (Figure 83). It is possible that some unfrozen soil sections reported in the ERT between the ice wedge complex and buried massive ice (approximately 997 and 993 m elevation) is attributable to underground water infiltration from the lake (Figure 84). Moreover, the DEMs show a slight relative elevation increase under the old road alignment just besides the thermokarst ponds. Permafrost re-aggradation could explain how the upstream water track diverged away from its normal course toward the lake by the polygon field and triggered thermokarst adjacent to the actual road.

Ground temperature records show that permafrost is relatively cold, below -2 °C, and therefore may be relatively resilient to an increase in air temperature over the next decades. However, climate changes are not limited to air temperatures but also include increased and warmer precipitation. This is especially problematic given the fact that rainwater has been shown to melt the ground ice, mix with melt water and seep down the bluff.

Overall, permafrost is very ice-rich, massive ground ice bodies are present, and there are possible pathways for ground water movement. The thaw of ice-rich permafrost and melt of massive ground ice bodies are responsible for the general subsidence observed all along this section of the road, as well as for the landslides along the cliff. Groundwater movements may also contribute to the general permafrost degradation in this area.

There are multiple possibilities for additional thaw based on various processes. For example, ice wedges could rapidly degrade if surface water was to initiate catastrophic ice wedge thermal erosion on the surface or at the shoulder of the bluff, where thermal erosion already occurs. Tunneling and gullying could quickly reach the ice-wedge network below the road and erode down to the local base level (Blackstone River at 987 m), which could be lower than the wedge ice level. Another possibility is the initiation of permafrost degradation from the bottom. Based on the permafrost depth seen in 2020 at borehole Bh-BI-2, it is possible that there is sub-permafrost groundwater flow, especially between the lake bottom and the riverbed where there might be a talik, based on the presence of multiple low resistivity areas below the ice wedges along the lakeshore ERT survey. In borehole Bh-BI-2, the relatively quick temperature changes under the permafrost reinforce the hypothesis of sub-permafrost groundwater flow. Despite the apparent top-down freeze back at the bottom of the borehole in 2021, it remains possible that this groundwater keeps flowing at a slightly greater depth and still contributes to the decay of the buried ice from below.

The combined thicknesses of upper wedge ice (up to 8 m) and of deeper massive ice bodies (>6 m) may exceed 14 m at some locations. The difference in elevation between the lake surface and the ground surface at Bh-BI1 is 14 m. Should the ice melt or be removed and underground water seepage occur, the possibility of the lake draining cannot be excluded. This confirms the need for ongoing monitoring at this site to prevent or anticipate such a catastrophic event.

More information is provided by isotope and hydrogeochemistry. In a general the roadside water isotopic signature tends to evolve with time toward that of the lake water, probably due to sustained evaporation and the absence of soil processes. Unlike for the soil water (including ice lenses from cryosuction), the seepage water has lower isotopic values than the river and shows a strong negative deviation from the trendline. These characteristics seem to link the seepages with: a) the roadside water and b) the glacier

ice that has been buried or ice wedges. However, the mixing of lake water in seepage water is not supported by the isotopic analysis.

Above the lake, another place represents a more direct hazard to the road. Water ponding on the left-hand side of the road near the most recent landslide is draining underground below the road and favoring further instability. It is unknown if ground ice occurs at this location but even without any, this sustained groundwater source has the effect of lowering the intergranular friction and favors plasticity and/or liquefaction (depending on the materials consistency indices). This can translate into road damage such as shoulder cracking, creep and deformation of embankment, and sinkholes if fine-grained sediments are removed by subsurface flow.

The combination of all these results confirms the need for ongoing monitoring at this site to prevent or anticipate a catastrophic road collapse from permafrost degradation enhanced by surface-to-ground water, and potentially magnified by lake drainage. The consideration of surface-to-ground water is paramount in the mitigation of the localized risk. The permafrost hydrogeomorphic assessment included here appears as a key component of the hazard assessment and monitoring at this site. It should be adapted and applied to other situations where water threatens permafrost stability.

Summary:

Issues

- Major subsidence is occurring along this section of the highway including multiple landslides in the slope between Chapman Lake and the Blackstone River.

Summary of Findings

- High resistivity areas extending to 10 m in depth in all ERT surveys are interpreted as an ice-wedge complex, as confirmed by the ice cored and identified in one such high-resistivity area.

- Massive ice is present at 14 m and 18 m in depth, and of at least 6 m in thickness.

- An unfrozen layer between ice wedges and buried ice found in the ERT surveys could sustain groundwater flow from the lake to the river.

- An unfrozen layer at the bottom of borehole Bh-BI-2 and a change in frozen interface elevation between years suggests that groundwater is flowing at this location.

- The thaw of ice-rich permafrost and massive ground ice bodies is responsible for subsidence and landslides in the area.

- Even without permafrost and ground ice, oversaturation of the unfrozen earth material near and in slopes (i.e., the scar of the landslides) can lead to sustained slope instability, and mass movements.

- Sediments from the landslides are deposited into and quickly eroded by the Blackstone River. Because of this erosion, the landslides cannot stabilize, and sliding is exacerbated.

- Groundwater flow contributes to permafrost degradation and furthers terrain deformations such as landslides, subsidence and potentially the formation of potholes and sinkholes.

- Surface and sub-surface water could initiate tunneling and gullying in the ice wedge network and mine down to the lake level, that could lead to a partial lake drainage to the river and a consequent road collapse

- The permafrost is cold (below -2°C) and may therefore be resilient in the face of rising air temperatures, but would likely not withstand large amounts of heat from more frequent and warmer precipitation and/or inappropriate drainage modifications

- Digging a ditch along the road to correct drainage could initiate gullying of the ice wedge network

- If significant ground ice melts and water seepage occurs in the area between Chapman Lake and the Blackstone River, severe ground instability and catastrophic drainage of the lake could occur.

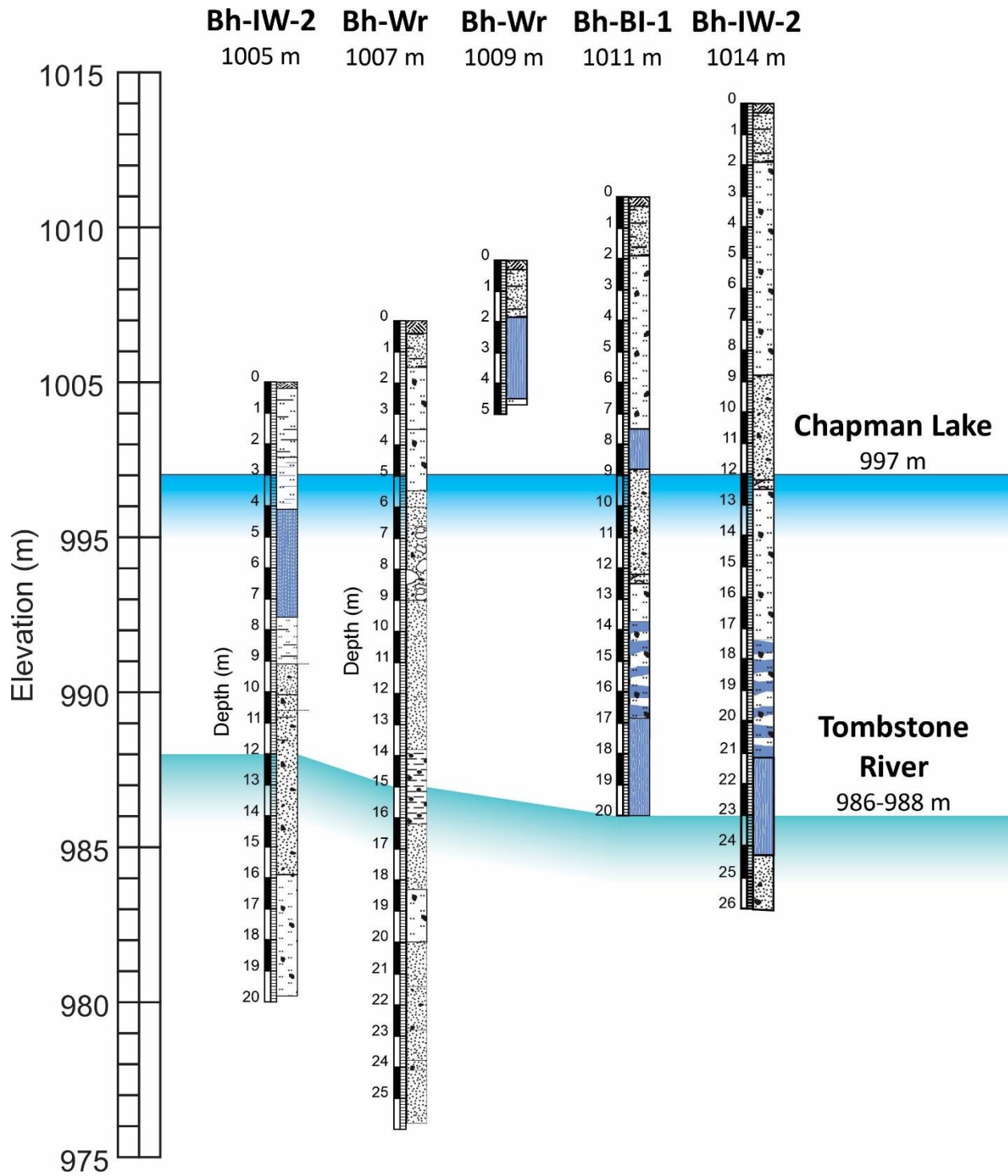- Ongoing monitoring of this area is recommended to prevent and anticipate such an event.

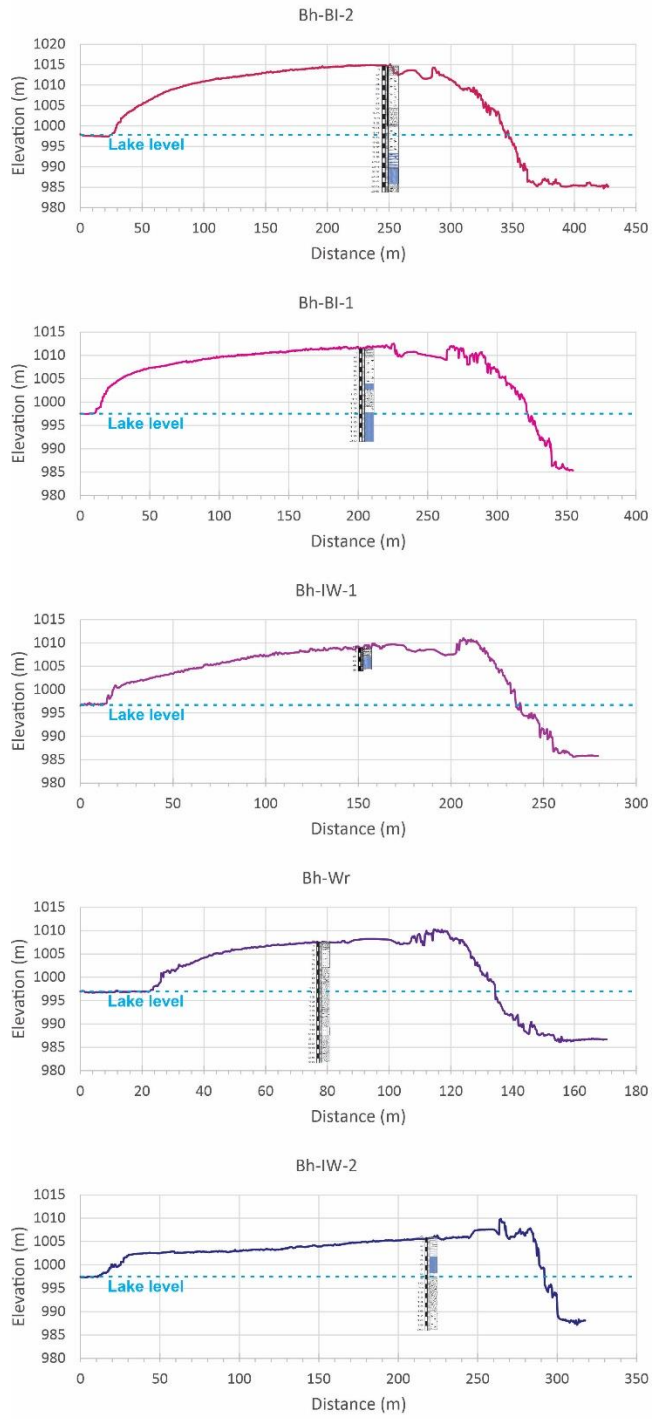**Figure 83** Bh-BI-1 borehole log compared to Blackstone River and Chapman Lake water levels.

Figure 84 Comparison between topography, borehole logs and the water-level of Chapman Lake

2.2.2. Alaska Highway study site: Takhini RTS (km 1456)

2.2.2.1. Introduction

The presence of an active retrogressive thaw slump (RTS) adjacent to the Alaska Highway at km 1456 was identified in April 2019 during a field study led in partnership with the Yukon Geological Survey (YGS). The slump developed on the hillslope along the shoreline of the Takhini River. Permafrost in this area is discontinuous and found in sporadic, isolated patches that can be significantly ice-rich and thaw-sensitive. This RTS is located 200 m west of another RTS that was initiated prior to 1979 and partially stabilized by 2004. Between these two features stands a wooded area showing signs of slope instability (collapsed trees, cracking) where a third RTS may soon develop (Figure 85).
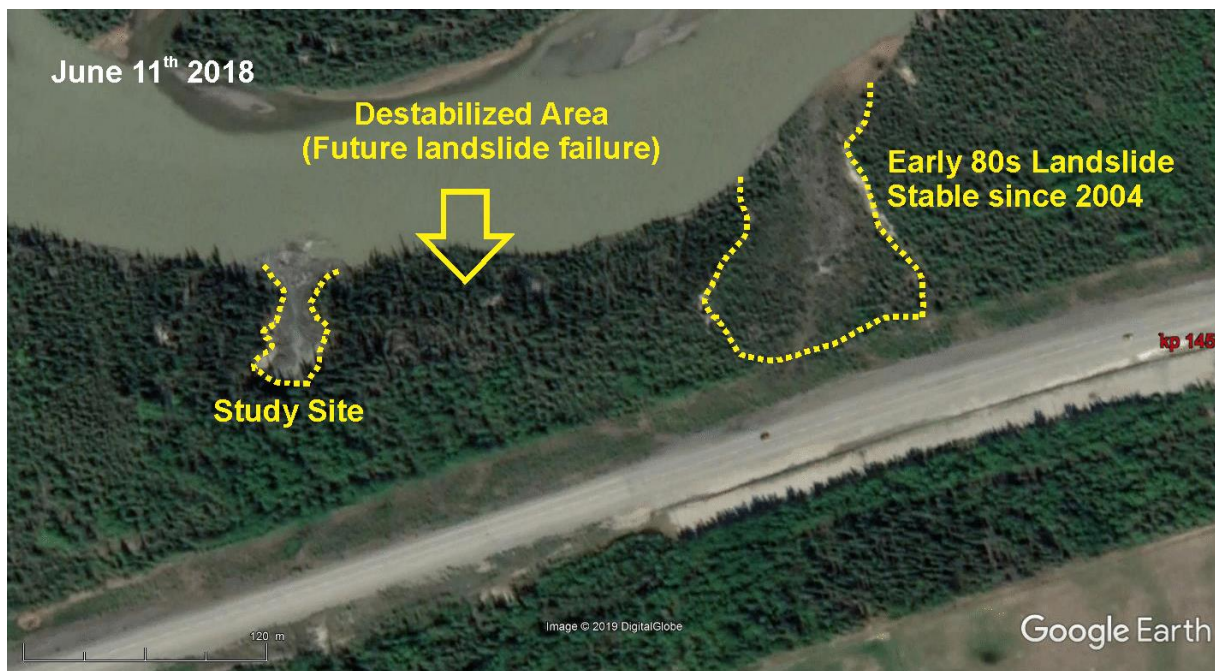
Figure 85 Study area at Km 1456 on the Alaska Highway.

When the site was first evaluated in May 2019, the 50 m wide and 5 m high RTS headwall provided an outstanding natural exposure of ice-rich permafrost with lenses up to 20 cm thick (Figure 86). At the time, the headwall was approximately 80 m away from the road embankment. A quick assessment estimated that the headwall has been retreating towards the highway at an average rate of 8 m/yr to its May 2019 position 81m from the highway embankment. Several multi-meter long tension cracks have formed between the RTS and the road, as close as 20 m from the road embankment.

Figure 86 A) View of the RTS; B) Headwall of the RTS exposing ice-rich permafrost; C- 10 cm thick ground ice lenses.

This was an alarming situation, but also one that presented an opportunity for climate change adaptation research, as well as outreach and engagement with Yukon transportation professionals, and Yukon University students. The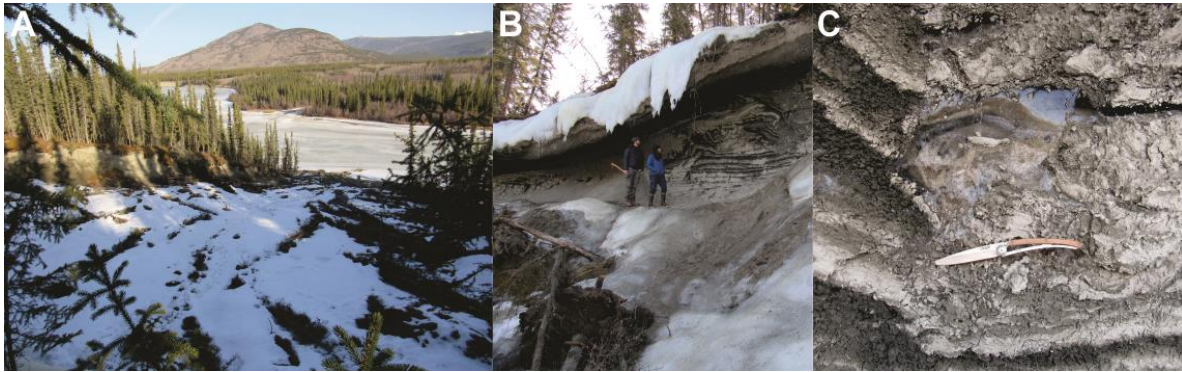 RTS has been active for six or seven years (initiated in either 2013 or 2014) based on an analysis of satellite and aerial imagery. According to aerial imagery, the 1979 RTS remained active for 25 years, suggesting that this RTS will likely continue expanding during the next several summers, with the potential risk of it eventually impacting the road. As a result, the research project "Assessment and monitoring of a new retrogressive thaw slump at km 1456 of the Alaska Highway: A rare opportunity" was designed and granted for funding by the Northern Transportation Adaption Initiation Program (NTAI) of Transport Canada.

The purpose of this study was to act before any serious damage occurred and take advantage of the site's location close to the city center to develop an intensive research program at a low cost. The objective was to develop an innovative research program around this RTS site that would:

- Develop a better understanding of retrogressive thaw slumps that impact road corridors in the North;
- Develop and test a multi-technical monitoring approach using complementary instrumentation for RTSs that to be used for the development of geohazard alarm systems;
- Inform an approach to mitigate the threat caused by RTSs on road corridors.
- Engage Yukon transportation professionals and Yukon University students in order to advance their understanding of the threats posed by RTSs; their lessons learned could then be applied to RTSs in more remote locations.

The study was completed in winter 2021, with final reporting in March 2021. The project report is provided as Appendix 3.2.2-A of this document. This section consists of an extended executive summary of the February 2021 report, updated, and improved with results of the summer/fall 2021surveys including UAV surveys, new borehole data, and a test of the alarm system on-site. The final part presents the concepts of a warning system intended to be implemented in spring 2022.

2.2.2.2.   Methods

In order to better understand the site dynamics, an extensive analysis was undertaken with many research activities carried out on site in 2019, 2020 and 2021, including:

- Drilling boreholes, from the RTS to the right of way, instrumented with ground temperature cables, soil moisture sensors, and inclinometer arrays to monitor ground parameters and RTS failure in real-time (2019 and 2020);
- Drilling boreholes, at the toe and at the top of the embankment, instrumenting one borehole with an alarm system prototype connected to ground temperature cables, and the other borehole with temporary ground temperature loggers (2021);
- Analyzing borehole samples for grain size distribution and excess ice content (2019 and 2020);
- Monitoring ground surface movement with differential GPS (DGPS) measurements tying in with benchmarks and existing legal survey pins and establishing surface survey monuments (2019, 2020, and 2021);
- Imaging and topography monitoring using unmanned aerial vehicle (UAV) photogrammetry (2019, 2020, and 2021);
- Imaging groundwater springs using UAV thermal imaging (2021);
- Two-dimensional Electrical Resistivity Tomography (ERT) surveying (2019 and 2020);
- Testing a new geophysical approach using 3D ERT and 3D electromagnetic (EM) surveys to map permafrost properties and ground water movements (2020);
- Mapping and monitoring the propagation of tension cracks and other ground movement markers as precursory indicators of failure (2019, 2020, and 2021).

The study addresses key knowledge gaps related to the mapping of RTS formation and evolution processes, as well as other methodological gaps in the monitoring of such geohazards. To develop a better understanding of RTS processes, the study focuses on four parameters:

- Frozen soil properties, which provide geotechnical information such as thaw sensitivity and potential consolidation;
- Ground thermal regime, which provides information such as ground temperature, active layer thickness, thaw rates and indications of water movement;
- Ground water dynamics, which provides links between ground moisture, environmental conditions and the timing and rate of the failure;
- Ground movements, which provide information on the rate of deformation as well as the slump's changing position in three dimensions.

The project monitored these parameters in real-time through the implementation of an array of sensors located in 2 boreholes instrumented with ground temperature cables, soil moisture sensors, and inclinometer arrays. One 20-25 m borehole (BH2) was drilled in the right of way (ROW), about 50 m from the location of the RTS headwall at the time of the drilling, to monitor failure indicators at a distance from the RTS over multiple years. This will provide long-term indicators of instability at depth. This monitoring station could be upgraded with warning and alarm systems in the future as part of a safety plan for monitoring the instability as it progresses towards the highway. A second, 6 m borehole (BH3) was located close to the RTS (5-6 m from the headwall) to monitor the parameters during RTS failure. This borehole was checked regularly to recover the instruments when the RTS headwall retreated to the location of the borehole.

Electro-resistivity tomography (ERT) surveys were conducted to complement borehole observations, characterize ice-rich permafrost thickness, distribution, and boundaries, as well as to identify ground water movements. An innovative approach was developed, combining 3-dimensional ERT and Electro-magnetic (EM) surveys.

DGPS monitoring of an array of benchmarks, matched with UAV imagery monitoring provided a complete assessment of ground surface movement that can be integrated with geophysical and borehole data to provide a complete 3D representation of the RTS development, integrated in a geo-database.

2.2.2.3. Results

2.2.2.3.1. Monitoring of the movements of the slump

From May 2019 to November 2021, the RTS was monitored monthly by the YukonU research team using a DJI Phantom 4 Pro V2 in 2019 and a DJI Matrice 210 RTK V2 in 2020

and 2021. An aerial imagery comparison of the slump from May 2019 to November 2021 is seen in Figure 87.

This drone imagery was complemented with satellite imagery and LiDAR data collected prior to 2019 to extend the period of monitoring to 2016. The result of this aerial imagery monitoring of the RTS is presented in Figure 88 and Table 14. For this 5-year period (with September 28, 2016 image serving as initial point of Summer 2017), the headwall of the slum progressed by 70 m between September 2016 and November 2021, an average of 14 m/year in those five consecutive summers. The headwall progressed by 24.9 m in the 2017-2018 period (avg. 12.5 m/yr), by 12.1 m in 2019, by 12.9 m in 2020, and by 19.3 m in 2021. The headwall retreated about 49.6% faster in 2021 compared to 2020, and 51.3% faster compared to the previous 4-year period.

The rapid erosion of the headwall in 2021 could be related to extraordinary weather events that occurred during summer 2020 and 2021. Whitehorse had its ninth-rainiest summer in the weather records in 2020, with 157.8 mm. Because of inertia in the system, the impact of this significant input of heat may only have been felt during summer 2021. In the summer 2021 the "heat dome", a mass of hot air sitting over the Pacific northwest, occurred in June and July which resulted in warmer than average temperatures in the Yukon territory, and could also have contributed to rapid erosion.

The evolution of the RTS headwall during the summer and fall 2021 can be seen in Figure 89. In September, a new retrogressive thaw slump has developed east of the main slump (Figure 89). This new feature will be monitored following the same protocol as the large slump in the coming year.
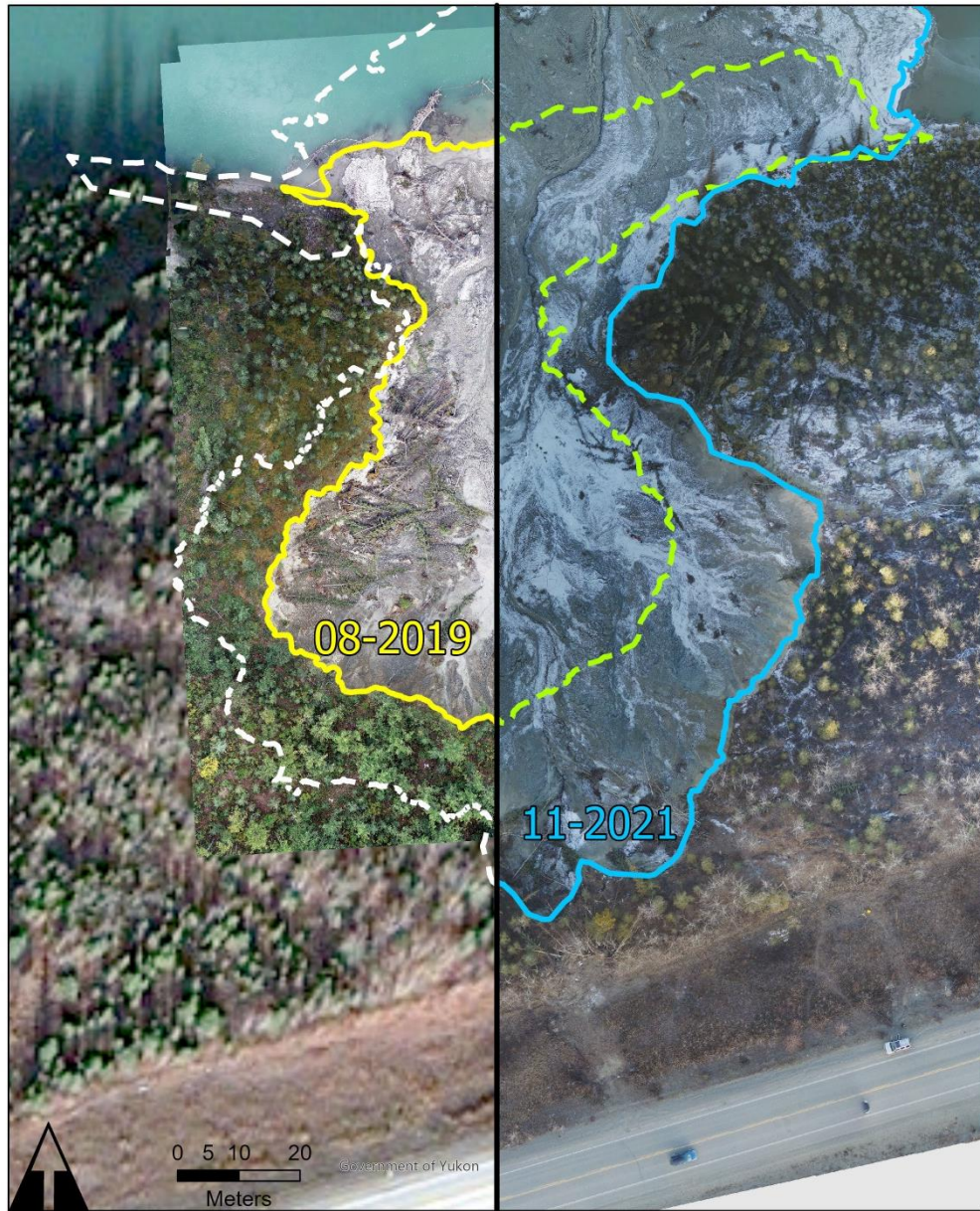
150

Figure 87 Split image comparison of the Tahkini RTS from the first drone survey in May 2019 to the latest one in November 2021.
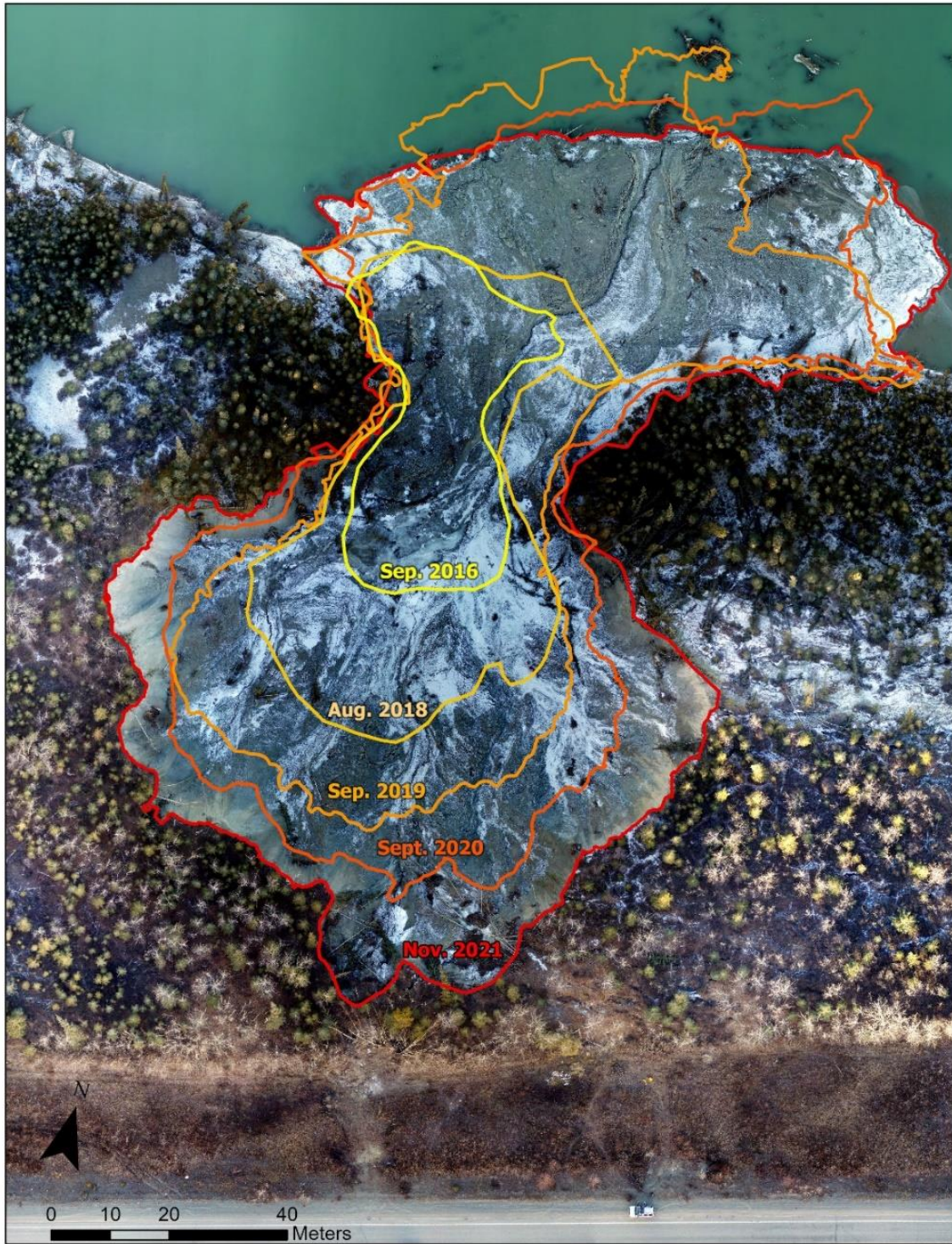
Figure 88 Movement of the Takhini RTS since 2016 using satellite and aerial imagery.

152

Table 14 Takhini RTS evolution from 2016 to 2021.

| DATE	Distance to road (m)	Length (m)	Width (m)
September 28, 2016	105.8	53.5	27.3
August 18, 2018	80.9	78	41.2
May 16, 2019	80.9	78	52.6
August 22, 2019	71.8	88.7	63.7
September 11, 2019	69.7	91.8	63.7
September 25, 2019	68	93	65.3
October 30, 2019	68.8	93	65.3
May 20, 2020	68	93	65.4
August 26, 2020	57.5	102.2	74.8
September 29, 2020	55.1	102.8	78.5
May 6, 2021	55.1	107.5	78.5
June 4, 2021	53	107.5	83.2
July 6, 2021	53	107.5	88.8
July 30, 2021	47	116.7	96.2
August 31, 2021	39.5	122.1	100.7
October 7, 2021	39.3	122.3	103.7
November 3, 2021	35.8	125.8	103.8
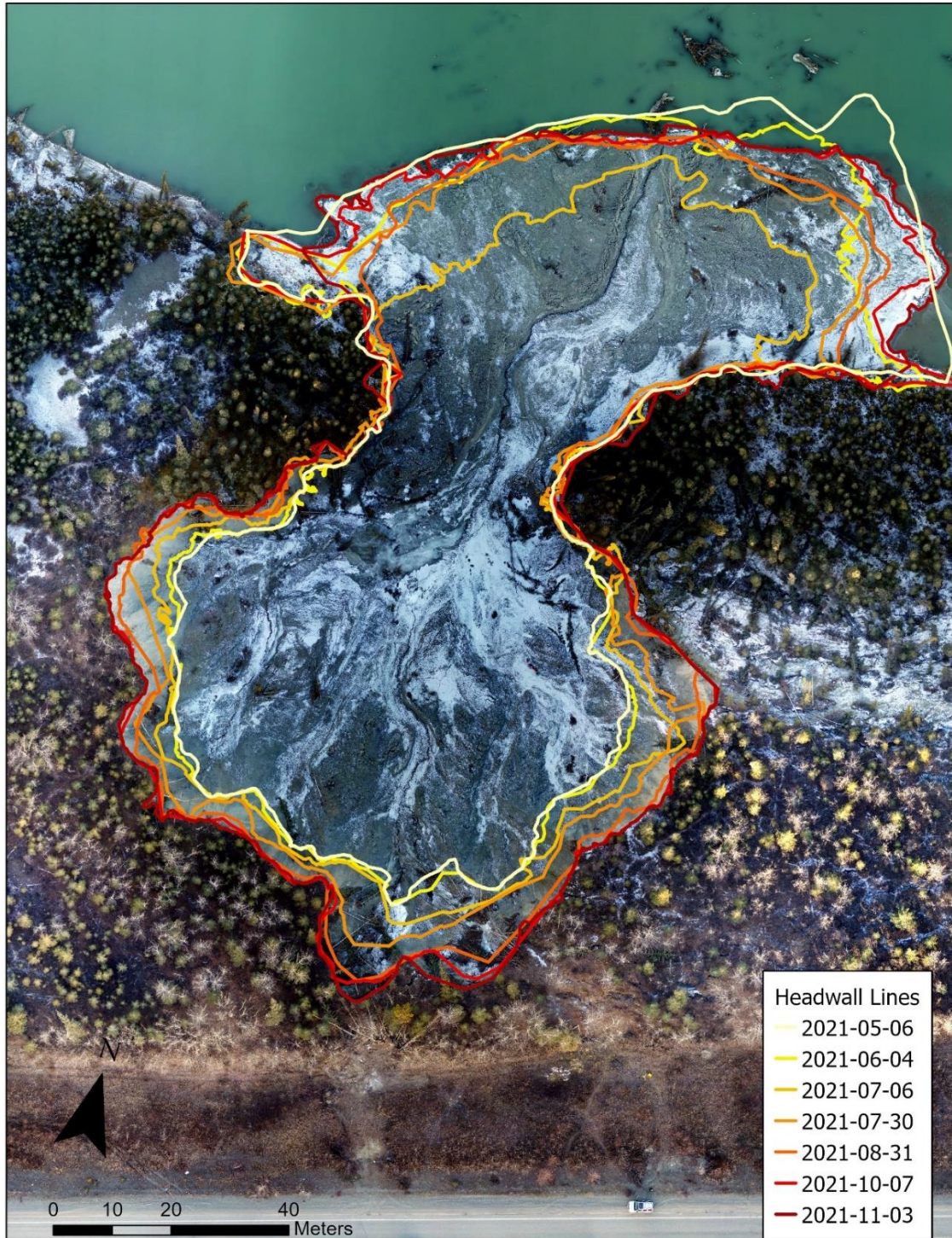
Figure 89 Movements of the Takhini RTS during the summer and fall 2021 using UAV aerial imagery.
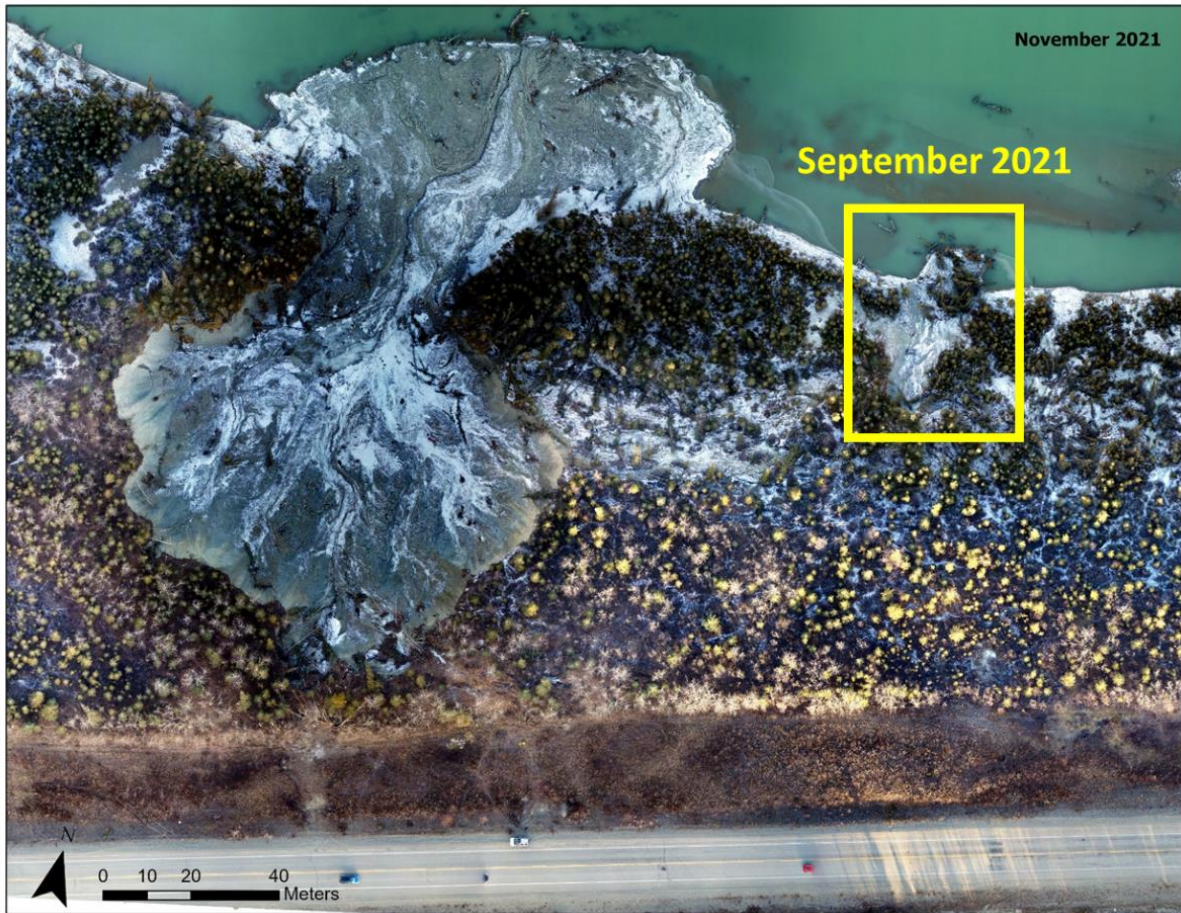
154

Figure 90 New retrogressive thaw slump forming east of the main RTS.

2.2.2.3.2. Monitoring of the movements of the surface benchmarks

Beginning in 2019, 33 rebar survey monuments (benchmarks) have been surveyed at least once a month, with the exception of June 2020, which is missing. These surveys offer an overview of ground creep occurring around the slump over a 3-summer period. The location of the benchmarks and movements during the 2019-2021 period can be seen in Figure 91. Some benchmarks have been eroded by the slump throughout the slumping period. In general, movement appears to be more intense on the east side of the monitored area. The yearly movements for each benchmark are compiled in Figure 92. Most of the benchmarks have moved less than 50 cm over the last three years, but a few have moved by a meter or more, and been lost to the slump. Figure 93 shows the movement of the two benchmarks that are highlighted in Figure 91, between 2019 and 2021. M30, on top, shows constant movement throughout this period for a total of. M22, on the bottom, shows similarly constant movement until August 2021, when the area

155

began to slump, and the benchmark was eroded. It is possible that the M30 area will follow the same trend as M22.

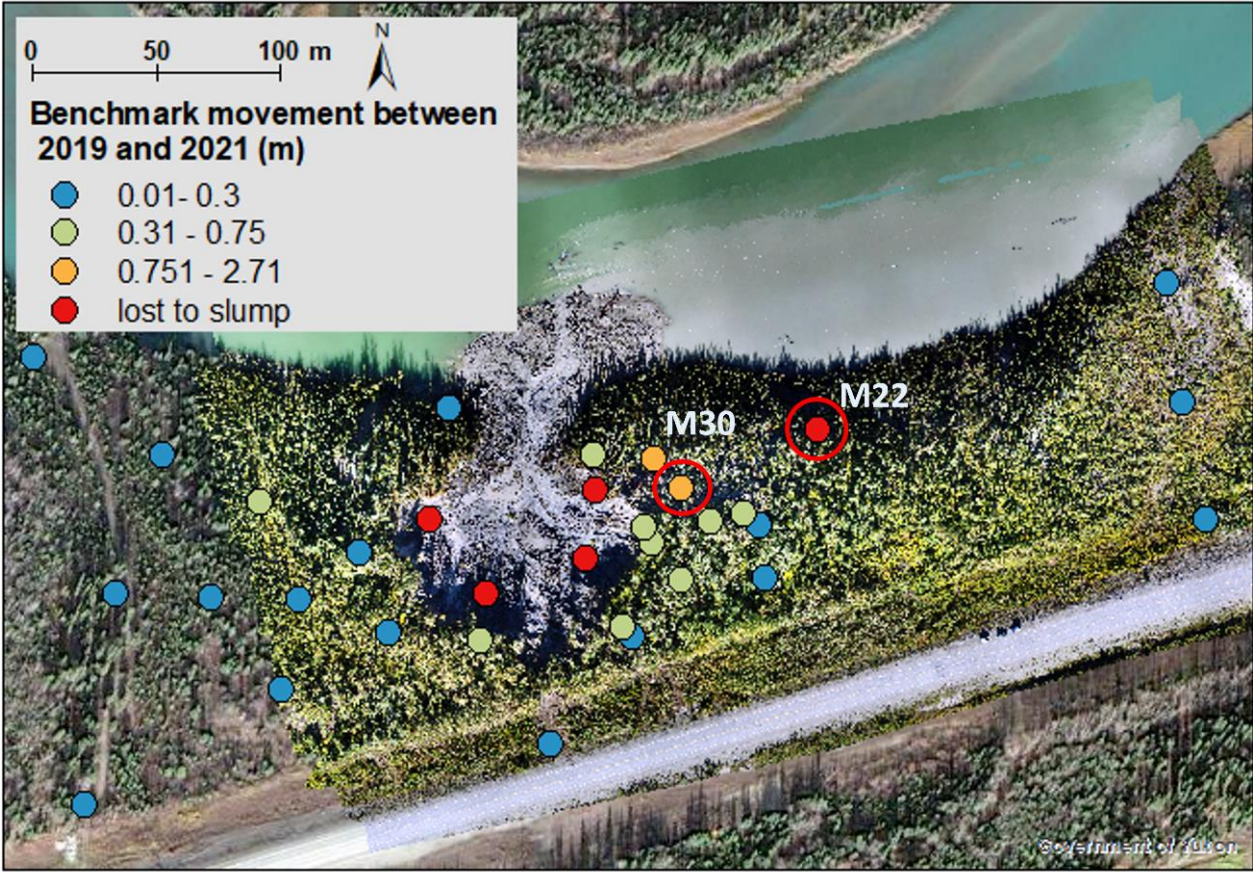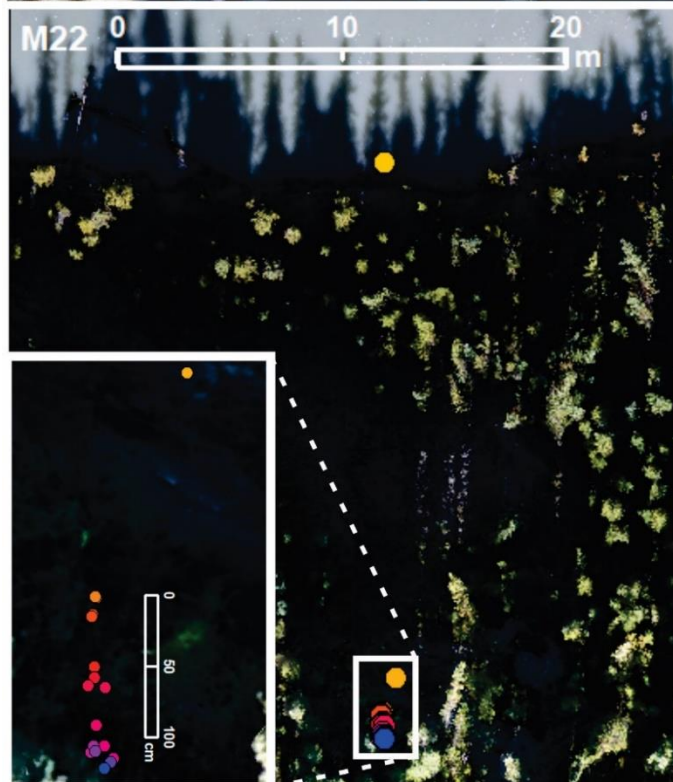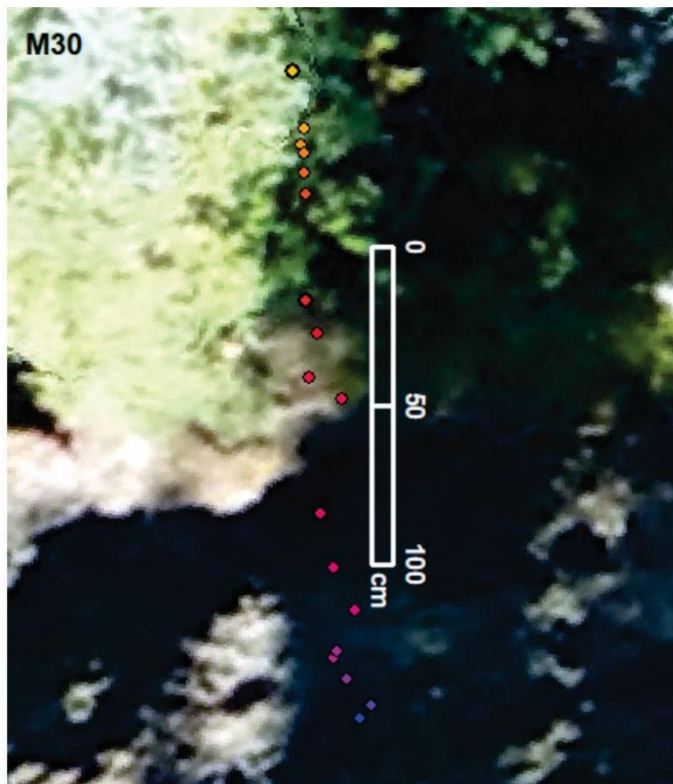**Figure 91** Benchmark movement between 2019 and 202, with the M30 and M22 benchmarks highlighted.

Figure 92 Annual benchmark movement at Takhini RTS

Figure 93 Movement of benchmark M30 (top) and M22 (bottom) from May 2019 to October 2021.

2.2.2.3.3. Analysis of the volume of soil lost to slumping

Using UAV photogrammetry, it was possible to create digital elevation models (DEM) from the aerial imagery of the Takhini RTS. When compared over time, these DEMs can be used to calculate the volume of sediment that is eroded by the slumping processes into the Takhini River. The estimated volume of eroded sediment from 2019 to 2021 are presented in Table 15. Approximately 17,024 m³ was eroded in the five years leading up to 2019; 9,497 m³ in 2019-2020, and 15,252 m³ in 2020-2021, with a potential error of 3% for all volumes. The total volume lost is equivalent to the volume of over 16 olympic-sized pools (2500 m³). These results emphasize the increasing amount of sediment that has flowed into the river as the headwall retreats over time. The change in elevation resulting from the development of the RTS was also calculated and can be visualized in Figure 94.

Table 15 Volume of lost soil at the Takhini RTS.

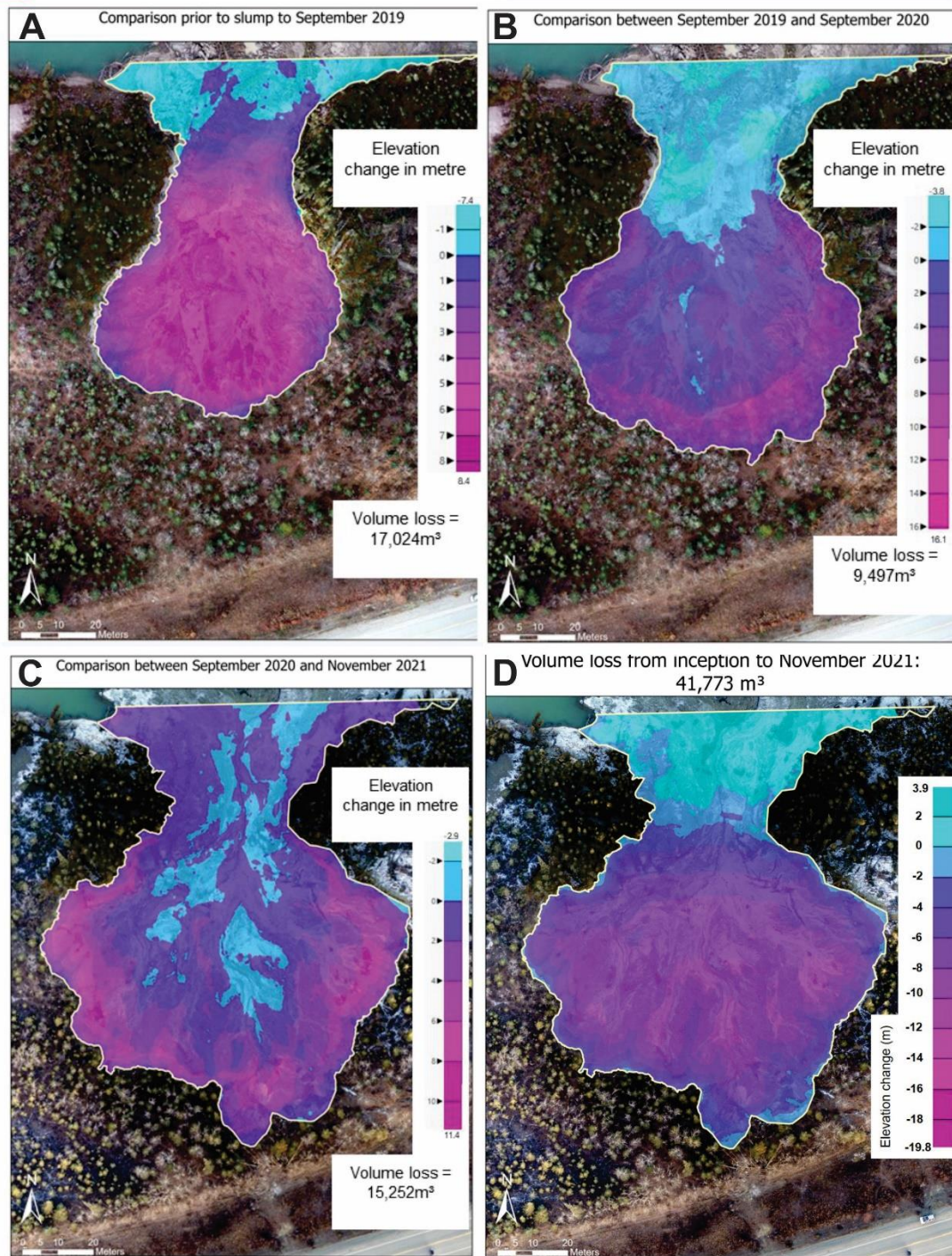| Date	Volume	Equivalent
Prior to slump until Sept. 2019	17,024m³	6.8 swimming pools
Sept. 2019 to Sept. 2020	9,497m³	3.8 swimming pools
Sept. 2020 to Nov. 2021	15,252m³	6 swimming pools
Total	41,773m³	16.6 swimming pools

Figure 94 Change in elevation derived from UAV photogrammetry as the Takhini RTS develops. A) Prior to slump until Sept. 2019; B) Sept. 2019 to Sept. 2020; C) Sept. 2020 to Nov. 2021; and D) total.

2.2.2.3.4. Borehole and geophysical data

2.2.2.3.4.1. Results from 2019 and 2020 surveys

The geotechnical boreholes and ERT data collected in 2019 and 2020 are consistent in defining the top and thickness of permafrost (2-3 m depth). The cores collected on site show the presence of clayey silts, which are frost susceptible, down to at least 25 meters in depth. The recorded temperature data suggest that the permafrost is warm, close to 0°C, and therefore vulnerable to thaw. The geophysical and geotechnical data showed thick, ice-rich permafrost at the headwall of the thaw slump and more sporadic clusters of ice-rich permafrost closer to the road. This could be explained by decades of permafrost degradation under the right of way of the Alaska Highway since its construction in 1942. However, the ERT data suggest that permafrost could still be present on the southern side of the highway.

Current warm ground temperatures (just below 0°C) and the distribution of ice rich permafrost in clusters (observed in the ERT surveys) seem to indicate that the permafrost may have formed in an environment that was colder and wetter than the one prevailing today. Moreover, the cryostratigraphical observations from the core samples and the headwall are consistent with syngenetic permafrost. The formation of this type of ground ice requires ample water supply, a slow thermal gradient, and typically, an organic cover. This type of permafrost is generally associated with permafrost plateaus and frost heave mound environments (Calmels et al, 2008). Such conditions may have existed in the Takhini Valley when the permafrost developed. Although the vegetation and the topography have changed, the original cryostratigraphical imprint, shown by the ERT and EM surveys in the form of ice-rich ground clusters, has remained unchanged. Shade provided by the newer deciduous forest may have contributed to the preservation of this relic permafrost. Therefore, the site might be underlain by relic permafrost that is precariously in balance with the current climate.

Figure 95 shows the approximate ground ice distribution based on the ERT profiles. The location of the ice suggests that the study site is vulnerable to further degradation even near the road. It is of note that the location of the inactive slump shows no ground ice, which could explain why this slump stabilized, or alternatively, that any ice present at that location has already melted out with the slump.

Figure 95 Approximate position of ground ice based on ERT profiles.

2.2.2.3.4.2. Results from 2021 surveys

Geophysical surveys suggested that permafrost and ground ice could be present in the right of way. To investigate this eventuality, YukonU and YHPW contracted a drilling company to assess ground conditions along the embankment.

The location of the boreholes was determined based on pockets of high resistivity from the 2019 ERT surveys, which suggest the presence of massive ground ice. The fourteen potential drilling locations, named from A to L, are presented in Figure 96. Seven were located on the LHS (A, B, C, D, E, K, L) including two near the fringe of the ROW (K and L), and five at the RHS (F to J). Figure 97 shows the location of the eight boreholes that were drilled.
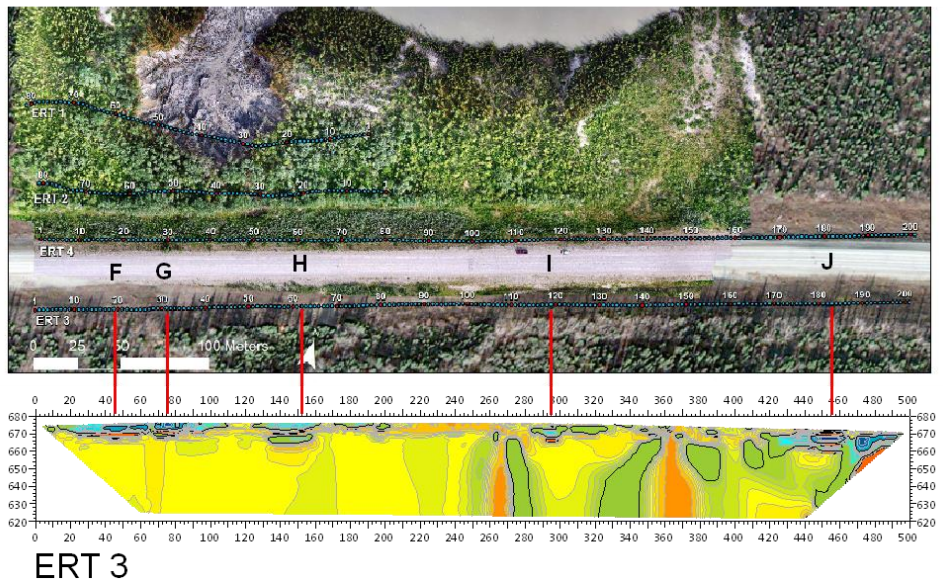
162
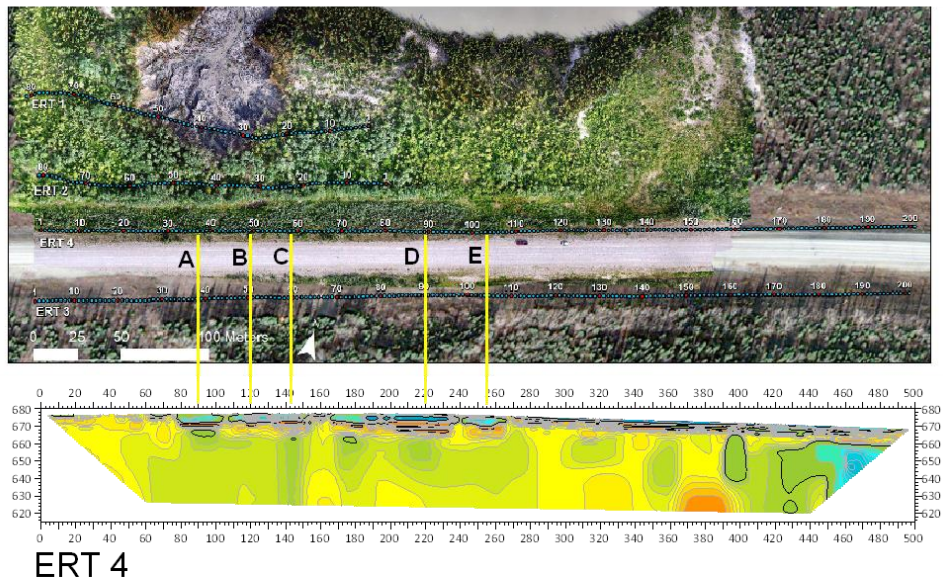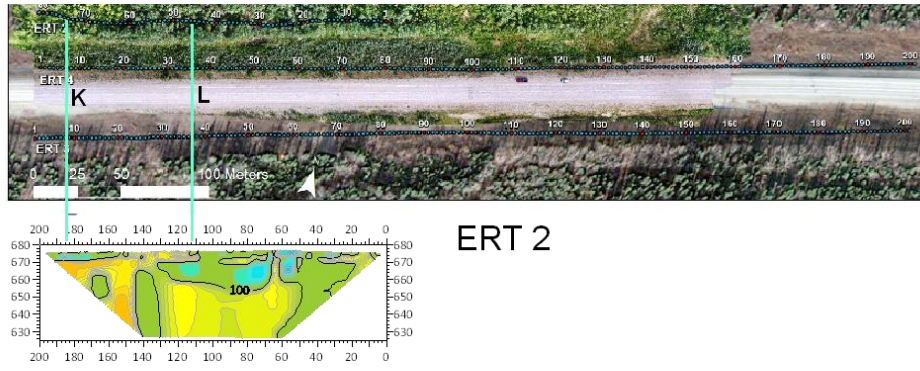
Figure 96 Selection of the borehole locations based on ERT surveys.

Figure 97 Locations of the boreholes drilled in July and September 2021.

The boreholes were drilled using a Direct Push Technology (DPT) system with a 3" core barrel (Figure 98). Once the drilling operation finished, all boreholes were cased with a 1-inch PVC conduit. Five boreholes were drilled on the RHS (slump side): A and C at the toe of the embankment down to 14 m depth each, K at the top of the embankment down to 9.3 m depth, and K' and L at the outer boundary of the ROW down to 14 m and 18 m respectively. Three boreholes were drilled on the LHS (farmland side): G and H at the toe of the embankment down to 14 m depth each, and J at the top of the embankment down to 14 m depth. Five boreholes were drilled under the YukonU team's supervision (A, C, G, H and J). The logs and some cores from these 5 boreholes are presented from Figure 99 to Figure 108. Because the drilling process has the potential to thaw warm, ice poor permafrost cores, the sampling was inconclusive regarding of the presence of permafrost, except for borehole J where a 60 cm thick massive ice layer was cored, followed by ice rich ground from 11 m to 12.2 m (Figure 107 and Figure 108). Regarding the other boreholes, the observed cryostructure could have been drilling artefacts.

164

Figure 98 Borehole drilling at Takhini RTS site using Direct Push Technology (DPT) system.

Figure 99 Log of borehole A.

Borehole A

Bh A: 10-10.4 m

Bh A: 12.8-13.10 m

Figure 100 Cores from borehole A.
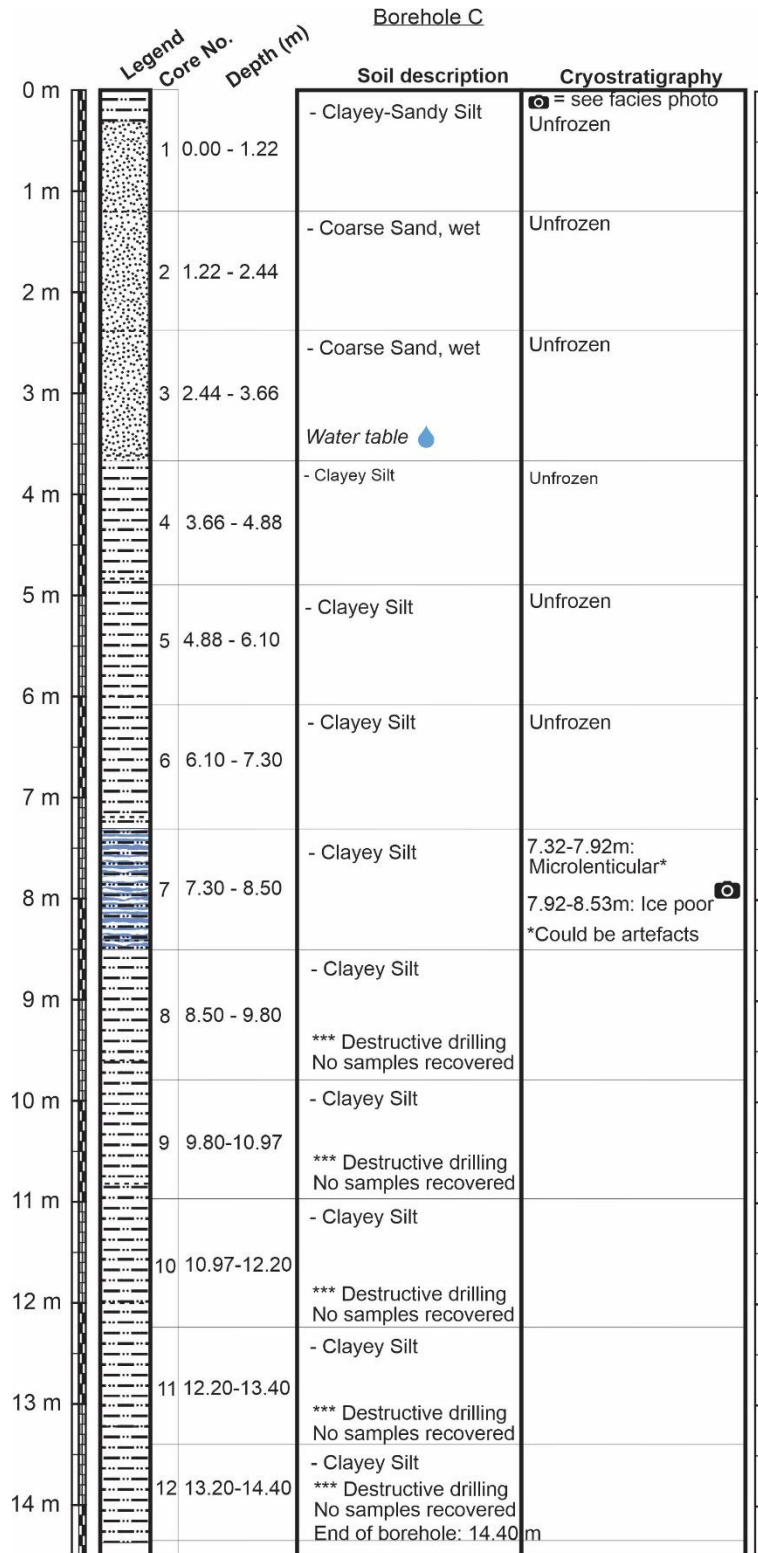
Figure 101 Log of borehole C.

168

Borehole C

Bh C: 7.9-8.2 m

Bh C: 8.5-8.8 m

Figure 102 Cores from borehole C.

Borehole G

Legend	Core No.	Depth (m)	Soil description	Cryostratigraphy
	1	0.00 - 1.22	- Coarse Sand, dry	📷 = see facies photo Unfrozen
	2	1.22 - 2.44	- Coarse Sand * humid at base	Unfrozen
	3	2.44 - 3.66	- Coarse Sand, wet *Water table* 💧	Unfrozen
	4	3.66 - 4.88	- Clayey Silt	Microlenses observed at base of sample *.
	5	4.88 - 6.10	- Clayey Silt - Possibly frozen	No visible ice. Ice poor.
	6	6.10 - 7.30	- Clayey Silt	Microlenticular*
	7	7.30 - 8.50	- Clayey Silt	Microlenticular*. - more ice rich at top
	8	8.50 - 9.80	- Clayey Silt	Microlenticular* 📷
	9	9.80-10.97	- Clayey Silt	Microlenticular* 📷
	10	10.97-12.20	- Clayey Silt	Microlenticular*
	11	12.20-13.40	- Clayey Silt	Microlenticular*
	12	13.20-14.40	- Clayey Silt End of borehole: 14.40 m	Microlenticular*

* The cryostructures observed during our analyses could be related to the deformation of the sample during the drilling process. The ice lenses could then be an artifact formed between the time the samples were placed in our freezers for storage and the moment we did our analyses.

Figure 103 Log of borehole G.

Borehole G

Bh G: 9.75-10 m

Bh G: 10.65-11 m

Figure 104 Cores form borehole G**.**

Figure 105 Log of borehole H.

Borehole H

Bh H: 7.6-7.9 m

Figure 106 Cores from borehole H.

Figure 107 Log of borehole J.

Borehole J

Bh J: 11-12.2 m Pure ice core encountered between 11.60 -12.20 m

Bh J: 1-12.2 m Enlarge picture of the pure ice core encountered between 11.60 -12.20 m.

Figure 108 Cores from borehole J.

To determine whether permafrost is present where no ground ice was observed, seven boreholes were instrumented with a temporary temperature sensor array for a few days to assess the ground temperature conditions, while the eighth borehole, A, was instrumented with a prototype Lo-Ra system logger. All boreholes, except, J, appear to be unfrozen as seen in Figure 109. The temperatures in the boreholes vary, with some (A,F, G,L) showing temperatures close to those of permafrost. The temperatures in borehole J are just barely below 0°C, suggesting precarious permafrost.
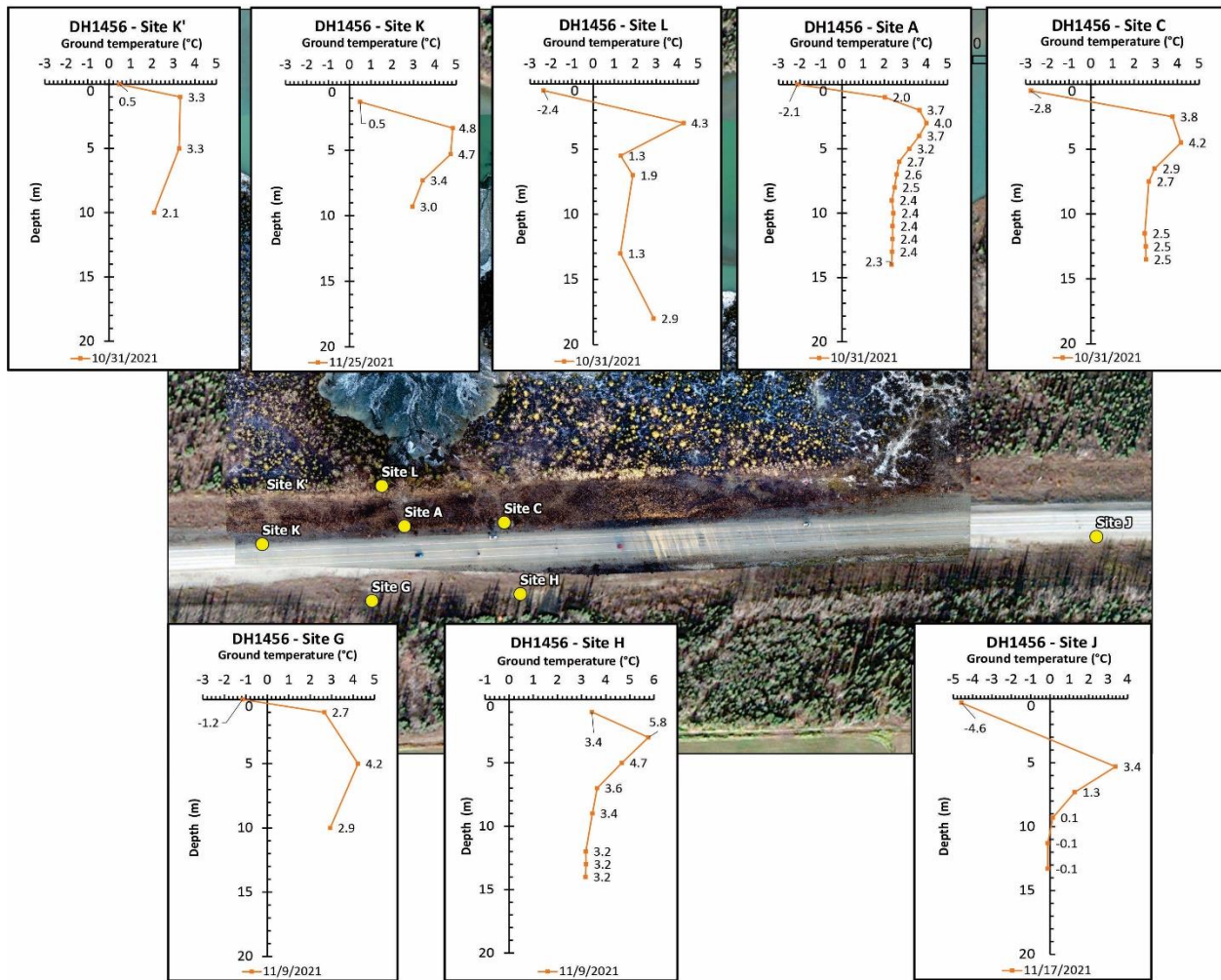
Figure 109 Ground temperature record in the ROW borehole at the Takhini RTS site.

176

2.2.2.4. Groundwater consideration

Groundwater can be seen seeping from the headwall of the slump (Figure 110). Geophysical and borehole data emphasize the ice-rich nature of the ground at this site, as well as the presence of flowing ground water. While the thaw processes may have been initiated by bank erosion on the Takhini River, they have been exacerbated by the high ground ice content and the thermal effect of ground water springs circulating within the ice-rich clusters as depicted in the 3D ERT models (Figure 111).

Since groundwater management will be a key matter when the site will be remediated, YukonU research team performed an UAV survey of the site using a thermal camera on November 24th, 2021. The thermal imagery showed ground water springs flowing in the slump and even generating icings (Figure 112). Moreover, the imagery was postprocessed to produce an ortho-mosaic image that can be superimposed on a DEM (Figure 113 (left)) or geolocated to accurately locate the springs along the headwall (Figure 113 (right)).

Figure 110 Groundwater spring seeping from the headwall at various locations.
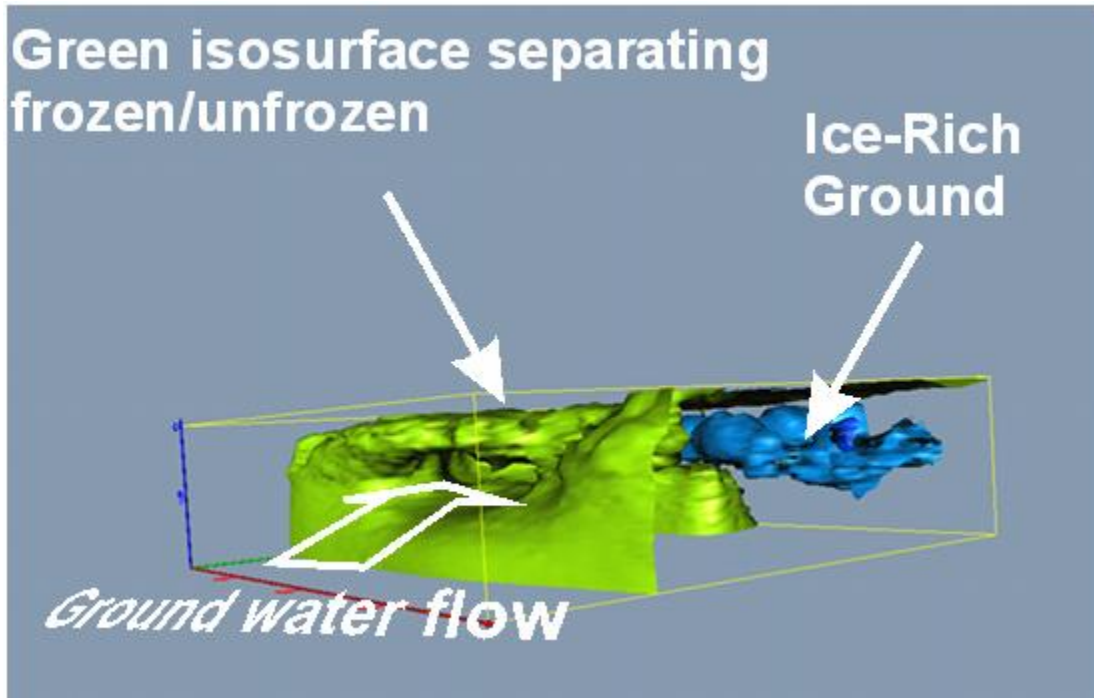
Figure 111 3-D ERT survey at km 1456 of the Alaska Highway. The blue bodies are ice-rich permafrost zones while the greenish iso-curve separate warm and/or wet and/or unfrozen areas from frozen ground.

November 24th, 2021
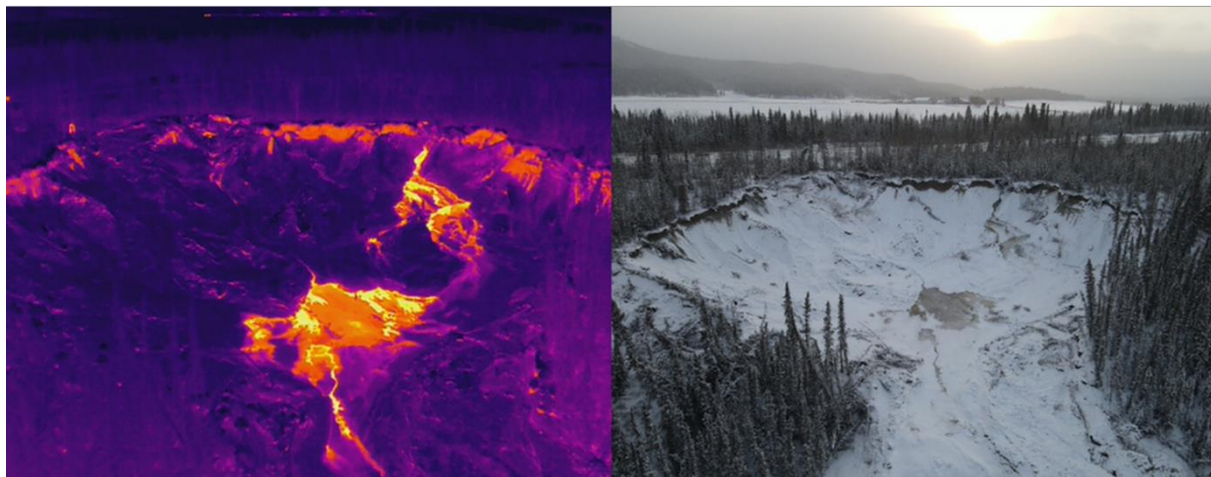
Figure 112 Oblique air photo of the Takhini RTS using Thermal (left) and RGB imagery (right) at the. In the thermal image, the red-yellow hues represent groundwater flowing.

November 24th, 2021
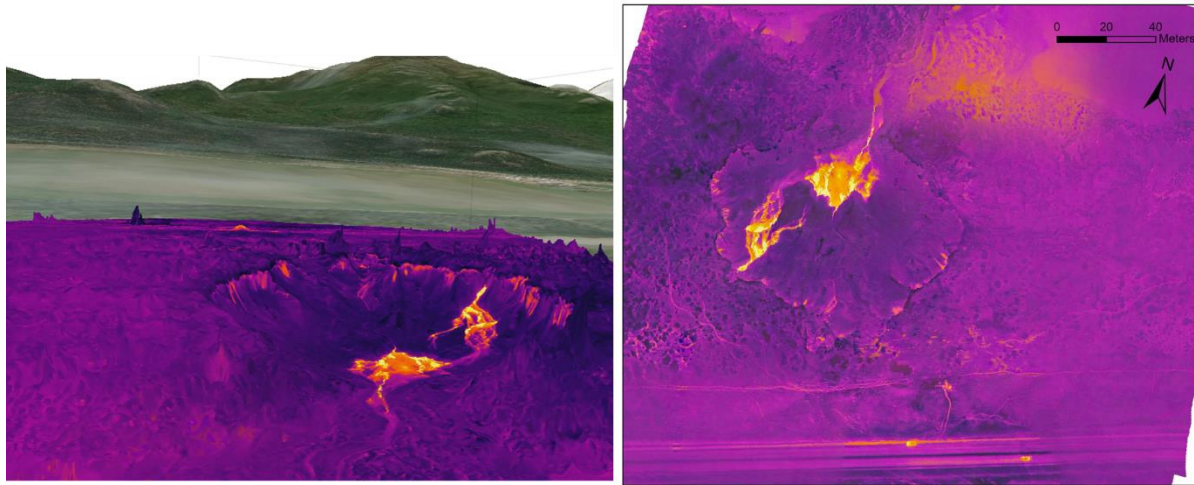
Figure 113 Thermal imagery from Takhini RTS form November 24th, 2021. Left - imagery warped over a digital elevation model; right - vertical ortho-mosaic photo from UAV thermal imagery.

Groundwater is mostly originating from the catchment located in the hills south of the highway, where paths can be inferred from satellite imagery (Figure 114). In addition, water is pumped from the river to irrigate the farmland located on the other side of the highway in the summertime, which may contribute to the degradation processes (Figure 114).
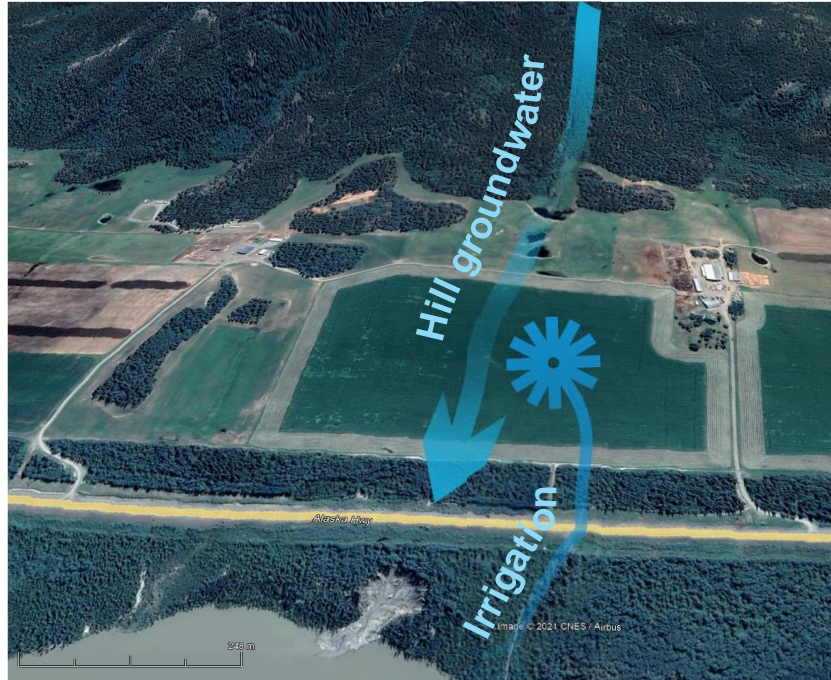
Figure 114 Groundwater sources, from hills and irrigation (vertical exaggeration: 3)

2.2.2.5.   Potential implementation of an Early Warning Alarm system: investigations, tests, and prospective design

2.2.2.5.1.   Early warning indicators

Insightful information was collected during the borehole BH3 experimentation that took place in summer 2020 (see Appendix 2.2.2-A for details). The ground temperature and inclinometer data show precursory indicators of the RTS failure processes. Temperatures recorded in BH3 show an increase 6 days before the headwall reached the borehole and the pipe collapsed (Figure 115 - top). Incremental displacement is minimal at the surface (0 m) and at 0.5 m of depth in BH3 until August 6th. After this, it increases until the borehole failure, 6 days later (Figure 115 - middle and bottom).

Farther away from the slump at BH2, inclinometer data also show a sudden displacement when the slump gained on BH3. This suggests that the slump eroded in one quick event rather than through slow incremental erosive processes.

All together, these records suggest that ground temperature and inclinometer data could be used as an anticipatory warning of failure for a specific point many days before a catastrophic event. Remote daily monitoring of this data could be used in an alarm system to trigger an alert for an upcoming collapse. Such a system could be used to monitor the thaw slump as it progresses towards the highway and help the highway operator ensure public safety.
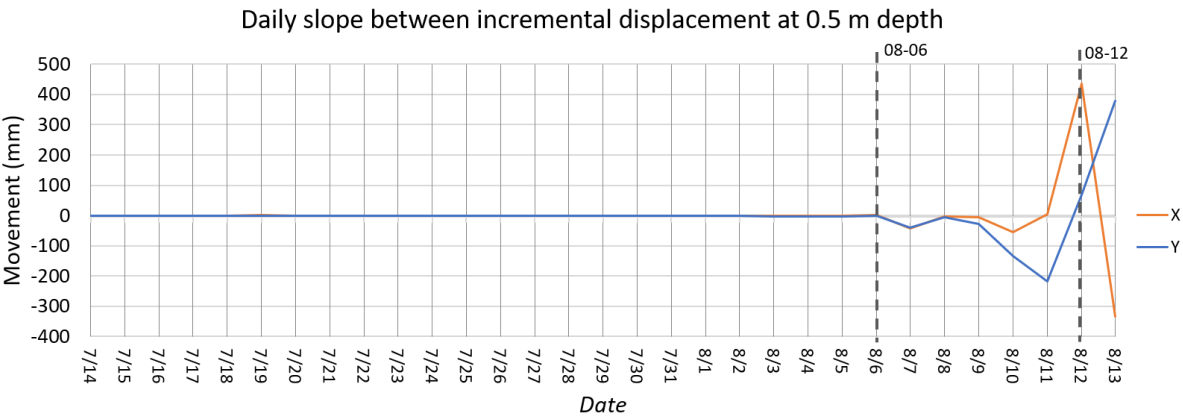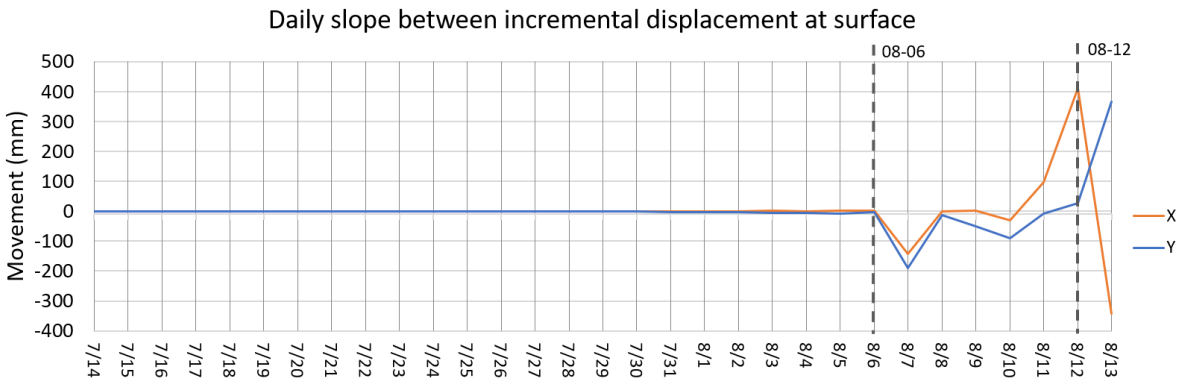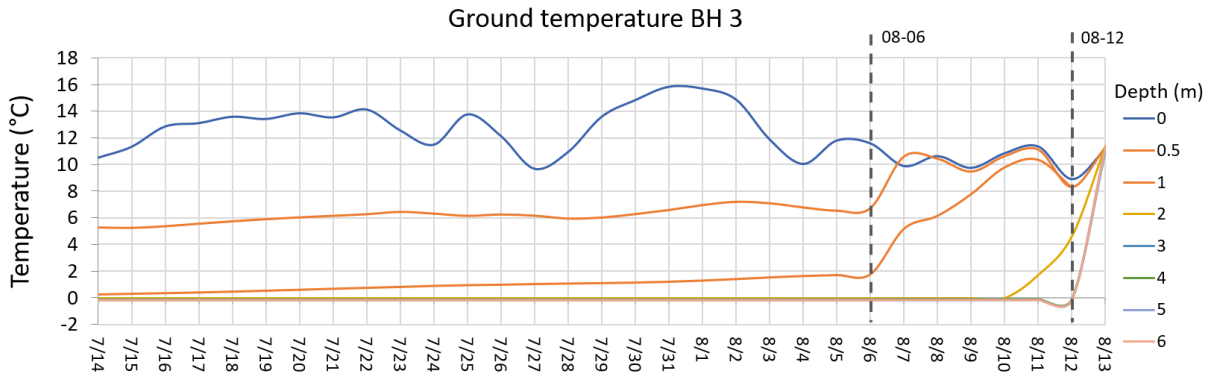
Figure 115 Comparison between ground temperature and displacement recorded by the inclinometer in BH3 at 0m and 0.5 m.

2.2.2.5.2. Prototype test

The borehole A was drilled on July 29th 2021 on the northern side of the highway at the toe of the embankment. After the drilling operation, the borehole was cased with a 1-inch PVC conduit and instrumented with a prototype 32-channel LogR Systems ULOGC32 LoRa+ logger. A custom-built thermistor string was made with 15 temperature sensors, and connected to the logger. The system records ground temperatures every meter between the surface and 14 m in depth. The logger was encased in a custom weatherproof casing to mitigate the risk of damage associated to gravel and snow projections from the nearby highway (Figure 116).

Figure 116 LogR Systems ULOGC32 LoRa+ logger inside ABS casing at Borehole A. The antenna connected to the logger allows communication with the Gateway using long range spectrum modulation.

Wireless data transmission using LoRa (Long Range) spectrum modulation was implemented on September 9th 2021 to transmit and access the data in real time. The Multitech gateway was installed at a nearby farm located 1060 m away from the logger prototype (Figure 117). The Multitech gateway is connected to the internet through the farmer's wi-fi gateway, while the LogR Systems ULOGC32 communicates to the Multitech

gateway using LoRaWAN® standard communication protocols (Figure 118). Using this new configuration, it was possible for the LogR Systems logger to transmit the recorded ground temperatures to the Multitech gateway each hour, which stored the records within its internal memory. The YukonU team was then able to remotely access the gateway at any time from a desktop computer, and to download the data through an internet connection. This downloaded data is in .DAT format, and can be opened in the LogR_App software where it can be exported as a CSV file (Figure 119).

Figure 117 Location of the Logger prototype and the Gateway.

Figure 118. Multitech gateway installation. Left – Gateway (blue box) connected to the internet at local farm. Right - Gateway antenna communicating with LogR Systems ULOGC32 LoRa+ logger located 1060 m away.

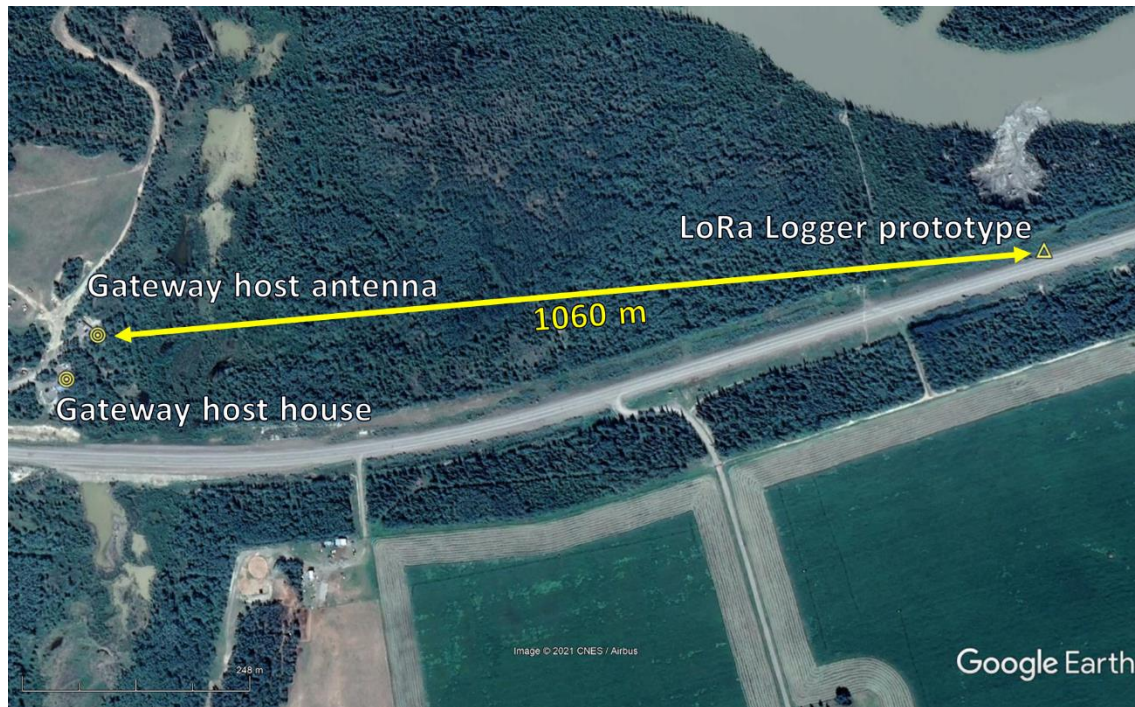| SensorId	timestamp	temperature	pressure	humidity	battery	accelX	accelY	accelZ	CH1	CH2	CH3	CH4	CH5	CH6	CH7	CH8	CH9	CH10	CH11	CH12	CH13	CH14	CH15
Label	Na	Na	Na	Na	Na	Na	Na	Na	0m	1m	2m	3m	4m	5m	6m	7m	8m	9m	10m	11m	12m	13m	14m
Group	Na	Int	Int	Int	Int	Int	Int	Int															
x	Na	Na	Na	Na	Na	Na	Na	Na	0	0	0	0	0	0	0	0	0	0	0	0	0	0	0
y	Na	Na	Na	Na	Na	Na	Na	Na	0	0	0	0	0	0	0	0	0	0	0	0	0	0	0
z	Na	Na	Na	Na	Na	Na	Na	Na	0	0	0	0	0	0	0	0	0	0	0	0	0	0	0
	2021-09-07 11:13	19.3700008	93.868	29.4375	3.17195	-544	44	-848	18.78	18.8	19	18.9	18.6	18.94	18.71	18.21	18.81	18.79	19	18.9	18.84	18.7	18.8
	2021-09-07 12:00	20.5100002	93.8399	29.4541	3.17381	-556	40	-848	19.24	19.2	19.5	19.3	18.9	19.38	19.12	18.51	19.13	19.2	19.43	19.3	19.23	19.1	19.1
	2021-09-07 13:00	21.8400002	93.7814	29.6729	3.17635	-532	16	-856	20.85	20.6	21.1	21.1	19.9	21.26	20.22	19.21	20.44	20.86	21.17	20.8	20.48	20.3	20.5
	2021-09-07 14:00	25.4300003	93.7108	28.1201	3.61421	-628	24	-808	21.79	21.8	22.6	22	21.2	23.15	22.03	20.55	21.49	22.08	22.62	22.7	21.91	21.6	21.7
	2021-09-07 15:00	24.7399998	93.6275	27.0811	3.62408	-768	24	-672	20.77	21.6	23.9	21.5	22.2	23.3	23.48	22.84	23.41	22.8	23.4	25.1	23.43	22.8	23.1
	2021-09-07 16:00	23.8700008	93.5589	26.3691	3.62155	-780	28	-652	21.91	23.3	24	22.4	23	24.12	24.17	23.94	24.13	24.21	24.25	24.2	24.35	24.1	24.2
	2021-09-07 17:00	23.4699993	93.5081	26.0459	3.62155	-780	32	-648	22.02	23.2	23.7	22.4	22.8	23.89	23.94	23.91	24.06	24.02	24.06	23.9	24.02	24	24
	2021-09-07 18:00	21.0300007	93.4557	26.6904	3.61927	-800	28	-624	18.99	20	21	19.4	19.5	20.89	21.37	21.23	20.64	20.58	21.2	21.3	21.34	20.9	20.6
	2021-09-07 19:00	21.6299992	93.4246	25.7236	3.61821	-804	24	-608	21.2	22.2	22.5	21.5	21.7	22.57	22.51	22.47	22.48	22.51	22.57	22.6	22.73	22.6	22.5
	2021-09-07 20:00	21.7099991	93.4069	25.6328	3.62115	-808	32	-612	21.3	22.2	22.6	21.6	21.9	22.65	22.56	22.53	22.5	22.5	22.63	22.7	22.77	22.6	22.5
	2021-09-07 21:00	18.7099991	93.401	32.2578	3.61193	-1000	8	280	21.18	21.2	21.2	19.5	20.1	20.06	20.09	20.64	19.89	20.15	20.7	19.9	19.84	20.1	19.6
	2021-09-07 22:00	12.2200003	93.5169	27.6797	3.59095	-544	4	872	9.674	9.46	9.58	9.42	9.62	9.292	9.289	9.553	9.264	9.266	9.203	9.11	9.236	9.39	9.17
	2021-09-07 23:00	8.35000038	93.3168	26.3691	3.56996	-556	4	876	8.718	8.63	8.64	8.66	8.7	8.576	8.506	8.598	8.534	8.481	8.478	8.46	8.5	8.57	8.48
	2021-09-08 0:00	7.07999992	93.2275	25.9912	3.56408	-560	8	876	7.485	7.39	7.44	7.36	7.42	7.096	7.211	7.381	7.248	7.201	6.997	6.8	7.123	7.33	6.76
	2021-09-08 1:00	6.28000021	93.4186	37.0869	3.56408	-552	4	892	7.19	7.15	7.18	7.12	7.19	6.891	6.971	7.138	6.994	6.991	6.923	6.85	6.97	7.06	6.58
	2021-09-08 2:00	5.03999996	93.2991	42.0254	3.56261	-560	4	880	5.708	5.54	5.59	5.49	5.62	5.414	5.303	5.493	5.626	5.549	5.155	5	5.446	5.31	4.95
	2021-09-08 3:00	5.13000011	93.3973	43.8848	3.56408	-560	4	880	6.31	6.17	6.21	6.17	6.27	6.03	6.078	6.18	6.084	5.986	6.026	5.92	6.02	6.17	5.91
	2021-09-08 4:00	4.0999999	93.335	45.9336	3.56261	-556	8	872	5.149	5.14	5.14	5.12	5.16	5.065	4.9	5.057	5.138	5.016	4.953	4.93	5.014	4.95	4.81
	2021-09-08 5:00	3.94000006	93.2997	47.1455	3.56261	-568	8	880	4.647	4.55	4.62	4.41	4.67	4.207	4.336	4.578	4.426	4.459	4.041	3.93	4.341	4.39	3.78
	2021-09-08 6:00	4.07999992	93.4711	47.9014	3.56261	-560	8	884	5.885	5.82	5.84	5.87	5.88	5.869	5.739	5.808	5.866	5.742	5.822	5.87	5.813	5.81	5.88
	2021-09-08 7:00	4.80000019	93.4735	48.1875	3.56996	-556	8	876	6.32	6.25	6.25	6.3	6.3	6.27	6.187	6.236	6.211	6.125	6.217	6.26	6.216	6.23	6.29
	2021-09-08 8:00	5.17999983	93.4848	48.4697	3.5729	-560	12	880	6.63	6.6	6.57	6.68	6.64	6.66	6.542	6.56	6.541	6.448	6.647	6.67	6.566	6.57	6.75
	2021-09-08 9:00	5.98000002	93.5575	48.7314	3.58172	-568	12	872	7.775	7.76	7.66	7.98	7.83	7.988	7.833	7.689	7.709	7.64	8.063	8.19	7.876	7.8	8.32
	2021-09-08 10:00	7.07999992	93.7316	48.6152	3.5836	-560	4	880	8.766	8.74	8.68	8.99	8.63	8.877	8.904	8.75	8.613	8.378	9.111	9.03	8.798	8.96	9.28

Figure 119 Example of data file collected from the LogR Systems ULOGC32 through the internet.

185

2.2.3. Potential implementation of an early warning alarm system at the Chapman Lake and Takhini RTS sites

The thaw slumps threatening the Alaska Highway and the Dempster Highway sections differ in many aspects but are driven by the same fundamental processes and result in identical threats to the highways. Some of the differences between the sites are that the Chapman Lake site along the Dempster Highway is underlain by colder permafrost than the Takhini River site along the Alaska Highway, and that the Chapman Lake's thaw slump is active only intermittently whereas the Takhini slump in active every year. The slumps are similar insofar as they both developed on ice-rich permafrost hillslopes and occur along rivers. Even though the nature of the ground ice differs between the sites, with ice-wedge and buried ice at Chapman Lake, and segregated ice at the Takhini slump, the mass-wasting processes remain the same. Therefore, a similar approach could be used to implement an early warning alarm system.

As the system developed during this project is primarily based on the use of temperature sensors buried in the ground, a method using ground temperature analysis was developed based on experiments carried out at the Takhini RTS site. At this site, our experiments have shown that a ground thermal signal could be recorded from sensors encased in a vertical borehole a few days before failure (section 2.2.2.5.1). Because the most noticeable signals were observed at shallow depths, it would follow that a similar approach using horizontal thermistor strings buried shallow within the active layer would be effective.

Such a system would include burying a temperature sensor cable 15-20 cm below the ground surface, within the active layer and with a 1-m spacing between each sensor. The cable would run between the edge of the headwall of the slump to a logging station near the road. The logic behind this design is that the layer of soil above the temperature cable would act as a buffer between the sensor and the air, dampening the effect of daily temperature oscillations. As the headwall retreats and exposes the cable to air temperature, the dampening effect of the soil layer will disappear and daily temperatures will oscillate with greater amplitude than the buried sensors, thereby sending the signal that the slump has eroded to this point.

To test the proposed setup, a short experiment was conducted in August 2021 at the Takhini RTS, where an 8-sensor cable was buried horizontally 10-15 cm deep in the ground, using a one-meter spacing between each sensor. The first sensor was buried one meter away from the slump headwall, to provide nine meters of erosion measurements. The temperatures recorded from sensor 5 and 7, originally located 5 and 7 meters away from the headwall can be seen in Figure 120. From July 20th to August 15th

the trends in temperature are similar for both sensors but beginning on August 16th sensor 5 begins to exhibit larger temperature fluctuations, suggesting that the headwall has retreated to this sensor, exposing it to the air.
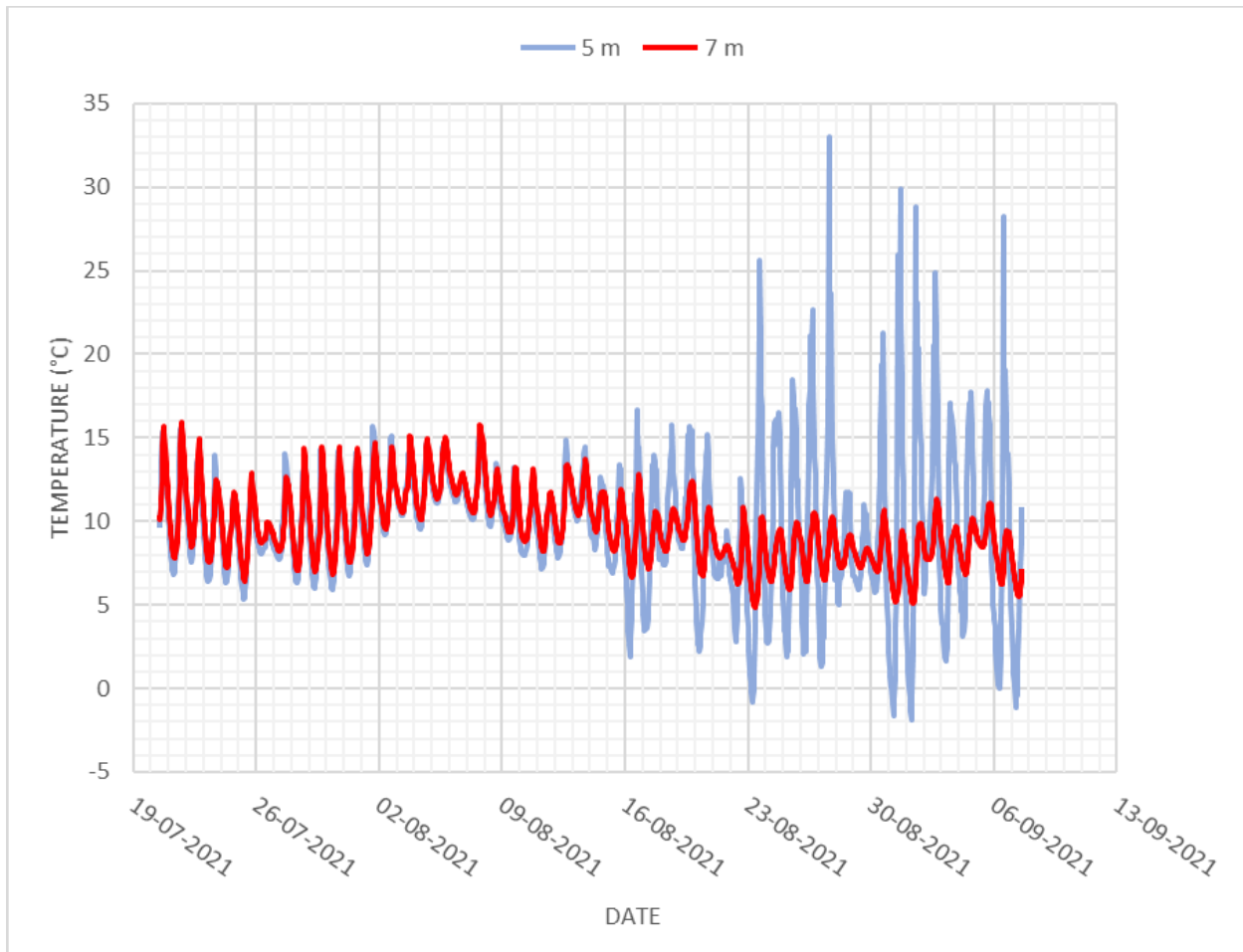
Figure 120 Shallow horizontal ground temperature record for sensor 5 m and 7 m during August 2021.

This experiment can be used as a model for the alarm system wherein the temperature measurements from horizontal sensors could be monitored daily using a simple algorithm based on the oscillation of daily temperatures to signal each time headwall retreat exposes a sensor.

Using the data from these experimental temperature sensors, an algorithm has been developed using the Pandas package in Python. The algorithm is based on the principle that if the sensor is buried in the ground, it will experience less of a temperature fluctuation than the if it were exposed to the air. Therefore, if the temperature recorded

by a sensor is greater than the mean temperature of all the other sensors that are further from the slump (i.e., not eroded), then it is likely exposed to the air. The algorithm is based on the following equations:

$$Warning_a = x_a > \left[\left(\frac{1}{n} \times \sum_{i=(a+1)}^{n} x_{i)} \right) + b \right]$$

Or

$$Warning_a = x_a < \left[\left(\frac{1}{n} \times \sum_{i=(a+1)}^{n} x_i \right) - b \right]$$

Where $Warning_a$ is a warning at a distance a;
x_a is the temperature at a distance a;
n is the number of sensors between a and the logger;
i is $a + 1$ if the sensor spacing is 1m;
And b is a constant ranging from 2-4 depending on the site.

An example of the algorithm written using the Pandas package in Python for these equations can be found in Figure 121 below, and an example of the output can be seen in Figure 122 below.

```
import pandas as pd
import os
os.getcwd()

#set dir
os.chdir('/Users/Fanny/Desktop/ntai algo')

#create df
temp=pd.read_excel("AHI456_2_python.xlsx", na_values= ['NA', 'M'])

# using the other columns to set a mean temp that each column is compared to
temp=temp[['Date','5m','6m','7m','8m']]
temp['mean_temp_5m']=temp[['6m','7m','8m']].mean(axis=1)
temp['mean_temp_6m']=temp[['7m','8m']].mean(axis=1)
temp['mean_temp_7m']=temp[['8m']].mean(axis=1)

#add 'warning' if temp value greater than mean of other temps
temp.loc[(temp['5m'] > (temp['mean_temp_5m']+3)) | (temp['5m'] < (temp['mean_temp_5m']-3)), '5m_warning'] = 'warning'
temp.loc[(temp['6m'] > (temp['mean_temp_6m']+3)) | (temp['6m'] < (temp['mean_temp_6m']-3)), '6m_warning'] = 'warning'
temp.loc[(temp['7m'] > (temp['mean_temp_7m']+3)) | (temp['6m'] < (temp['mean_temp_7m']-3)), '6m_warning'] = 'warning'

m5_failure_time=temp.loc[temp['5m_warning']== 'warning']
m6_failure_time=temp.loc[temp['6m_warning']=='warning']
m7_failure_time=temp.loc[temp['7m_warning']=='warning']
```

Figure 121 Screenshot of the algorithm as written in a Python environment, showing the algorithm script.

Index	Date	5m	6m	7m	8m	mean_temp_5	mean_temp_6	mean_temp_7	mean_temp_8	5m_warning	6m_warning
627	2021-08-16 03:00:00	5.023	7.959	8.841	9.026	8.60867	8.9335	7.336	7.27433	warning	nan
628	2021-08-16 04:00:00	3.457	7.368	8.371	8.675	8.138	8.523	6.5	6.39867	warning	nan
629	2021-08-16 05:00:00	2.785	6.661	7.898	8.31	7.623	8.104	5.91867	5.78133	warning	nan
630	2021-08-16 06:00:00	2.645	6.344	7.47	7.96	7.258	7.715	5.64967	5.48633	warning	nan
631	2021-08-16 07:00:00	1.862	5.562	7.11	7.644	6.772	7.377	5.02267	4.84467	warning	nan
632	2021-08-16 08:00:00	3.011	5.719	6.796	7.363	6.626	7.0795	5.36433	5.17533	warning	nan
637	2021-08-16 13:00:00	11.655	7.787	7.525	7.603	7.63833	7.564	9.015	8.989	warning	nan
640	2021-08-16 16:00:00	16.695	10.972	10.047	9.438	10.1523	9.7425	12.3683	12.5713	warning	nan
641	2021-08-16 17:00:00	15.182	12.361	11.269	10.188	11.2727	10.7285	12.577	12.9373	warning	nan
647	2021-08-16 23:00:00	6.977	9.972	10.632	9.958	10.1873	10.295	8.969	9.19367	warning	nan
648	2021-08-17 00:00:00	5.722	9.03	10.05	9.549	9.543	9.7995	8.10033	8.26733	warning	nan
649	2021-08-17 01:00:00	4.405	8.619	9.492	9.128	9.07967	9.31	7.384	7.50533	warning	nan
650	2021-08-17 02:00:00	3.701	7.959	8.961	8.711	8.54367	8.836	6.79033	6.87367	warning	nan
651	2021-08-17 03:00:00	3.492	7.505	8.478	8.316	8.09967	8.397	6.43767	6.49167	warning	nan
652	2021-08-17 04:00:00	3.625	7.23	8.079	7.984	7.76433	8.0315	6.27967	6.31133	warning	nan
653	2021-08-17 05:00:00	3.51	7.028	7.759	7.708	7.49833	7.7335	6.082	6.099	warning	nan
654	2021-08-17 06:00:00	3.656	6.753	7.495	7.473	7.24033	7.484	5.96067	5.968	warning	nan
661	2021-08-17 13:00:00	12.684	8.793	8.657	8.475	8.64167	8.566	9.984	10.0447	warning	nan
662	2021-08-17 14:00:00	13.403	9.554	9.182	8.945	9.227	9.0635	10.634	10.713	warning	nan

Figure 122 Screenshot of an example of the output of the script showing the time of the warning signal.

The algorithm will require some adjusting as more and better-quality data become available. For example, with more data, the algorithm can be validated more thoroughly. In addition, better care will be taken to bury the sensors at exactly the same depth, and to infill the trenches where the sensors are buried with homogeneous material. Additionally, having access to air temperature sensors could help improve the algorithm by removing the signal from air temperature. Moreover, additional sensors can be included near the logger to serve as more permanent controls for the mean calculations. As such, there is room for improvement, but the foundations for the algorithm have been laid to remotely analyze the data and trigger an alarm.

2.2.3.1. Alaska Highway implementation

The YukonU team currently has two prototype 32-channel LogR Systems ULOGC32 that can be deployed at two locations. The first location would be borehole A, where a prototype is already in place. At this location a cable with 27 sensors could be deployed allowing for a monitoring length of 26 m. The second possible location would be BH2,

where an inclinometer array is already installed. At this location a cable with 21 sensors could be used, therefore allowing for 20 m to be monitored. The proposed setup is shown in Figure 123.

Given the current proximity of the RTS headwall to the road embankment, and the progress made with the alarm system prototype, the implementation of a monitoring and early-alarm system could be possible as soon as spring 2022.
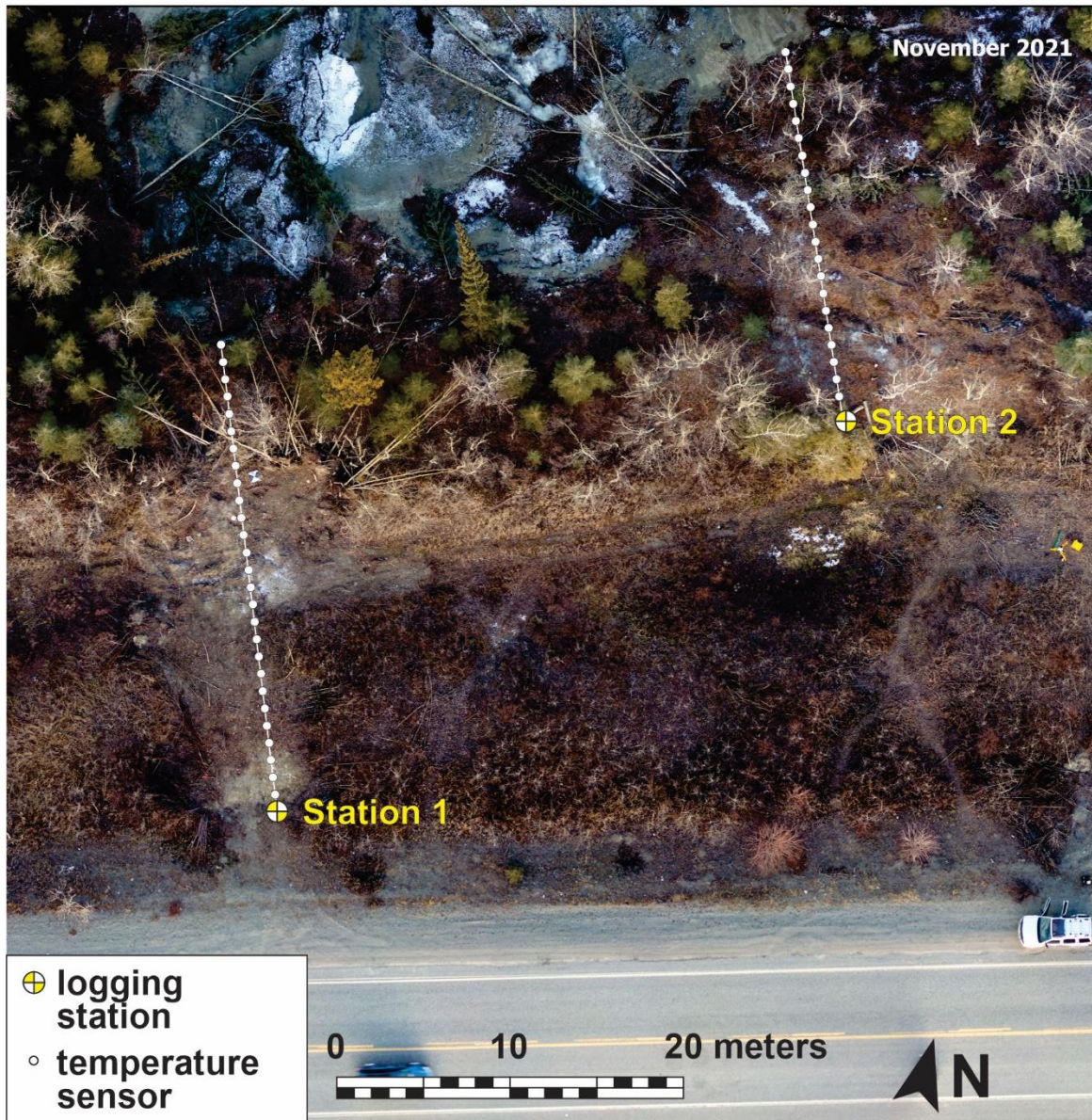

Figure 123 Proposed installation of an early warning alarm system at Takhini RTS site.

2.2.3.2. Dempster Highway implementation

Both the 2006 and 2017 RTS at Chapman Lake along the Dempster Highway were surveyed using UAV imagery to identify locations with pre-failure indicators such as surficial tension cracks.

The 2006 RTS location shows several signs of deformation show in Figure 124. The lobes of the 2006 RTS now encroach on the former road embankment. The coarse material from the abandoned section is caving in the slump covering the natural ground exposure and potentially concealing movement in the bluff. Nevertheless, ground movements are visible above the cliff as tension cracks and subsidence features are developing in the old road (Figure 124 A, B and C). These features, mainly parallel to the bluff, are likely precursory signs of an impending slumping event at this site. An approach similar to that of the Alaska highway could be used here to implement an early warning alarm system. Horizontal arrays of sensors could be deployed at 4 locations perpendicular to the road, using the prototype 32-channel LogR Systems ULOGC32 (Figure 125). Depending on the location, sensor arrays of various lengths will be connected to this logger to a maximum of 32 sensors.

In this configuration two types of signals could be used to trigger an alarm: 1- daily temperature fluctuation thresholds indicating when the headwall reaches a sensor, like for the Alaska Highway site, or 2- a loss of signal from the sensor, when the wire has been snapped due to an abrupt ground movement.

The 2017 RTS location shows deformation signs similar to those of the 2006 site (Figure 126). Tension cracks are visible in the shoulder of the road between the cliff and the concrete barrier installed by HPW to secure the site (Figure 126A and B). Much like the 2006 RTS site, these features are mainly parallel the road and bluff, and could indicate impending slumping. An approach similar to that of the 2006 RTS could be used to implement an early warning alarm system. At this site, three arrays of six temperature sensors could be used set perpendicular to the road and connected to a prototype 32-channel LogR Systems ULOGC32 (Figure 127). The same two types of signals to trigger an alarm could be used including daily temperature fluctuation thresholds, and/or the loss of signal from the sensor.

The proposed design, shown in Figure 127, is intended for a relatively quick implementation, yet could be completed with addition instrumentation. The experimentation led at the Alaska Highway Tahkini RTS has proven that monitoring ground temperature and ground movements using inclinometer or other similar device

within boreholes could be used to trigger a warning. Therefore, the four deepest boreholes located in the field between the Chapman Lake and the road could be instrumented with ULOGC32 LogR Systems to monitor ground temperature and detect signs of groundwater movement in the permafrost. It could trigger an alarm in the case of an unlikely yet possible drainage of the lake with groundwater channeling its way thought massive ice and ice-rich permafrost which may lead to disastrous consequences. In addition, the experimentation has proved that ground movement can be detected at relatively shallow depth for 0 to 2 m. Therefore an array of shallow boreholes could be drilled near the toe of the road embankment, river side, and fitted with 2-m long inclinometer array to be used to detect the movement of a forthcoming slump. There should be located at the star of each horizontal temperature sensor array, as shown in Figure 125 and Figure 127. Such array could be easily retrieved and repositioned should them be at risk.

Unlike at the Alaska Highway site, where a Wifi signal is available, additional work is needed to develop a system using a satellite link. Therefore, the implementation of a monitoring and early-alarm system at the Chapman Lake site will likely only be possible by the summer of 2023.
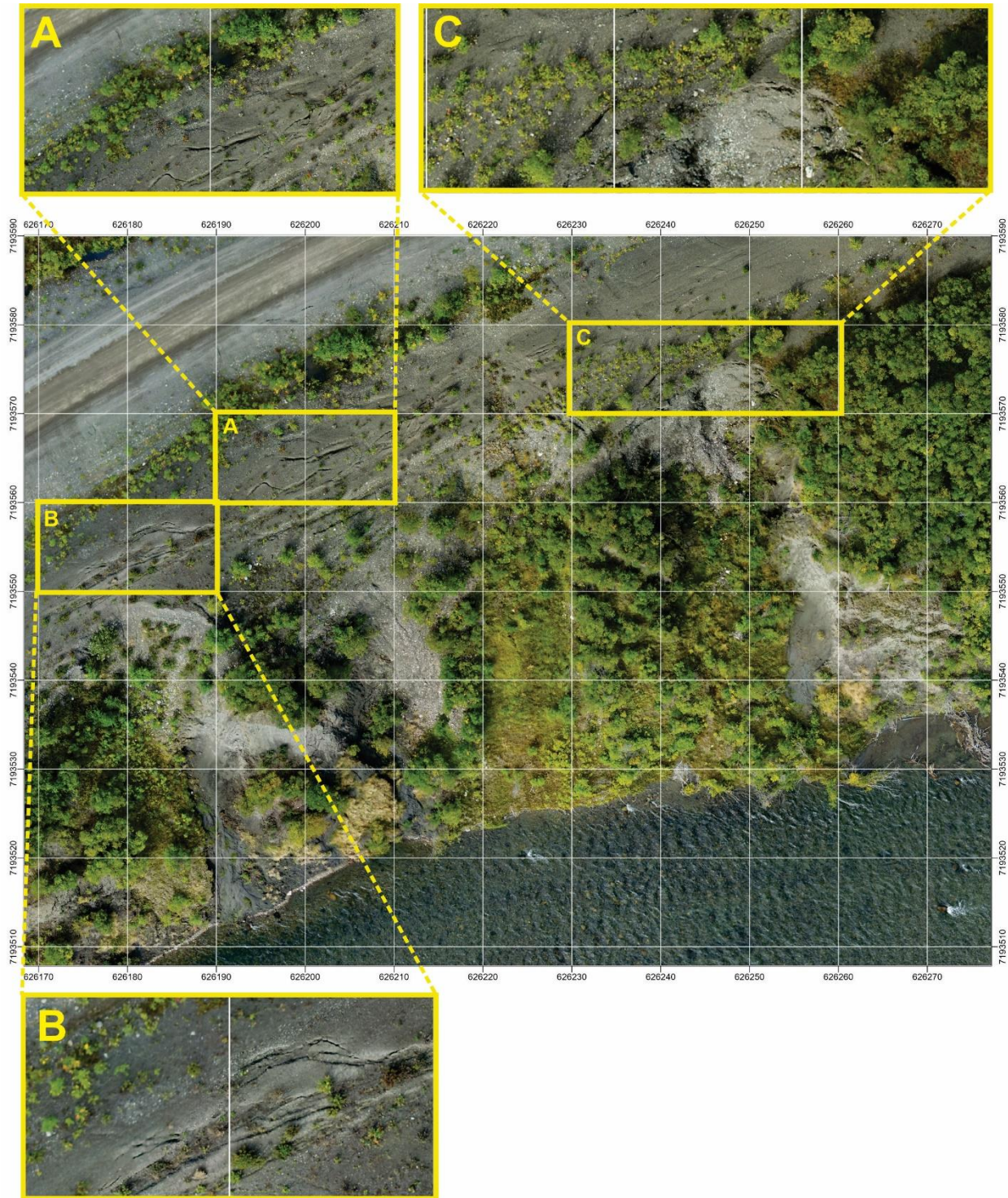
Figure 124 2006 RTS at km 116 of the Dempster Highway in August 2021; A, B and C show pre-failure tension cracks.
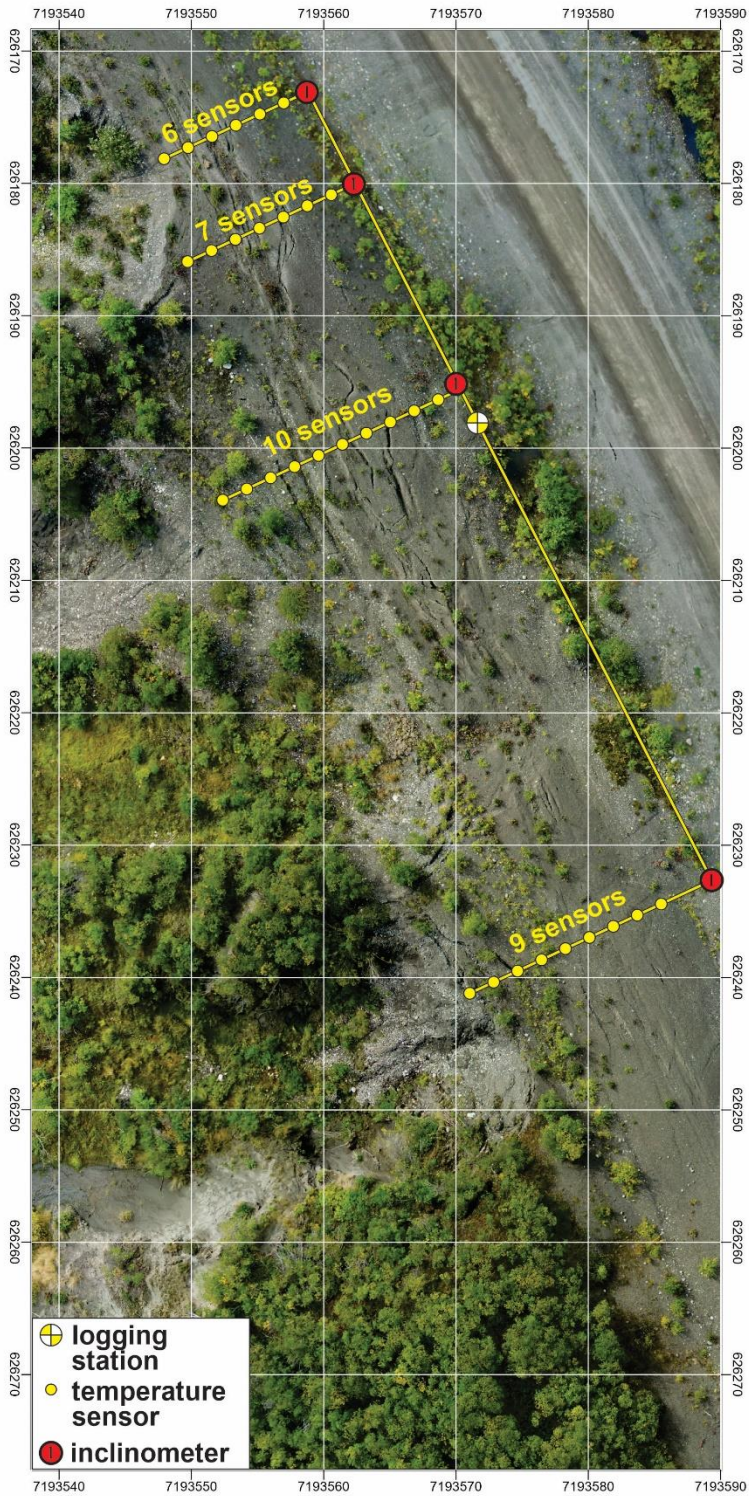
Figure 125 Proposed monitoring array at the 2006 RTS at km 116 of the Dempster Highway.
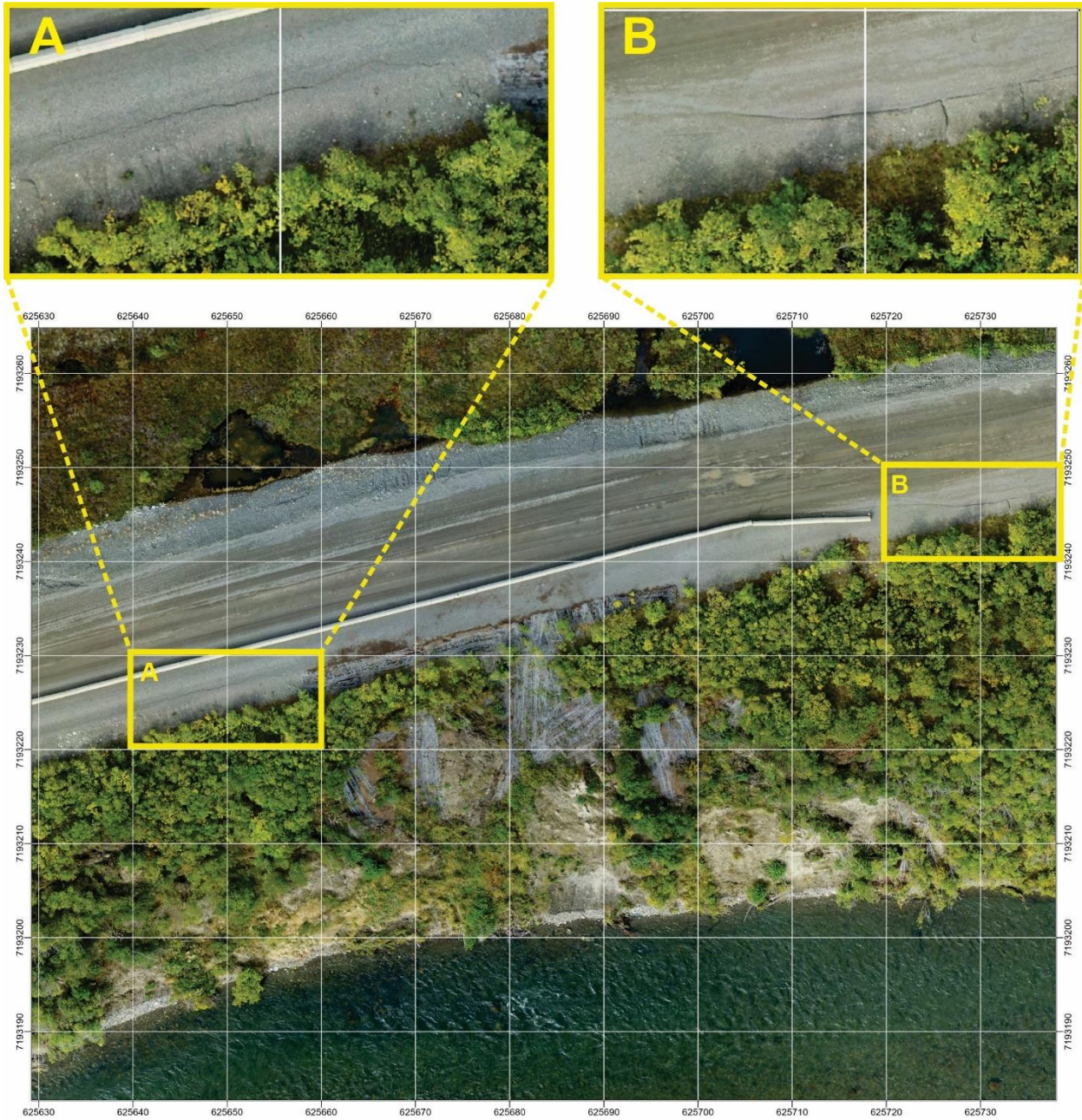
Figure 126 2017 RTS at km 116 of the Dempster Highway in August 2021; A and B show prefailure tension cracks.
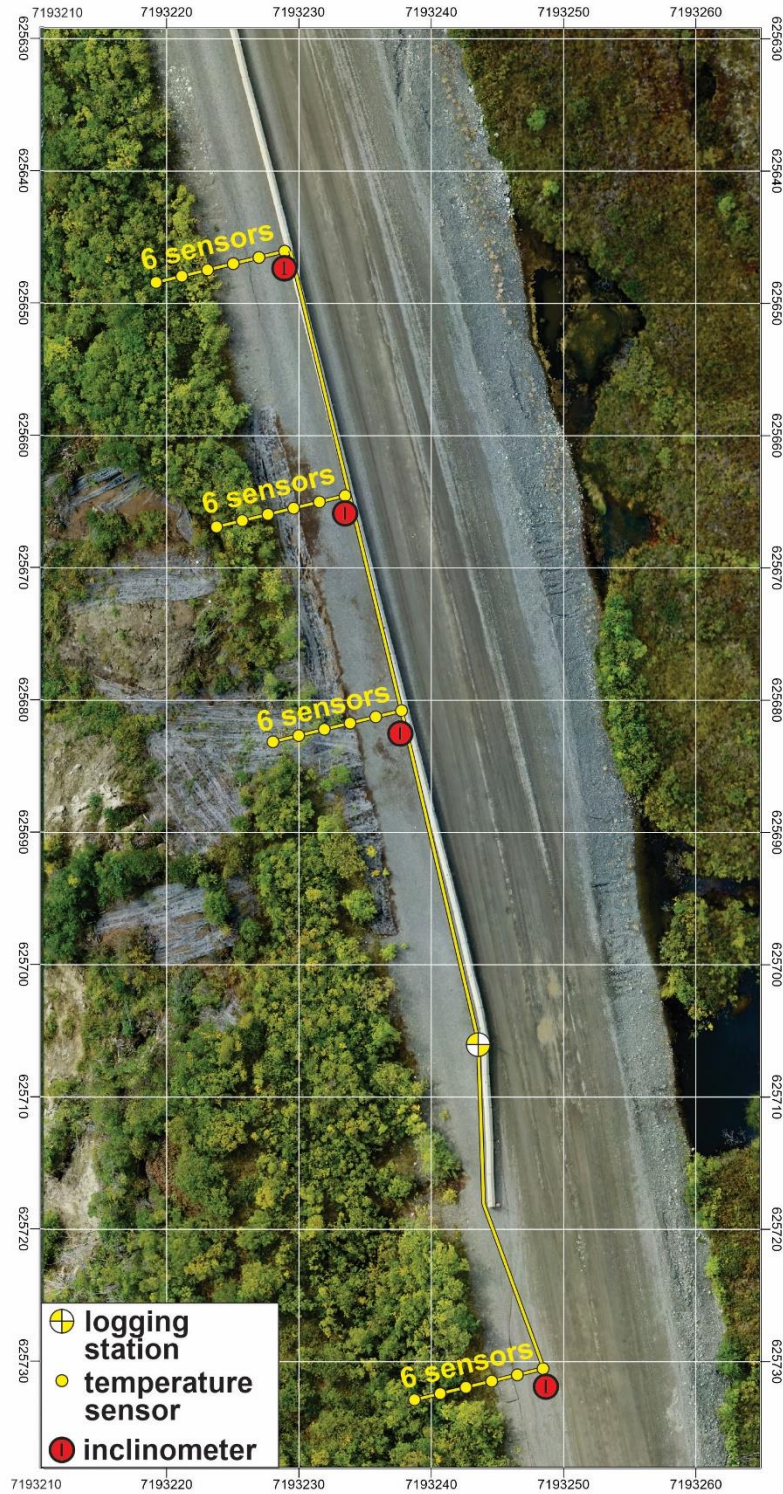
Figure 127 Proposed monitoring system at the 2017 RTS at km 116 of the Dempster Highway.

3. Summary and prospective outcomes

3.1. Current outcomes from the project in Nunavik and Yukon

This project has focused on two main research streams. The first was to expand knowledge on the forms and processes of the geohazards that threaten infrastructure built on permafrost. The second was to develop an alarm system to warn infrastructure operators of impending failures using the information provided by the in-depth site studies.

Over the course of this project, considerable knowledge and a deeper understanding were developed of mass movements resulting from permafrost thaw, most notably of retrogressive thaw slumps. Two Yukon sites have been extensively studied using an innovative methodology combining both above and below-ground assessments.

Below-ground surveys included data collection from geotechnical boreholes drilled mostly to a depth exceeding 10 meters. This allowed for the analysis of deep ground layers, which is crucial to understand the processes leading to infrastructure failure. These boreholes also allowed for the establishment of ground temperature recording stations, which provided information on the thermal regime of the permafrost. This thermal data served as the basis for the development of an automated alarm system that could trigger and send a warning to the infrastructure operator. Additionally, some boreholes were instrumented with inclinometer arrays that allowed for the detection of pre-failure signals several days before the headwall retreated to the borehole. Geophysical surveys including electrical resistivity tomography, electro-magnetism, and ground penetrating radar allowed for the mapping of massive ice which is the catalyst for thaw settlement and retrogressive thaw slumping. These techniques also allowed for the identification of groundwater flows within permafrost which can exacerbate thaw slumping or cause additional risk to infrastructure.

Above-ground surveys consisted mostly of DGPS and UAV surveys. Benchmark monitoring using DGPS provided information about differential ground-surface creep allowing for the identification of new slumping zones. UAV surveys allowed for high spatial and temporal resolution monitoring of RTS evolution over a three-year period. The surveys also allowed for the mapping of features related to permafrost degradation and deformation, such as tension cracks, thereby highlighting potential failure zones. Moreover, UAV imagery was used to produce digital elevation models that allowed for the monitoring of elevation change and the volume of eroded sediment at an RTS.

Finally, thermal imagery was used to observe and locate groundwater springs seeping from the headwall of a retrogressive thaw slump, which will be crucial in shaping remediation plans for the site.

Similar methodological approaches were used on two sites that are impacted by similar processes, suggesting that the general approach could be implemented at similar sites across northern Canada, in both continuous and discontinuous permafrost zones. These in-depth site assessments in the Yukon provide important information for the designing of a tailored monitoring approach to implement an early warning alarm system at the Alaska and Dempster highway geohazard sites.

The second stream of research led to the complete development, from conception to functional physical prototype of an early warning alarm system using LoRa transmission technology. The alarm system allows for the monitoring of geohazards threatening a linear transportation infrastructure in northern communities. The system monitors critical sites in real-time using loggers that communicate with a gateway, thereby transferring data every hour to a server in the cloud. The information can then be downloaded from any location in the word and processed trigger a warning for a potential or imminent risk to linear infrastructure.

This rugged, durable, low-energy system has been successfully implemented in three Nunavik communities along roads and airstrips that are at risk of vertical and/or horizontal ground movements resulting from permafrost thaw. In addition, the system was tested in Yukon, where implementation strategies were devised, and should lead to the implementation of a fully functional early warning alarm system at the Alaska Highway RTS site, as soon as spring 2022.

3.2. Prospective outcomes

There are two main prospective outcomes from this project. The first is the technical evolution and improvement of the new early warning alarm system. The second is the potential for this system to be applied to different contexts and environments.

The system currently allows for the monitoring of at-risk sites based only on ground temperature recordings. This configuration is adapted to the context of this study, where the ground thermal regime is the most relevant variable to monitor, and where transportation infrastructure is located within or at close proximity to communities and

housing. Nevertheless, experimentation led at the Tahkini RTS has proven that monitoring ground movements using inclinometers or other similar devices could be used to trigger a warning. Therefore, adding new functionalities to the loggers like connecting to and reading other sensors such as movement detectors and humidity sensors, will expand the utility of our warning system.

The system currently requires an internet connection for the data to be transferred through a gateway to the cloud. Therefore, the system cannot be used to monitor a remote site at the present time. A workaround for this will be to use a satellite link to connect to the cloud. However, advances in satellite internet technology (for example, Starlink by SpaceX) suggest that this may be an affordable and easy solution to adapt this system to remote sites. As such, there are some technical improvements that will allow of more widespread and flexible use of this system.

In fact, the use of this system is not restricted to permafrost-thaw induced geo-hazards and transportation infrastructure. Its capabilities to transmit important amounts of data in real-time make it ideal to monitor several sites within a community. In addition to linear infrastructure, buildings and other types of infrastructures could be monitored through a constellation of networked loggers. Pending the use of new movement detecting sensor, mass movements could be monitored along road networks in many environments in the south. Different types of geo-hazards, such as flooding and washouts could be monitored too, in a more flexible and reliable way than is currently possible. The system developed for this project may render geo-hazard monitoring more affordable and user-friendly with little more development.

4. References

Allard, M., Fortier, R., Gagnon, O. et Michaud, Y. (2004). Problématique du développement du village de Salluit, Nunavik. Salluit: Une communauté en croissance sur un terrain sensible au changement climatique. Rapport final. Québec, Centre d'études nordiques, Université Laval. 93 pp.

Allard, M., Fortier, R., Sarrazin, D., Calmels, F., Fortier, D., Chaumont, D., Savard, J.P. et Tarussov, A. 2007. L'impact du réchauffement climatique sur les aéroports du Nunavik: caractéristiques du pergélisol et caractérisation des processus de dégradation des pistes. Université Laval, Centre d'études nordiques, 192 p.

Allard M., L'Hérault, E., Gibéryen, T. et Barrette, C. (2010). L'impact des changements climatiques sur la problématique de la fonte du pergélisol au village de Salluit, Nunavik. Rapport final : Salluit : s'adapter et croître. Réalisé pour le compte du ministère des Affaires Municipales, des Régions et de l'Occupation du territoire du Québec. Québec, Centre d'études nordiques, Université laval. 64 pp.

Allard, M., Chiasson, A., B. St-Amour, A., Mathon-Dufour, V., Aubé-Michaud, S., L'Hérault, E., Bilodeau, S. et Deslauriers, C., (2020). Caractérisation géotechnique et cartographie améliorée du pergélisol dans les communautés nordiques du Nunavik. Rapport final. Québec, Centre d'études nordiques, Université Laval.

Andersland, O. B., & Ladanyi, B. (2003). Frozen ground engineering. John Wiley & Sons.

Beaulac, I. et G. Doré (2005). Bilan de la condition des pistes et des chemins d'accès menant aux aéroports du Nunavik, Université Laval, Département de génie civil, rapport GCT-2005-09, 123 p.

Beierle, B. D. (2002). Late Quaternary glaciation in the Northern Ogilvie Mountains: revised correlations and implications for the stratigraphic record. Canadian Journal of Earth Sciences, 39(11), 1709-1717.

Bilodeau, S., B. St-Amour, A., Chiasson, A. et Allard, M. (2020). Analyse de données géophysiques et recommandations sur les mesures d'adaptation aux changements climatiques pour les travaux de rechargement des aires de mouvement de l'aéroport d'Inukjuak. Rapport final réalisé pour le compte du ministère des Transports du Québec, Centre d'études nordiques, Université Laval, 27 p.

Bostock, M. G. (1996). Ps conversions from the upper mantle transition zone beneath the Canadian landmass. Journal of Geophysical Research: Solid Earth, 101(B4), 8393-8402.

Burn, C. R. (1994). Permafrost, tectonics, and past and future regional climate change, Yukon and adjacent Northwest Territories. Canadian Journal of Earth Sciences, 31(1), 182-191.

Burn, C., Moore, J., O'Neil, B., Hayley, D., Trimble, R., Calmels, F., Orban, S., and Idrees, M. 2015. Permafrost characterization of the Dempster Highway, Yukon and Northwest Territories. GEOQuébec2014: 64th Canadian Geotechnical Conference & 7th Canadian Permafrost Conference, Sept. 20-23, 2015, Québec, Québec. Canadian Geotechnical Society.

Calmels, F., Roy, L.P., Grandmont, K. and Pugh, R. 2018. A Summary of Climate- and Geohazard-Related Vulnerabilities for the Dempster Highway Corridor. Yukon Research Centre, Yukon College, 200 p.

Centre d'etudes Nordiques (2021a). *Permafrost Data Nunvik.* Github. *https://github.com/PermafrostDataNunavik/CEN_Project.git*

Centre d'etudes Nordiques (2021b). *Monitoring of landslide risk level in Salluit, Nunavik.* ArcGIS online. https://bit.ly/Landslide-Risk-Monitoring_Salluit-Platform

Cilfone, Antonio, Luca Davoli, Laura Belli, and Gianluigi Ferrari. 2019. "Wireless Mesh Networking: An IoT-Oriented Perspective Survey on Relevant Technologies" *Future Internet* 11, no. 4: 99. https://doi.org/10.3390/fi11040099

French, H., & Shur, Y. (2010). The principles of cryostratigraphy. Earth-Science Reviews, 101(3-4), 190-206.

Gauthier, S. (In prep). Développement de méthodes de diffusion des données climatiques et environnementales en appui à l'aménagement du territoire en zone de pergélisol (Salluit, Nunavik) [Doctoral thesis]. Département de géographie, Université Laval. Québec, Qc, Canada.

Idrees, M., Burn, C., Moore, J., and Calmels, F. 2015. Monitoring permafrost conditions along the Dempster Highway. GEOQuébec2014: 64th Canadian Geotechnical Conference & 7th Canadian Permafrost Conference, Sept. 20-23, 2015, Québec, Québec. Canadian Geotechnical Society.

Hegginbottom, J.A., Dubreuil, M.A. and Harker, P.T. 1995. Canada, Permafrost. National Atlas of Canada. 5th ed., Natural Resources Canada, MCR 4177.

Lacelle, D., Lauriol, B., Clark, I. D., Cardyn, R., & Zdanowicz, C. (2007). Nature and origin of a Pleistocene-age massive ground-ice body exposed in the Chapman Lake moraine complex, central Yukon Territory, Canada. Quaternary Research, 68(2), 249-260.

Lee, H. C. and Ke, K-H. (2018). Monitoring of Large-Area IoT Sensors Using a LoRa Wireless Mesh Network System: Design and Evaluation. IEEE Transactions on Instrumentation and Measurement. p. 1-11. 10.1109/TIM.2018.2814082

L'Hérault, E. (2009). Contexte climatique critique favorable au déclenchement de ruptures de mollisol dans la vallée de Salluit, Nunavik. Département de Géographie. Québec, Université Laval. Thèse (M. Sc.), 149 p.

L'Hérault, E., M. Allard, C. Barrette, G. Doré, et D. Sarrazin (2012). Investigations géotechniques, caractérisation du pergélisol et stratégie d'adaptation dans un contexte de changements climatiques pour les aéroports d'Umiujaq, Inukjuak, Puvirnituq, Akulivik, Salluit, Quaqtaq, Kangirsuk et Tasiujaq, Nunavik. Rapport final. Réalisé pour le compte du ministère des Transports du Québec. Québec, Centre d'études nordiques, Université Laval, 224 p.

L'Hérault E., Doré G., Kong X., Brooks H., Baron Hernandez M. F., Lemieux C. et Allard M. (2021). Adapter la conception et développer des outils de gestion intégrés pour soutenir l'adaptation aux changements climatiques des infrastructures de transport du Ministère des Transports du Québec en région de pergélisol au Nunavik (CC19.1). Rapport final réalisé pour le compte du Ministère des Transports du Québec. Département de génie civil et de génie des eaux et Centre d'études nordiques, Université Laval, Québec, 432 p.

L'Hérault, E., B. St-amour, A., Roy-Léveillée, P. and Allard, M (in prep.). Travaux de modification de l'instrumentation pour le suivi thermique du pergélisol et d'auscultation géotechnique par forages peu profonds, piste d'atterrissage d'Inukjuak. Rapport réalisé pour le compte du Ministère des Transports du Québec. Centre d'études nordiques, Université Laval, Québec.

Savard, C. (2006). Imagerie électrique de la sous-fondation pergélisolée des pistes d'atterrissage au Nunavik. Québec, Université Laval. 244 p.

Smith, C.A.S., Meikle, J.C., and Roots, C.F. (editors), 2004. Ecoregions of the Yukon Territory: Biophysical properties of Yukon landscapes. Agriculture and Agri-Food Canada, PARC Technical Bulletin No. 04-01, Summerland, British Columbia, 313 p.

Coudé, R. (2021). Radio Mobile Online (VE2DBE), http://www.ve2dbe.com/rmonline.html

Semtech (2019). LoRa® and LoRaWAN®: A Technical Overview. Technical Paper26 p.

Zazula, G. D., Froese, D. G., Schweger, C. E., Mathewes, R. W., Beaudoin, A. B., Telka, A. M., … & Westgate, J. A. (2003). Ice-age steppe vegetation in east Beringia. Nature, 423(6940), 603-603.